Coventry University

DOCTOR OF PHILOSOPHY

Sustainable design of "green" concrete overlays - shear failure at cracks and inadequate resistance to reflection cracking

Xu, Yi

Award date:
2014

Awarding institution:
Coventry University

Link to publication

General rights
Copyright and moral rights for the publications made accessible in the public portal are retained by the authors and/or other copyright owners and it is a condition of accessing publications that users recognise and abide by the legal requirements associated with these rights.

- Users may download and print one copy of this thesis for personal non-commercial research or study
- This thesis cannot be reproduced or quoted extensively from without first obtaining permission from the copyright holder(s)
- You may not further distribute the material or use it for any profit-making activity or commercial gain
- You may freely distribute the URL identifying the publication in the public portal

Take down policy
If you believe that this document breaches copyright please contact us providing details, and we will remove access to the work immediately and investigate your claim.

Download date: 04. May. 2023

Sustainable Design of "Green" Concrete Overlays - Shear Failure at Cracks and Inadequate Resistance to Reflection Cracking

By

Yi Xu

November 2014

Sustainable Design of "Green" Concrete Overlays - Shear Failure at Cracks and Inadequate Resistance to Reflection Cracking

By

Yi Xu

November 2014

A thesis submitted in partial fulfilment of the University's requirements for the Degree of Doctor of Philosophy

To my family

Acknowledgements

This research project was co-funded by the Engineering and Physical Sciences Research Council (EPSRC) and Aggregate Industries Ltd (AI). Their financial support is highly appreciated.

First, I am especially grateful to my supervisor Dr. J. N. Karadelis who not only encouraged and supported me during this study, but also inspired and trained me to become a research-minded engineer.

I wish to express my sincere thanks to the technicians Kieran Teeling, Ian Breakwell and Terry Teeling for their great help on the experimental work. Also I would like to acknowledge my colleagues Yougui Li, for his friendship and inspirational work that encouraged an active research environment.

I am particularly grateful to my beloved parents for their love, understanding, support and endurance throughout these years. Furthermore, my heartfelt appreciation goes to my husband who has been an invaluable support during my research work. Certainly, this thesis is dedicated to them.

There are also many other people who supported and helped me directly or indirectly during my study. I wish to express my deepest gratitude to all of them that are not named in this short page.

Yi Xu

Summary

Concrete overlays have been used as a rehabilitation technique since 1913 - the first practice of using Portland cement concrete to resurface existing pavements, took place in United States. Today, the need for durable and environmentally-friendly construction technologies with low life-cycle costs has brought the world vision to bonded concrete overlays (BCO), which is recognized as a sustainable and effective solution by making maximum use of the existing, structurally damaged concrete pavement. Most research and investigations on BCOs has been carried out in several American states but generally with normal ordinary Portland cement concrete. There is no method readily available for a fast and sound bonded repair of damaged concrete pavements which both fully utilises the potential of the worn concrete pavement and enhances the mechanical properties to give a performance which should equal or even surpass the original.

A Pavement Repair Management System (PRMS) has been developed at Coventry University offering a pioneering approach to concrete road rehabilitation. It aims to enhance the structural and functional deficiencies and extend the life of the pavement and at the same time introduce substantial benefits, such as savings in construction material, time, labour and costs, by bonding a layer of high strength concrete on top of the existing, damaged pavement. The utilization of the residual structural potential of the existing worn pavement makes it more sustainable in both environmental and economic terms, as an alternative to the wholesale demolition and reconstruction of the existing pavement.

Shear failure at cracks/joints is a major cause of degradation of concrete pavements. Not only it leads to serviceability problems but also introduces reflective cracks and becomes an issue of structural integrity, durability, riding quality and safety for the users. The optimized overlaid material benefits from its high strength and stiffness. However, it raises some concerns regarding its shear performance due to the potential brittleness and relatively smooth fracture surface. This research aims to make a contribution in understanding the behaviour of a concrete pavement overlay under shear loading, and to control and evaluate reflective cracking due to shear by means of utilisation of steel fibres to provide adequate resistance to reflective cracking.

A new mix design approach was developed and described in Chapter 3 to produce mixes with high bond strength to the underlying pavement and to facilitate the rapid construction process. The shear capacity of the developed mix was scrutinized experimentally in Chapter 4 employing the purposely developed single notch shear beam test. Not only it enabled the evaluation of the material performance under predominant shear mode but also allowed for analysis on a progressive failure process (crack development). It was shown that the superior quality of the new overlay material achieved high early strength and provided an efficient resistance to reflective cracking. The developed mix design method, laboratory testing data and recorded performance are instructive for the industry, and for future development of pavement overlay design guidance.

Last but not least, the progressive failure process was successfully simulated using finite element modelling techniques, as presented in Chapter 6. The cohesive zone model (CZM) was adopted in fracture simulations of the test to reflect the fibre bridging effect and aggregate interlock at the crack interface. Nomographs deduced from finite element analysis showed increasing overlay thickness can effectively reduce the susceptibility to shear failure and reflective cracking and minimise the differential displacement at underlying joints/ cracks. The multi-cracking feature of steel fibre reinforced concrete (SFRC) overlay can provide a safe buffering zone and an effective crack control.

List of Symbols

Greek

ν	Poisson's ratio
ρ	material density
ε	strain
σ	stress
γ	shear strain
τ	shear stress
δ	displacement
Δ	amplitude or range

Subscript

min	minimum
max	maximum
optm	optimum
t	tension
x, y, z	axis directions
ult	ultimate
eq	equivalent
del	delamination
cr	cracking
a, ad	adhesive
stb	splitting tensile bond strength
sb	direct shear bond strength
s	smooth interface
r	roughened interface

Supercript

a	analytical
e	experimental

Abbreviations

2D	Two Dimensional
3D	Three Dimensional
ACPA	American Concrete Pavement Association
ACV	Aggregate Crushing Values
BCO	Bonded Concrete Overlays
CA	Coarse Aggregate

CBM	Cement Bonded Material
CEM	Cement
CRCP	Continuously Reinforced Concrete Pavement
CZM	Cohesive Zone Model
Conv.	Conventional
CTD	Crack Tip Displacement
FA	Fine Aggregate
FE	Finite Element
FEA	Finite Element Analysis
FRC	Fibre Reinforced Concrete
JCPC	Jointed Plain Concrete Pavement
LEFM	Linear Elastic Fracture Mechanics
LF	Long Steel Fibre
LPD	Loading Point Displacement
LVDT	Linear Variable Differential Transformers
M-P	Modified Proctor
MTK	Metakaolin
M-VB	Modified Vebe
NTD	Notch Tip Displacement
OPCC	Ordinary Portland Cement Concrete
PFA	Pulverized Fuel Ash
PM	Polymer Modified
PMC	Polymer Modified Concrete
PRSS	Pavement Repair and Strengthening System
PVA	Polyvinyl Alcohol
RCC	Roller Compacted Concrete
SBR	Styrene Butadiene Rubber
SIF	Stress Intensity Factor
SF	Steel Fibre/Short Steel Fibre
SFRC	Steel Fibre Reinforced Concrete
SFRCC	Steel Fibre Reinforced, Roller Compacted Concrete
SF-RC-PM-BCO	Steel Fibre Reinforced, Roller Compacted, Polymer Modified, Bonded Concrete Overlay
SNSBT	Single Notch Shear Beam Test
S-P	Standard Proctor
Stren.	Strength
VCCT	Virtual Crack Closure Technique

Table of Contents

CHAPTER 1 INTRODUCTION

1. Introduction

1.1 A historic review

Concrete overlays have been used as a rehabilitation technique since 1913 - the first practice of using PCC to resurface existing pavements in the United States. (Hutchinson 1982) Around 1960s, this technique was employed in more rehabilitation projects in America (McGhee 1994). Till 1990s, a peak increase in use of concrete overlays arrived with the improvements in concrete paving technology (ACI Committee 325 2006).

Nowadays, the need of safer, faster, more durable and environmentally friendly construction technologies with lower life-cycle costs has now been widely recognised. Among the rehabilitation methods, concrete overlays have the predominance to extend service life and to add durability and strength to existing pavements without massive traffic disturbing or 'appalling' budgets, which are not desired by any road authorities, especially during an economic downturn.

When a section of roads reaches a level of deterioration, the overseeing organization will be facing the choices of reconstruction or repair. The former is generally undesired for the high cost, the site waste generated from demolition and the long duration of road closure or traffic control. In contrast, constructing a course of bonded concrete material on top of the worn pavement makes use of the residual strength of the existing construction but enhanced structural performance and extended the service life. It is considered to be more cost-efficient and environmentally-friendly. The cost of a properly designed and constructed Bonded Concrete Overlay (BCO) is only half that of a full depth reconstruction (Delatte Jr. and Fowler 1998).

The other most commonly-used material to form the overlays is bituminous mix. It is still being used as an effective solution when a pavement surface deteriorates to a point of needing repairs. It is favoured for low noise as a surface material, and for low cost and fast construction, despite the fact the asphalt overlay has a typical life expectation of 8-12 years, while a treated concrete surface can last 17 years. There are proven techniques, such as "grind and groove" and "exposed aggregate concrete surface", which were proved to have the noise level even less than hot rolled asphalt. (Donegan 2012) As the concept of whole-life cost being introduced to the industry, the highways authorities are encouraged to re-

evaluate the two options – cement concrete and asphalt concrete. The whole-life cost includes not only the initial construction cost but also the following maintenance cost and allowance for future repairs during the total life span of the structure. Meanwhile, the continuous increase in bitumen prices also reduces the initial cost difference between concrete and asphalt road treatment. With all these components taken into account, the transportation agencies realized cement concrete overlays may be more economical in the long term than asphalt concrete (AC) overlays (Hutchinson 1982). Furthermore, the "stiff and rigid" concrete pavements, in a number of European studies, were reported to be more efficient in fuel consumption in Heavy Goods Vehicles (HGVs) than flexible asphalt pavements, which present concrete pavements in a favourable position in de-carbonation and being more sustainable. The fuel consumption difference is mainly attributed to macro texture differences (Per Jonsson and Bengt-Ake Hultqvist 2008).

Judging from the bonding features between new overlays and existing pavements, there are three main types of concrete overlays – thin bonded overlay, BCO and much thicker overlay. Thin and ultrathin concrete overlays (i.e. whitetoppings) of 50-100mm are commonly used to rehabilitate deteriorated asphalt pavement, but rarely used in rehabilitating concrete pavement. Much thicker unbonded concrete overlays can restore or surpass the original mechanical response of worn pavement. It is recommended for jointed reinforced concrete pavement (JRCP) to avoid the stress concentration above the existing joints and to accommodate the corresponding movements. However it makes little use of the existing construction. Although it could be more economical than complete reconstruction, it is still not regarded as an effective rehabilitation solution. The proposed bonded concrete overlay (BCO) is designed to be fully bonded to continuously reinforced concrete pavements (CRCP) and make the maximum use of the existing structural concrete pavement. Hence the required thickness is reduced and a more economical and sustainable solution is established (Hughes 2003).

The application experience of BCO somehow has not been very successful, except for a few exceptions. "They almost failed rapidly due to excessive reflection cracking and/or excessive delamination" (Delatte Jr. and Fowler 1998).

To tackle the problems, a Pavement Repair and Strengthening System (PRSS) is under development at Coventry University offering a pioneering approach to road rehabilitation. It

aims to develop a bonded polymer modified overlay with the superior mechanical properties of concrete and the versatility of asphalt to facilitate fast construction by asphalt paving machinery. The utilization of the residual structural potential of the existing worn pavement makes it more sustainable in both environmental and economic terms as an alternative to the reconstruction of the existing pavement. This overlay has to provide adequate bond with the substrate, high tensile and flexural strengths and sufficient resistance to reflective cracking. With the modern technique of using roller compaction of low workability concretes, it should be able to avoid the formworks needed for conventional concrete pavements and makes the construction process easier and quicker.

As a great technical innovation and breakthrough, it will bring a fast, economical, environmental friendly and sustainable rehabilitation solution. However, as all the other new techniques at early stages, this new paving method still has considerable unknown areas. This research will be focusing on the development of the mix design, the shear resistance at cracks to control the problem of reflective cracking.

1.2 Rationale

The classic failure modes of BCO were discussed elsewhere (Hughes 2003) and summarized in Table 1.1. Pavement distress occurs as a consequence of the continuous engagement of the initial cement hydration process, daily and seasonal temperature variation and traffic loading during construction and the subsequent operation. The shrinkage cracking and temperature induced cracks were studied for material characterization in this study. Delamination is only discussed briefly in this research since the topic is covered in a parallel study by Olubanwo (Olubanwo 2013).

Table 1.1 Causes to BCO Failure

Causes	Phenomena and Defects
Cement hydration process	Cracking due to drying shrinkage Delamination
Variation of temperature	Short term temperature induced cracks Long term temperature induced cracks Delamination
Construction and Traffic Loading	Delamination Reflective cracking – flexural & shear

Being one of the main reasons causing failure of concrete overlays, reflective cracking occurs when the existing cracks in the underlying pavements reflect into the newly constructed overlay under traffic loads. Cracking in overlays reduces load carrying capacity, generates low cycle fatigue failure and considerably shortens the pavement serviceable life. Furthermore, cracks in overlays offer large chance of having de-icing salt creeping through the overlay to contact with the reinforcement, which leads to reinforcement corrosion and rupture (Zhang and Li 2002).

Reflective cracking is almost inevitable. However the crack width must be restricted to an acceptable value, so that the overlay can provide adequate flexural and shear resistance even after cracking. Reinforcement in the BCO should also be properly designed to provide at least a similar overall post-cracking resistance in any direction to the un-cracked pavement. As traffic passes by, pavement undergoes repetitive loading under flexure and shear. Flexure problem is dealt with in another parallel study. This research is to investigate the shear failure and reflective cracking in concrete pavements.

Shear failure at cracks/joints is a major cause of structural degradation of concrete pavements. A regime of pavement deterioration is likely to occur at existing joints/cracks. The high concentration of tensile stress (fracture mode I) and shear stress (fracture mode II) at crack tip can lead to the result of reflective cracking in pavement overlays. As a moving wheel approaches an underlying crack, a high concentration of shear stress is introduced at the crack tip. When the load is located right above the crack, the tensile stress becomes dominant. As the wheel moves to the departure side, the shear stress increases to another peak with an opposite sign. When the load is located either side of a crack, a relative vertical displacement is expected to take place at crack edges, which leads to reflective cracking under repetitive traffic loads, which is called “rocking effect”, as demonstrated in Figure 1.1. Hence, it is crucial to provide adequate resistance to shear failure and prevent reflective cracking due to “rocking effect”.

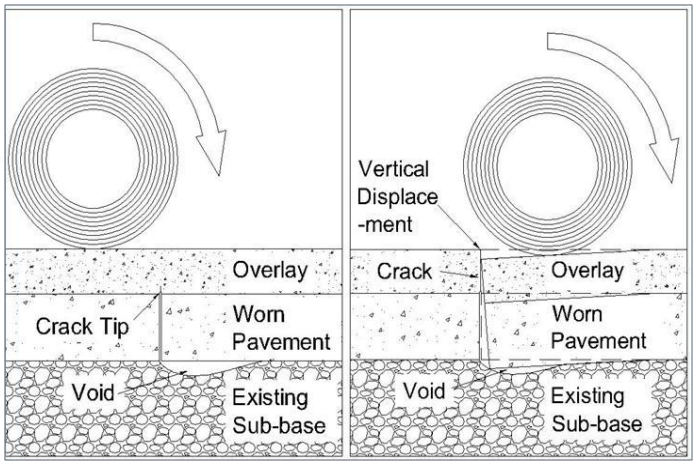

Figure 1.1 Reflective Cracking under Repetitive Traffic Loads

The concrete mix has the additive of polymer to enhance the bond with substrate and improve the strengths. Steel fibre is introduced to the mix instead of conventional reinforcement for ease of construction and effective crack control. It also enhances the flexural and shear strengths and toughness.

A unique mix design method was developed for steel fibre-reinforced, roller compacted and polymer modified bonded concrete overlays (SF-RC-PM-BCO) in the study, which is the key to achieve both the good mechanical performance and rapid construction process.

1.3 Aims and Objectives

Based on the previously developed concept of sustainable "green" concrete overlay in the form of a roller compacted steel-fibre-reinforced polymer modified concrete, this research aims to design the concrete mix, analyse the material performance subjected to dominant shear loading and provide design guidelines/recommendations. The study on flexural failure (mode I failure) is carried out in a parallel study by Y. Lin at Coventry University. The experimentally-obtained intrinsic parameters are referenced in the thesis to assist with the understanding of the mixed-mode behaviours and the procurement of mixed mode parameters. The principle objectives of the research include:

- To study and review the current state-of-the art literature dealing with shear design of concrete structures, with emphasis on shear failure at cracks including the problem of reflective cracking.

- To review the current literature on the modern technology of roller compacted concrete (RCC), steel fibre reinforced concrete (SFRC) and polymer modified concrete (PMC) and develop an optimized steel fibre reinforced, roller compacted, polymer-modified, bonded concrete overlay (SF-RC-PM-BCO) material, to achieve the superior mechanical properties of the overlay and to facilitate fast construction by asphalt paving machinery.

- To investigate the new concrete overlay's shear resistance by means of laboratory testing accompanied by finite element modelling techniques.

- To control and evaluate the problem of shear failure by means of utilisation of various types and contents of steel fibres to provide adequate resistance to reflective cracking.

- To recommend new/additional guidelines for an optimum design approach for "green" concrete overlays in the form of SF-RC-PM-BCO.

1.4 Methodology and Context

To achieve the above objectives, the study consists of two parts: 1) material development to find the optimal water content in the mix to enable adequate bond with the substrate and facilitate the use of asphalt paving machinery; 2) a comprehensive laboratory test programme to study the shear behaviour and resistance to reflective cracking, accompanied by a 2D/3D numerical study scheme for comparison and validation.

With the understanding that the appropriate water content is the focal point of a successful "green" overlay, the mix development criteria were established for the new concrete overlays. The existing compaction methods, such as the modified proctor method, modified Vebe method, and the standard proctor method, were investigated and assessed together with the other criteria, such as "roller compactability", "paver placability" and the bond strength with ordinary Portland cement concrete. A modified method was later developed to obtain the suitable compaction result, and hence the most favourable water content. (Section 3.4) This new method was employed to determine the optimal water content of the mixes used in the following shear investigation. The modulus of elasticity and Poisson's ratio were tested

in accordance with ASTM C469 for various mixes (Section 3.8), providing necessary properties in the FE simulations later on.

- Study into shear failure at cracks and inadequate resistance to reflection cracking. The following tests are conducted as well as finite element simulations.

  - Block Splitting Test (Section 3.3.1): a simple device to perform tests on splitting tensile bond strength at interface between overlay and old concrete pavement.

  - Cylinder Direct Shear Test (Section 3.3.2, 4.2.3): an efficient test to evaluate direct shear bond strength at interface between overlay and old concrete pavement. A contact element layer with coulomb shear friction model with parameters from these two tests was utilized to simulate various bond conditions in a composite beam.

  - Single Notch Shear Beam Test (Section 4.1.3, 4.2.4-4.4): to simulate the condition of reflective cracking under static shear load. Mode II stress intensity factors were calculated based on test results and later verified by FE simulations (Section 6.3). A bilinear cohesive zone model (CZM) with parameters derived from this test was employed to model the fibre bridging effect and aggregate interlock at the crack interface.

  - Foundation Test (4.5): to simulate the reflective cracking caused by rocking and pumping effects under shear loading near weak supports. Test results were later verified by 3D FE simulations (Section 6.4).

  - Cylinder Torsion Test (Section 4.1.4): addition tests conducted to increase confidence.

The thesis is set out in the following chapter structure. A representative methodology proceeding diagram is shown in Figure 1.2.

Chapter 1 presents an introduction, a brief historical review, justifies why the research is needed, explains the mechanism of shear failure in concrete pavement overlays in Section 1.2, sets up the aim and objectives and the context of the thesis.

In *Chapter 2* a comprehensive literature review on the shear design of concrete structures, including literature on existing codes and standards and other established design equations based on regression analysis and analytical models is conducted. The fracture mechanics is consulted with regard to the reflective cracking in opening and sliding failure modes. The characteristic properties are identified to quantify the shear capacity and resistance to reflective cracking in SFRC.

The previous research works on "green overlays" and the existing literature on roller compacted concrete necessitate the need for a new mix design approach to determine the optimal water content in SF-RC-PM-BCO, so that it facilitates the use of asphalt paving machinery and satisfies the requirement of high bond strength to the underlying pavement. The material optimization and characterization of some basic material properties are contained in *Chapter 3*.

Following the material development in the previous stage, considerable laboratory tests were conducted on concrete beams made of newly-developed mixes and conventional concrete as comparison to investigate both strengths and resistance to reflective cracking. Early age strengths were also considered. Composite beams with the overlay materials on top of ordinary concrete to simulate the overlay system were tested subject to shear loading condition, to examine its performance in a composite system. The crack opening, sliding and its final trajectory were carefully recorded for analysis in the following phase. In addition, composite beams with the "green" overlay were placed on a foundation with artificial weakened support to closely simulate the reflective cracking under static loads. Conventional overlaid system was also tested for comparison. The above experimental investigation is contained in *Chapter 4*.

Chapter 5 analyses and discusses the strengths and fracture parameters obtained from laboratory tests. Semi-empirical models were established to predict the onset and ultimate shear strength of SFRC. Analysis of fracture parameters such as fracture energy and mixed-mode stress intensity factor was conducted to describe the progressive fracture process and resistance to reflective cracking.

In parallel with laboratory tests, high standard numerical works is also carried out. Finite element model (FEM) is set up to identify problems, limitations and pitfalls so that the

relevant solutions can be proposed. This is included in *Chapter 6*. Finite element analysis (FEA) of single notch shear test configuration using ANSYS software (2013) on monolithic and composite beams based on the material properties derived in experiments was conducted. The effect of crack bridging, overlay stiffness and bond characteristics on crack tip stress concentration was discussed. The crack pattern development in 3D models was visualized and verified against experimental results. The FEA of beam-on-foundation test with the material properties derived in the previous tests to predict the overlay performance and reflective cracking. Based on the calibrated models for interface properties and crack bridging law, the pavement overlay system was simulated to explore the relation between overlay stiffness and stress intensity factors. So the resistance to reflective cracking in real overlay system was predicted subject to future verification. Design recommendations were derived for "green" concrete overlays in the form of SF-RC-PM-BCO.

Finally, based on all the above works, *chapter 7* develops design guidelines and also discusses its advantages and disadvantages, assumptions and limitations. Following summarizing the conclusions, directions were given for future works.

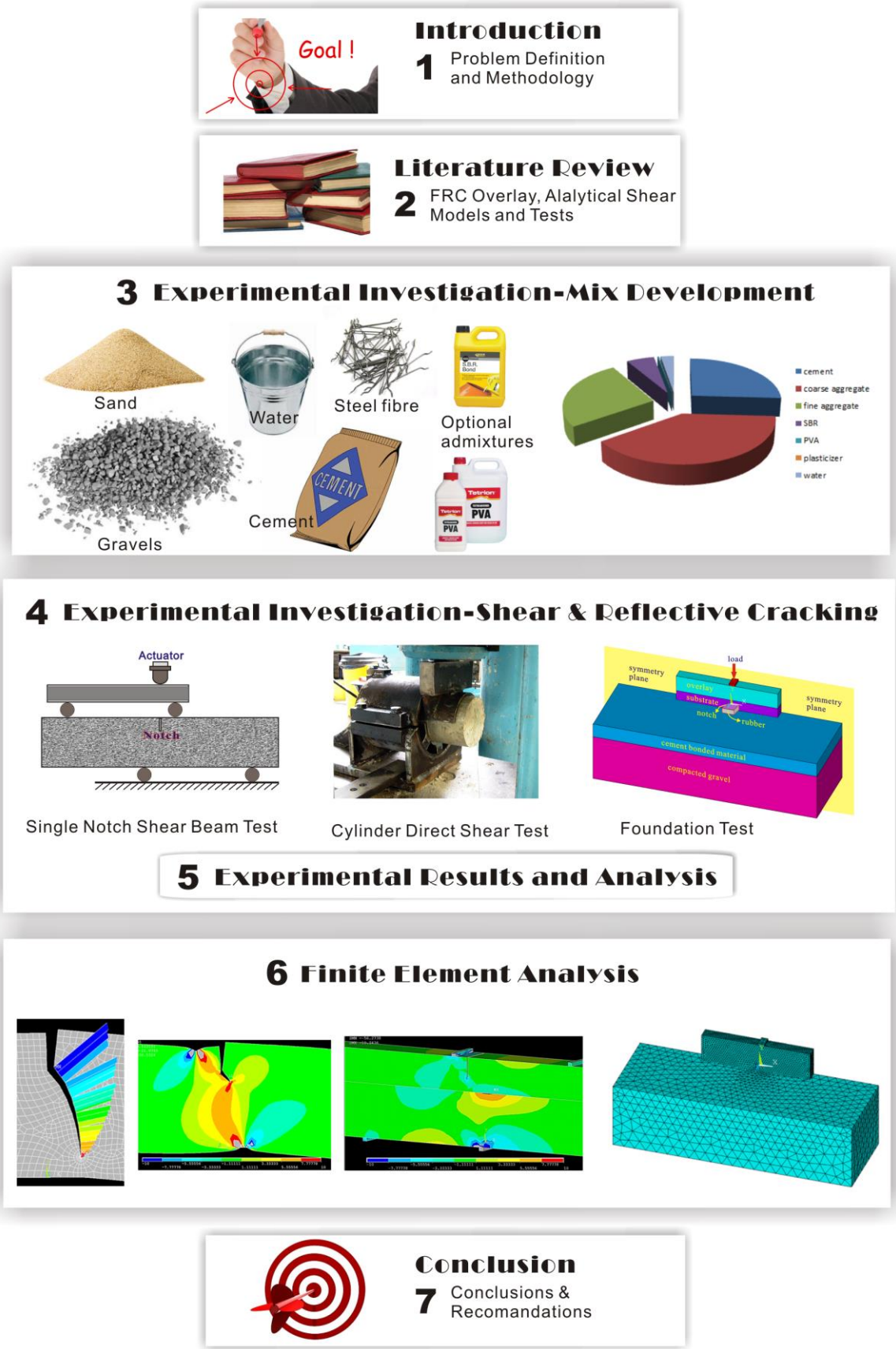

Figure 1.2 Methodology

CHAPTER 2 LITERATURE REVIEW

2. Literature Review

The existing literature on the key features of this new "green" overlay is reviewed, based on which the question of optimum water content is brought to surface. The established methods and recent researches are introduced. A comprehensive literature review is conducted on existing shear design codes and standards and other established design equations based on regression analysis and an analytical model. The fracture mechanics is consulted with regard to the reflective cracking in opening and sliding failure modes. The shear test configurations in the current literature are discussed, such as single notch shear beam test. With the aid of fracture mechanics the mechanism of reflective cracking in pavement overlays is reviewed. The characteristic properties are identified to quantify the shear capacity and resistance to reflective cracking in SFRC.

2.1 Development of the New Overlay

2.1.1 Bonded Concrete Overlay

Since the early application of Bonded Concrete Overlay (BCO) in 1913 in America, several guidelines and technical bulletins have been published by the American Concrete Pavement Association (ACPA). (American Concrete Pavement Association 2014) It states that BCO is usually only suitable when the existing pavement is in an acceptable condition. Most applications of BCO in US are in the form of jointed plain concrete pavement overlay (JPCP on JPCP base), with extra attention to match the joints, therefore, avoiding reflective cracking. There have been some cases of Continuously Reinforced Concrete Pavement Overlays (CRCP on CRCP base), primarily in Texas. However, it was considered not appropriate to construct a BCO where "the load-carrying capabilities of the underlying pavement are already compromised" (Delatte Jr. 2008). Even though some projects had very good performance, others suffered from reflective cracking and early debonding.

Pumping and rocking effect is likely to occur at existing cracks/joints in the substrate and causes weakness in the sub-base and prompt reflective cracking into the overlay under repetitive loading, as depicted in Figure 1.1. Hughes (2003) once stated that reflective cracking is not preventable, but it should happen under a controlled manner. Closely-spaced fine cracks are more welcomed than further-spaced wide cracks. Reinforced concrete is

known to enhance resistance to crack opening. The corresponding shear sliding is also restrained with closed crack. However, instead of conventional reinforcement, Hughes (2006) suggested a combination of conventional rebars with fibres to achieve effective crack control and maintain the required resistance, as an alternative and potentially more economical solution. Nevertheless, an even bolder plan was favoured by practitioners and contractors, to have no conventional reinforcement at all and replace it all with fibres. This complies with the principle of fast and cost-effective construction process with heavy-duty vibrating roller. The technique of roller compaction construction usually serves without reinforcing bars or dowel bars.

2.1.2 Roller Compacted Concrete and Steel Fibre Reinforced Concrete

Roller compacted concrete (RCC) has been primarily used on mass concrete dams. The application in pavements has experienced an accelerated growth in the last few years in the United States (National Concrete Pavement Technology Center 2010). It offers economical and rapid construction, long durability and load carrying capacity. RCC is Portland cement concrete containing the usual ingredients as in conventional concrete, but with zero-slump workability, which enables fast construction using asphalt paving machineries. Usually no joints or conventional dowel bars or reinforcement is included in RCC paving. Hence the construction process is much simplified and cost-efficient. Meanwhile, RCC features high compressive and flexural strength, which facilitate long durability. The sacrificial problems of rutting and potholes in asphalt pavements are also eliminated due to its high shear strength. Therefore, RCC is now widely applied in industrial fields, military fields, ports, roads and airfields etc.

Despite the fact that RCC is an economical, durable and versatile solution in pavement construction, researchers are also looking to perfect it in terms of crack control by introducing fibres in RCC (Kagaya et al. 2001, Nanni and Johari 1989). Fibre reinforced concrete (FRC) is reported of enhanced toughness, provided an adequate amount of fibre is added in the composite. Meanwhile, close-placed fine cracks are generally obtained (Hughes 2006).

Polymeric fibres was reported to have excellent performance in controlling the shrinkage crack at the early stage due to the similar Young’s modulus as early age concrete (Karihaloo

1995). Hence, trials with synthetic fibres were carried out in the previous study (Koutselas 2010). Despite the high flexural strength achieved with the addition of synthetic fibres, the failure took place in a brittle manner.

In contrast, steel fibres exhibit promising post-peak performance and load carrying capacity over other types of fibres, given the same volume fraction in the mix (Beaudoin 1990). Reinforced concrete with 6% volume fraction of steel fibres can reach the fracture energy of 100 times larger than normal reinforced concrete without steel fibres (Bache 1987). The critical volume fraction of steel fibre is defined as the minimum amount of fibre required to sustain the load when the matrix fails. It is illustrated by the equation below (Beaudoin 1990).

$$V_{cr} = \frac{\sigma_{mu}}{\sigma_{mu}+(\sigma_{fu}-\sigma_f')} \quad 2.1$$

Where σ_f' is the stress in fibre when matrix fails; σ_{mu} is matrix strength at 28 days and σ_{fu} is the ultimate strengths of steel fibre. The dominant type of steel fibre used in this study has an ultimate tensile strength of 1050MPa provided by product brochure, i.e. σ_{fu}=1050MPa. The plain polymer modified concrete (PMC) has a flexural strength of 5.66MPa, i.e. σ_{mu} = 5.66MPa (Lin 2013). If a perfect bond between steel fibre and concrete matrix is maintained till the matrix fails, the following relation is derived (Beaudoin 1990).

$$\sigma_{mu}/E_{mu} = \sigma_f'/E_f \quad 2.2$$

E_{mu} and E_f are the young's moduli of the matrix and steel fibre respectively. Let E_{mu} = 26GPa in plain PMC (The Highway Agency 1992). E_f is taken as 200GPa for common steel. Then σ_f' is derived as 0.74MPa. Substituting the above in Eqn. 2.1, the critical volume fraction is calculated, V_{cr} = 0.54%. Thus, only when the volume fraction of steel fibre in PMC is higher than 0.54%, the load can be sustained after matrix fracture occurs. On the other hand, high volume of fibre is not economic or practical and may even lead to problems, such as fibre grouping. These basics are employed when selecting the volume of fraction of steel fibre, as in the following chapters.

The fibre pull out mechanism is considered an essential contribution to the toughness of steel fibre reinforced concrete (SFRC) (Taerwe and Gysel 1996). SFRC usually exhibits much

improved ductility. It was even indicated that the addition of steel fibre in the concrete can prompt the failure mode from shear to flexure (Narayanan and Darwish 1987). It was reported that the hooked-end SF – RCC presented a 0.31-1.88N/mm^2 higher flexural toughness than RCC reinforced by indented steel fibre (Kagaya et al. 2001). A variety of hooked end steel fibres are available on the market which could provide improved anchorage and crack control facility, such as, Dramix 5D, which is claimed to have the capacity of holding up to 100kg of force (Bekaert 2012). Long steel fibre in RCC was reported to improve the flexural toughness effectively (Kagaya et al. 2001).

The strain hardening in SFRC under tension is explained in Figure 2.1. The dash lines present the tension softening effect in unreinforced concrete and the effect of fibre bridging. The sum of the two forms the stress – crack width diagram of a SFRC (Voo and Foster 2003). Depending on the volume fraction of steel fibre and fibre properties, the fibre bridging could be weaker or stronger, which influences the shape of the SFRC curve, i.e. behaviour of the composite. However, it is obvious that even after the presence of crack SFRC can still sustain a considerable load level, indicating vigorous post-cracking capacity. If the fibre bridging is strong enough, the load carrying capacity of the cracked section could even surpass the un-cracked section. In other words, the peak load occurs after cracking. A similar stress level could result in a finer crack than ordinary concrete. This is to say the energy consumed to crack the material may be only a small portion of the total fracture energy. To fracture the structure, a much higher load and/or repeatability of load occurrences is needed. Hence, a good endurance and long-lasting performance can be expected. Moreover, it depicted the necessity of a large deformation before the final deterioration. It could lead to stress redistribution and the contribution from boundary restraints. The structural ductility is also enhanced. The improvement of shear response is reflected by the strain hardening tensile properties of the FRC. The success of keeping the cracks closed in FRC leads to effective shear friction. Consequently the shear performance is largely improved.

Voo and Foster (2003) proposed a variable engagement model based on a simple assumption that the fibres are effectively engaged at half of the peak load in uniaxial tension test.

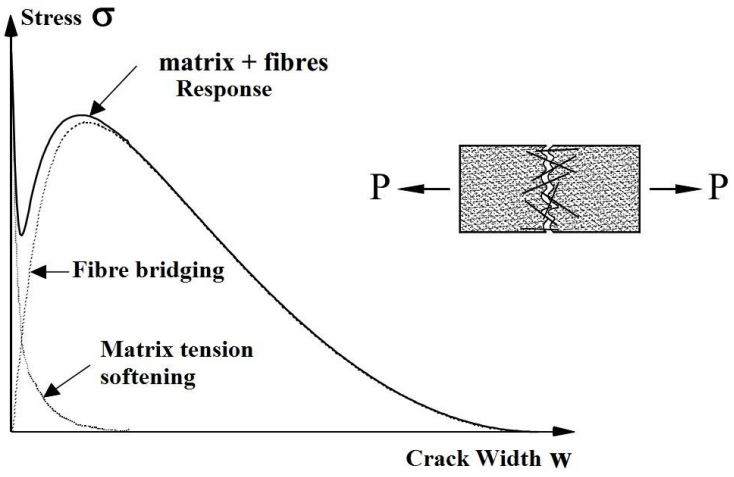

Figure 2.1 Strain Hardening and Softening of Fibre Reinforced Concrete under Tension (Voo and Foster 2003)

2.1.3 Polymer Modified Concrete (PMC)

A successful concrete overlay requires not only a superior load carrying capacity, but also robust bonding to the underlying material, based on the lessons learnt in the past. Polymer Modified Concrete (PMC) generally has better resistance to water penetration and chemicals. It also has excellent bonding to old concrete or steel. It has a track record of successful applications in bridge decks, structural concrete flooring and pavement overlays.

There are a variety of polymer latexes as cement modifiers which are commercially available, mainly in the groups of elastometric and thermoplastic polymers. The most commonly available one in the former group is Styrene-Butadiene Rubber Latex (SBR), which was recommended in a previous research on the "green" overlays project (Koutselas 2010). The chemistry expression is  . The liquid form of SBR was considered effective in dispersion and can be added with water to the mix in the mixing procedure (Koutselas 2010). In addition, it was reported to have good permeability resistance and high bond strength, and perhaps more favourable than other types of polymers, based on its performance and cost (Clear and Chollar 1978). Hence, it was employed in this research as well. A PVA product of the latter group, polyvinyl alcohol, was employed by Hughes and Lubis (1996) to develop a modified cement mortar. High flexural strength and bond strength to concrete were achieved in the samples compacted by a small

roller compactor in the laboratory in this study. The chemistry expression is $\left[-CH_2-\underset{OH}{CH}-\right]_n$. Hughes and Lubis (1996) find that the PVA additive could be very effective in the application of roller compacted concrete overlays. Hence, it was also employed in our research. It is in powder form and mixed with cementitious materials prior to mixing with liquid or aggregates.

Hughes concluded that, in both groups, polymer coalesces a film on the surface of specimens following the initial moist curing, which helps retaining moist and aids the cement hydration process. Ohama (1995) and Beaudoin (1990) suggested that a shortened water curing duration would suffice. Ohama states that an excessive water immersion or moist curing, such as in ordinary concrete could even be detrimental to polymer modified concrete. An appropriate curing method was considered vital. Hence, an experimental investigation was carried out in this study. The details are included in Chapter 3.

2.2 Steel Fibre Reinforced, Roller Compacted, Polymer Modified Bonded Concrete Overlay

This research introduces an innovative concept to combine the modern technology of RCC, SFRC and PMC to form a successful concrete overlay system. A potential dilemma in the research is that RCC usually contains little water to enable the use of asphalt paving machinery whilst a certain amount of water is demanded in the cement hydration process (cement hydration requires a minimum water-cement ratio w/c of 1:4 or a proportion of 0.25) to allow for strength development in concrete. A mix with a w/c ratio of closing to 0.25 may not mix thoroughly and may not flow well enough to be placed. Moreover, good bonding to the underlying concrete also requires sufficient water to moisturize the interface. Therefore, the focal point of the mix design is balancing the water content.

Some existing mixture proportioning methods for RCC is to determine the w/c ratio based on the desired strength level. The workability is adjusted by a consistency measurement using equipments, such as Vebe. The typical methods in this group are Corps of Engineers method, high paste method and roller-compacted dam method etc as illustrated in ACI 207.5R. (1999) Some other methods are based on the geotechnical approach used for soil or other cement stabilized base materials. They determine the compaction effort and water content required to achieve the engineering properties. Usually, a certain compaction effort

is applied on samples using proctors. Then the dry density is assessed against the water content. In these methods, "the desired water content is determined by moisture-density relationship of compacted specimens." (1999) Nevertheless, all the above relate exclusively to soils and plain RCC, which is without any form of reinforcement.

Recently, Kagaya et al (2001) carried out laboratory studies with steel fibre reinforced RCC, using the modified Vebe (M-VB) method. Neocleous (2011) employed the modified Proctor (M-P) compaction method to develop mixes containing recycled steel fibre reinforced in RCC pavements. However, the abovementioned mix design methods are for pavements resting on a sub-base or a sub-grade. They could be unsuitable for bonded concrete overlays, where bond to the underlying concrete must be assessed and satisfied. Despite the fact that the bond between the horizontal lift joints may be of concern in the existing literature, the bond with the substrate is considerably more difficult to achieve. Hence it must be taken into the mix design consideration. With the above in mind, a new mix design method for SF-RC-PM-BCO has been developed in determining the optimal water content. It is detailed in Chapter 3.

2.3 Shear Resistance

Shear resistance is of particular importance in structural design. The representative fundamental factor in shear evaluation is shear strength (v_c), which is usually derived from the total shear force (V) divided by the vertical cross sectional area ($b_w d$) in beam theory, as in Eqn. 2.3.

$$v_c = \frac{V}{b_w \cdot d} \tag{2.3}$$

It is well acknowledged that shear design for concrete is indirect. Unlike metal, direct shear rarely happens in concrete due to the material heterogeneity and non-linearity. It is always accompanied by bending moment, although shear may prevails in certain circumstances, such as deep beams and corbels. It is very difficult to have a separated shear from bending, although there are tests configured to study concrete behaviour under shear. They will be summarized and demonstrated in the following section. Nevertheless, there is always engagement of bending effect to a certain extent. A failure plane under direct shear is expected to follow the same direction as the applied load. But they generally develop in an

inclined direction due to the involvement of tensile stresses. Hence the nominal shear strength v_c in a beam reflects the integrated flexure and shear. As a matter of fact, it is rather *flexural-shear strength* by nature, or "fictitious vertical shear strength", as Leet and Bernal stated (1997).

The results from experimental tests on shear strength could be influenced by many factors, such as concrete heterogeneity, reinforcement details, test configurations, and boundary conditions etc. Existing literature points out shear test results always present large scatter, which can be evident by comparing the laboratory results in dots with ACI empirical shear design formula in dash line presented in Figure 2.2 (Leet and Bernal 1997). When bending moment M becomes negligible, i.e. pure shear, the abscissa becomes infinite. The corresponding shear strength varies from approx. $3.2\sqrt{f_c}$' to $4.5\sqrt{f_c}$'. If the bending moment is relatively large, v_c is stated to be no more than $3.5\sqrt{f_c}$'. The nominal shear strength is clearly affected by the magnitude of bending moment. In other words, perhaps more commonly seen in design formulas, it is in the form of shear span-to-depth ratio (a/d).

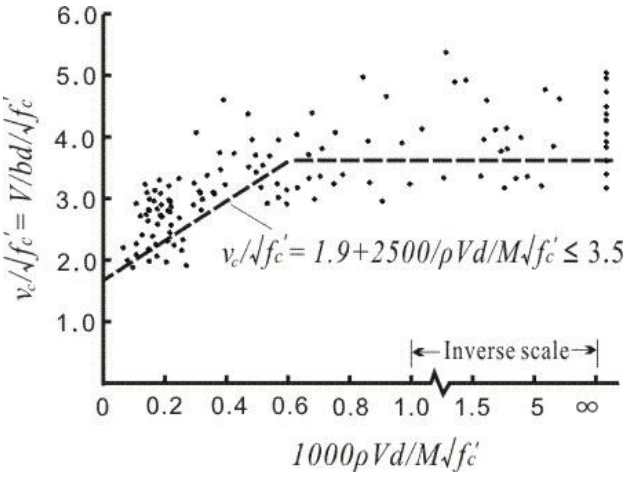

Figure 2.2 Correlation of ACI Equation with Lab Data (Leet and Bernal 1997)

A number of shear design formula in standards or proposed by other scholars are summarized in Table 2.1. b_w , d are width and depth of effective cross section in mm. f_t is tensile strength of concrete, MPa. ρ is tensile reinforcement ratio. a/d is shear span to depth ratio. All the formulae are in lb/in^2 in ACI 318 (2002) and are converted into N/mm^2 herein. Since the formulae are intended for conventional reinforced concrete, it is understood that some empirical formulae may become invalid in the case of concrete without longitudinal reinforcement. The engagement of flexure is considered in terms of the shear span-to-depth

ratio (a/d). A large a/d ratio indicates large bending moment and low design values in shear. As the a/d ratio becomes smaller, the failure mode transfers from flexural to shear. Hence to study the shear failure mechanism, the shear span-to-depth ratio employed in this study was relatively small, as detailed in Chapter 4.

Despite the fact that the design codes specify that the shear strength is directly proportional to compressive strength $(f_c)^{0.67}$ in Eurocode 2 (Beeby and Narayanan 1995), and JSCE Code (2002), or $(f_c)^{0.5}$ in ACI 318-05 (2002) and A23.3-94 (1994), shear strength does not always increase as the compressive strength does. It has been reported by many researchers that the hypothesis is not always valid, especially when $f_c^{'} > 69$MPa. (ACI Committee 318 2002) It also indicates for high strength concrete, the nominal shear strength increases at a less rate with the increase of $f_c^{'}$.

Table 2.1 Summary of Selected Shear Design Codes

Design Codes	Shear Strength in MPa	Comments
Eurocode 2 (Beeby and Narayanan 1995)	$\tau_{Rd}=(0.25f_{ctk0.05})/\gamma_c$ $f_{ctk0.05}=0.7f_{ctm}$ $f_{ctm}=0.3(f_{ck})^{0.67}$ $\gamma_c=1.5$	
		If the safety factor $\gamma_c=1.5$ is omitted.
BS 8110 (1997)	$v_c=\frac{790}{\gamma_m}(100\rho)^{1/3}\left(\frac{0.4}{d}\right)^{1/4}\left(\frac{f_c}{25}\right)^{1/3}$	γ_m = 1.25, $f_c \leq 40MPa$, $100\rho < 3$
ACI 318-02 (2002)	$v_c=0.16\sqrt{f_c'}+17\frac{V_u d}{M_u}\rho_w, but \leq 0.16\sqrt{f_c'}$	for $\frac{a}{d} \geqslant 2.5$, i.e. relatively large shear span-to-depth ratio
	$v_c=\left(3.5-\frac{2.5M_u}{V_u}\right)\left(0.16\sqrt{f_c'}+17\frac{V_u d}{M_u}\rho_w\right)\ but\ \leq\ 0.29\sqrt{f_c'}$	for $\frac{a}{d}$<2.5, i.e. relatively small shear span-to-depth ratio
	$v_c=0.166\sqrt{f_c'}.$	General
	$v_c\ \leq\ 0.83\sqrt{f_c'}$	Deep beams ($l_n \leq 4d$)
Canadian Standard A23.3-94 (1994)(2002)(2002)(2002)	$v_c=0.2\sqrt{f_c'}.$	No consideration for a/d

Design Codes	Shear Strength in MPa	Comments
Zsutty Equation (Zsutty 1968, Zsutty 1971)	$v_c=11.42\left(f_c' \rho \frac{d}{a}\right)^{1/3}$	a/d > 2.5 or a/d < 2.5 under indirect load, as provided by side flanges
	$v_c=28.55\left(f_c' \rho\right)^{1/3}\left(\frac{d}{a}\right)^{4/3}$	1.5 < a/d < 2.5 with direct loading (top load & bottom supports)
Sudheer et al (2010)	$V_c = 32\left(\frac{f_t}{a/d}\rho\right)^{0.8} b_w d$	
Li et al (1992)	$f_v = 9.16\left[(f_f)^{2/3}\rho^{1/3}(d/a)\right]$	for a/d < 2.5
	$f_v = 1.25 + 4.68\left[(f_f f_t)^{3/4}(\rho\, d/a)^{1/3}(d)^{-1/3}\right]$	for a/d > 2.5
Slater et al (2012)	$v_u = 1 + \frac{9}{100}f_c' - 7.4\times10^{-4}f_c'\frac{l_f}{d_f} + 2V_f\frac{l_f}{d_f}$	linear regression for steel fibre reinforced concrete beams
	$v_u = -0.7 + 0.4f_c'^{0.67} - 9.2\left(V_f\frac{l_f}{d_f}\right)^{-0.1}$	Non-linear regression for steel fibre reinforced concrete beams
CEB-FIP (Design Code, Comité Euro-International du Béton 1993)	$V_{cr} = 150\left(1+\sqrt{\frac{0.2}{d}}\right)\left(\frac{3d}{a_s}\right)^{1/3}(100\rho)^{1/3}f_c^{1/3}bd$	V_{cr} in kN; b,d in m and f_c in MPa
Gastebled and May Model (2001)	$V_{cr} = \frac{1.109}{\sqrt{H}}\left(\frac{H}{a_s}\right)^{1/3}\left(1-\sqrt{\rho}\right)^{2/3}\rho_s^{1/6}f_c^{0.35}\sqrt{E_s}\cdot bH$	
Xu et al 's Model (2005)	$V_{cr} = \frac{0.446}{\sqrt{H}}\sqrt{\frac{E_s}{E_c}}\left(\frac{H}{a_s}\right)^{1/3}\left(1-\sqrt{\rho}\right)^{2/3}\rho^{1/6}K_{IIC}bH$	

It is commonly acknowledged that as far as flexural shear concerned, on a macro scale, the shear strength of concrete slabs is taken by a) concrete compression zone; b) reinforcement, such as shear reinforcement (stirrups) or longitudinal reinforcement; c) aggregate interlock. As mentioned above, shear strength is proportional to compressive strength in normal strength concrete, but may become less sensitive in high strength concrete. As an intention to reduce the construction cost and overlay thickness, the option of conventional reinforcement was not considered in the overlay system. Instead, steel fibre was introduced to act as a crack

control measure and enhance the flexural resistance. It is different from conventional rebars as dispensed steel fibre in concrete does not necessarily provide effective dowel actions. Rather, it enhances the shear resistance indirectly by keeping the cracks closed and implementing high flexural resistance. Londhe (2010) published a paper on experimental results on shear strength of steel fibre reinforced concrete beams with longitudinal reinforcement. The tests were carried out on a series of beams with various volume fraction of steel fibre as well as the steel ratio of steel rebar in four point loading configuration. Hooked-end steel fibre was used. The results are plotted in the following figure showing the shear strengths in beams with the same steel ratio but various fibre volume fraction as well as the beams with constant steel fibre volume fraction but different steel ratio. As a result, the green line shows a steeper trend compared to the blue line, which indicates increasing longitudinal reinforcement is a more effective way to enhance the shear resistance than increasing steel fibre. However, it also proves that steel fibre substantially increased the shear strength of the concrete beams, although with the presence of conventional reinforcement.

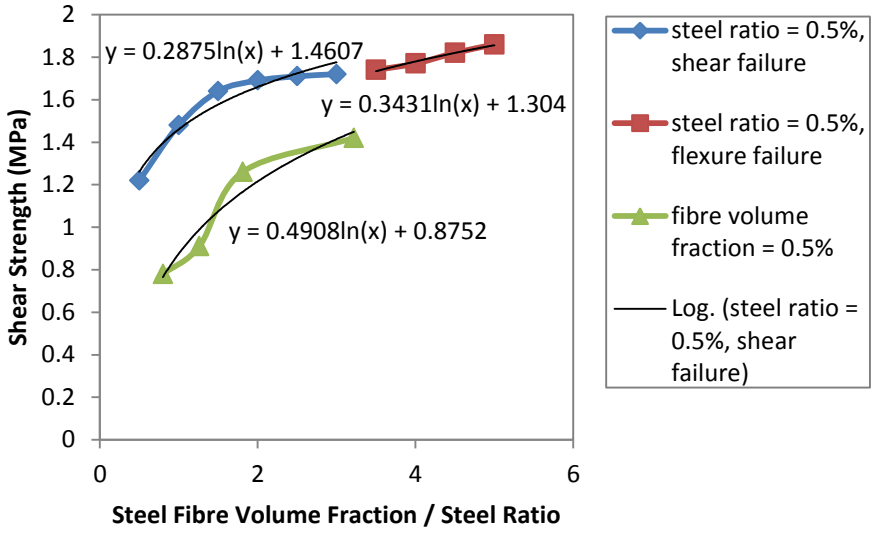

Figure 2.3 Shear Strength in SFRC with Conventional Reinforcement (Londhe 2010)

The efficiency of aggregate interlock was also found to be compromised in high strength concrete by many other researchers (Song et al. 2010, Taylor 1974, Walraven 1981). Taylor (1974) pointed out that 35-50% of shear capacity was attributed to aggregate interlock in

normal concrete, the rest by compression zone and dowel action. Meanwhile, he also suggested that smooth-sided cracks could develop in high strength concrete. In contrary to fracture at the interface between aggregate and cement matrix, the effective bond at the interface due to the high strength concrete could redirect fracture plane to go through aggregates. Hence, weak aggregate interlock may be evident. He also suggested that the suitability of the codes in determination of nominal shear stresses should be limited to concrete strength up to 50MPa. Hamadi and Regan (1980) also pointed out contribution of aggregate interlock varied with aggregate types and mortar strength. If mortar strength is relatively high, the crack face can be smooth and little resistance can be expected from aggregate interlock. Consequently the nominal shear strength may be less than expected.

The aggregate interlock is a highly complex process, involving the crack width, the strength of concrete (both aggregate and concrete paste), the size and distribution of aggregate. The ACI Guidance on RCC recommended to use well-graded aggregate and higher quantity of aggregates less than 4.75mm than in conventional concrete to avoid segregation. Furthermore, crushed aggregate is found to be less prone to segregation than rounded aggregates (ACI Committee 207 1999). However, with wider cracks and/or more frequent heavy traffic load, the efficacy of aggregate interlock falls off promptly. Therefore, it is critical to restrict the crack width as well as undertake other measures to increase the shear strength of BCO, such as introducing fibres.

2.4 Analytical Shear Models in RC

Explicit evaluation of shear capacity is a highly complex task. So far all the pre-mentioned components in determining shear strength need reassessed according to the features of the overlay materials and the loading conditions. Early experimental studies on shear transfer in rigid pavement also identified that the shear transfer efficiency and shear resistance rely on many factors, such as crack width, pavement thickness, traffic load, foundation type, subgrade and aggregate shape (Colley and Humphrey, 1967). The literature review carried out to date on shear resistance has been following the main threads of aggregate interlock, fibre reinforced concrete and crack development.

Most of the shear design formulas in reinforced concrete are based on empirical results and involve a number of simplified assumptions. Until recently, Gastebled and May (2001)

introduced an analytical model on flexural shear in reinforced concrete based on the concept of fracture mechanics – "Much of the increase in the crack growth resistance is due to the energy consumed by debonding, frictional sliding and eventual pull-out of the fibres from the matrix." In their model, it is assumed that the shear takes place as the two halves rotate with reference to diagonal crack tip, as sketched in Figure 2.4. The formula, as quoted in Eqn. 2.4, had high resemblance with the established formula in CEB-FIP model code (1993). Following this successful analytical model capturing the true failure mechanism in reinforced concrete, it was further developed in reinforced concrete without stirrups (Xu, Reinhardt and Zhang 2005) and reinforced concrete with steel fibres (Nguyen-Minh and Rovnak 2011). The model also shed some light on the shear design in SFRC at a later stage, as detailed in Chapter 5.

$$V_{cr} = \frac{1.109}{\sqrt{H}} \cdot \left(\frac{H}{a_s}\right)^{1/3} \left(1 - \sqrt{\rho}\right)^{2/3} \rho_s^{1/6} f_c^{0.35} \sqrt{E_s} \cdot bH \qquad 2.4$$

This image has been removed

Figure 2.4 Gastebled and May Model (2001)

2.5 Cracking

Hughes (2006) stressed that in pavement design attention should be paid to restraining the crack width. Hughes (2006) argued that closely spaced fine crack is more favourable than wide cracks apart from each other, which was supported by other experimental and finite element studies. The DMRB suggested the crack classification in pavement as in Table 2.2. The crack width of less than 0.5mm is considered functional. Hughes suggested that 0.2mm for transverse cracks and 0.15mm longitudinal cracks in BCO using a similar reinforcement ratio to the ratio in many conventional CRCP designs. Furthermore, replacing conventional rebars partially with fibres is a prospective crack-control option and the maximum crack width of 0.1mm could be achievable (Hughes 2006).

Table 2.2 Crack Classification from DMRB 7.4.2 (HD 32/94) (1994)

Crack Definition	Width (mm)	Condition Assumed
Narrow	< 0.5	Full aggregate interlock and load transfer
Medium	0.5 - 1.5	Partial load transfer. Permits ingress of water
Wide	> 1.5	No load transfer. Permits ingress of water and fine detritus

The numerical modelling of cracks in concrete or reinforced concrete structures was carried out, either by smeared crack approach or by discrete crack approach. The former one is to model cracking by correcting the strength and stiffness of the concrete material, while the latter one is to introduce a discontinuity interface and describe its behaviour by 'a discrete traction-separation law' (Theiner and Hofstetter 2009). The study carried out by Zhang and Li (2004) pointed out a theoretical direction to predict structural performance of concrete and fibre reinforced concrete in the light of crack propagation. They stated that as long as the related material properties $K_{IC,}$ K_{IIC} and the stress-crack width (σ-δ) is known, the structural performance can be predicted by the simple fracture mechanics model. In the case of SFRC, the stress-crack width relationship is the so called "crack bridging law" or "fibre bridging law". K_{IC} and K_{IIC} are the critical stress intensity factors in fracture mechanics. In fracture mechanics, there are three cracking modes as shown in Figure 2.5, Mode I (opening mode), Mode II (shearing mode) and Mode III (tearing mode) (Karihaloo, 1995). The corresponding stress intensity factors K_I, K_{II} and K_{III} use the geometric and load distribution properties to determine stress levels and predict crack growth under each mode. As far as shear is concerned, mode II is the dominant cracking mode. However, it is usually accompanied by

mode I. Hence, a mixed-mode situation is generated. These will be detailed in the following chapters and not repeated herein.

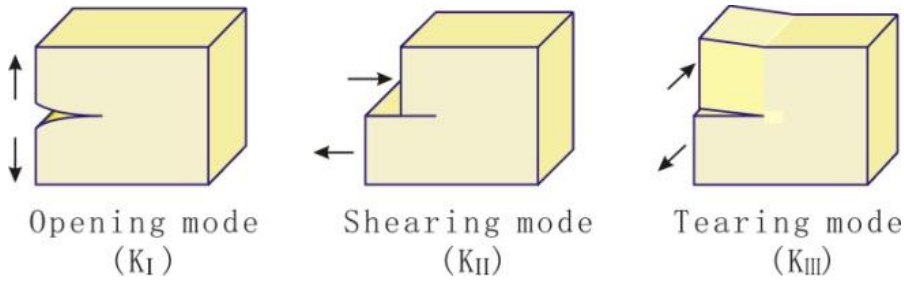

Figure 2.5 Three Basic Modes and Associated Stress Intensity Factors (adopted from <http://www.ansys.stuba.sk/html/guide_55/g-str/GSTR10.htm>)

2.6 Shear Test Configuration

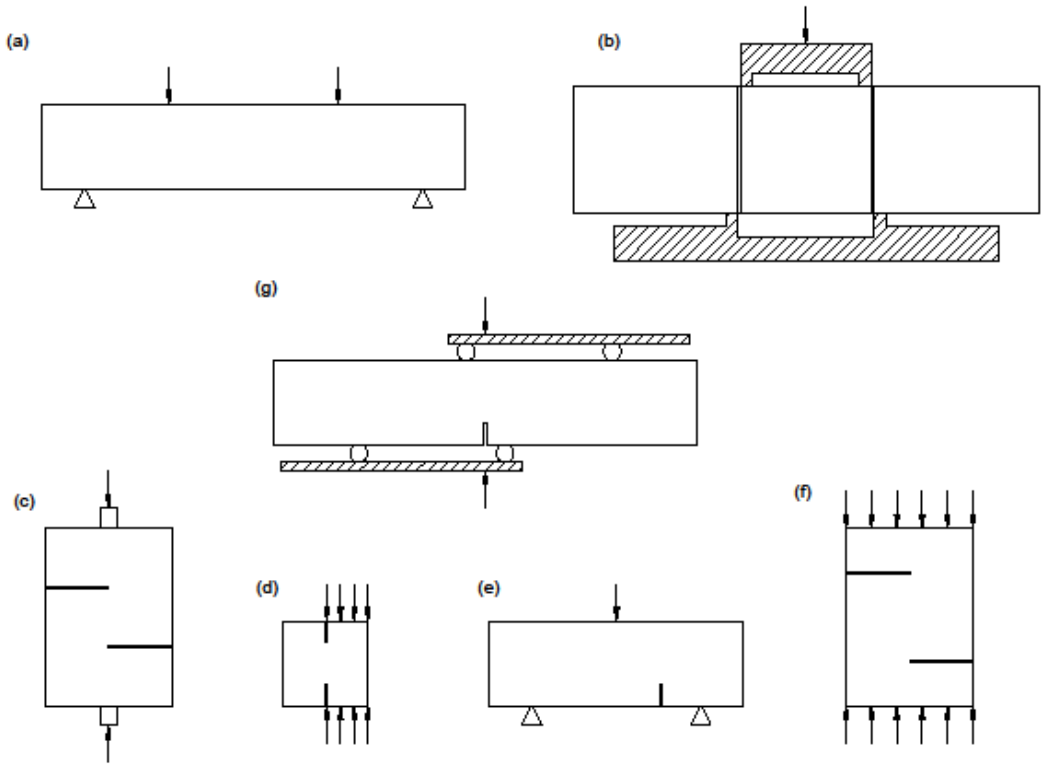

Figure 2.6 Shear Test Configurations

Figure 2.6 displays the collection of the current shear test configurations. Generally speaking, the shear test configuration is not standardized in the UK or many other countries. So a variety of test configurations was chosen to serve different purposes. For example, four point bending tests (4PBT) (a) or three point bending tests (3PBT) with small shear spans are

commonly applied in analysing the flexural shear failure in reinforced concrete beams. Most of shear design guidance of RC beam theory in established design standard/codes are based on this setup. (b) is a specific shear beam test for SFRC issued by the Japanese Society of Civil Engineer (JSCE 1990). Concentrated forces are applied on either side of the knife edges. Direct shear occurs at the reduced cross sectional area. The effect of added fibre on the concrete performance subject to direct shear can be quantified. The push-off test (c) usually comprises of two L-shape components, which are subject to shear at the interface. Djazmati (2004) employed the method to examine the shear stiffness of horizontal construction joints. He also cast four monolithic plain concrete specimens as benchmarks, the average shear strength of which was found to be 6.4MPa. No significant aggregate interlock was evident since coarse aggregate at interface was sheared off (Djazmati and Pincheira 2004, Mattock and Hawkins 1972).

Early in 20^{th} century, researchers turned their interest in fracture mechanism. Fracture mechanics was developed based on analytical solid mechanics to study the crack propagation in materials, although the boost of its application in concrete structures did not arrive until 1970s-1980s. The understanding and acquisition of the fracture parameters can be very useful in controlling the reflective cracking in the overlay. As pre-mentioned, pure mode II (shearing mode) rarely exist in engineering applications. It always involve mode I (opening mode) to a certain extent. There are standardized testing methods to test concrete under tension and to evaluate mode I parameters. But for mode II or mixed-mode, various testing configurations were developed by researchers. Reinhardt and Xu (1998) claimed that they found the test configuration to evaluate pure mode II stress intensity factor (K_{II}), as shown in Figure 2.6(d). The status at the onset cracking was deemed as the pure mode II, from which the K_{II} was obtained. The eccentric notched three point bending test (EN3PBT), as presented in Figure 2.6 (e), has the same set up as the common three point bending test, except that the beam specimen is saw-cut off the centre. It has been employed by many researchers in investigating the mix-mode failure (Jenq and Shah 1988, Swartz et al. 1988). Soroushian (1998) tested plain and fibre reinforced concrete beams measuring the displacement at loading point and the crack tip opening displacement (CTOD), crack tip sliding displacement (CTSD) and crack mouth opening displacement (CMOD) using four linear variable differential transformers (LVDT) and a clip gauge. The linear and non-linear fracture parameters were derived, such as energy release rates, mix-mode stress intensity factors and

fracture energy. It was found that the addition of 0.3% volume fraction of fibre improved the post-peak performance of concrete significantly, with regards to both crack opening and slippage. Steel fibre is more efficient compared to polypropylene fibre, considering the same volume fraction of fibre.

Last but not least, Nicolae Iosipescu (1967) proposed an asymmetrical four-point loading arrangement on a beam with two 45^{o} notches facing each other at the mid span. This arrangement guaranties pure shear and little flexure at the middle region of the beam. It was mainly applied on metallic materials, such as welded joints, and later on was developed into an ASTM standard (ASTM D5379) (2005) for testing the shear properties of laminated composite materials. A concentrated shear zone in the near absence of bending moments at the notch was created. It brought a new wave to the study of mix-mode fracture, which inspired an extensive range of studies and discussions on shear fracture, shear strength, mode II and mixed mode fracture energy (Bazant and Pfeifer 1986, Ingraffea and Panthaki 1985, Swartz and Tada 1990, Watkins and Liu 1985). In the last three decades, this configuration on either single-notched (as presented in Figure 2.6(g)) or double-notched specimens were exploited extensively in concrete with the attention to mode II – relating fracture failure experimentally and numerically albeit conflicting results (Barr and Derradj 1990, Bazant and Pfeifer 1986, Geers, de Borst and Peerlings 2000, Ingraffea and Panthaki 1985, Shi 2004). Bazant (1986) claimed that it was a pure mode II testing configuration following his test on double notched concrete beams with narrow shear zone between the middle loading points. He pointed out that the fracture energy was thirty times larger than mode I fracture energy. And crack propagated following the direction where the energy release rate is maximized, rather than mode I. However, it was later questioned and criticized that "the final failure may have been of a dynamic nature" as it was literally load controlled. It explains the "explosive" failure after the peak load.

Soroushian (1998) also employed a similar shear test configuration but on beams with double notches to assess the linear and non-linear fracture parameters. The test was conducted using a CMOD-controlled, servo-hydraulic close-loop system. Mode II stress intensity factor was derived based on Tada's formula (2000), as below. Where: Q = applied shear at the notch at the onset of slow crack growth; a = crack depth; b = height of the beam; B = width of the beam.

$$K_{II} = \frac{2Q}{B\sqrt{\pi a}} \frac{1.30 - 0.65(a/b) + 0.37(a/b)^2 + 0.28(a/b)^3}{\sqrt{1-(a/b)}} \quad 2.5$$

Swartz (1988) carried out experimentally investigation on 18 concrete beams employing single notch shear test configuration aiming to measuring mode II fracture parameters. It was pointed out that crack development can only be detected under stain controlled condition. The load was controlled by crack mouth sliding displacement (CMSD) using a customer-designed and fabricated fixture. Swartz found that the crack initiated in mode II but soon as the crack propagates, it involves mode I and becomes a mixed mode scenario. The onset cracking fracture energy was much larger than the one in mode I. It was explained as the contribution of aggregate interlock forces, which do not engage as much in the case of bending or tensile. Schlangen (1993) concluded that the test only provide very gross estimate of mode II parameters but could be improved with an appropriate analytical model with the effect of aggregate interlock and friction taken into consideration.

This image has been removed

Figure 2.7 Schlangen's SNSBT Setup (1993)

Schlangen (1993) in his report stressed the importance of a symmetrical loading setup. The setups employed by Arrea and Ingraffea (1982) or Carpinteri (1989) have one upper supporting spreader beam and two roller supports at the base, which were deemed as asymmetrical loading setup. Schlangen carried out experimental tests on a similar asymmetrical loading setup (as sketched in Figure 2.7(a)) and a symmetrical loading setup with one upper supporting spreader beam and one lower supporting spreader beam at the

base (as sketched in Figure 2.7(b)). The forces at the loading positions was detected and measured by strain gauges glued on the pendulum bars. The deformation at the far end loading position (δ_2) was measured by a LVDT. Based on his test geometry, the ratio of F_1/F_2 or F_{1R}/F_{2R} should be 10 in theory. However, it shows that in the old (i.e. asymmetric) loading system, the distribution varied considerably as the increase of deformation. In contrast, the symmetrical new system managed to keep the ratio constant for a much longer duration. Hence it was considered of vital importance to have a symmetrical loading setup to have a reliable load distribution. It was later incorporated in this study.

Though Bazant and Pfeiffer (1986) in their paper claimed that the fracture mode was mainly shear fracture, in fact, shear loading test does not necessarily leads to shear fracture, which was generally agreed by later researchers. Swartz et al (1988) stated that mode II testing arrangements cannot eliminate the influence of mode I, "compromises must be made which will lead to approximations—perhaps fairly gross--in the estimates of mode II fracture parameters."

Despite of the arguments on the fracture mode of this test setup, it simply simulates the problem of crack propagation due to shear loads in concrete beams, which can potentially provide a well presented indication for reflection cracking in concrete pavements due to shear. The SNSBT is predominantly a shear test configuration, but meanwhile, it allows the crack to open (i.e. crack dilation). Only the crack opening is only restrained by the fibre bridging. Hence potentially a material constitutive property can be obtained from this test configuration. The research should focus on investigating the effect of shear resistance on crack propagation in the overlay system. If the crack is trapped in the pavement with sufficient remaining shear resistance, the shear design is considered successful in solving the problem of reflective cracking.

The shear resistance can be provided by aggregate interlocking, reinforcement and shear capacity in the compression region. In the phenomenological analysis, the abovementioned factors will be investigated by means of existing literature, advanced FEA techniques and well-planned and executed laboratory tests. In the macroscopic scale, fracture mechanics defines the problem using more sophisticated parameters, e.g. fracture energy G_f & stress intensity factor K, which receive increasing recognition in the academia. For example, in the short bean shear test, it is considered nearly pure shear with minimum bending. However, in

the macroscopic scale, the mode I failure probably takes place initially which triggered the process of crack propagation. Thus, "pure shear" only exists at the phenomenological level. Hence, the shear problem in this study herein is defined as where shear becomes critical failure mechanism at the phenomenological level.

2.7 Overview of Rigid Pavement and Pavement Overlay Design

Professor Harald Malcolm Westergaard was the pioneer in rigid pavement design. As early as in 1923, his theory was published in Danish, which provided a series of calculations on stresses in rigid pavement at slab centre, edges and corners. Later on, it was translated in English and became the fundamental of modern pavement design, which is still being used nowadays (Westergaard 1926).

The stress and strain where reflective crack presents differ considerably from the non-cracking pavement (Kazimierowicz-Frankowska 2008). RILEM committee organizes regular conferences every 3-4 years since 1989 discussing the state-of-the-art research works on the cracking in pavements.

Despite the fact that no horizontal restraints are applied in the laboratory condition, in reality the axial stresses exist due to kerb's restraint.

There are established pavement overlay design guidance documents, i.e. ACI Committee 325 (2006) and National Concrete Pavement Technology Centre (2008). However, most of them are applicable in the case of asphalt concrete overlays or conventional concrete overlays. The use of roller compacted concrete overlay is rarely seen, not to say the relevant guidance. Hence, it is necessary and important to develop the first-hand experience working with roller compacted concrete overlays. Its recorded performance and laboratory testing data will comprise of the fundamental of future development of the guidance documents.

As a result of the environmental and/or traffic impact, once stresses in pavements exceed the maximum resistance, cracks are introduced in the pavement and furthermore giving rise to concentrated stresses in the overlay system. The causes of reflective cracking include:

- Traffic, especially heavy goods vehicles passing over/near an existing crack in the old pavement. It causes vertical and horizontal movement

- Temperature. The daily or seasonally temperature change could lead to cycles of crack opening and closure. Tensile stresses could be introduced in the overlay.

- Moisture. But concrete pavement is considered less susceptible to moisture than asphalt pavement. Moisture is one of the main factors that reduce the adhesion between asphalt and aggregates, while the concrete matrix is more stable.

With regards to shear resistance, only traffic loading is considered in this research. The crack initiation is usually induced by a defect already present in the underlying layer. Subjected to constant traffic loading, it propagates upwards passing the interface into the overlay until it reaches the surface. An idealized fully effective bond can be assumed between the two layers. However, the bond characterization was conducted experimentally to produce a more realistic simulation.

As above-mentioned, the nature of crack edge movement includes: mode I opening; mode II shearing and mode III tearing. In terms of propagation of reflective cracking due to shear failure, the mode II is the key failure mode. It occurs when vehicle travelling alongside of a continuous longitudinal crack or approaching a transverse crack (as shown in Figure 2.8), although it evokes both the mode I and mode II movements (Vanelstraete and Francken 1997). Occasionally Mode III tearing also takes place at crack tips. Mode I, II and III usually happens simultaneously, depending on the position of traffic with respect to the crack and the geometry of the crack. However, in this study, only mode I and mode II are considered, which refers to as “mixed – mode”.

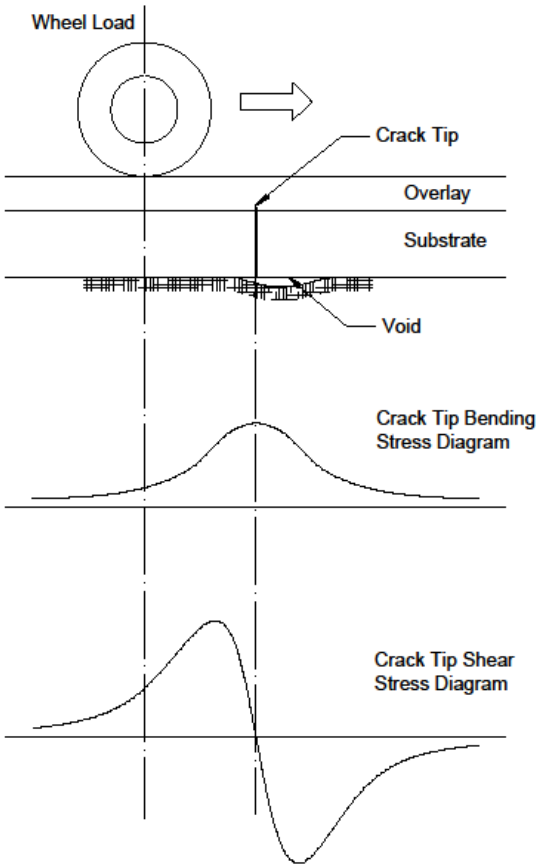

Figure 2.8 Stresses induced at the cracked section of an overlay due to a moving wheel load (Jayawickrama and Lytton 1987, Zhou et al. 2010)

According to AASHTO pavement design guide (1993), the bonded concrete overlay thickness design employs the structural deficiency approach: $D_{OL} = D_f - D_{eff}$, where D_f is the required thickness of a new concrete pavement and D_{eff} is the effective thickness of the existing pavement. Therefore, an effective evaluation of the existing pavement is a key to successful design and construction of BCO. The ACI Committee 325 report (2006) suggests that the evaluation requires a visual survey of present and severity of pavement distresses, deflection testing using falling weight deflectometer (FWD) and coring.

2.8 Conclusions

From the literature review it can be concluded:

- It is tenable that bonded concrete overlay is usually only suitable when the existing pavement is in an acceptable condition. However, whether a steel fibre reinforced concrete overlay can do the job lacks investigation.

- Roller compacted concrete is an economical, durable an versatile solution in pavement construction. Further investigations are needed in terms of crack control by introducing fibres in it, roller compactibility, mix water content and mix workability, etc.

- Existing mix design methods are for pavements resting on a sub-base or sub-grade. They could be unsuitable for bonded concrete overlays where bond to the underlaying concrete must be assessed and satisfied.

- Research should focus on investigating the effect of shear resistance on crack propagation in the overlay system. If the crack is trapped in the pavement with sufficient remaining shear resistance, the shear design is considered successful in the reflective cracking problem.

- Established pavement overlay design guidance are applicable in the case of asphalt concrete overlays or conventional concrete overlays. The use of roller compacted concrete overlay lacks development and experiences.

CHAPTER 3 EXPERIMENTAL INVESTIGATION –

MIX DEVELOPMENT

3. Experimental Investigation – Mix Development

3.1 Introduction

As explained in the previous chapters, a particular concrete overlay material is needed to provide adequate strength and resistance to reflective cracking and meanwhile, facilitate rapid construction technique. This chapter is dealing with the mix development and characterization of mechanical properties. It comprises of the development of the new mix design method for Steel Fibre-reinforced, Roller Compacted and Polymer Modified Bonded Concrete Overlays (SF-RC-PM-BCO).

Bonded concrete overlays suffer from delamination with the substrate layer. To rectify the problem, polymers, in the forms of Styrene Butadiene Rubber (SBR) and Polyvinyl Alcohol (PVA), were added to the mixes to enhance the bond (Hughes 2006, Delatte Jr. 2008). On the other hand, BCO is known for suffering from thermal cracking, shrinkage cracking and reflective cracking. Hence steel fibres were added to the mixes to improve the resistance of pavement to cracking (Delatte Jr. 2008). The mixes are named as "steel fibre reinforced, roller-compacted and polymer modified, bonded concrete overlay", SF-RC-PM-BCO for short. The mix constituents of this PMC overlay were initially assessed in a previous study conducted by Koutselas (2010), in which the types of aggregate, glass fibre, SBR, PFA and MTK were extensively investigated and carefully selected.

3.2 Mix Constituents and Properties

The physical properties of materials used are presented in Table 3.1. The physical properties of cement (CEM), Styrene-Butadiene Rubber (SBR), Polyvinyl Alcohol (PVA), Steel Fibre (SF), Metakaolin (MTK), Pulverized Fuel Ash (PFA) and Superplasticizer (SP) were provided by the suppliers, while coarse aggregate and fine aggregate were tested in accordance with the relevant British Standards.

Table 3.1 Materials and Properties

	Properties	Supplier /Manufacturer	
Cement (CEM)	Cement-I, 52.5N, specific density 3150 kg/m^3	Hanson Heidelberg Cement Group, UK	
Coarse aggregate (CA)	Crushed gritstone, size 4.75 - 10mm, impact value 12.9%, apparent particle density on oven dry 2790kg/m^3, particle density on saturated surface-dried basis 2770kg/m^3, water absorption 0.5%. See the following section for extra details.	Bayston Hill Quarry, Tarmac Ltd, UK	
Fine aggregate (FA)	Quartz river sand, apparent particle density 2670kg/m^3, fineness modulus 2.476, water absorption 0%. See the following section for extra details.	Coventry Building Supplies, UK	
SBR	White liquid, solid ingredient content 46% by weight, water content 54%, specific density 1040kg/m^3.	Everbuild Building Products, UK	
PVA	Polyvinyl alcohol GH-17S, white powder and water soluble, specific density 1250 kg/m^3.	Nippon Gohsel, Japan	

	Properties	Supplier /Manufacturer	
Steel fibre (SF)	length 35mm, hooked-end, rectangular section 0.45mm ×0.6mm, tensile strength 1050MPa, aspect ratio 60.	Propex Concrete Systems Corp., UK	
Metakaolin (MTK)	white powder, specific density 2507kg/m^3, loss on ignition 1% ,water demand (Mars cone) 900g/kg.	AGS Mineraux, France	
Pulverized Fuel Ash (PFA)	powder, specific density 2090kg/m^3	Drax Power Station, UK	
Superplasticizer (SP)	Auracast 400, liquid, dark straw, specific density 1020kg/m^3.	Fosroc Ltd, UK	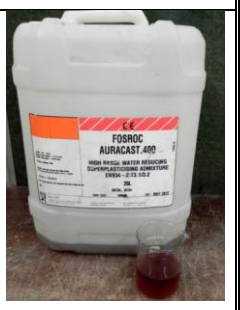
Retarder	Sika 50, liquid, pale straw, relative density 1.215	Sika Ltd, UK	

3.2.1 Coarse Aggregate (CA)

The aggregate crushing value (ACV) was tested in accordance with BS 812-110:1990 (1990a). ACV is defined as the percentage of mass passing a certain size of sieve after crushing under a gradually applied compressive load. The smaller the value is, the higher the resistance to crushing. The gritstone of nominal size of 14mm reached 9.67%, close to the

specified ACV by the supplier, 9%. The gritstone of nominal size of 10mm reached 11.4%, and the granite of the same size reached 19.98%. Usually the larger the aggregate size, the higher the ACV value, the lower the resistance to crushing. However, the 14mm gritstone produced a lower value than 10mm gritstone. This can be explained by the different sizes of apparatus were specified for 14-10mm and 10-5mm graded aggregate. The standard specified the cylindrical container of 152mm diameter and passing sieve size of 2.36mm for the former. A testing cylindrical container of 78mm diameter and passing sieve size of 1.7mm are specified for the latter. Hence, the test results do not contradict the common sense.

Additionally the aggregate impact value (AIV) was tested in accordance with BS 812-112:1990 (1990b). AIV is defined as the percentage of mass passing a certain size of sieve followed by aggregate subjects to a standard amount of impact produced by falling weight. The coarse aggregate tested were gritstone, granite and limestone. All had a dominant size of 10mm. The AIV values were measured to be 12.9, 22.7 and 27.4.

Generally speaking, both ACV and AIV indicate aggregate strength with regards to crushing and impact. Both tests reached the same conclusion that gritstone has better resistance than granite or limestone. Pavement surface course usually requires high strength aggregate, since it needs to withstand high stress due to wheel loads. Weak aggregate may be specified for underlying layers. For example, the AIV of more than 35 is usually regarded as too weak to use in road surface.

Therefore, the use of granite in the preliminary stage of laboratory tests was eventually replaced by gritstone at a later stage owning to its higher resistance to crushing and impact.

Gritstone aggregate with three different nominal maximum sizes of 10mm, 14mm and 20mm were employed in the research. The moisture content was found to be 0.36% comparing with the samples left in the oven at 105°C for 6 hours. The apparent particle densities and water absorption ratios are summarized in Table 3.2. The gradation of 4/10 coarse aggregate, 10/14mm coarse aggregate and 14/20mm coarse aggregate are drawn in Figure 3.1. To avoid segregation of the single-sized 20mm coarse aggregate in the mix, the 14/20 aggregate was mixed with 4/10 aggregate at a ratio of 4:1 to conform to the recommended overall grading

limits for $G_c^{90/15}$ by PD 6682 (British Standards Institution 2009b). The graded aggregate 4/20 is also presented in Figure 3.1.

3.2.2 Fine Aggregate (FA)

Quartz river sand was used. The apparent particle density and water absorption are 2670kg/m^3 and 0% (Table 3.2), tested in accordance to BS EN1097-6 (2000). The fineness modulus is 2.476. Sand gradation is as shown in Figure 3.1. Sand ratio, hereinafter, is defined as sand (fine aggregate) to total aggregate (fine aggregate plus coarse aggregate) ratio by weight. Three different sand ratios, i.e. 0.34, 0.4 and 0.5, were used in the study. Their gradations are presented in Figure 3.1 and Table 3.3.

Table 3.2 Aggregate Density and Water Absorption

	Apparent Particle Density	Particle Density on an Oven-dried Basis	Particle Density on a Saturated and Surface-dried Basis	Water Absorption
	ρ_a (mg/m^3)	ρ_{rd} (mg/m^3)	ρ_{ssd} (mg/m^3)	WA_{24}
0/4 FA	2.67	2.66	2.66	0.0%
4/10 CA	2.79	2.76	2.77	0.5%
4/14 CA	2.80	2.76	2.77	0.5%
Supplier's Info on CA	2.79	2.70	2.73	1.3%

Table 3.3 Gradation of All-in Aggregate

Size	Sand ratio	Cumulative passing by weight (%)											
		20	14	10	6.3	4.75	4	2.36	1.18	0.6	0.3	0.15	0.075
0/10	0.345	100	100	95.32	45.22	42.39	33.25	26.85	23.71	19.77	7.32	2.41	0.27
0/10	0.4	100	100	95.72	49.82	46.54	38.17	31.13	27.49	22.92	8.49	2.80	0.32
0/10	0.5	100	100	96.43	58.18	54.08	47.10	38.91	34.36	28.65	10.61	3.50	0.40
0/14	0.5	100	93.13	56.11	50.65	46.55	-	38.91	34.36	28.65	10.61	3.50	0.40
0/20	0.5	99.05	62.54	59.40	51.70	47.60	46.21	38.91	34.36	28.65	10.61	3.50	0.40

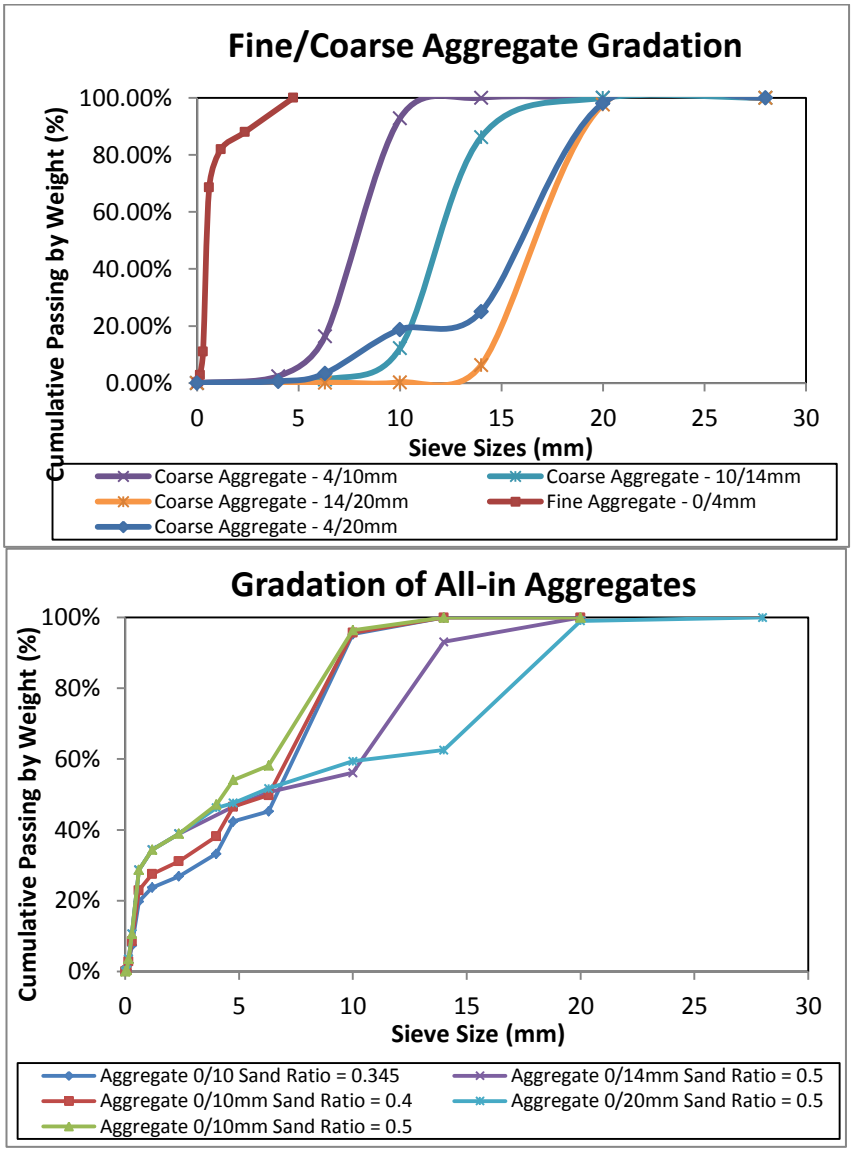

Figure 3.1 (a) Aggregate Gradation (b) Gradation of All-in Aggregates

3.2.3 Cement, Metakaolin and Pulverized Fuel Ash

The physical properties and chemical compositions of Cement (CEM), Metakaolin (MTK) and Pulverized Fuel Ash (PFA), provided by the suppliers are listed below .

Table 3.4 Physical Properties and Chemical Composition of CEM

Physical property	Chemical compound by weight (%)								
Loss on ignition	SiO_2	Al_2O_3	Fe_2O_3	CaO	MgO	SO_3	K_2O	Na_2O	Cl
3.30%	20.06	4.42	2.67	64.04	1.19	3.1	0.71	0.21	0.05

Table 3.5 Physical Properties and Chemical Composition of PFA

Physical Properties		Basic Oxide Composition (average by weight, %)						
Loss on ignition	Fineness	SO_3	CaO	MgO	K_2O	Al_2O_3	Fe_2O_3	SiO_2
4.80%	25.10%	0.77	2.8	1.5	3.1	24.7	8.8	51.2

Table 3.6 Physical Properties and Chemical Composition of MTK

Physical Characteristics			Basic Oxide Composition (average by weight, %)					
Loss on ignition	Pozzolanic index	Specific area	TiO_2	CaO+MgO	Na_2O+K_2O	Al_2O_3	Fe_2O_3	SiO_2
1%	1100mg $Ca(OH)_2$/g	17m²/g	1.5	0.3	0.8	40	1.4	55

3.2.4 Polyvinyl Alcohol (PVA)

Two PVA products, GH-17S and NH-18S, were compared and examined for the suitability in the overlay mix. The former has higher viscosity of 27-33 centipoise, while the latter has 25-30 centipoise. With regards to degree of hydrolysis, the GH-17S is lower, 86.5-89.0 mol% in comparison with 98.0-99.0 mol% in NH-18S. After dissolving in water, the GH-17S solution presented high viscosity, which was considered favourable in the application of bonded concrete overlay. Hence it was selected. As detailed in the following paragraphs, the inclusion of GH-17S managed to improve the bond strength as predicted.

3.3 Mix Design Criteria

The focal point of a successful SF-RC-PMC overlay mix design is to determinate the appropriate water content. The dilemma is having either little water and dry mix but weak bond to the underlying pavement, or plentiful water and 'lumpy' mix but relatively low strength. In this study we used the water-cement grouts as the bonding medium between fresh and old concrete. The cement paste in a wet mix is a practical and economical, which would be able to moisten the interface with the old pavement, and consequently provide a decent bond. Epoxy resin grouts specially formulated for each application also are on the market. Nevertheless, high water content will result in high water-cement ratio and therefore, low strength. Moreover, 'lumpy' mix is unsuitable for placing and spreading using asphalt paving machinery. The terms of '*paver placeability*' and '*roller compactability*' are defined in assessing the mix workability for fast construction using asphalt pavers and vibrating rollers. A mix with the appropriate workability should be suitable for roller compaction and in the meantime, viable to be placed by asphalt pavers. In conclusion, mixes should be relatively dry for fast construction, but also wet to achieve good bond.

To setup a baseline for the bond with substrate, ordinary Portland cement concrete (OPCC) to OPCC bond was employed. They are generally used in conventional concrete overlays. The mix proportion in Table 3.7 is similar to that used in successful conventional BCOs applications in America. (Mokarem, Galal and Sprinkel 2007) The block splitting tests and cylinder direct shear tests are introduced to examine the bond performance. The tests details are elaborated in section 3.3.1 and 3.3.2. The tensile bond strength in Mokarem et al (2007)'s report is 1.65 MPa compared to 2.17 MPa in our study. Our baseline strength is slightly higher. The 28-day strengths are listed in Table 3.7. Refer to the following sections for the test details. The cube compressive strength (f_c) is 60.4MPa. The flexural tensile strength in three point beam bending test (f_t) is 4.66MPa. The cylinder direct shear strength (τ) is obtained as 7.0MPa. The cylinder splitting tensile strength (f_{st}) is 4.57MPa. The OPCC-to-OPCC bond strengths obtained in the cylinder direct shear test is 4.09MPa and 2.17MPa in the block splitting tensile test. Hence, these two figures were chosen to be lower limits of the bond strengths of SF-RC-PM-BCO. In other words, the bond strength to the existing pavement in SF-RC-PM-BCO design should be at least equal to the bond strength in conventional BCO.

Table 3.7 OPCC Proportions and Mechanical Properties

Quantities for 1 m³ concrete (kg)				Mechanical properties (MPa)				OPCC-to-OPCC bond strength (MPa)	
CEM	CA	FA	water	f_c	f_t	τ	f_{st}	f_{sb}	f_{stb}
402	1116	648	205	60.4	4.66	7.0	4.57	4.09	2.17

From the practical point of view, the mix should be dry and solid enough to sustain the load from vibrating rollers.

- The mixes determined by modified proctor (M-P) (ASTM 2012) method and the modified Vebe (M-VB) (British Standards Institute 2010) method are generally relatively dry and suitable for heavy duty vibrating rollers.

- Light rollers are usually used to compact soils-alike materials, where the optimal water content is determined by the standard proctor (S-P) method (ASTM 2002).

Hence, if the mixture contains more water than the one determined by the S-P method, light rollers may have problems in compacting it. This reveals another manifest criterion that the optimal water content should be no more than the one determined by the S-P method.

Last but not least, visual examination in laboratory trial samples can also provide a few characteristics, such as cohesiveness, tendency for segregation etc. (ACI Committee 207 1999).

In summary, mixes with appropriate water content for roller compacted bonded concrete overlays should satisfy the following criteria simultaneously:

- The mix should not be lumpy during placing and spreading; rather, it should behave like a granular material for paver placeability.
- The water content should be less than or equal to that determined by the S-P method for roller compactability.
- The cylinder direct shear bond strength and the block splitting tensile bond strength of PMC-to-OPCC should be at least equal to or greater than that of the OPCC-to-OPCC bond strength.
- The compacted specimens with optimal water content should have satisfactory appearance, e.g. no visible voids on the surface.

3.3.1 Block Splitting Test

Figure 3.2 Block Splitting Test (a) Sample (b) Jig (c) Subject to Splitting

The interface between overlay and old concrete pavement undergoes shear, tension and compression under vehicular and thermal loading during its service life. Accordingly, the bond performance is evaluated by both the direct shear bond strength and splitting tensile

bond strength. The block splitting test employs the testing jig as shown in Figure 3.2(b). The specimen of $150mm \times 150mm \times 100mm$ comprises 50mm thick OPCC simulating the substrate material and 50mm thick of overlay material, as pictured in Figure 3.2(a). The preparation of composite specimens is detailed in Section 3.6. A hydraulic machine of 2000kN capacity jointly with a Si-Plan servo controller was employed to apply the compressive load at a constant loading rate of 1.4kN/s, which falls in the range of 0.04-0.06MPa/s as specified in BS EN 12390-6:1990 (2009a). Figure 3.2(c) shows the crack appearing at the interface in the test. The maximum load (P) was recorded and the block splitting tensile strength f_{stb} is calculated as in Eqn.3.1.

$$f_{stb} = \frac{P}{A_b} = \frac{P}{150 \times 150} \qquad 3.1$$

Following the execution of the tests, it was double-checked to ensure the loading position was not misaligned and the failure occurred at the interface. Otherwise, the result was discarded. The same checking procedure was repeated for the cylinder direct shear bond test as well. The strength for each mix was derived by averaging the results of three individual specimens.

3.3.2 Cylinder Direct Shear Bond Test

Figure 3.3 Cylinder Direct Shear Test (a) Sample (b) Testing Rig

The cylinder direct shear test is similar to the Iowa Testing Method 406-C (Iowa Department of Transportation 2000). The OPCC cylinder base is 100mm in diameter and 100mm in height. The overlay material is approx. 80mm in height. The test rig was purposely manufactured to provide a firm grip on the OPCC section, while the overlay material was overhanging. A vertical compression load is applied on the overhanging section right next to

the interface through a curved applicator, as pictured in Figure 3.3 (b). A hydraulic machine of 500kN capacity was employed in conjunction with a Si-plan servo-controller to apply the load at a constant rate of 0.39 kN/s, which is equivalent to 0.05MPa/s. The peak load (P) was recorded and the direct shear bond strength was calculated by Eqn. 3.2.

$$f_{sb} = \frac{2P}{\pi A} = \frac{2P}{\pi^2 \times 50^2} = \frac{P}{1250\pi^2} \quad 3.2$$

Where: f_{sb} is the splitting tensile strength (MPa); P is the maximum load (N); A is the area of the splitting section (mm^2).

3.4 Determination of Optimal Water Content

The study originated by scrutinizing the appropriate compaction effort with the existing established methods, as specified below.

- The S-P compaction method(2002): 2.5 kg rammer drops from 300mm height on samples in 3 layers, 27 blows each
- The M-P compaction method(2002): 4.5 kg rammer drops from 450mm height on samples in 3 layers, 27 blows each
- The M-VB method (2006): vibrating with a total weight of 22.7kg of surcharge and plate on top until the appearance of mortar around the rim

The above methods were experimentally investigated and assessed by the abovementioned criteria. A modified method was later developed by adjusting the number of rammer drops and the number of compacting layers to obtain the suitable compaction result, and hence the most favourable water content. A wide range of mixes were employed for validation. The volume fraction of steel fibre varied at three levels - 0%, 1% and 1.5%. The SBR to cement ratio by solid ingredient in SBR, varied from 3% to 10% by weight. The PVA to cement ratio varied at four levels - 0%, 1%, 2% and 3%. Furthermore, the nominal maximum size of coarse aggregate varied between 10mm and 14mm.

The moisture content w, wet density γ_w , dry density γ_D and air content α were used to determine maximum dry density and optimal moisture content. The relationships used are

presented below. The method of ASTM C138/C 138M-01a(2001)was used to determine the sample density and air content.

$$w = \frac{W_T - CA \times WA_{24}}{CEM+PFA+MTK+CA+FA+SBR\times 46\%+PVA+SF} \quad 3.3$$

$$\gamma_D = \frac{\gamma_w}{1+w} \quad 3.4$$

$$W_T = W_a + SBR \times 54\% \quad 3.5$$

$$\beta = \frac{\gamma_w}{CEM+PFA+MTK+CA+FA+SBR+PVA+Sp+W_a+SF} \quad 3.6$$

$$V_{a1} = \frac{CEM_1}{3150} + \frac{PFA_1}{2090} + \frac{MTK_1}{2507} + \frac{CA_1\times 1.005}{2770} + \frac{FA_1}{2670} + \frac{SBR_1}{1040} + \frac{PVA_1}{1250} + \frac{Sp_1}{1020} + \frac{W_{a1} - CA_1 \times WA_{24}}{1000} + \frac{SF_1}{7800} \quad 3.7$$

$$a = 100 \times (1 - V_{a1}) \quad 3.8$$

$W_e = W_T\text{-}A \times 0.5\%$Where: w is the moisture content (%); γ_w is the wet density in kg/m^3 determined by experiments; γ_D is the dry density in kg/m^3; W_T is the total mass of water including added water plus the water fraction contained in SBR in kg; W_a is the mass of added water in kg; WA_{24} is the water absorption of coarse aggregate, 0.5% as specified in Table 3.2, CEM, PFA, MTK, CA, FA, SBR, PVA are the masses in kg; Sp is Super-plasticiser and SF is the mass of Steel fibre in kg. Their values are listed in Table 3.8.

3.4.1 Modified Vebe Method and Modified Proctor Method

All the mixes employed in the compaction test are listed in Table 3.8. The test procedures of the Modified Proctor (M-P) method and the Modified Vebe (M-VB) method complied with BS 1377-4:1990 (2002) and ASTM C 1170-06 (2006).

Table 3.8 Mixes Used for Various Compaction Methods (Unit: kg)

Mix ID	CEM	PFA	MTK	CA	FA	SBR	Total Water	SF
M1	486	109	40	1053	554	31	variable	0
M2	486	109	40	1053	554	31		39
M3	486	109	40	1053	554	31		117
M4	635	0	0	964	643	138		0
M5	635	0	0	964	643	138		117

Figure 3.4 and Figure 3.5 plot the dry density – water content curve determined by the M-P, M-VB and S-P methods. They follow an approximately parabolic relation. The peak points correspond to the maximum dry density and the so-called optimum water determined by the

specific method. As listed in Table 3.8, the steel fibre content varies from 0%, 0.5% to 1% in mixes M1, M2 and M3. The figures dictate that the more steel fibre in the mix, the more water it requires to attain the maximum dry density. Furthermore, the M-VB test results in a higher optimum water content using the same mix than the M-P method., while the S-P method provides even higher optimum water contents than the M-VB test. As stated at the beginning of this section, the S-P uses a much lighter standard proctor than the M-P method. Hence, with the same number of impacts on the same quantity of samples in each compacting layer, the M-P method produces the maximum compaction effort, while the S-P produces the lightest compaction effort and the M-VB lies somewhere in between. In short, the compaction effort follows the order of M-P > M-VB > S-P. The optimum water content determined follows the order of $W_{S\text{-}P} > W_{M\text{-}VB} > W_{M\text{-}P.}$

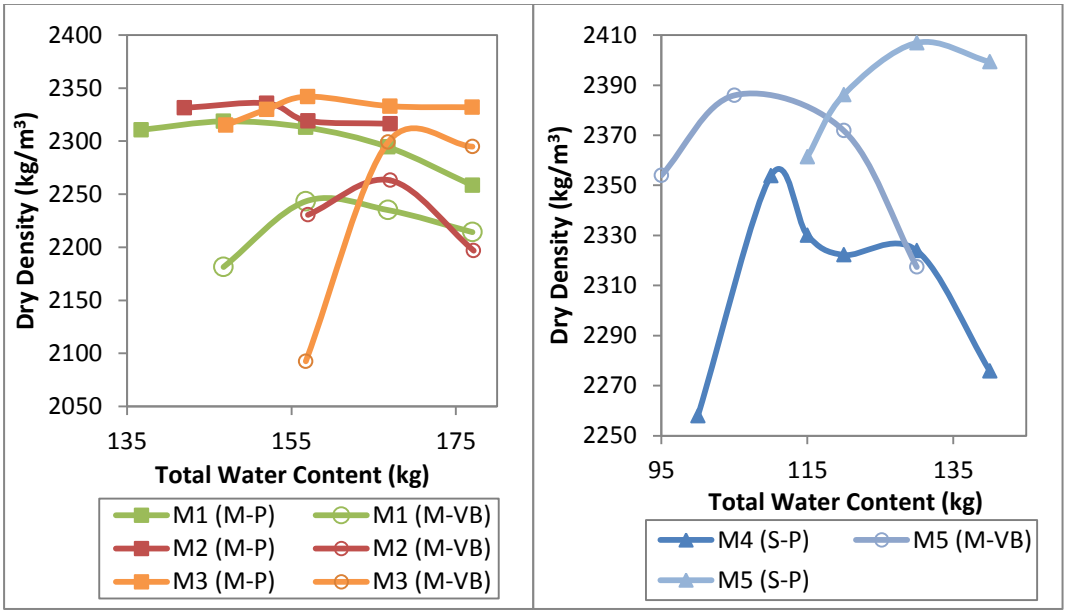

Figure 3.4 Optimum Water Contents Determined by the M-P & M-VB Methods

Figure 3.5 Optimum Water Contents Determined by the M-VB & S-P Methods

Table 3.10 presents the maximum dry density, the corresponding wet density and air content, and the mix proportion with optimal water content. The added water contents are calculated accordingly using Eqn. 3.3. The mass of each ingredient in 1 m^3 concrete can be evaluated using the wet density and mix proportion listed in Table 3.10.

The experimental work disclosed that the mixes with the optimum water content determined by the M-P and M-VB methods were granular-like and suitable for roller and paver construction. However, the appearance of voids on the surface of the VB samples dictates

unsatisfactory air content in the mixture. It is pictured in Figure 3.7 together with the Vebe consistometer in Figure 3.6. The air content calculated using Eqns. 3.5 and 3.6 further affirmed the conclusion. As listed in Table 3.10, the air contents in the mixes with optimum water contents determined by the M-VB method are commonly higher than those determined by the comparable tests. It can be foreseen that the concrete durability could be sacrificed if the M-VB method were to be used to determine the optimum water content in the SF-RC-PM-BCO. Composite cylinders were prepared for the direct shear test. The details of the preparation, specimen formation and curing can be found in sections 3.6. It caused attention that voids always present at the interfaces where the optimum mixes determined by the M-P method were adopted for the overlay. Hence, it was questioned whether the M-VB and the M-P method are suitable in this application. The answer was ascertained following the bond strength tests.

As aforementioned, the OPCC-to-OPCC bond strengths in the cylinder direct shear test and the block splitting test are 4.09MPa and 2.17MPa, which are the lower limits for a satisfactory bond performance.The optimal mixes (M1, M2, M3 and M5) determined by the M-VB and the M-P methods, as detailed in Table 3.10, were tested in the cylinder direct shear test. The results are summariezed in Table 3.9. None of them reached 4.09MPa. Also, mix M5 determined by the M-VB method only reached 1.27MPa in the block splitting test, lower than 2.17MPa in OPCC-to-OPCC. Apparently, the above mixes are too dry to form sufficient cement paste moistening the interface. As a result, low bond strength was attained. In conclusion, both the M-P and M-VB methods are unsuitable and rulled out for this application.

Table 3.9 Cylinder Direct Shear Test Results

	M1	M2	M3	M5	OPCC
M-VB	2.52	2.93	2.41	3.79	4.09
M-P	1.48	1.76	1.04	-	

Figure 3.6 Vebe Consistometer

Figure 3.7 Compacted Sample with Optimal Water Content by M-VB Method

It should be pointed out that the low bond strengths for the mixes M1, M2 and M3 were partially attributed to the low SBR content. Nevertheless, the mix of M5, containing more than 4 times the SBR content, with the optimal water content determined by the M-VB method, still produced lower direct shear bond strength and splitting strength than the corresponding strengths of OPCC-to-OPCC.

Table 3.10 Mix Proportions Determined by M-P, M-VB and M-L

	Mix ID	Mix Parameters			Mix Proportion								
		Max. Dry Density kg/m³	Max. Wet Density kg/m³	Air Content %	CEM	PFA	MTK	CA	FA	SBR	added water	SF	Total water w/c
M-P	M1	2304	2446	1.62	1	0.224	0.082	2.167	1.140	0.064	0.267	0	0.3
	M2	2319	2467	1.56	1	0.224	0.082	2.167	1.140	0.064	0.278	0.080	0.31
	M3	2342	2492	2.34	1	0.224	0.082	2.167	1.140	0.064	0.288	0.241	0.32
M-VB	M1	2226	2376	3.85	1	0.224	0.082	2.167	1.140	0.064	0.288	0	0.32
	M2	2247	2405	3.15	1	0.224	0.082	2.167	1.140	0.064	0.309	0.080	0.34
	M3	2280	2438	3.87	1	0.224	0.082	2.167	1.140	0.064	0.309	0.241	0.34
	M5	2386	2485	5.1	1	0	0	1.518	1.013	0.217	0.048	0.184	0.17
M-L	M4	2352	2454	2.92	1	0	0	1.518	1.013	0.217	0.056	0	0.17
	M5	2424	2539	3.04	1	0	0	1.518	1.013	0.217	0.072	0.184	0.19

3.4.2 Standard Proctor (S-P) Method

Following the failure of the M-P and M-VB methods, a lower compaction effort which may result in higher water content, seemed more favourable. So the S-P method (2002) was introduced. The optimum water contents for Mix M4 and M5 were found following the principle of maximum dry density. The graphs were plotted in Figure 3.5. As expected the optimum water in Mix M5 was higher than that determined by the M-VB test. The visual examination found that the mix turned very lumpy and not suitable for asphalt paver construction. Hence, the S-P method is ruled out for the determination of optimal water content in SF-RC-PM-BCO as well.

Nonetheless, as above-mentioned, years of experience proves that the corresponding construction machinery for compacting mixture determined by the S-P method is light-weight roller compactors. If water content is higher than that determined by the S-P method, the existing roller compactors may not be able to fulfil the requirement for a proper compaction. Due to the availability of existing construction machinery, the desired water content should be less than or equal to that determined by the S-P method for roller compactability. Despite the fact the S-P method is deemed unsuitable for this application, it still serves a basis in the design criteria.

3.4.3 Modified Light (M-L) Method

Since the above methods failed to conduct a suitable compaction effort in the application of SF-RC-PM-BCO, it became clear that a compaction effort set between the ones conducted by the M-P and the S-P method is in need. It was decided to employ the procedure in the S-P method but with different compaction effort by applying various numbers of blows on various numbers of layers. They are detailed herein: (a) five layers and twenty-seven blows per layer (5×27 blows); (b) four layers and twenty-seven blows per layer (4×27 blows); (c) four layers and twenty blows per layer (4×20 blows); (d) three layers and twenty-seven blows per layer (3×27 blows, namely the S-P method).

The optimum water content in Mix M5 was evaluated with the above compaction levels. The resulting dry densities are plotted in Figure 3.8. The peak points with solid marker fills correspond to the optimum water contents. It can be seen that the optimum water content decreases with the increasing compaction effort. The mix by 4×20 blows produced the

closest optimum water content (i.e. 120kg) to that determined by the S-P method (i.e. 130kg). However, the mixture did not show any sign of lumpiness in the visual examination. The same test was repeated on Mix M4. The water content of 110kg was determined by 4×20 blows. It also appeared a satisfactory granular-like material in lab observation, which suggests adequate paver placeablity.

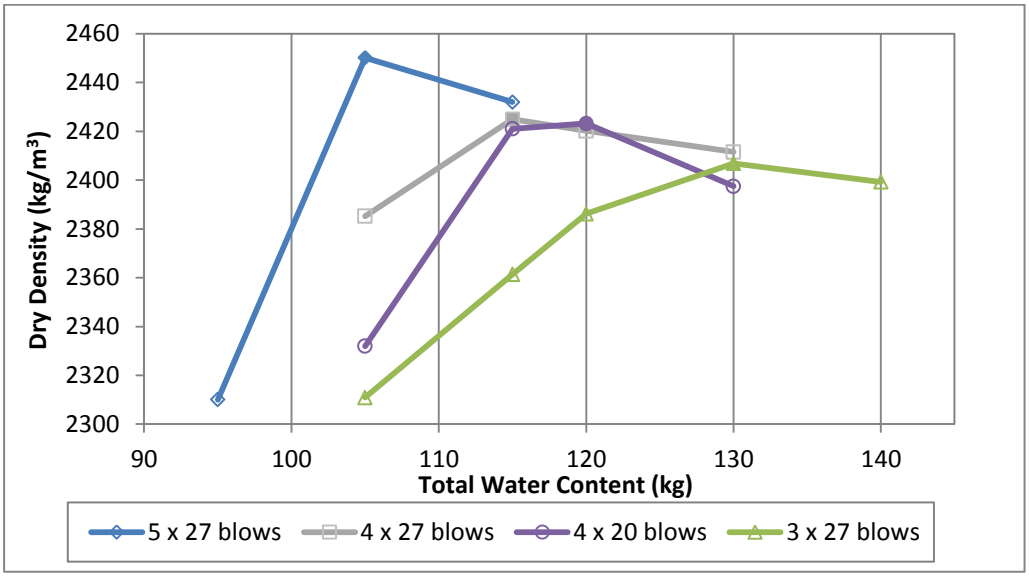

Figure 3.8 Optimum Water Contents by Various Compaction Efforts

Further laboratory tests on bond strength were conducted on nine additional mixes determined by the compaction effort of 4×20 blows for verification. Meanwhile the visual examination was executed for "roller compactability" and "paver placeablity". The results met all the design criteria. Hereafter, this method is shorted for "modified light (M-L) method".

The nine mixes assessed by the M-L method are listed in Table 3.11. It involves the use of coarse aggregate of nominal size 10mm and 14mm, superplasticizer, sand ratio of 40% and 50% and polymer types of SBR, PVA and the SBR-PVA hybrid polymer at various dosages. The sand ratio is defined as the proportion of fine aggregate in the sum of fine aggregate and coarse aggregate by weight. The percentage values in brackets under SBR, PVA and superplasticizer are the solid content to cement by weight. The properties of the mix constitutes can be found in Section 3.2.

The M-L method was first verified by using the mix M5, as shown in Figure 3.8, with maximum aggregate size of 14mm. The optimal water content (total water content) obtained

was 115kg. The mix behaved like granular, not lumpy. This is reassuring for the adequacy of the M-L method on mixes with 14mm coarse aggregate.

Table 3.11 Mixes for Verifying M-L Method (Unit: kg)

Mix ID	CEM	CA	FA	SBR	PVA	SP	Total Water	SF
M6	635	964	643 (40%)	138 (10%)	6.35 (1%)	0	variable	117
M7	635	964	643 (40%)	138 (10%)	12.7 (2%)	0		117
M8	635	964	643 (40%)	138 (10%)	19.05 (3%)	0		117
M9	635	804	804 (50%)	138 (10%)	0	0		0
M10	635	804	804 (50%)	138 (10%)	0	0		117
M11	635	804	804 (50%)	138 (10%)	12.7 (2%)	0		117
M12	635	804	804 (50%)	0	6.35 (1%)	9.53 (1.5%)		117
M13	635	804	804 (50%)	0	12.7 (2%)	9.53 (1.5%)		117
M14	635	804	804 (50%)	69 (5%)	12.7 (2%)	0		117

The experimental results, namely the relationships between dry density and total water content are plotted in Figure 3.9. Table 3.12 gives the mix proportions with optimum water contents determined by this method. The maximum dry densities, the corresponding wet densities and air contents are also summarized in the table. The ingredient quantity for 1 m^3 concrete can be attained easily by multiplying the wet density by mix proportions in Table 3.12. Summarizing from Table 3.12 and Figure 3.9, it is manifest that the optimum water content increases with the increasing amount of steel fibre and PVA. As stated in Table 3.10 and Table 3.12, the plain mixes M4 and M5 had sand ratio of 40%, while the fibre-reinforced mixes M9 and M10 had sand ratio of 50%. The other mix proportions were similar. Comparing M4 with M9 and M5 with M10, it is also found that the higher the sand ratio, the higher the optimum water content was revealed. Obviously the increase in particle surface area necessitates the increase of the corresponding optimal water content.

The mixes containing PVA presented high cohesion. The workability is largely affected as the dosage increased. Mix M8 with 3% PVA appeared to be too sticky to be spread and placed by asphalt pavers. The other mixes presented modest moisture and cohesion and were considered appropriate in terms of “roller compactability” and “paver placeability”. Furthermore, there were no voids visible on the sample surfaces. Figure 3.10 presents the samples with the optimum water in mixes M9 – M14, which appeared to be solid and satisfactory. Their air contents were approx. 3%, as detailed in Table 3.10 and Table 3.12, slightly higher than that in conventional concrete (1%).

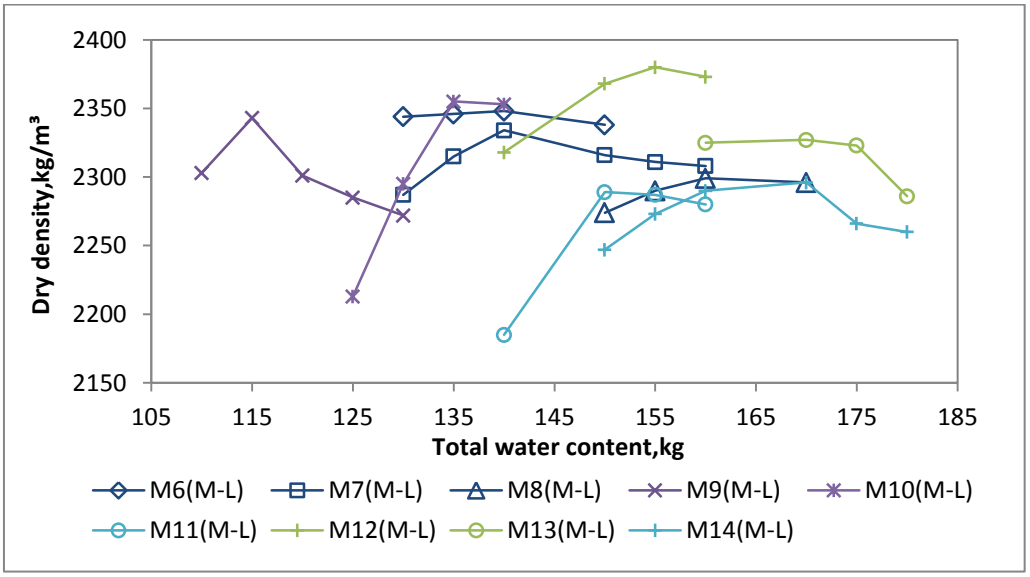

Figure 3.9 Water Content by the M-L Method for Mixes in Table 3.11

Table 3.12 Mix Proportion and Parameters Determined by M-L Method

	Mix Parameters			Mix Proportion								
Mix ID	Max Dry Den. kg/m³	Wet Density kg/m³	Air Content%	CEM	CA	FA	SBR	PVA	Superplasticizer	added water	SF	Total water w/c
M6(M-L)	2348	2479	2.98	1	1.518	1.013	0.217	0.01	0	0.103	0.184	0.22
M7(M-L)	2334	2464	3.32	1	1.518	1.013	0.217	0.02	0	0.103	0.184	0.22
M8(M-L)	2299	2445	2.68	1	1.518	1.013	0.217	0.03	0	0.135	0.184	0.25
M9(M-L)	2343	2456	2.30	1	1.266	1.266	0.217	0	0	0.064	0	0.18
M10(M-L)	2355	2482	3.16	1	1.266	1.266	0.217	0	0	0.094	0.184	0.21
M11(M-L)	2289	2427	3.96	1	1.266	1.266	0.217	0.02	0	0.119	0.184	0.24
M12(M-L)	2380	2531	2.01	1	1.266	1.266	0	0.01	0.015	0.244	0.184	0.24
M13(M-L)	2327	2490	2.94	1	1.266	1.266	0	0.02	0.015	0.268	0.184	0.27
M14(M-L)	2296	2455	3.23	1	1.266	1.266	0.109	0.02	0	0.209	0.184	0.27

Figure 3.10 Mixes M9 (M-L) - M14(M-L) Samples

As the key to a successful BCO design, it cannot be overstressed how important the bond with the underlying material is. Thus, the cohesive behaviour in the overlay material is favoured, unless it impairs the workability. As abovementioned, the mix M8 (M-L) containing 3% PVA was too sticky and not suitable in this application. In case that the 1% PVA is insufficient to produce adequate adhesion in the overlay material, the PVA dosage of 2% was opted for, i.e. M7 (M-L) in Table 3.12. Further bond tests were conducted and revealed satisfying high bond strength

The block splitting test and the cylinder direct shear test were carried out to evaluation the bond strength between the mixes and OPCC. The test procedures are stated in Section 3.3.1 and 3.3.2. The specimen formation is detailed in 3.6.

As tabulated in Table 3.13, the 28-day direct shear bond strengths of M5 (M-L) and M7 (M-L) are 5.47MPa and 6.07MPa. Both are much higher than 4.09MPa in OPCC-to-OPCC bond. In the same way, the splitting tensile strengths are also higher than that of OPCC-to-OPCC. The direct shear bond strength and splitting tensile bond strength of M7 (M-L) at the age of 42 days are included in the table as well. The bond became stronger as they were aging.

Table 3.13 Bond Tests Results (Unit: MPa)

	M5 (M-L)	M7 (M-L) 28d	M7 (M-L) 42d	OPCC
Direct Shear Bond Strength	5.47	6.07	6.81	4.09
Splitting Tensile Bond Strength	2.21	2.56	3.43	2.17

The cylinder direct shear test on OPCC using the same set-up produced 7.0MPa, which is comparable to the 6.81MPa direct shear bond strength of M7(M-L) at 42 days. It implies that the bond between M7(M-L)-to-OPCC can perhaps approach the strengh level as a monolithic OPCC material after 42 days. This signals a proximity to an idealized structrual integrity in a BCO system. In other words, the overlay and the substrate together form a solid, consistant, one-layer structure.

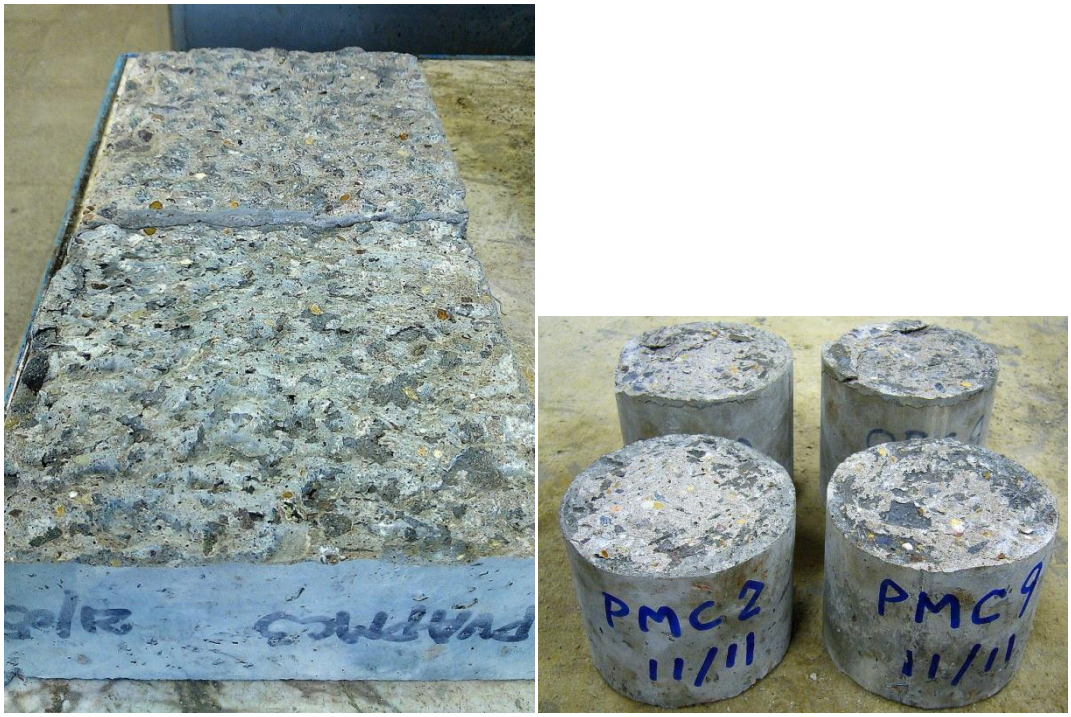

Figure 3.11 Failed Interfaces: (a) Block Splitting Test. (b) Cylinder Shear Test

Figure 3.11 shows the failed interfaces after the tests. Almost half area of the interface was still covered by the opposite material in the PMC-to-OPCC composites made of M5 (M-L) and M7 (M-L), which achieved high bond strength. In contrast, when the bond strength was low, the interface was fairly clear from the bonded material.

In summary, the M-L method employing 2.5kg rammer dropping from 300mm in height on 4 layers and 20 blows per layer satisfied all the design criteria. It is experimentally verified as an appropriate mix design method for SF-RC-PM-BCO.

3.4.4 Experimental Verification

The optimal water content determined by the maximum dry density was originally proposed in soil compaction to evaluate compactability. The hypothesis is that the more the solid content in a unit volume the higher the strength. More solid content in soil means less water and less air void content, which could lead to reduction in soil strength. However, strength of concrete is not only dependent on air content, but also on water content, cement hydration, aggregate type etc. This means for the same mix proportion, concrete having the maximum solid content may not guarantee the highest strength. To the authors' knowledge, the

verification of utilizing the soil compaction method in RCC mix design is not available to date. Therefore the experimental verification for the M-L compaction method was essential.

With this in mind, the mixes M9–M14 with various water contents (see Figure 3.11) were also tested at 28 days for splitting tensile strength following the M-L compaction, so that correlation between the maximum dry density and concrete strength could be established. The compacting apparatus used were exactly the same as in the M-L method. The container was first moistened with a concrete release agent, and then excess oil was carefully removed with a tissue. The surface of each compacted layer was roughened before accepting the next layer. After compaction, sample and container were covered with polythene sheets and de-moulded in 24 hours. Curing was carried out for 5 days in water, followed by 22 days in air under normal laboratory conditions. The experimental results indicated that four out of six mixes reached the highest strength at optimal water content, corresponding to maximum dry density. The other two mixes did not exhibit the same phenomena although only one sample was actually prepared for each strength test.

The typical correlation between the splitting tensile strengths and dry densities corresponding to different water contents (total water content, W_{T1}, in 1 m^3 concrete), are plotted in Figure 3.12. It is observed that the optimal water content corresponding to the maximum dry density determined by the M-L compaction method also dictates the highest strength. Hence the M-L method is further justified.

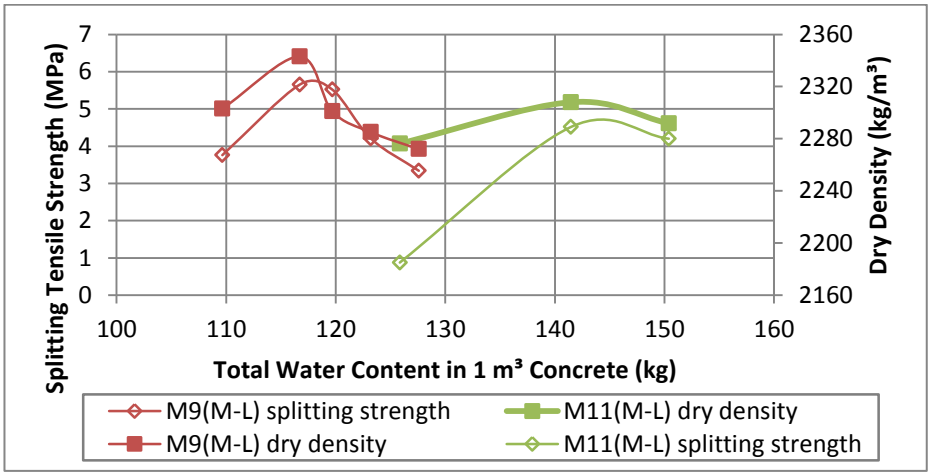

Figure 3.12 Corresponding Dry Density and Splitting Tensile Strength

3.5 Mixing Procedure

The mixing procedure for SBRPMC conforms to ASTM C 1439-99 (1999). As pictured in Figure 3.13, it was carried out in nine steps: 1. Add SBR to coarse aggregate in a rotating drum mixer; 2. Add half the total amount of water to the coarse aggregate; 3. Mix for a few revolutions; 4. Add fine aggregate; 5. Add cement; 6. Add the remaining amount of water during the mixing. Then spread and throw steel fibres in the mixer while mixing; 7. Mix for three minutes, then check if mixed properly and leave for one minute; 8. Mix for another minute; 9. Finish mixing.

Figure 3.13 Mixing Procedure

For hybrid polymer (SBR and PVA) modified cement concrete, the mixing procedure remains the same, except that the cement and PVA are mixed uniformly in a separate mixer, prior to the main mixing procedure. The same applies for PVAPMC. If a superplasticizer is to be used, the procedure will not change, other than the latter being mixed with the water prior to being added in the main mix.

3.6 Specimen Formation

The OPCC specimen and conventional PMC with the normal workability were compacted on a vibrating table in the normal way. The roller compacted concrete specimens were formed in a specially-manufactured vibrating compactor comprising a vibrator and steel

plates designed to fit various specimen sizes, as pictured in Figure 3.14. The vibrator features a 780W motor vibrating at the speed of 2860/min. The compaction force was 5kN. The acceleration generated was 7.43m/s2. And the weight was 23kg. The dimensions and weight of the attachments are specified in Table 3.14. Due to heavy impact of the compaction, the moulds had to be either made of heavy duty mild steel or strengthened timber, as shown in Figure 3.14. Three shapes of specimens were adopted either in the form of single-material monolithic specimens or composite specimens. The basic dimensions are all detailed in Table 3.15, in the groups of monolithic specimens and the base material and overlay material in composite specimens. However, the dimensions of each specimen may vary by a few millimetres. To ensure the accuracy, all dimensions were recorded for each individual specimen and adopted in the subsequent calculations.

Table 3.14 Vibrating Compactor Attachments

Attachment Shape	Length / Diameter (mm)	Width (mm)	Weight (kg)	To Form	Dimensions (mm)
Rectangular	495	95	7.3	Beam	500 × 100
Square	146	146	2.95	Block	150 × 150
Circle	95		1.9	Cylinder	100Ø

Table 3.15 Shape and Dimension of Specimens

		OPCC or OPCC Base (mm)	PMC or PMC Overlays (mm)	OPCC Overlay (mm)	Tests
Beams	Monolithic	500 × 100 × 100	500 × 100 × 80	-	SNSBT [1] & Foundation[2]
	Composites	500 × 100 × 50	500 × 100 × 80	500 × 100 × 100	
Cylinders	Monolithic	100Ø × 200	100Ø × 180	-	Direst Shear[3]
	Composites	100Ø × 100	100Ø × 80	100Ø × 100	Direct Shear Bond[4]
Blocks	Composites	150 × 150 × 50	150 × 150 × 50	150 × 150 × 50	Block Splitting[5]

[1] Single Notch Shear Beam Test (SNSBT), see Chapter 5.

[2] Beam Test on Foundation, see Chapter 5

[3] Cylinder Direct Shear Test, the same setup as in the cylinder direct shear bond test, loaded at the mid-length of a monolithic cylinder, instead of the interface.

[4] Cylinder Direct Shear Bond Test, see Section 3.3.2

[5] Block Splitting Test, see Section 3.3.1

Specimens were compacted in lift layers. Each single lift was 40-50mm thick. The surface of compacting layer was roughened before accepting the next layer to avoid weak plane at lift joints. Vibration was stopped when a rim of mortar formed around the perimeter of the vibrating plate, lasting 30s. The specimens were left in the moulds overnight covered with polythene sheets to minimize moisture evaporation after finishing compaction.

Figure 3.14(a) Vibrating Compactor and Attachements (left) (b) Beam Compaction (top right) (c) Composite Beam Moulds (bottom right)

The surface of OPCC base was brush-roughened approx. 4hr after casting, to remove surface mortar and expose coarse aggregate. The texture of the treated OPCC bases is shown in Figure 3.15. The treated surface appeared to be similar to a treated concrete pavement in field. The sand patch method, conforming to BS 598-105:1990 (1998) was employed to quantify the texture depths, as pictured in Figure 3.16. The average texture depths of OPCC cylinder and block surfaces were 1.75mm and1.65mm, respectively.

All the OPCC bases were at least 14 days old prior to usage. The surface was dampened and covered with a wet cloth for approx. 30 min to achieve a surface-dry saturated condition before applying the overlaying material.

The wet densities of compacted samples were tested in accordance with BS EN 12390-7:2009 (2009c). The results were close to those determined by the corresponding compaction methods described previously.

Figure 3.15 Surface Texture of OPCC in Lab(a) & (b) and in Real Site (c)[6]

Figure 3.16 Sand Patch Method (a) Apparatus (b) Test in Progress

3.7 PMC Curing

A shortened water curing duration is specified for polymer modified concrete in established documents (ACI Committee 548 2003, Ohama, Yoshihiko. 1995, Neville, Adam. M. 1996). A typical water curing duration of 28 days is required for ordinary concrete. However, due to the formation of a thin film on the surface of PMC, the moist retained under the film could be sufficient for cement hydration process following the initial water curing. Thus, a 1-3

[6] Figure 3.15(c) Picture Taken from Guide to Concrete Overlay Solutions (National Concrete Pavement Technology Centre 2008)

days moist curing followed by dry curing at ambient temperature is recommended for polymer modified concrete and mortars in Yoshihiko's handbook (Ohama 1995). ACI (ACI Committee 548 2003) also specified 1-2 days moist curing followed by dry curing. It is understood that a longer curing under water may even impair the concrete performance. (Ohama 1995) So it is important to find out the optimum curing duration. Roller compacted concrete, employed herein, exhibits much drier properties than concrete with ordinary workability. There is no guideline, to the author's knowledge, on curing of polymer modified no-slump concrete. Hence the optimal curing duration was determined experimentally by testing small cubes of $50 \times 50 \times 50$ dimensions in compression test at 28 days, subject to 3-day, 5-day, 7-day, 14-day and 27-day water curing followed by dry curing. There were three mixes investigated as follows. In brief, mix 1 is the SBR modified mortar; mix 2 is the PVA modified mortar; mix 3 is the hybrid polymer modified mortar. They correspond to the mixes determined by the M-L method, the proportions of which were tabulated in Table 3.12. The coarse aggregate and steel fibres were removed from the mortar mixes, although the water contents were kept the same. Details of the proportioning are in Table 3.16. All three mixes exhibited high viscosity. The specimens were compacted and formed by hand. The averaged compressive strengths of three identical samples in each group are presented in Figure 3.17. It is seen that very high compressive strengths were received, around 50MPa or even up to 70MPa, although a clear trend of strength reduction was affirmed as the water curing duration increased to 27 days. The optimal water curing durations corresponding to the maximum compressive strengths – mix 1: 5 days; mix 2: 7 days and mix 3: 7 days. Based on the above, the following curing method was followed in the subsequent experimental works. The PMC specimens containing PVA were cured underwater for 7 days prior to curing in air condition. The PMC with SBR were immersed in water for 5 days followed by air curing. The OPCC specimens were cured underwater for 28days in the normal way. The air curing took place in the laboratory at the temperature between 18-23°C and the humidity between 52-60%.

Table 3.16 Mortar Mix Proportions

	Corresponds to Table 3.12	CEM	FA	SBR	PVA	Superplasticizer	added water
Mix 1	M10(M-L)	1	1.266	0.217	0	0	0.094
Mix 2	M13(M-L)	1	1.266	0	0.02	0.015	0.268
Mix 3	M14(M-L)	1	1.266	0.109	0.02	0	0.209

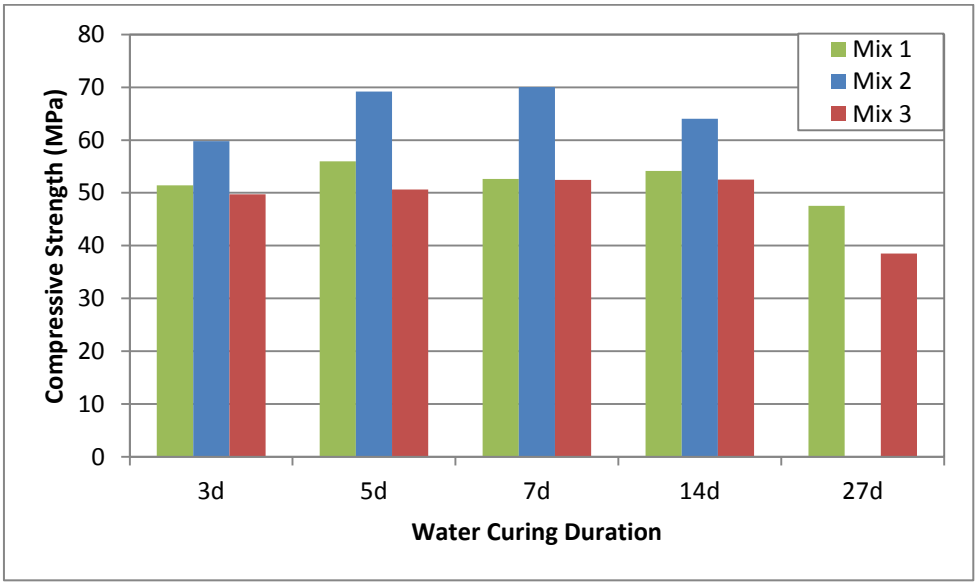

Figure 3.17 Determination of Water Curing Duration

3.8 Determination of Some Other Material Properties

The modulus of elasticity (E) and poisson's ratio (ν) were tested in accordance with ASTM C469 (2010) on three mixes - SBRPMC, PVAPMC and OPCC. Three specimens were tested in each group. The coefficients of linear thermal expansion (α) were also tested in accordance with MCHW Clause 871 between temperatures 18.4°C and 55.0°C (The Highways Agency 1992). The averaged testing results are summarized in Table 3.17.

Table 3.17 E-Value and Poisson's Ratio

Mix	Modulus of Elasticity (GPa)	Poisson's Ratio	Coefficient of Linear Thermal Expansion ($\times 10^{-6}$)
SBRPMC	32.365	0.187	13.5
PVAPMC	37.357	0.239	13.4
OPCC	25.195	0.21	16.9

Figure 3.18 Test for E-value and Poisson's Ratio

CHAPTER 4 EXPERIMENTAL INVESTIGATION – SHEAR AND REFLECTIVE CRACKING

4. Experimental Investigation – Shear and Reflective Cracking

Shear failure at cracks/joints is a major cause of structural degradation of concrete pavements. A regime of pavement deterioration is likely to occur at existing joints/cracks. When a load is located either side of a crack, a relative vertical displacement is expected to take place at crack edges, which leads to reflective cracking under repetitive traffic loads (rocking effect), as demonstrated in Chapter 2.

This chapter consists of a series of laboratory tests. As stated in the previous chapters, this research aims to develop a concrete overlay material and to provide adequate resistance to reflective cracking. In order to understand the uniqueness of this purposely-developed roller-compacted steel fibre reinforced, polymer modified concrete, the laboratory tests were carried out to obtain the intrinsic properties of the material and to assess its performance under shear loading in a much smaller scale. It is hoped to set a stepping stone in shaping the design basis in pavement overlays, although long term field tests should be needed in the future to verify the findings.

4.1 Preliminary Investigation

4.1.1 Introduction

The preliminary investigation formed an important transition from Koutselas' study on "green overlay" (2010) to the improved mixing, mix components, compaction and curing method described in the previous chapter. The shear performance was proved to be enhanced by the new procedure.

4.1.2 Material

Three concrete mixes were developed based on Koutselas' study (2010) and tested in Stage I. To differentiate them from the mixes in a later stage, a subscript of "p" was used meaning that they were used in the preliminary study. They are Ordinary Portland Cement Concrete ($OPCC_p$) for comparison purpose, plain Polymer Modified Cement Concrete ($PMC1_p$) and Polymer Modified Cement Concrete with 4kg/m^3 glass fibre ($PMC2_p$). The water/cement ratio is 0.21 (the water here is sum of water content in liquid admixture and added water) and cement-sand-coarse aggregate ratio is 1:1.27:1.27. As of the nature of the application of pavement

overlays, the PMC_p mix previously developed is of high strength and high modulus of rapture and compactable using a kango hammer. (Karadelis and Koutselas 2003, Koutselas 2010) Nevertheless, the mixes at this stage were still of higher workability than the ones determined by the M-L method described in Chapter 4. Under laboratory conditions, a specially modified Kango hammer was used to consolidate the specimens. The compacting effort was relatively low. Size 10mm granite was employed for coarse aggregate. The 28-day mean compressive strengths of $OPCC_p$, $PMC1_p$ and $PMC2_p$ were recorded as follows: 38.0 MPa, 60.5 MPa and 54.5 MPa.

To enhance the shear performance of PMC_p, further attempts were made by replacing the coarse aggregate and revising the mixing, compacting and curing method. In addition to the three mixes in stage I, three additional concrete mixes were produced. All six mixes are summarized in Table 4.1.

In $OPCC2_p$, $PMC3_p$ and $PMC4_p$, the new coarse aggregate, gritstone, was used instead of granite. The aggregate crushing value (ACV) was tested in accordance with BS 812-110:1990 (1990). Granite achieved 19.98% and gritstone 11.40%. It demonstrates a higher resistance to crushing is available in gritstone than granite.

$PMC4_p$ was cast following a new mixing and curing method. As recommended by ACI 548-3 (2003), the new mixing procedure allows an initial blend of coarse aggregate and polymer and half water with the aim of improving the cement paste-aggregate bond. The traditional curing method was modified for $PMC4_p$ as well. Usually concrete is cured in water for 28 days. However, wet curing is considered unfavourable for polymer modified concrete due to fusion of polymer. (Ohama 1995) Therefore, a four-day moist curing at the temperature of $22 \pm 3^{o}C$ and relative humidity of approx. 95% was carried out followed by 24 days air curing at room environment. As a result of the questioning of the effectiveness of the Kango compactor, a new handheld vibrating – compacting device was manufactured to undertake not only the hammering impact, but also the vibrating action. A suitable compactor head was attached depending on the shape and dimensions of the mould so that an even compaction can be delivered, as pictured in Figure 4.1. It was later replaced by a vibrating compactor fixed by a frame bolted into the strong floor to avoid “white fingers”, as pictured in Figure 3.14.

Table 4.1 Summary of Concrete Mixes in First Setup

	Coarse Aggregate	Fibre	Mixing	Curing Method	Compaction
OPC_p	Granite	N/A	Traditional	Traditional	Kango
$OPC\ 2_p$	Gritstone	N/A	Traditional	Traditional	Kango
$PMC\ 1_p$	Granite	N/A	Traditional	Traditional	Kango
$PMC\ 2_p$	Granite	Glass	Traditional	Traditional	Kango
$PMC\ 3_p$	Gritstone	N/A	Traditional	Traditional	Kango
$PMC\ 4_p$	Gritstone	N/A	New	New	Handheld Vibrating Compactor

Figure 4.1 Handheld Vibrating Compactor

4.1.3 Single Notch Shear Beam Test

Based on Arrea and Ingraffea's single notch shear beam test (Arrea and Ingraffea 1982), a short concrete beam test was carried out in the preliminary laboratory test aiming to simulate the reflective cracking under static shear loading by creating a concentrated shear zone in the near absence of bending moments at the notch and to study the shear behaviour. The size of the specimens was approximately one-third of the original dimensions proposed by Arrea and Ingraffea with 100mm in breath and width, 500mm length and a 27mm deep notch at the mid-span in the tension area . The geometry and loading arrangements are shown in Figure 4.2. The notch was introduced by fixing a 2mm thick perspex plate in the mould while casting, to avoid micro-cracks introduced in the process of saw cutting.

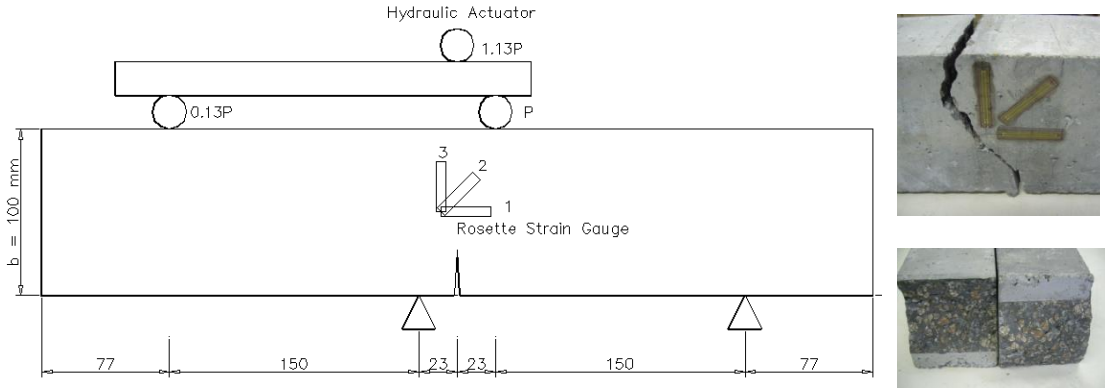

Figure 4.2 First Setup Geometry and Loading and Typical Crack Plane

Three 30mm-long strain gauges were attached on the side of each beam in a 45^{o} rosette arrangement as displayed in Figure 4.2, to capture the change in shear strain at the region as the load increased. Usually the rosette dimensions should be able to span over the distance between inhomogeneities, e.g. aggregates, fibres etc, to provide a relatively reliable indication of the strain state. As a rule of thumb, the length of strain gauges should be four to five times of the dominant coarse aggregate size in the concrete. However due to the limited breath of the high shear zone, an adjustment was made accordingly to attain the best valid results.

The JJ Lloyd LS100 test machine and the RDP modular 600 interface linked to a computer were used as the loading and data acquisition system as demonstrated in Figure 4.3.

Twelve beams were produced for the test, comprising four beams per mix. Each beam was carefully prepared with marked loading support positions to avoid any misplacement. The loading cell was aligned right above the notch. Extra care was taken to position every component of the testing rig, as arranged in Figure 4.2. The loading process was controlled by crosshead displacement at 1mm/min till 5kN followed by 0.5mm/min till failure. It was monitored and recorded via the Nexygen and Ondio v4.5 software (Lloyds Instruments Ltd 2002) on the computer in the remote control mode. Following each test, the real time, machine extension, load, strain gauge readings 1, 2 and 3 were exported.

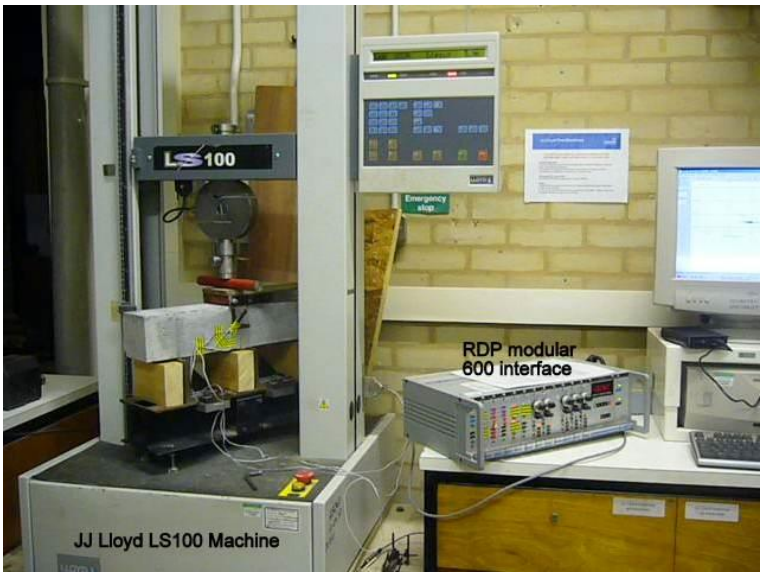

Figure 4.3 Preliminary Test SNSBT Setup

All twenty-four beams failed abruptly with the crack propagating from the tip of the notch in an inclined direction of approx. 45^{o}, reaching the top of the specimen to the opposite side of the applied force P, as shown in Figure 4.2. The results were summarized in Table 4.2. Despite the high compressive strengths of PMC, the latter failed earlier under shear than ordinary concrete. This is in harmony with existing literature. (Song et al. 2010, Taylor 1974, Walraven 1981)

Figure 4.4 shows the variation of shear stress versus shear strain for a magnitude of shear stress up to 2.5MPa, before failure occurs. A wide range of scatter points (hatched areas) was present in the results. The same scatter was reported in the correlation of ACI 318-02 with experimental data in Chapter 2 (Leet and Bernal 1997). Both PMC 1_p and PMC 2_p mixes show steeper slopes, i.e. higher shear modulus than the OPCC 1_p. Comparing plain PMC (i.e. PMC 1_p) with glass-fibre reinfoced PMC (i.e. PMC 2_p), it is observed that despite the smooth climb at the very beginning, the shear stress grows faster in PMC 2_p. This indicates that the introduction of glass fibre did enhance the shear resistance of PMC but not the ductility.

Overall, PMC has high compressive strength but lower shear strength, possibly due to insufficient compaction. The addition of glass fibre enhanced the shear properties of the PMC. A good consistency exists between the average saturated densities and

the shear strengths. In descending order, both rank as: OPC1 > PMC2 > PMC1, as listed in Table III. Serving as a roller-compacted concrete, compaction in the PMC is critical. Insufficient compaction may induce voids in the mix, i.e. low density. When subject to shear, the voids become weak points where the deterioration tends to initiate from, and eventually lead to failure at a 'lower-than-expected' load. However, in compression, the microstructures developed by superior ingredients still allow for good performance.

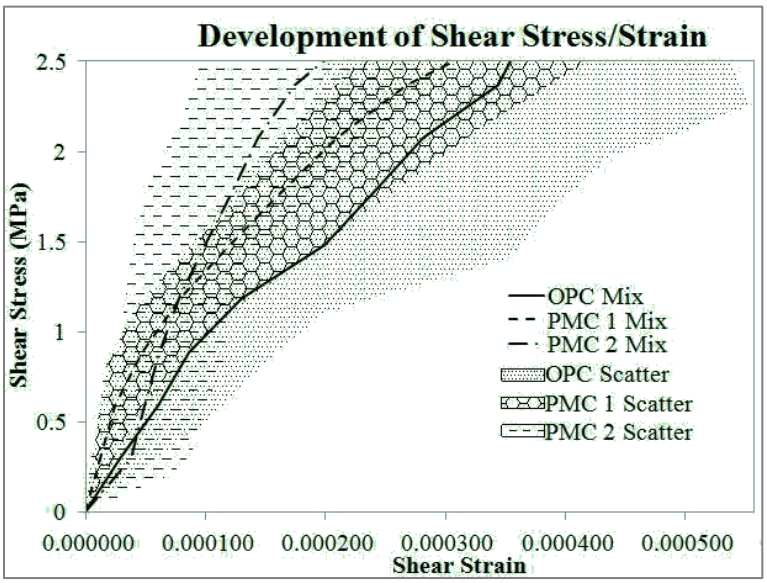

Figure 4.4. Shear Stress/ Strain at the Initial Stage

In linear elastic fracture mechanics, the stress intensity factor K is used to describe the stress field at a crack tip evoked by a load, or by residual stresses from a distance, as described by the Eqns. 4.1-4.3, where r is the distance to the crack tip. K_I, K_{II} and K_{III} correspond to the mode I (opening mode), mode II (sliding mode) and mode III (tearing mode).

$$K_I = \lim_{r\to 0} \sqrt{2\pi r}\,\sigma_{yy}(r,0) \quad 4.1$$

$$K_{II} = \lim_{r\to 0} \sqrt{2\pi r}\,\sigma_{yx}(r,0) \quad 4.2$$

$$K_{III} = \lim_{r\to 0} \sqrt{2\pi r}\,\sigma_{yz}(r,0) \quad 4.3$$

A crude estimate of the mode II stress intensity factor is presented in this preliminary study since the testing geometry is frequently used for determination of fracture

parameters for mode II failure (shear failure). For a single edge crack subject to in-plane shear as shown in Figure 4.5, a relationship has been developed by Tada (2000) for K_{II}, the mode II stress intensity factor, as shown in Eqn. 4.4.

$$K_{II} = \frac{2Q}{B\sqrt{\pi a}} \frac{1.30 - 0.65\left(a/b\right) + 0.37\left(a/b\right)^2 + 0.28\left(a/b\right)^3}{\sqrt{1-\left(a/b\right)}} \quad 4.4$$

Where: Q = applied shear at the notch at the onset of slow crack growth; a = crack depth, 27mm in the testing geometry; b = height of the beam, 100mm; B = width of the beam, 100mm. Substituting the above values into Eqn. 4.1, the latter is reduced to Eqn. 4.5.

$$K_{II} \approx 0.002940621 \times Q \text{ in } N \cdot mm^{-3/2} \quad 4.5$$

All beams failed abruptly. Owing to the rapid crack development, the load at the onset of slow crack growth was not detected. A close-loop displacement controlled test is required to detect crack development. If the failure loads were to be used in the assessment, the average K_{II} for OPCC 1_p, PMC 1_p and PMC 2_p would be 2435, 2136 and 2390 $kN \cdot m^{-3/2}$ respectively. As failure occurs at a higher load than that needed for initial crack growth, the actual critical mode II stress intensity factor K_{IIC} values are likely to be smaller than those calculated. The definitive estimates of K_{II} were not obtained at this stage, as it was not possible to detect the onset crack development in the load-controlled setup. This was rectified in the improved setup as detailed in 4.2. However with the current material mix, the PMC_p returned with smaller toughness than the $OPCC_p$. Additional tests conducted in the preliminary investigation are cylinder torsion tests and direct shear tests as explained in the following paragraphs.

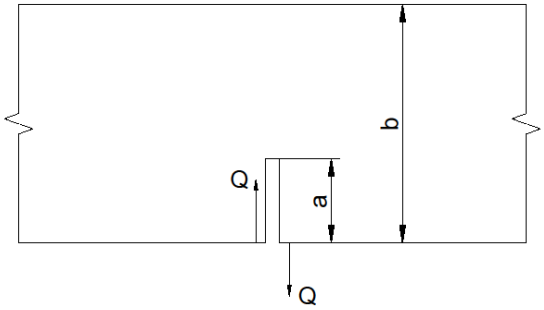

Figure 4.5 Beam Subject to Shear (Tada, Paris and Irwin 2000)

Table 4.2 Stage I SNSBT Test Results

Material Properties	Compressive Strength f_c (MPa)	Saturated Density (kg/m3)	Mean Shear Strength v_c (MPa)	Estimated Mean Shear Modulus G (GPa)
$OPCC_p$	38.0	2361.1	3.59	15.5
PMC 1_p	60.5	2298.7	2.90	24.7
PMC 2_p	54.5	2323.6	3.52	26.2

For PMC 1_p (plain PMC), this was 2.90MPa; for PMC 2_p (with glass fibre), it was 3.52MPa; and for $OPCC_p$, it was the highest, 3.59MPa. In spite of the high compressive strengths of 60.5MPa in PMC 1_p and 54.5 MPa in PMC 2_p, they failed earlier under shear than ordinary concrete, which agrees with existing literature. (Song et al. 2010, Taylor 1974, Walraven 1981, Wong et al. 2007). Song et al (2010) pointed out that the local roughness at a crack plane influences the shear resistance. The wider the crack is and/or the smaller the aggregate size is, the lower shear capacity it can achieve. Nevertheless, the above principle may not apply in high strength concrete, in which aggregates can fracture through resulting in a relatively smooth crack plane. Taylor (1974) suggested 33-50% of shear transfer in reinforced concrete could be contributed by aggregate interlock and for concrete with compressive strength of over 50MPa, the shear strength may not increase with concrete strength. Walraven (1981) explained that the strength of hydrated cement paste (HCP) in high strength concrete is sufficiently high to cause aggregate crushing under sheared fracture. In normal concrete, in contrast, the predominant shear

transfer is provided by the interlock mechanism between HCP and aggregate, which is significantly reduced in high strength concrete. As pictured in Figure 4.2, the smooth-side failure plane with aggregate sheared-off discloses possible low interlock capacity in the PMC mixes.

Additional tests conducted to increase confidence are cylinder torsion tests and direct shear tests as explained in the following paragraphs.

4.1.4 Cylinder Torsion Test

A total of eight concrete cylinders, four OPCC 1_p and four plain PMC 1_p with 100mm diameter and 200mm length were cast. Table 4.3 provides all necessary properties and results. Studying failed specimens of $OPCC_p$ and PMC_p showed that the fractured plane in PMC_p was smoother than that of $OPCC_p$. Hence, the aggregate failed to demonstrate good interlocking abilities.

4.1.5 Cylinder Direct Shear Test

The Iowa Testing Method 406-C (Iowa Department of Transportation 2000) on four 150mm diameter by 300mm long $OPCC1_p$ cylinders and four $PMC2_p$ (glass fibre) cylinders was adopted. To enhance the shear strength performance of PMC_p, the coarse aggregate as well as the mixing, compacting and curing methods were revised in stage II. Gritstone replaced granite in $OPC2_p$, $PMC3_p$ and $PMC4_p$. The new mixing, compaction and curing methods were deployed for $PMC4_p$, as described earlier. The test arrangement is pictured in Figure 4.6 (a). All cylinders were sheared off in a vertical plane, as shown in Figure 4.6 (b). $PMC2_p$ (with glass fibre) delivered higher shear strength than plain $PMC1_p$, similar to $OPCC1_p$. The results were summarized in Figure 4.7.

Figure 4.6 Cylinder Direct Shear Test (left); Failed Section ($PMC2_p$) (right)

4.1.6 Summary of Preliminary Tests

The results in all three tests are summarized in Table 4.3. Results involving gritstone and the new mixing/compaction/curing methods have been discussed in the previous chapter and therefore are not repeated herein.

It is noted that the tests carried out have excellent consistency on the evaluation of shear performance. Despite high compressive strength, plain PMC_p failed to provide an equivalent shear resistance as the $OPCC_p$. This is attributed to the high strength hydrated cement paste (HCP) in PMC_p and the relatively weak coarse aggregate, which led to less efficient interlock at the failure planes. The $OPCC_p$ failure face exposes a great amount of aggregates and most of the failure takes place at the HCP-aggregate interface. In contrast, the PMC_p shows a much smoother face through crushed aggregates. Hence, the replacement of granite with gritstone.

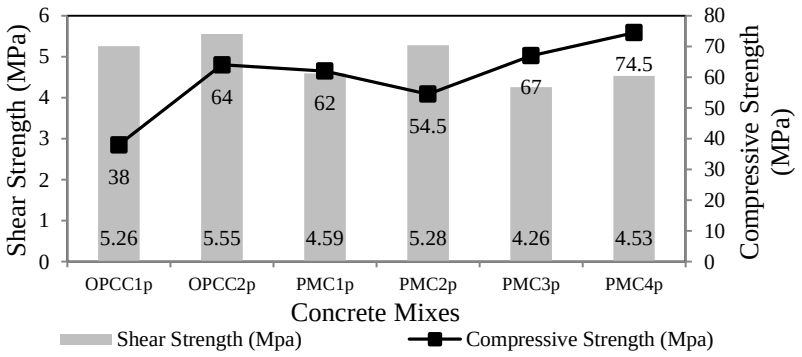

Figure 4.7 Summary of Results from Cylinder Direct Shear Test

Compaction was also blamed for the "lower than expected" shear resistance of PMC. Different from high/normal-workability concrete, potent compaction in PMC is essential to attain the desired strength. After examining the cube densities, it was deduced that there were voids in the mix due to insufficient compaction. Hence, it was decided to invest on a new vibrating-compactor.

Table 4.3 Summary of Preliminary Results

Mat. Prop.	Compr.Stren.f_c (MPa)	Density (kg/m3)	Mean Shear Strength v_c (MPa)			Estimated Mean Shear Modulus G (GPa)	
Tests	Cube Compre. Test		SNSBT	Torsion	Direct Shear	SNSBT	Torsion
$OPCC1_p$	38.0	2361.1	3.59	3.59	5.26	15.5	15.9
$PMC1_p$	60.5	2298.7	2.90	2.79	-	24.7	17.2
$PMC2_p$	54.5	2323.6	3.52	-	5.28	26.2	-

$PMC2_p$ with a glass fibre input did improve the shear properties of $PMC1_p$ to a similar level of $OPCC_p$, but failed to provide the required ductility. This could be attributed to insufficient amount of added glass fibre. Hence, glass fibres were replaced with steel fibres to enhance the shear performance and to provide the required a similar level of resistance even after cracking.

4.2 Experimental Investigation

4.2.1 Material

OPCC was employed as a baseline material for reference and also act as the substrate material in the composite specimens. PMC in the shear tests were varied in the following aspects:

(a) polymer types - SBR and PVA;

(b) maximum size of coarse aggregate – 10mm, 14mm and 20mm;

(c) volume fraction of steel fibres – 0%, 1%, 1.5% and 2%;

(d) steel fibres length – short fibre and long fibre;

(e) curing duration – 3 days, 7 days and 28 days and

(f) workability – conventional PMC with a slump of approx. 130mm and roller compacted no slump PMC.

Details of the material constituents were given in Chapter 4, except for the long steel fibre, which is listed in Table 4.4. The specimen formation and curing methods were also provided in Chapter 4 and not repeated herein.

Table 4.4 Mechanical Properties of Hooked End Steel Fibres

Type	Length l (mm)	Fibre Width b_f (mm)	Fibre Thickness h_f (mm)	Equivalent Diameter d_f (mm)	Aspect Ratio l_f/d_f	Tensile Strength (MPa)	Supplier
Short Fibre (SF)	35	0.6	0.45	0.59	60	1050	Propex (2007)
Long Fibre (LF)	50	0.6	0.5	0.62	80	1270	Dramix (2008)

For ease of presentation, the main variable for each group of specimens was shortened and assigned to the group name. The mix proportions by weight are provided in Table 4.5, except that steel fibre was given in volume fraction. The wet densities were derived from the M-L method for roller compacted concrete (RCC) as mentioned in the previous chapter and cube density tests for conventional concrete (British Standards Institution 2009b). A few examples are set below to demonstrate the abbreviated mix names.

SBRPMC – basic version of the roller compacted no slump PMC featuring SBR polymer; 10mm coarse aggregate; 1.5% volume fraction of short steel fibre and subject to tests after 28 days curing.

1%Vf PMC – PMC with 1% of steel fibre in volume fraction

14Agg PMC – PMC with the nominal coarse aggregate size of 14mm

3d PMC – PMC tested on the 3rd day after casting

LF PMC – long steel fibre used in this mix rather than short fibre in other mixes;

PVAPMC – use of PVA in the PMC, rather than SBR in other mixes

Table 4.5 Mixes Proportions and Density

ID	Material Mix Designation	C	CA	FA	SBR	PVA	SP	Added Water	SF (V_f)	Wet Den. (kg/m^3)	w/c
1	OPCC 1	1	2.78	1.70	-	-	-	0.51	-	2386	0.51
2	OPCC 2	1	1.52	1.01	-	-	-	0.40	-	2399	0.40
3	SBRPMC	1	1.27	1.27	0.22	-	-	0.09	0.015	2486	0.21
4	Plain PMC	1	1.27	1.27	0.22	-	-	0.09	-	2308	0.18
5	1%Vf PMC	1	1.27	1.27	0.22	-	-	0.07	0.01	2479	0.19
6	2%Vf PMC	1	1.27	1.27	0.22	-	-	0.10	0.02	2521	0.22
7	14Agg PMC	1	1.27	1.27	0.22	-	-	0.09	0.015	2436	0.21
8	20Agg PMC	1	1.27	1.27	0.22	-	-	0.09	0.015	2498	0.21
9	3d PMC	1	1.27	1.27	0.22	-	-	0.09	0.015	2457	0.21
10	7d PMC	1	1.27	1.27	0.22	-	-	0.09	0.015	2474	0.21
11	LF PMC	1	1.27	1.27	0.22	-	-	0.09	0.015	2443	0.21
12	PVAPMC	1	1.27	1.27	-	0.02	0.03	0.23	0.015	2466	0.23
13	Plain Conventional PMC	1	1.27	1.27	0.22	-	-	0.24	-	2297	0.36
14	Conventional PMC	1	1.27	1.27	0.22	-	-	0.24	0.015	2330	0.36

The 3d PMC and 7d PMC were cured in water for 1 day and 5 days respectively and tested on the 3rd day and 7th after casting.

4.2.2 Compression Test and Cube Density

The cube density test was carried out in accordance with BS EN 12390-7:2009 (2009a). The cube crushing test was carried out in accordance with BS EN 12390-3:2009 (2009b). Some specimens were recycled beams following single notch shear beam tests. At least three identical specimens were tested, the averaged results of which are presented in Figure 4.8 and Table 4.6. The mix ID in Figure 4.8 corresponds to the mix designation in Table 4.6. The standard deviations of compressive strengths are indicated by the error bars in the figure.

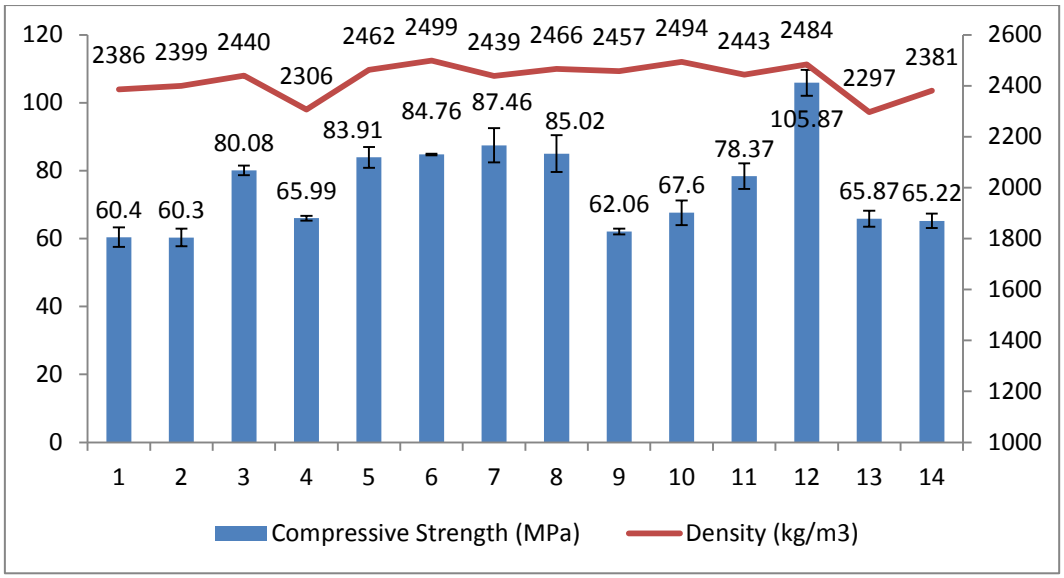

Figure 4.8 Compressive Strength and Density

Table 4.6 Compressive Strength and Density

ID	Material Mix Designation	Compressive Strength (MPa)	Density (kg/m^3)
1	OPCC 1	60.4	2386
2	OPCC 2	60.3	2399
3	SBRPMC	80.08	2440
4	Plain PMC	65.99	2306
5	1%Vf PMC	83.91	2462
6	2%Vf PMC	84.76	2499
7	14Agg PMC	87.46	2439
8	20Agg PMC	85.02	2466
9	3d PMC	62.06	2457
10	7d PMC	67.6	2494
11	LF PMC	78.37	2443
12	PVAPMC	105.87	2484
13	Plain Conventional PMC	65.87	2297
14	Conventional PMC	65.22	2381

4.2.3 Cylinder Direct Shear Test

The Iowa Testing Method 406-C (Iowa Department of Transportation 2000) was repeated in the following stage, but on small cylinder specimens of 100mm diameter by 200mm long, due to the availability of casting moulds. The Denison 500

hydraulic machine was employed jointly with the servo controller to apply a direct shear load at the rate of 0.39kN/s. At least three identical specimens were tested in each group at 28-day curing. It is worth noting that the PMC specimens were compacted from the top in four layers with the steel moulds standing upright and the lift joints horizontal. The fracture plane was selected between lift joints and marked on specimen surface. The specimens were carefully placed in the holder aligned with the marking line, where the direct shear load would be applied. The test setup and the failed sample are pictured in Figure 4.9. It can be seen that the fracture plane was in the same direction as the applied load. Therefore, the nature of the failure mechanism is direct shear failure.

Figure 4.9 (a) Cylinder Direct Test (b) Failure Plane (c) Lift Joint Cracking

The averaged shear strengths based on the peak load are provided in Table 4.7, along with the standard deviations. Where the results were deemed invalid due to cracking at the nearby lift joints, as shown in Figure 4.9 (c), they were discarded.

Table 4.7 Cylinder Direct Shear Strength

ID	Material Mix Designation	Shear Strength (MPa)	Standard Deviation
1	OPCC 1	7.00	0.59
2	OPCC 2	6.19	0.65
3	SBRPMC	8.93	0.91
4	Plain PMC	5.70	0.83
5	1%Vf PMC	8.14	1.57
6	2%Vf PMC	9.13	1.61
7	14Agg PMC	8.87	1.43
8	20Agg PMC	8.92	1.47
9	PVAPMC	12.24	1.54
10	Conventional PMC	7.87	0.59

4.2.4 Prism Splitting Test and Short Beam Three Point Bending Test

After beams failed in SNSBT, one part of the beams was subject to prism splitting tests with the 2000kN servo-controlled hydraulic machine at the rate of 0.5kN/s. The remaining half were subject to three point bending test with a span of 200mm with the 150kN servo-controlled Denison machine at the rate of 0.1kN/s. The results are presented in Table 4.8.

Table 4.8 Prism Splitting Test and Short Beam 3PBT Results

ID	Material Mix Designation	Splitting Tensile Strength (MPa)	Flexural Strength (MPa) Span: 200
1	SBRPMC	14.73	14.29
2	1%Vf PMC	13.75	15.22
3	2%Vf PMC	17.53	15.09
4	14Agg PMC	13.38	12.24
5	20Agg PMC	14.13	14.17
6	3d PMC	11.93	14.86
7	7d PMC	13.82	-
8	LF PMC	12.13	16.69
9	Conventional PMC	11.69	11.04

4.2.5 Improved Design

The single notch shear beam test (SNSBT) was applied on top-notched beams in an asymmetrical four point loading arrangement, as sketched in Figure 4.10 for arrangements and shear force / bending moment diagrams.

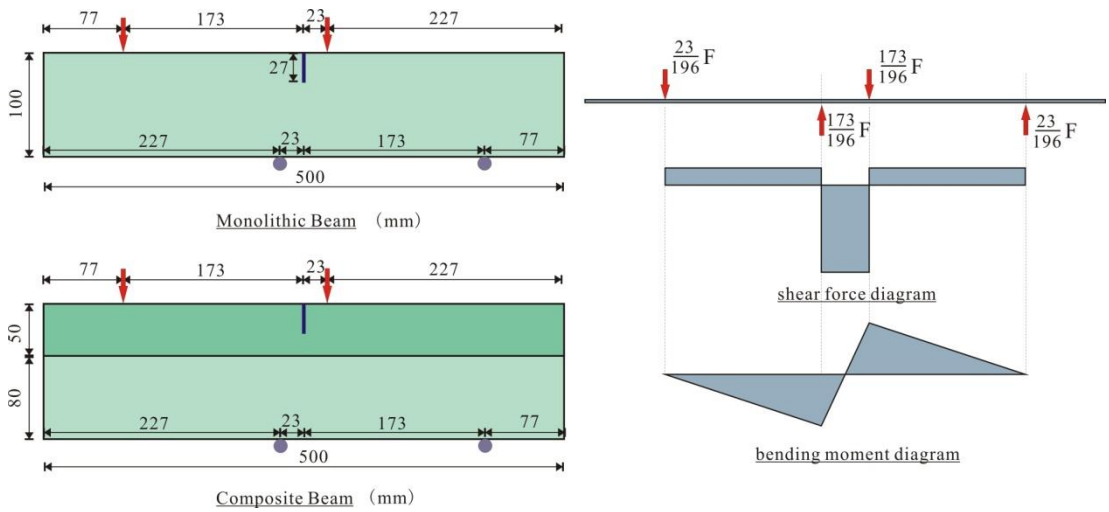

Figure 4.10 Arrangements for Monolithic Beams and Composite Beams (Left) Shear Force and Bending Moment Diagrame (Right)

It is to investigate the performance under high shear and in the near absence of bending moment at the notch.

It was pointed out by Schlangen (1993) that the loading configuration must be vertically symmetrical to keep the distributed load constant for a longer duration. Hence, instead of the single spreader beam on top, the system was modified to incorporate two identical spreader beams and sets of rollers, one on top and one at bottom. The self-weight of the spreader beam and rollers were taken into consideration in the calculations. To analyze the load displacement and thereafter to derive the fracture energy, four linear variable differential transformers (LVDTs) were introduced to measure the displacements at the loading rollers, two at front and two at back. The averaged values from front and back were used in the calculation to eliminate any influence from twisting. A minimal rotation is allowed in the system to minimize the influence from horizontal friction. Two referencing bars were attached to the glued pins on the beams. As shown in Figure 4.13, the gluing points were located right above the bottom rollers. The abovementioned LVDTs were then attached to the referencing bar. In other words, the measured displacements δ1 to δ4 were the relative displacement to the two gluing points above the bottom rollers. Effort was made to eliminate eccentricity in the loading system. The rollers were grooved for a width of approx. 5mm, which were in contact with the beams. This was investigated in a previous research carried out by Ross (2002), in which the

comparison was made among full circle rollers, half circle rollers and ¾ circle rollers in a similar test setup. It was found that the ¾ circle rollers produced the most consistent results with the least coefficient of variation (COV). To investigate the crack tip displacement, a LVDT was placed across the crack tip to measure the crack tip opening displacement (CTOD). In the meantime, a clip gauge was employed to measure the crack sliding displacement (CSD) with the aid of two small attachments, as illustrated in Table 4.9.

The test was carried out on a 150kN Denison machine jointly with a Servo hydraulic close-loop system. The loading rate was started at 0.00002mm/s and increased once the system was stabilized. Typically it took approx. 3hr until a specimen completely failed. The linear variable differential transformer (LVDT RDP D5/300AG) reading δ2, in Figure 4.13, was employed as the feedback signal to enable a displacement-controlled loading. As pointed out by many researchers (Schlangen 1993, Swartz et al. 1988), only displacement controlled loading can capture a stable post-peak crack development. The Denison machine load reading, the controlled displacement (δ2) and the CMSD reading by the clip gauge were recorded by the servo controller. The remaining LVDTS including δ1, δ3, δ4 and the CTOD, as appeared in Figure 4.13, were recorded by an independent data logger together with a load cell for synchronization. The data was recorded at 4Hz. A typical load-displacement relationship for load is demonstrated in Figure 4.12. After beams failed in SNSBT, half segment of the beams was subject to prism splitting tests. The remaining halves were subject to three point bending test with a span of 200mm.

OPCC specimens were cast as reference beams. PMC beams comprise mixes with varied steel fibre volume fractions of 0%, 1%, 1.5% and 2% and curing time varying from 3, 7 and 28 days. The optimal water contents of PMC mixes were determined based on the M-L method as explained in Chapter 4. The PMC beams were of 100H x 80W x 500L millimetres. The OPCC beams were 100 x 100 x 500 millimetres. All beams were saw-cut to a depth of 27mm at mid-span. Each mix comprises three identical beams. The results presented below are the averaged values.

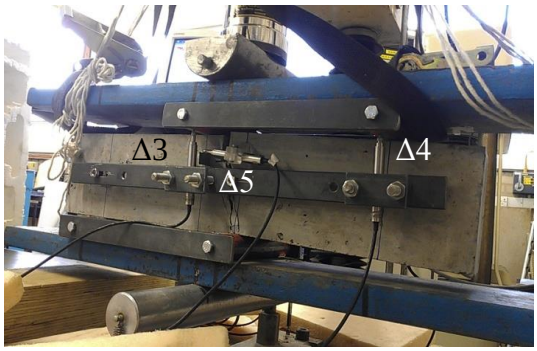

Figure 4.11 Single Notch Shear Beam Test (SNSBT) Configuration (Left)

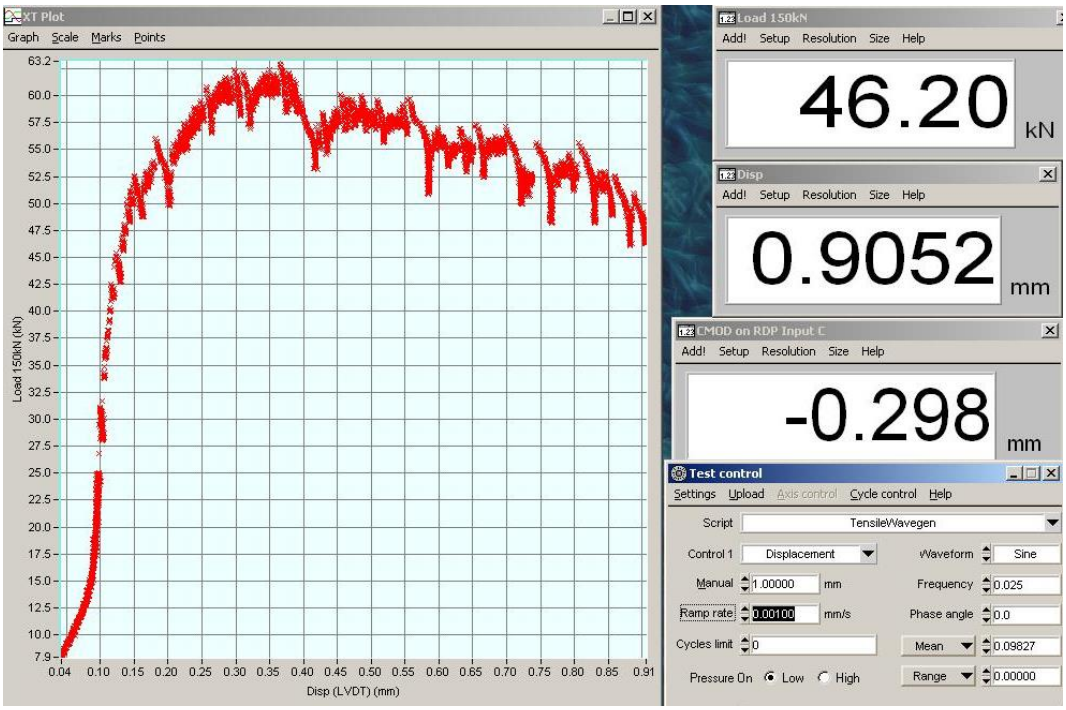

Figure 4.12 Servo Interface with Data Recording

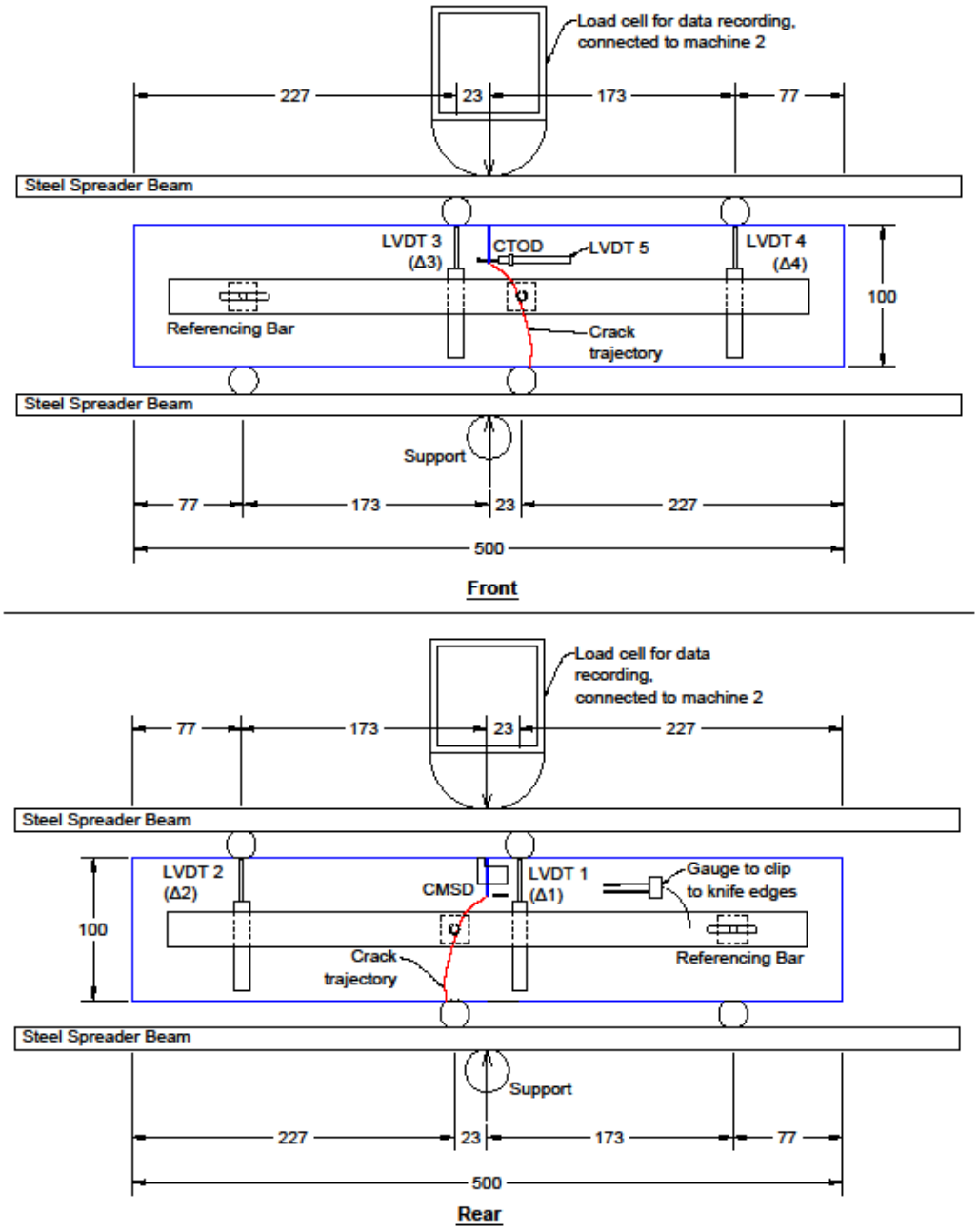

Figure 4.13 Test Arrangement (Monolithic Beam)

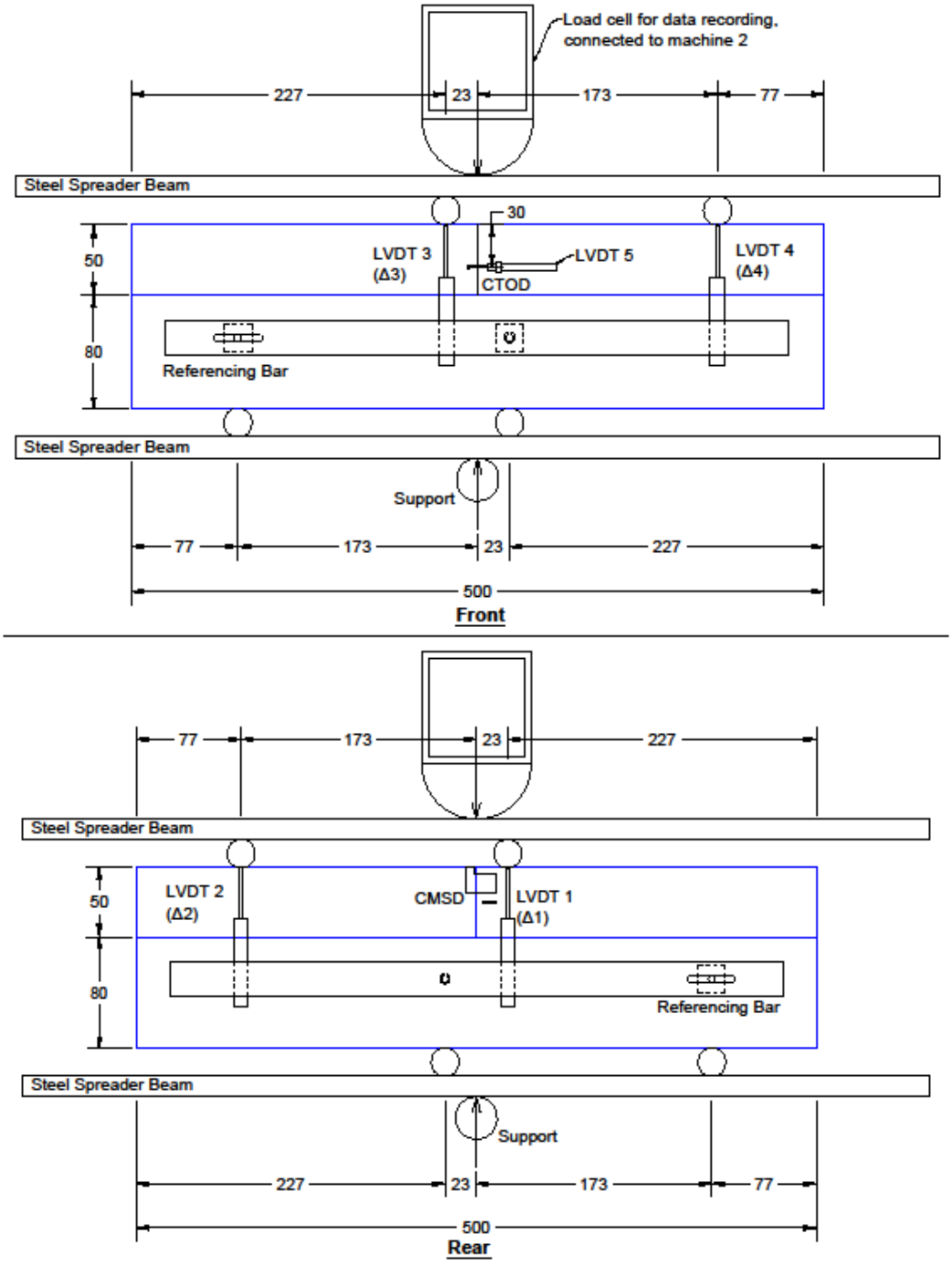

Figure 4.14 Test Arrangement (Composite Beam)

4.2.6 Testing Equipments and Attachments

Table 4.9 Testing Equipment and Fixings

Equipments& Fixings	Descriptions and Sketches (Unit: mm)	
Spreader Beam × 2	Two identical steel spreader beams were used in the test – one on the top, one at the bottom, as shown in Figure 4.13. Dimensions:666 × 150 × 25 Weight: 16.87kg	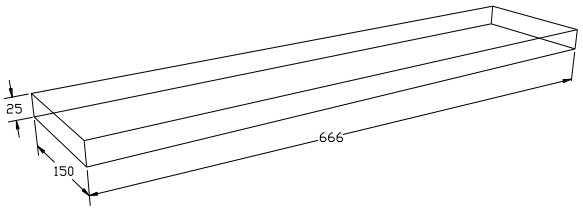
Set of Rollers× 2	Rollers were screwed with two parellel aluminium bars to keep the spacing constant. Meanwhile, the rollers were allowed to rotate freely during testing. Spacing between rollers: 176mm Weight: 1.607kg Details of rollers are as follows.	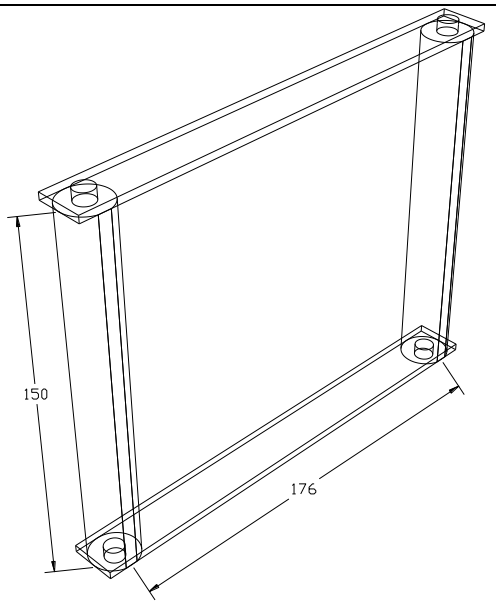
Roller × 4	Cross section of Ø20 with a flattened edge of approx. 5mm wide Length: 150mm	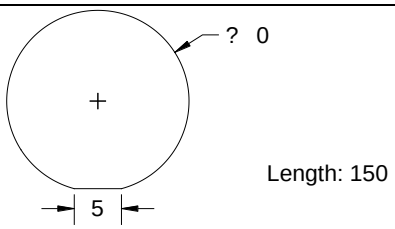

Equipments& Fixings	Descriptions and Sketches (Unit: mm)	
Referencing Bar Attachment × 4	Four attachments were attached on beams – two on either side. Exact positions are as shown on Figure 4.13. The referencing bars were then placed on the attachments and fixed with screws. Base: $20 \times 20 \times 1$ Screw: $\emptyset 5 \times 20$	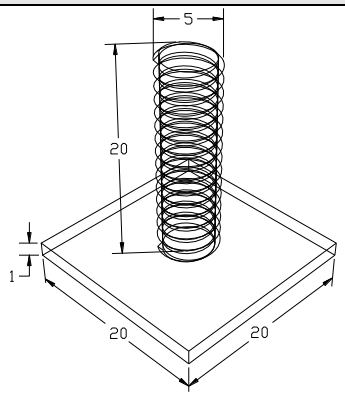
LVDT Holder	Made from perspex of approx. 13mm thick. Attached on the beam surface to hold a LVDT measuring crack tip opening displacement (CTOD).	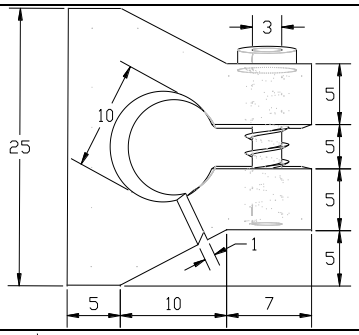
Clip Gauge Attachments	A set of clip gauge attachments was attached on the beam surface as positioned in Figure 4.13. The knife edges were facing inwards. Extra care was taken to ensure clean and sharp knife edges for firm connection with the clip gauge.	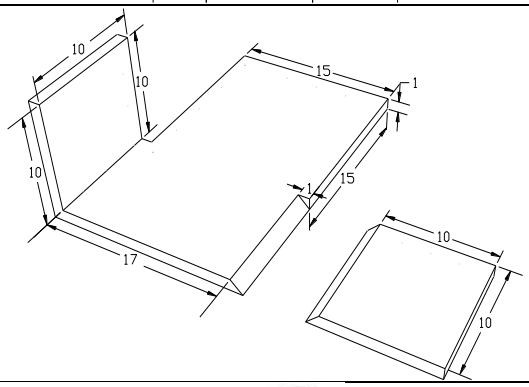
Clip Gauge	Epsilon Model: 3541-012M-120M-ST. Gauge Length: 12mm Travel Range: +12.0mm/-2.0mm Measuring to the accuracy of 0.001mm	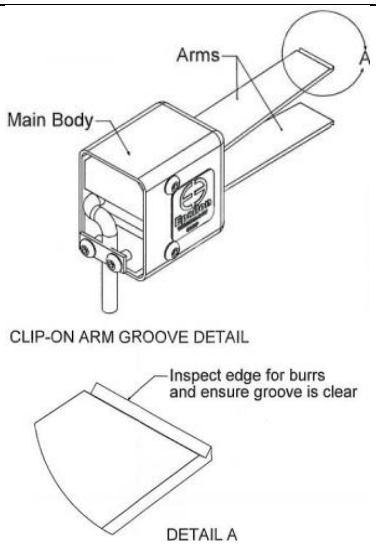 (Courtesy of Epsilon Technology Corp.) (Epsilon Technology Corp. 2003)

Equipments& Fixings	Descriptions and Sketches (Unit: mm)	
LVDT	1no. RDP Model D5/300AG, travel range: ±7.5mm 4no. RDP Model D6/02500A, travel range: ±2.5mm	
Load Cell	Hollow-core load cell from W. H. Mayes & Son, Windsor Ltd., Windsor, capable of measuring up to 100kN, type 406, input 10V, weight 2.313kg	
RDP Data Logger	RDP modular 600 multi-channel signal conditioning system comprises of three strain gauge channels, five LVDT channels and two load cell channels. It is connected to the computer interface for real-time reading and data recording. The maximum number of data recorded at a time is 10000 rows of readings. The recording rate was set at 0.05s per reading.	
Si-Plan Trolley	Si-Plan digital servo controller connected with RDP module 600 multi-channel system comprising two strain gauge channels and three LVDT channels. One of the strain gauge channels was calibrated to read the clip gauge readings. The servo software allows recording multi-channels simultaneously with no limit of maximum data.	

Equipments& Fixings	Descriptions and Sketches (Unit: mm)
Referencing Bar × 2	Referencing bars were fixed onto the corresponding attachments through the openings and slots. One bar is positioned on either side of the beam. Two LVDTs were held by the clamps (dimension:50×25) on each bar. Refer to the sketch below and Figure 4.13 for dimensions and LVDT positions.

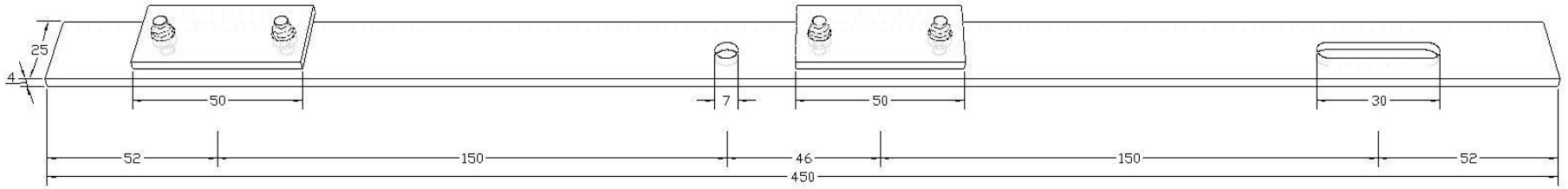

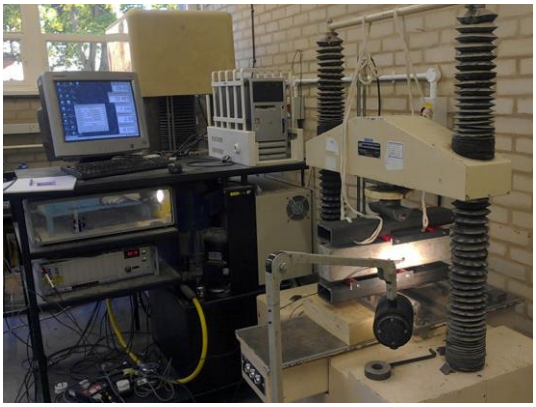

Figure 4.15 Si-Plan Trolley and 150kN Denison Machine

4.2.7 Testing Rig Mechanism

As illustrated in Figure 4.16 below, the black line represents the original status before loading, while the red line represents the post cracking position. Eccentricity is avoided by mark-ups on the beam surface and testing rigs for easy alignment. Usually in a mix-mode setup, the horizontal restraint takes an important part and needs to be evaluated accurately to correctly assess the shear resistance and material capacity. The horizontal restraint comprises internal and external components. To simplify the problem, there is no external restraint in the setup. So the only horizontal restraint to provide the resistance is the steel fibres. In this setup, there is no horizontal restraint, but the steel fibres in the concrete acted as internal horizontal resistance.

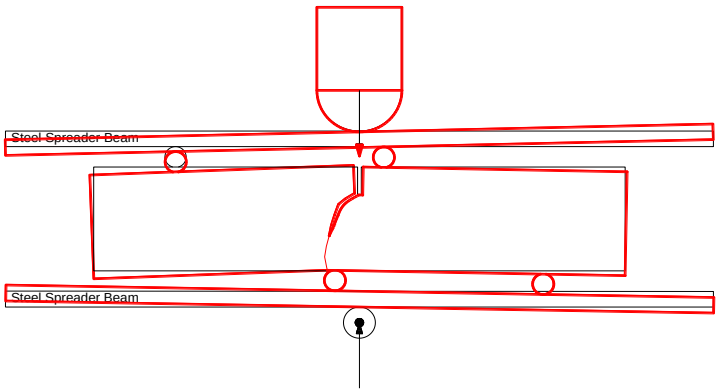

Figure 4.16 Testing Rig Mechanism

4.2.8 Test Preparation

Where notches were present in the beams, they were cut using a 2mm thick diamond tipped saw blade, usually two days prior to the planned date for testing. The finishing notches were approx. 3mm wide. On the following day, the positions for beam attachments and loading points were marked on beams, as shown in Figure 4.17.

In the case of PMC composite beams, the loading positions were on the compaction face of the beam where compaction was applied. Normally, it appears to be less smooth than the other faces. To avoid any errors caused by surface unevenness, the regions which would be in contact with the loading rollers were grinded to ensure firm and uniform contact in the test. It is pictured in Figure 4.17 (c). The LVDT holder, referencing bar attachments and clip gauge attachments were glued onto the beam surface using epoxy resin, as shown in Figure 4.17 (b). At least 4hr, and in most cases overnight, was allowed for the resin to fully set before tests started.

In the case of composite beams,

Figure 4.17 Specimen Preparation (a) Markup on Beams (Top Left) (b) Loading Positions Grinded Flat (Right) (c) Attachments Glued (Bottom Left)

4.2.9 Composite Beams

Three groups of composite beams were cast with the PMC overlay on top and the notched OPCC as the substrate to simulate the overlay beams. Two overlay mixes were involved – SBRPMC and PVAPMC. Two groups were with the full-depth notch in the centre of OPCC substrate. A full length (500mm) OPCC substrate with roughened surface was cut into two equal halves. They were then reassembled together to form the base in the following overlay casting. The other group of SBRPMC composite beams were saw-cut to the depth of 30mm in the mid-span of OPCC two days prior to testing, as all other monolithic beams. The mix proportions are listed in Table 4.5. The curing and preparation are the same as in monolithic beams, as previously explained. Following the SNSBT, a 150mm long section was cut from the tested samples and was subject to block splitting tests. The bonding between the two materials was then characterized, as listed in Table 4.10. The procedure for block splitting test was illustrated in chapter 4 and not repeated herein. The beam designations and approximate dimensions are given below, although the true dimensions for each beam were measured and used in the calculations.

Table 4.10 Composite Beam Designation and Bond Strength

Beam Designation	Overlay Mix	Substrate Mix	Substrate Thickness (mm)	Overlay Thickness (mm)	Width (mm)	Notch Depth (mm)	Bond Strength (MPa)
SBRPMC Compo	SBRPMC	OPCC 1	50	80	100	50	2.755
SBRPMC Compo 30	SBRPMC	OPCC 1	50	80	100	30	2.755
PVAPMC Compo	PVAPMC	OPCC 1	50	80	100	50	4.53

4.3 Monolithic Beam SNSBT Results

4.3.1 Description of Fracture Process

As shown in Figure 4.18, the crack development was divided into three stages – (a) before crack initiation, (b) from crack initiation to crack extended to the boundary of high shear zone and (c) further crack development till failure. The original position before loading is shown in black and the developed crack and the corresponding testing rig position is shown in red. A shear force/bending moment diagram is presented on the right hand side of Figure 4.18. As the test was controlled by displacement, it managed to capture and record the crack

initiation and propagation, even in the case of unreinforced concrete specimens. Details of the crack initiation angles and trajectories are described in 4.3.4. It typically developed from the notch front at an angle of approx. 50° towards the opposite roller, as indicated in Figure 4.18.

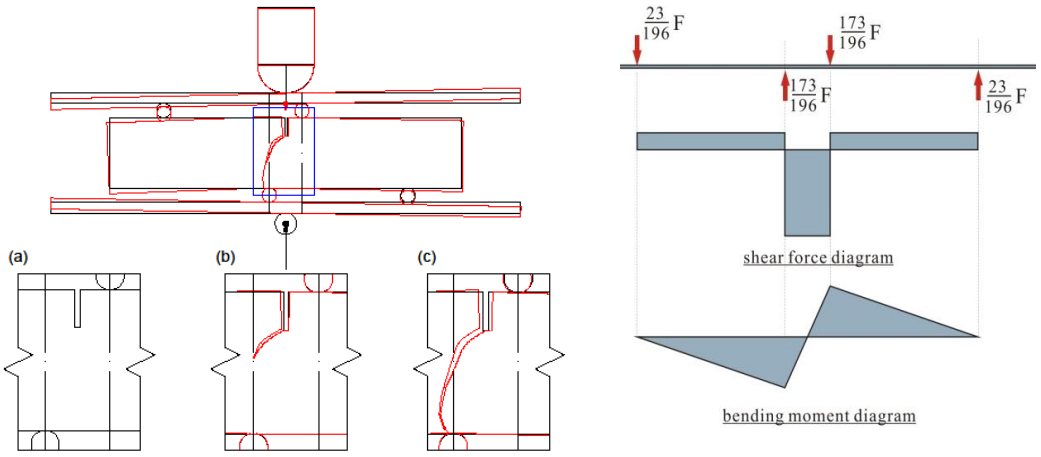

Figure 4.18 Crack Development & Shear Force/Bending Moment Diagram

The first stage corresponds to Figure 4.18(a). At this stage, the whole ligament remains integrated to provide resistance. At the notch tip, it is subject to high shear and minimal bending moment, as illustrated in the shear force and bending moment diagram. As crack deviates from the central line towards the boundary of the high shear zone, bending moment increases from zero to 17.6F at the boundary of the high shear zone, as shown in Figure 4.18(b), while shear force still equals to 173/196F. It is assumed F is the total applied load including the self weight of top spreader beam, top rollers and the load cell. The continuously engagement of bending moment adds the weighing factor of flexure on the general performance of the specimens. It is a mix-mode problem combining mode I (opening) and mode II (shearing) with mode II dominant. In fact, pure shear rarely exists in real engineering problems. It is always accompanied by flexure or other loading scenarios. The same applies in pavements.

As the crack propagates further outside the high shear zone, as shown in Figure 4.18(c), the engagement of bending moment becomes dominant. It is observed in the case of steel fibre reinforced concrete (SFRC) beams that the peak load was reached long after the crack initiation, as presented in Figure 4.20. In other words, the load bearing capacity continued to

increase after cracking. Most commonly, the peak load was attained after the crack extended outside the high shear zone. Fibre fraction in SFRC was evident before the final fracture of specimens. Therefore, the peak load P_{max} cannot be regarded as a pure shear parameter, but an indication of the shear strength under mix-mode subject to the influence of both shear and flexural resistance. In practical engineering, the shear strength is usually derived from a four point bending beam test, in which case, it is also referred to as "flexural-shear".

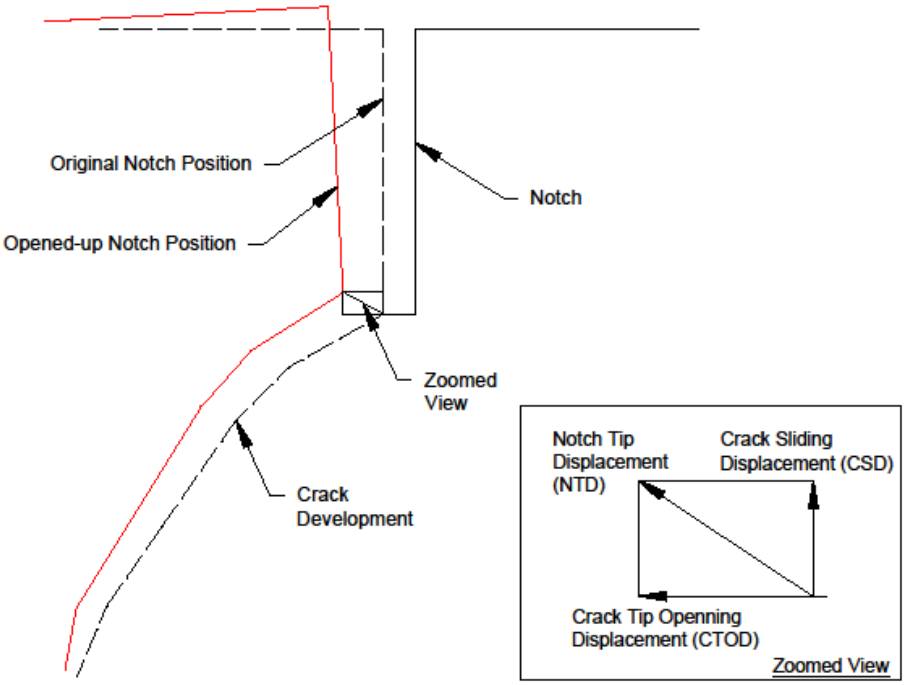

Figure 4.19 Sketch of Notch Tip Displacement (NTD)

A LVDT and a clip gauge were instrumented at the notch tip to record the crack tip openning displacement (CTOD) and crack sliding displacement (CSD) respectively, as sketched in Figure 4.13. The vector sum of the two is deemed as Notch Tip Displacement (NTD), as demonstrated in Figure 4.19, which describes the local displacement across the crack in the whole loading process.

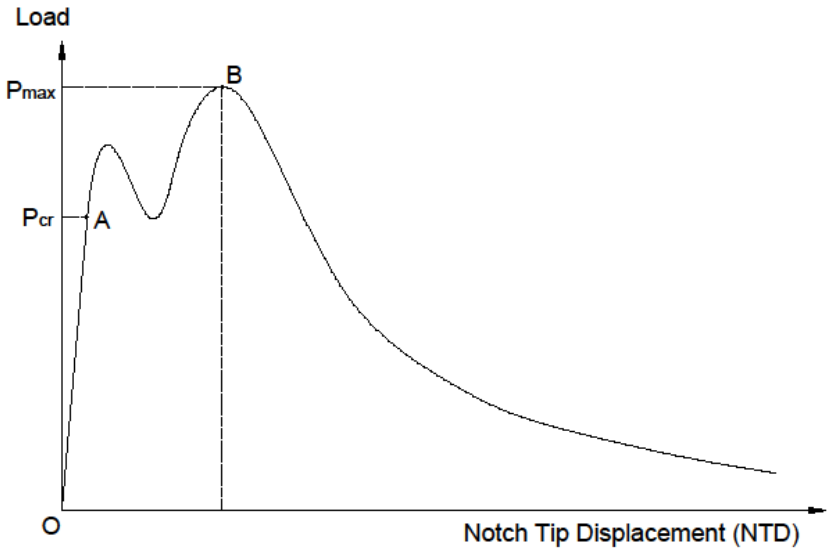

Figure 4.20 General Load – Notch Tip Displacement Diagram (P-NTD)

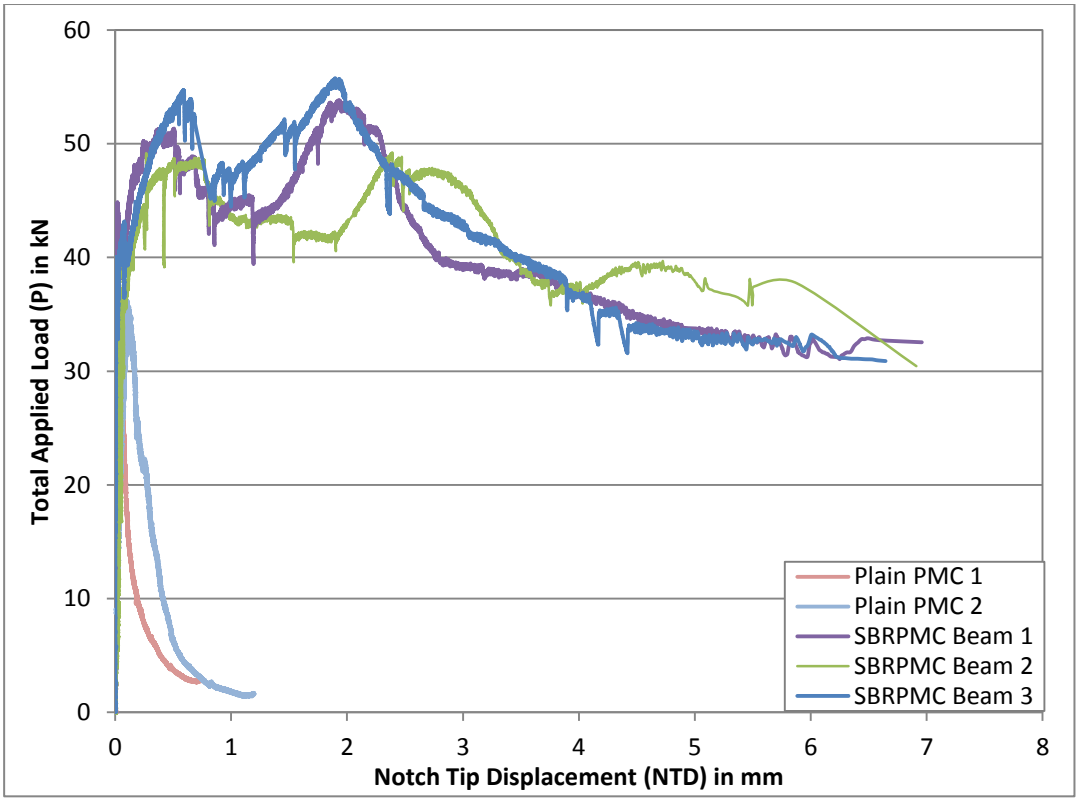

Figure 4.21 SBRPMC Beam P-NTD Diagram

Figure 4.20 dictates the typical P-NTD curve for a SFRC beam. The P-NTD curves for SBRPMC and plain PMC beams are plotted in Figure 4.21. In SBRPMC beams, the initial linear elastic stage is followed by the strain softening and stain hardening due to steel fibres.

The shape of the curve varies with different mechanical properties of SFRC, such as quantity of steel fibre, aspect ratio etc. At first the load increased rapidly in a linear manner. Then the load incremental rate was reduced as it approached the onset cracking load. This nonlinearity was due to the heterogeneity in the mix, such as aggregate interlock and fibre bridging. The shear resistance can be estimated by dividing the shear force F_1 by the area of the ligament section.

The onset crack initiation is defined as the point at the end of the linear progression of the P-NTD curve, shown as point A in Figure 4.20. Section OA corresponds to the linear elastic phase in the tests. The crack length remains the same in section OA. Point A signals the inception of fracture process zone and development of microcracks ahead of the notch tip. P_{cr} is derived from the experiments to calculate the onset shear strength and the mode II critical stress intensity factor K_{IIC} based on Tada's expression (2000), as presented in 4.3.2.

As presented in Figure 4.21, the maximum NTD has been considerably increased from approx. 1mm in plain PMC to approx. 7mm in SBRPMC with 1.5% volume fraction of steel fibre. The NTD at peak load was approx. 1.9-2.3mm in SBRPMC beams, while it was 0.1mm or less in plain PMC beams. Undoubtedly, steel fibre considerably improved the concrete ductility. The ultimate nominal shear strength at the peak load was derived and provided in 4.3.3. The fracture energy G_{II} is also determined from the load-displacement curves (F_1-δ_1 & $F_2 - \delta_2$) and presented in 4.3.5.

4.3.2 Onset Crack Resistance

As sketched in Figure 4.20, the end point of the initial linear section corresponds to the onset crack development, i.e. crack initiation. This is further affirmed by the observed results. Table 4.11 lists both the observed crack initiation during the tests and the onset critical loads for comparison purposes. In most cases, the crack initiation was observed at the length of 5-15mm. This could be the main reason for the slight discrepancy. Generally there is good agreement between the loads corresponding to the observed crack initiation and the analyzed onset crack propagation. The onset shear strength was calculated by having the onset shear load divided by the vertical shear cross sectional area. It is considered that the full cross sectional area was available to provide the shear resistance at this stage. These values represent the pre-cracking shear resistance. Accordingly, the mode II stress intensity factor

$K_{IIonset}$ was calculated based on Tada's formula (2000) in Eqn.4.6, where F_{CR1} = applied shear force at the notch at the onset of slow crack growth; a = crack depth, usually 27mm in the testing geometry; b = height of the beam, nominally 100mm with slight variations from beam to beam; B = width of the beam, nominally 75mm. Exact dimensions for each beam were applied in the calculation.

$$K_{IIonset} = \frac{2F_{CR1}}{B\sqrt{\pi a}} \frac{1.30-0.65(a/b)+0.37(a/b)^2+0.28(a/b)^3}{\sqrt{1-(a/b)}} \quad 4.6$$

Table 4.11 Onset Crack Resistance and Mode II SIF

Mix Designation ID	1st Crack Noticed (kN)	Onset Shear Load F_{CR} (kN)	Onset Shear Stren. (MPa)	Ave. (MPa)	$K_{IIonset}$ (kN·m$^{-3/2}$)	Ave. $K_{IIonset}$ (kN·m$^{-3/2}$)
OPCC 1	-	26.329	3.523	3.31	2793	2624
OPCC 2	26.50	21.737	2.957		2349	
OPCC 3	30.70	25.487	3.444		2731	
Plain Conv. PMC 1	18.19	18.064	2.409	2.83	1966	2299
Plain Conv. PMC 2	20.00	21.431	2.756		2268	
Plain Conv. PMC 3	32.39	25.105	3.359		2663	
Plain PMC 1	33.50	27.171	4.769	4.55	3781	3629
Plain PMC 2	26.60	26.635	4.331		3477	
Conv. PMC 1	-	38.191	5.232	4.74	4086	3772
Conv. PMC 2	45.00	34.135	4.582		3676	
Conv. PMC 3	40.50	32.375	4.419		3552	
PVAPMC 1	-	37.120	6.440	6.02	4998	4792
PVAPMC 2	40.80	32.528	5.558		4519	
PVAPMC 3	63.60	39.952	6.053		4860	
1%V_f PMC 1	30.00	32.758	5.490	5.63	4773	4604
1%V_f PMC 2	37.00	31.304	5.530		4385	
1%V_f PMC 3	-	33.447	5.874		4653	
SBRPMC 1	40.60	34.426	5.977	6.17	4702	4437
SBRPMC 2	35.50	30.998	5.297		3906	
SBRPMC 3	41.30	38.038	7.240		4701	
14Agg PMC 1	-	30.998	5.375	6.01	4208	4564
14Agg PMC 2	45.32	37.212	6.677		4769	
14Agg PMC 3	-	34.740	5.983		4714	
20Agg PMC 1	43.68	37.816	7.393	6.79	4802	4821
20Agg PMC 2	-	-	-		-	
20Agg PMC 3	47.20	35.283	6.197		4839	

Mix Designation ID	1st Crack Noticed (kN)	Onset Shear Load F_{CR} (kN)	Onset Shear Stren. (MPa)	Ave. (MPa)	$K_{IIonset}$ ($kN{\cdot}m^{-3/2}$)	Ave. $K_{IIonset}$ ($kN{\cdot}m^{-3/2}$)
2%V_f PMC 1	63.00	40.028	6.850	6.66	5355	5357
2%V_f PMC 2	48.10	37.480	6.493		5149	
2%V_f PMC 3	48.60	36.737	6.622		5568	
LF PMC 1	44.40	40.916	7.678	7.71	6011	6306
LF PMC 2	38.60	42.056	7.629		6241	
LF PMC 3	58.50	43.418	7.832		6667	
3d PMC 1	31.00	26.023	4.986	5.76	4177	4468
3d PMC 2	42.51	32.100	5.866		4534	
3d PMC 3	41.48	35.436	6.437		4693	
7d PMC 1	41.30	32.390	5.916	5.78	4522	4569
7d PMC 2	46.20	31.418	5.589		4735	
7d PMC 3	42.20	32.153	5.840		4450	

4.3.3 Shear Strength

As explained in chapter 2, the shear strength is usually calculated using Eqn. 2.3, with the total shear force divided by the vertical cross sectional area. This is effectively a flexural shear strength reflecting the shear resistance under a mix-mode shear condition. Hence, it is also referred to as "Nominal Shear Strength". The results are provided in Table 4.12 together with the standard deviation. Maximum load, F, is the maximum total load applied on the beams taking into consideration the self weight of the top spreader beam, the top set of rollers and the load cell, as listed in Table 4.9. The shear load is the proportional shear load applied in the high shear zone in the middle, $\frac{150}{196} \cdot F$, as shown in the shear force diagram in Figure 4.18.

It can be seen that the results of identical specimens in a group are consistent with relatively low standard deviation. Results from beam specimens, Plain PMC 3 and Conventional (Conv.) PMC 1, are discarded due to systematic error. As plotted in Figure 4.22, the averaged nominal shear strength is compared with the base line value of the shear strength of OPCC. It is found that the SF-RC-PMC (Steel Fibre Reinforced, Roller Compacted, Polymer Modified Concrete) could reach far beyond the shear resistance that an OPCC or what a conventional SFRC could offer. For example, OPCC only provided the shear strength of 3.71MPa, as represented by the red line in the figure while the conventional PMC reinforced by 1.5% steel fibre achieved 5.59MPa. Nevertheless, the SF-RC-PMC with even less fibre

reached around 7MPa, even at the age of 3 days. Larger size of coarse aggregate or increasing the amount of fibre addition resulted in higher shear resistance. It is discussed in Chapter 5.

Table 4.12 Peak Load and Shear Strength

Mix Designation ID	Max. Load F (kN)	Max. Shear Load (kN)	Beam Depth (mm)	Notch Depth (mm)	Beam Width (mm)	Shear Stren. (MPa)	Ave. Shear Stren. (MPa)	Standard Deviation (MPa)
OPCC 1	38.905	29.93	101.0	27.0	101.0	4.005	3.71	0.35
OPCC 2	31.723	24.43	100.0	26.5	100.0	3.324		
OPCC 3	36.653	28.21	101.0	27.0	100.0	3.812		
Plain Conv. PMC 1	23.886	18.44	101.0	26.0	100.0	2.350	2.83	0.49
Plain Conv. PMC 2	29.723	22.90	104.0	27.0	101.0	2.822		
Plain Conv. PMC 3	33.875	26.08	101.0	27.0	101.0	3.332		
Plain PMC 1	35.335	27.20	101.0	27.0	77.0	4.773	4.65	0.17
Plain PMC 2	36.190	27.85	102.0	27.0	82.0	4.529		
Conv. PMC 2	55.696	42.78	101.0	26.5	100.0	5.742	5.61	0.18
Conv. PMC 3	52.309	40.19	100.0	26.0	99.0	5.486		
PVAPMC 1	61.208	46.999	99.5	27.0	79.5	8.154	7.49	1.41
PVAPMC 2	44.732	34.390	103.0	27.0	77.0	5.877		
PVAPMC 3	72.619	55.732	102.0	27.0	88.0	8.444		
1%Vf PMC 1	56.008	43.019	102.5	24.5	76.5	7.209	7.00	1.22
1%Vf PMC 2	41.831	32.169	101.0	27.0	76.5	5.683		
1%Vf PMC 3	60.054	46.115	99.0	26.0	78.0	8.099		
SBRPMC 1	53.847	41.37	106.0	26.0	72.0	6.511	6.93	0.54
SBRPMC 2	62.361	47.88	103.0	26.0	76.0	7.537		
SBRPMC 3	55.769	42.84	101.0	27.0	71.0	6.743		
14Agg PMC 1	63.967	49.110	100.0	27.0	79.0	8.516	8.16	0.67
14Agg PMC 2	53.613	41.186	98.0	27.0	78.5	7.390		
14Agg PMC 3	64.836	49.775	100.5	27.0	79.0	8.572		
20Agg PMC 1	67.556	51.856	100.0	34.0	77.5	10.138	9.07	0.95
20Agg PMC 2	61.166	46.966	98.0	26.5	79.0	8.315		
20Agg PMC 3	64.994	49.896	100.0	27.0	78.0	8.763		
2%Vf PMC 1	83.069	63.729	101.0	27.5	79.5	10.906	9.91	1.13
2%Vf PMC 2	65.327	50.151	101.0	27.0	78.0	8.689		
2%Vf PMC 3	73.356	56.296	101.0	25.0	73.0	10.147		
LF PMC 1	69.206	53.120	100.0	27.0	73.0	9.507	9.52	0.84
LF PMC 2	65.210	50.062	100.0	25.5	74.0	8.677		
LF PMC 3	78.133	59.952	102.0	25.0	72.0	10.361		
3d PMC 1	52.177	40.087	100.0	27.0	71.5	7.680	7.02	0.92

Mix Designation ID	Max. Load F (kN)	Max. Shear Load (kN)	Beam Depth (mm)	Notch Depth (mm)	Beam Width (mm)	Shear Stren. (MPa)	Ave. Shear Stren. (MPa)	Standard Deviation (MPa)
3d PMC 2	42.505	32.685	99.0	27.0	76.0	5.973		
3d PMC 3	53.120	40.809	105.0	28.0	71.5	7.412		
7d PMC 1	49.884	38.333	100.0	27.0	75.0	7.001	7.03	0.64
7d PMC 2	56.165	43.139	102.0	25.0	73.0	7.675		
7d PMC 3	45.833	35.232	99.0	27.5	77.0	6.399		

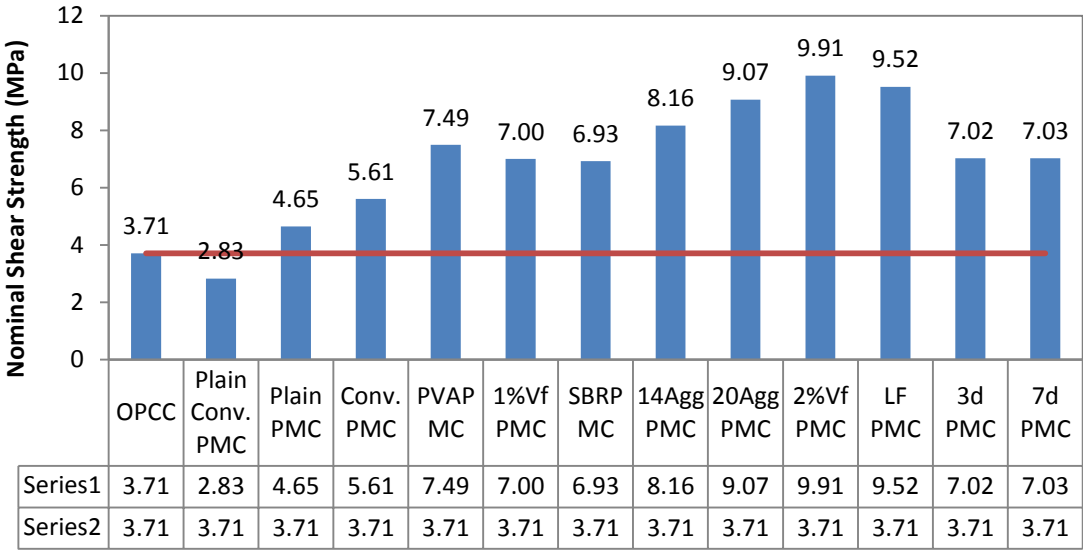

Figure 4.22 Average Nominal Shear Strength

4.3.4 Crack Planes and Initiation Angle

The failure sections were marked up by gridlines on the beam surfaces from the notch tips at the intervals of 5mms and 10mms. Both the front and the back surfaces of each beam were marked up, measured, recorded and plotted in the following figures. The lengths of crack trajectories were estimated based on gridline measurements and converted into the areas of crack planes by multiplying measured beam depths. They were later employed to calculate the fracture energy required to propagate the crack for a unit length. An example of the gridline marking of crack trajectory is given in Figure 4.23. The crack trajectories at front and back were both recorded to a reasonable accuracy, to provide the best estimation of the roughness of the cracking surface. This could be improved in the future with the employment of some delicate surface scanning system to portray the true roughness contour of the fracture plane.

It was observed that coarse aggregate was more exposed in the failure plane of OPCC, while in RC-PMC most of the cracks went through aggregates. The high strength mortar matrix compared to the coarse aggregate is the main cause and this has been reported in many previous studies (Song et al. 2010, Taylor 1974, Walraven 1981, Wong et al. 2007, Xu and Karadelis 2012) and discussed in 4.1.3.

In addition, the phenomenon of multiple cracking in SFRC is conspicuous. The crack trajectories presented below are the dominant cracks only. When there is more than one dominant crack, the average length was provided, as in Table 4.13. It is difficult to measure and record all the co-existent cracks due to tortuosity. In uniaxial tensile tests, Bazant (1983) developed the crack band theory considering the width of a band of cracks as a material property. However, the multiple cracks in SNSBT are far more diverted, as presented in the crack trajectory envelop diagram, Figure 4.26. Plus, the envelop width is not a material property in the case of mix-mode loading. Hence, the concept of crack band theory is not adopted. Only the dominant cracks were plotted below. The accompanying cracks are omitted for the sake of clear presentation, although it is obvious that the number of co-existent cracks increased with the amount of steel fibres added. The recorded crack trajectories are drawn in Figure 4.24 and Figure 4.25. The surface cracks on both sides of the beams were plotted on the same sketch with one towards the right and one towards the left. The recorded crack lengths were summarized and converted into crack plane areas in Table 4.13. The unit is in mm or mm^2.

A series of crack trajectories were plotted in the same sketch exhibiting the trend for crack propagation. It is typically deviated from the centre towards the opposite loading position (23mm from the centre line). Once the crack tip reaches the position right above the loading point, it enters a “buffer zone”, where it may continue in the same direction for approx. 5mm then return back towards the loading point. It is found that most of the crack lengths fall in the range of the blue hatched area in Figure 4.26. A straight line was drawn between the notch tip and the loading point as the inner boundary of the blue hatched area. The outer boundary is set at 39° angle from the notch tip until it reaches the line at 5mm offset from the loading point. It was found that nearly 90% of dominant crack trajectories fall in this range. The lengths of the two boundary lines are 76.538mm and 86.235mm respectively, the mean value of which is 81.39mm. The initiation angles in relation to the vertical axis are measured

and listed in Table 4.13. Where multi-cracks were present, the angle of the dominant one was measured. The averaged vertical initiation angles are in the range between 46 ºand 58.5 º. It is revealed that it increases with the size of coarse aggregate, which is also dictated in the crack trajectories shown in Figure 4.24. A picture of crack initiation taken during the loading process on PVAPMC beam 1 is presented in Figure 4.27.

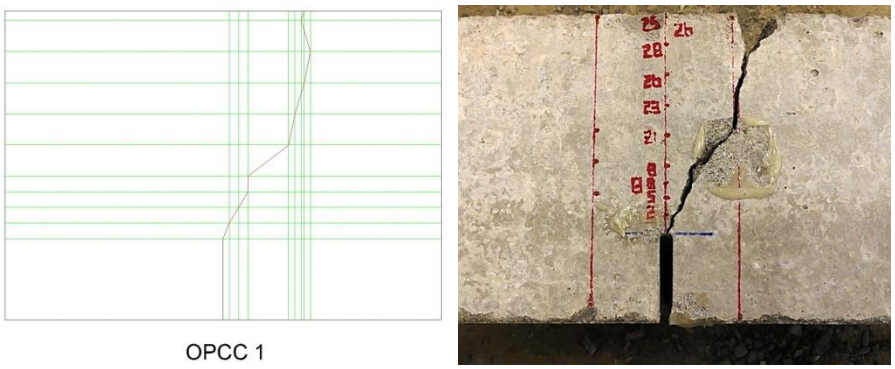

Figure 4.23 Gridline Recording of Crack Trajectories (OPCC Beam)

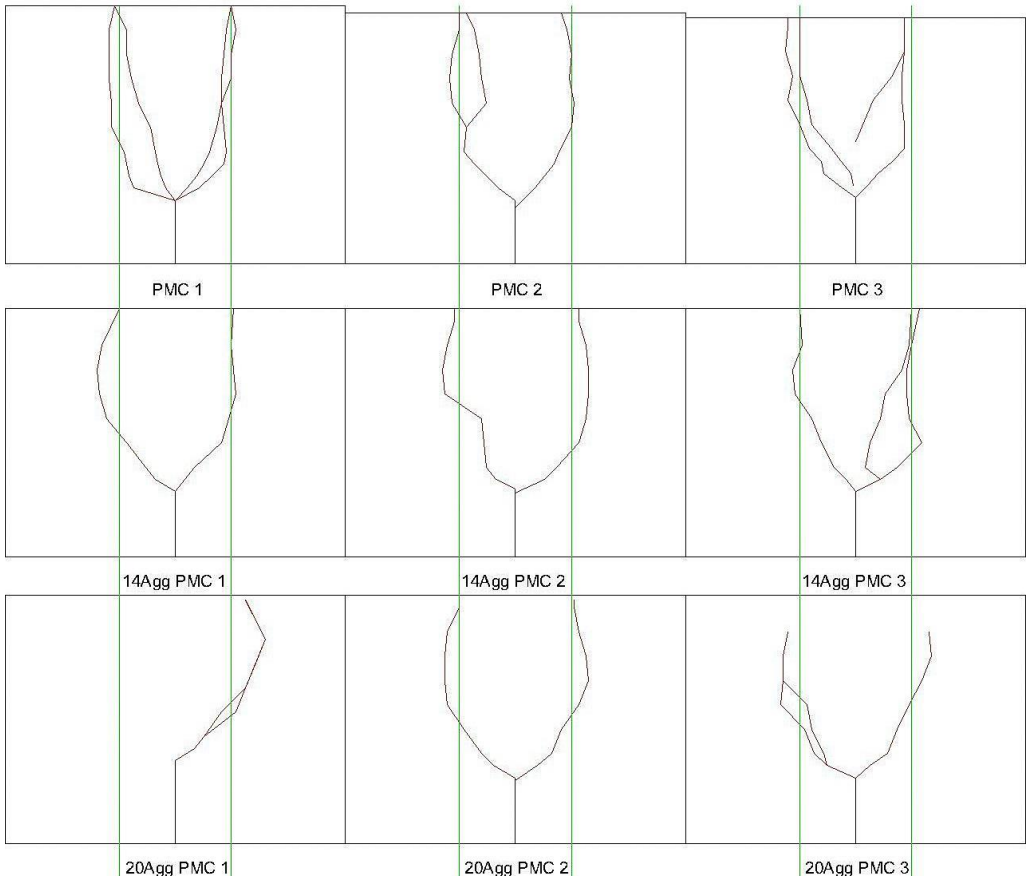

Figure 4.24 Schematic Crack Trajectories with Different Aggregate Sizes

(Row 1: 10mm aggregate; Row 2: 14mm aggregate; Row 3: 20mm aggregate)

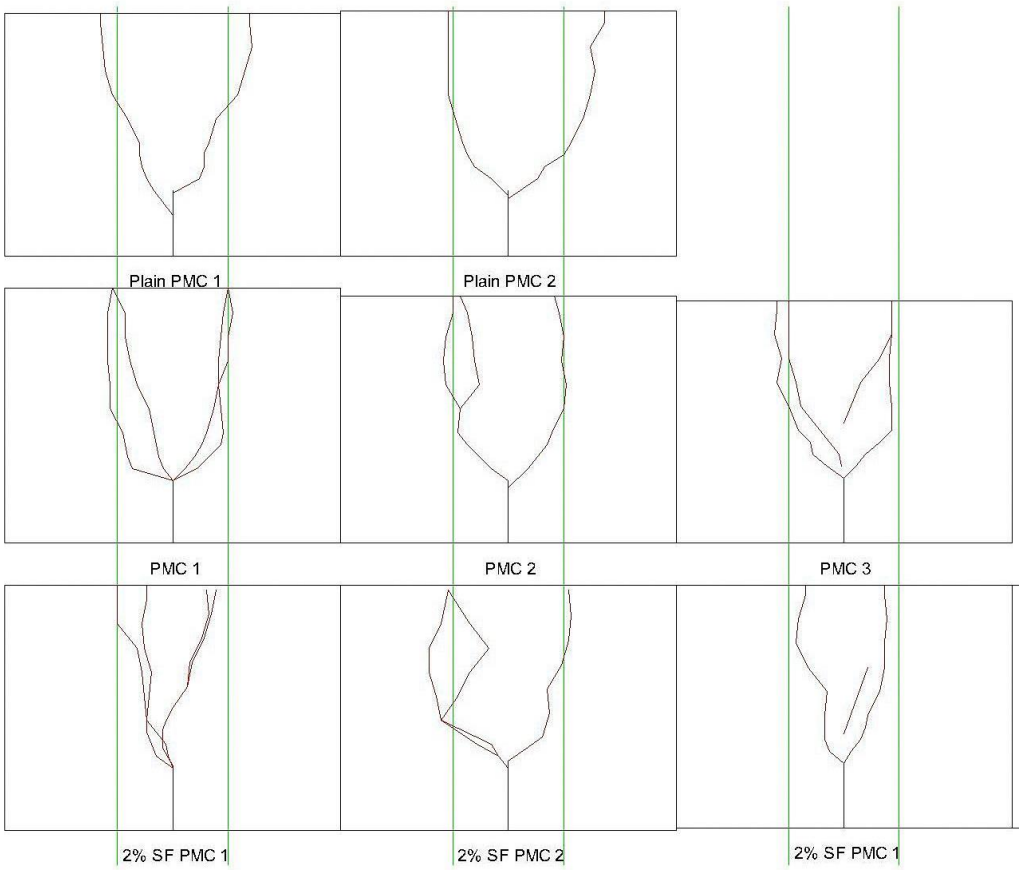

Figure 4.25 Schematic Crack Trajectories with Different Steel Fibre Contents

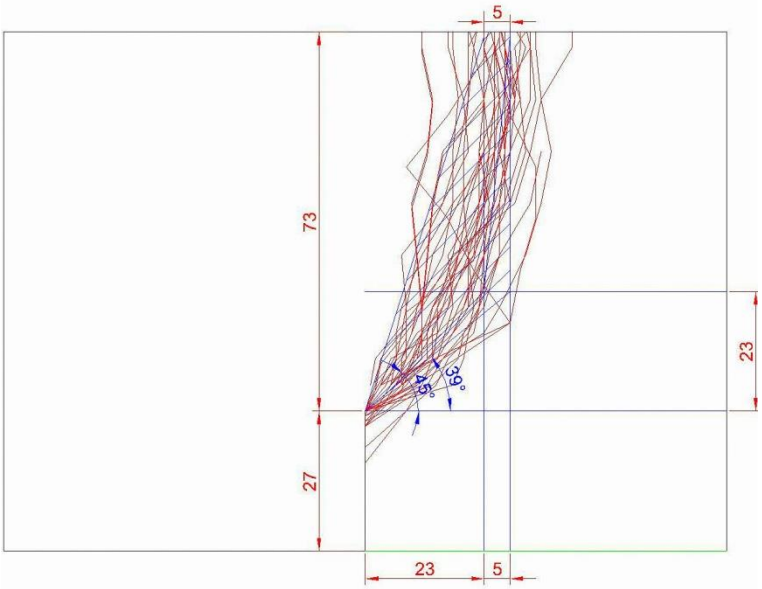

Figure 4.26 Crack Trajectory Envelope

Table 4.13 Crack Trajectory, Fracture Plane and Initiation Angle

Mix Designation	Front Crack	Rear Crack	Averaged Crack Length	Beam Width	Area of Crack Plane	Averaged Crack Plane Area	Averaged Vertical Initiation Angle (°)
OPCC	85.34	82.89	77.17	101.00	8495.59	7744.85	47°
	86.35	91.05		100.00	8870.12		
	52.94	64.44		100.00	5868.85		
Plain Conventional PMC	84.22	83.36	84.31	100.00	8378.78	8487.48	-
	84.99	85.16		101.00	8592.59		
	85.89	82.25		101.00	8491.07		
Plain PMC	91.50	87.19	89.62	77.00	6879.78	7125.69	50°
	85.60	94.20		82.00	7371.60		
Conventional PMC	80.51	79.62	79.90	99.00	7926.43	7950.04	-
	79.85	79.62		100.00	7973.66		
PVAPMC	85.34	82.89	83.32	77.00	6476.84	6869.51	46°
	81.89	83.16		88.00	7262.18		
SBRPMC	91.69	94.73	82.23	72.00	6711.09	5985.26	52°
	88.40	50.87		76.00	5292.16		
	85.22	82.46		71.00	5952.53		
14Agg PMC	88.70	83.69	85.23	79.00	6809.17	6719.84	54.5°
	89.16	89.70		79.00	7065.11		
	83.48	76.66		78.50	6285.69		
20Agg PMC		82.44	80.03	77.50	6388.94	6288.65	58.5°
	86.06	86.06		79.00	6798.79		
	75.23	70.36		78.00	5678.21		
2%V_f PMC	78.20	81.72	83.47	78.00	6236.82	6416.72	46.5°
	80.08	83.48		73.00	5969.76		
	78.82			79.00	6226.65		
	101.10	80.88		79.50	7233.65		

Figure 4.27 Crack Initiaton in PVAPMC Beam 1

In the cast of SBRPMC beams with 20mm deep notch only (usually 27mm deep), splitting cracks co-existed with shear cracks. A splitting crack developed between the two central rollers in an inclined angle, even before the appearance of shear crack at the notch tip. Hence the onset shear crack resistance must be higher than the splitting strength.

4.3.5 Determination of Fracture Energy

The fracture energy is deemed as the energy dissipating per unit crack length. Swartz (1990, 1988) used the stain energy U at the onset of unstable crack growth divided by an approximate crack plane area, as presented below. Where U is the area under the Load – Loading Point Displacement (P-LPD) curve up to the point of instability, $^1/_2\, mg\bar{\delta}_0$ is the potential energy of the concrete section between the two central loading points, a_α is the inclined crack length. The value 1.15 was used as a compensation factor to the surface roughness. This has been a pioneering research at the time. However, only the energy till the point of instability crack growth was taken into account, which clearly underestimates the total energy. Plus, the off-centre load – load point displacement also contributes to the total work, which was neglected in the study. Furthermore, as the author stated, the loading process past the onset crack growth was not under control, which resulted in a monotonic failure. The test duration lasted typically 30-60s for a single beam. The sudden failure cannot

provide an accurate and trustworthy result. Nevertheless, the author stated that the fracture energy per unit area G_c derived here is not a pure mode II parameter, but it involves both mode I and mode II, i.e. mixed mode. This is later incorporated in the derivation of the stress intensity factor K.

$$G_c = \frac{U - {}^1/_2 mg\bar{\delta}_0}{1.15B\, a_\alpha} \qquad 4.7$$

As previously mentioned, the SNSBT in the study was conducted by displacement-control. A full load – displacement relationship became available. The crack development occurred in a stable and controlled manner. Instrumented with four LVDTs at both loading positions, two on one side and two on the other, it was possible to record the loading point displacements. The fracture energy was calculated as the total areas under P-LPD curves F_1-δ_1 and $F_2 - \delta_2$ divided by the measured area of fracture plane. The displacements δ_1 and δ_2 were taken as the averaged values between the front and back LVDTs to eliminate any twisting effect. The area under the F - δ curves was calculated using integrals. Due to the enormous number of data, the F – δ curves were divided into a number of segments to attain reasonably accurate approximation lines, i.e. linear or polynomial lines up to the power of 6. For the sake of brevity, an example of the F - δ curve in 50LF PMC 1 beam is plotted in Figure 4.28 and Figure 4.29. The total area under F – δ curves was calculated using Eqn. 4.8. The averaged fracture energy values for a variety of mixes were summarized in Figure 4.30. It is noticed that the fracture energy for unreinforced concrete, including OPCC, plain conventional PMC and plain PMC, are in the order of 10^{-4} kN/mm. The introduction of steel fibre by as little as 1% magnified the fracture energy by ten times. The fracture energy could be amplified by increasing the nominal size of coarse aggregate or the volume fraction of steel fibre. However, the addition of a low volume of steel fibre has very significant effect on the fracture energy. SFRC continued to carry loads long after the initial cracking occurred, in which case large fracture energy value implied good post-cracking resistance.

$$A_{F-\delta} = \sum_{s=1}^{n} \int_{\delta_{beg}}^{\delta_{end}} (a\delta^6 + b\delta^5 + c\delta^4 + d\delta^3 + e\delta^2 + f\delta + g)d\delta \qquad 4.8$$

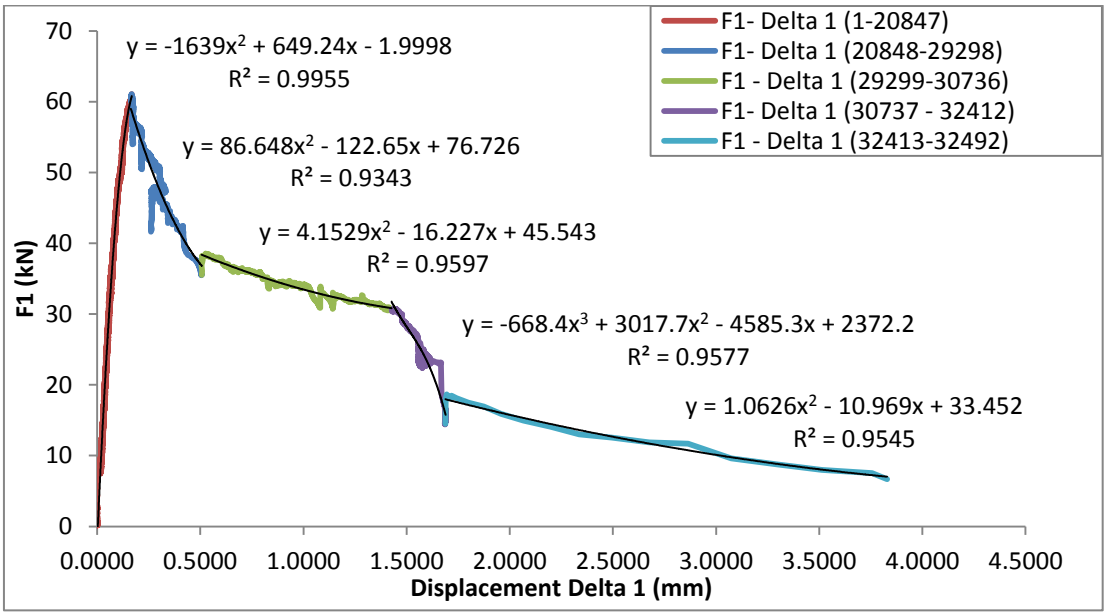

Figure 4.28 Load – Displacement Curve (F_1-δ_1) of Beam LF PMC 1

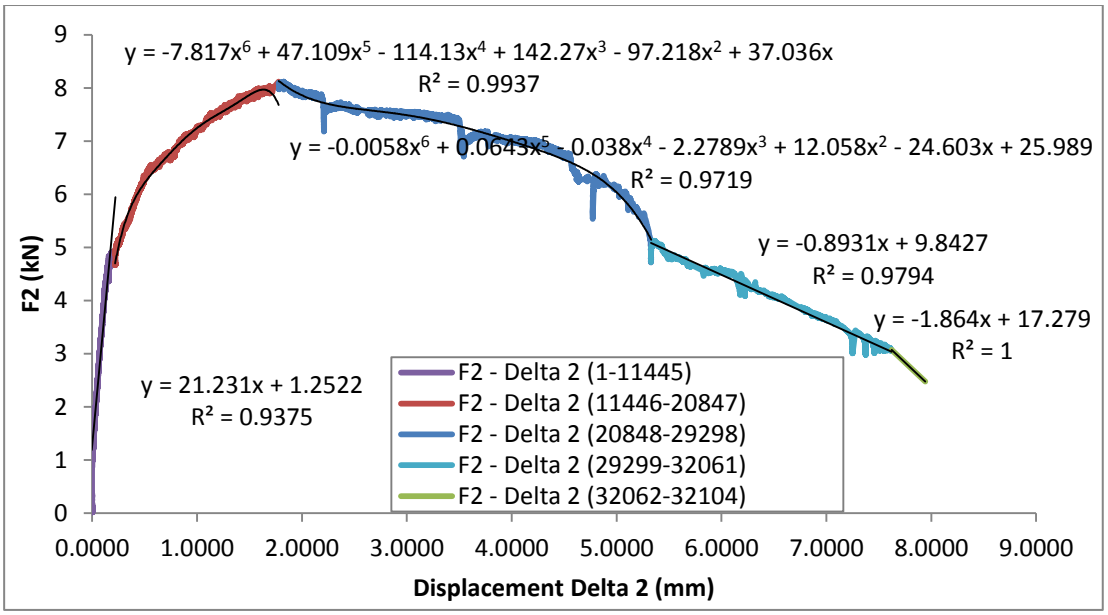

Figure 4.29 Load – Displacement Curve (F_2-δ_2) of Beam LF PMC 1

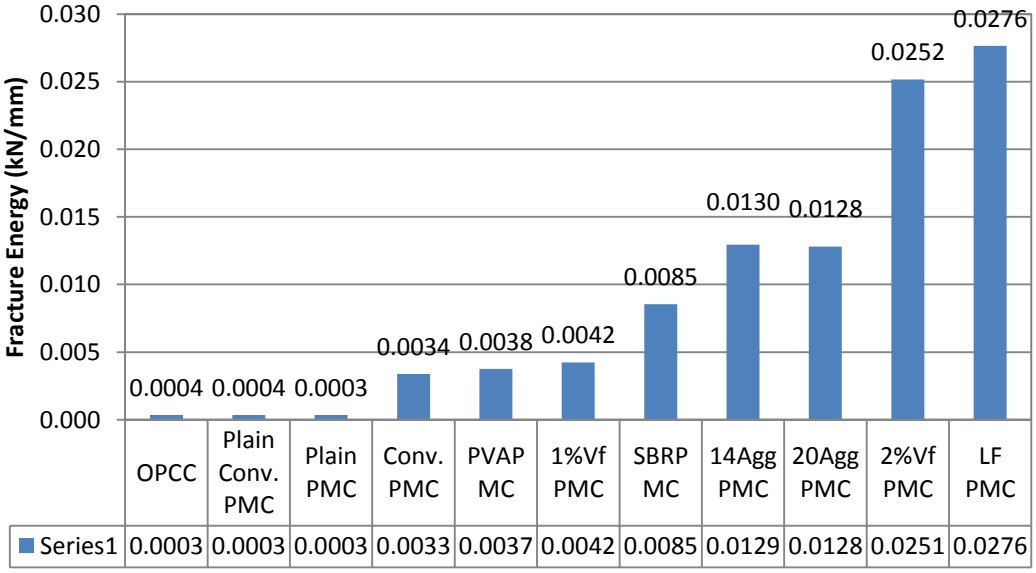

Figure 4.30 Fracture Energy Values (kN/mm)

4.4 Composite Beam SNSBT Results

This test was performed on composite beams with OPCC substrate overlaid by PMC materials to examine the behaviour of the composite system under shear loading conditions. Three groups of composite beams were tested. They are SBRPMC and PVAPMC composite beams with full-depth notch in the OPCC substrate, approx. 50mm. The other group was SBRPMC composite beam with 30mm deep notch in the OPCC substrate. The tests configuration and instrumentation were presented in 4.2.

4.4.1 SBRPMC Composite Beams with Full Notch

The crack trajectories and corresponding loads were provided in Figure 4.31, Figure 4.34 and Figure 4.37. They are oriented with OPCC at the base and PMC overlay on top, for easy of interpretation. The crack trajectories were recorded in the same way, which was already described in 4.3.4. The cracks at front and back were plotted in the same graph. To distinguish between them, one was plotted towards right from the notch tip and the other one towards left. However, it should be noted that all cracks developed towards the top roller positioned at 23mm off the centre line in the test. The crack propagation and the corresponding loads were demonstrated by the annotation pointing to the specific positions along the crack trajectories.

It is obvious that SBRPMC Compo Beam 1, in Figure 4.31, has a single crack initiating from notch tip or near notch tip upwards. In contrast, SBRPMC Compo Beam 2 and 3 presents multiple cracks and cracks at interface. Monotonic failure happened in Beam 1, a result of fixed roller supports. Rollers were screwed tight for ease in positioning and were usually loosened prior to testing. Some of the screws were unreleased, which triggered a failure of dynamic nature. The peak load was comparably larger than the other two beams. Hence the result is discarded in data analysis. In Beam 2 and 3, the first crack developed at 62-65kN along the interface for 12-23mm, followed by the initiation of shear cracks at 67-70kN. Although the interface cracks may continue to propagate to 23mm or even further (35mm in Beam 3), the dominant failure was caused by shear cracks in the same way as in monolithic beams due to the shear loading condition. As shear crack propagated, the stress re-distributed and the interface cracks were closed. As load incremental rate decreased and eventually load reduced, localized shear crack coalesced, widened and formed one or two major cracks. A picture of the Beam 2 is shown in Figure 4.32, in which the surface spalling, multiple cracking and interface cracking are present. The corresponding $F - \delta$ curve is very similar to the ones derived in monolithic beams, as provided in Figure 4.33.

It is noted that the cracks at front and back do not always follow the same track or propagate at the same pace, as in homogeneous materials. Quite often, the crack tip on one side appeared at 20mm up. The one on the opposite side only just initiated. Or perhaps the phenomenon of multi-cracking was more pronounced on one side than the other. Or the interface crack appeared at the front but not at the back side as in Beam 2. Apart of any possible systematic errors in the setup, such as misalignment of the load cell, the rational explanation is considered to be the heterogeneity of concrete. The fibre/aggregate distribution, the surface roughening of OPCC substrate, the voids introduced during casting and compaction could all lead to local defect or obstacles for cracks to deviate. It is a highly complex process. Hence it will only be presented as approximation.

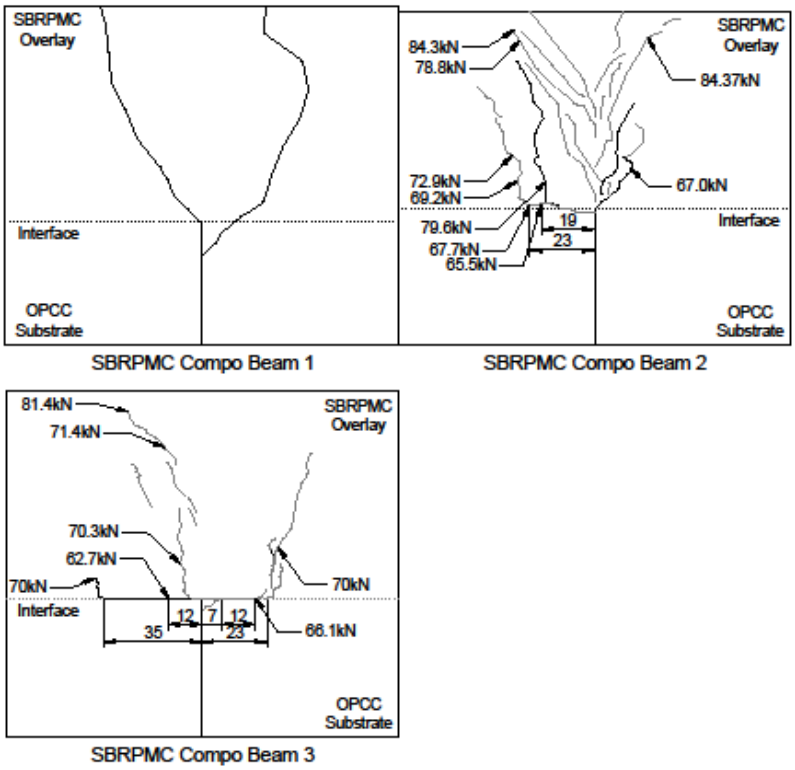

Figure 4.31 SBRPMC Compo Beam Crack Trajectory

Figure 4.32 Failure Cracks in SBRPMC Compo. Beam 2

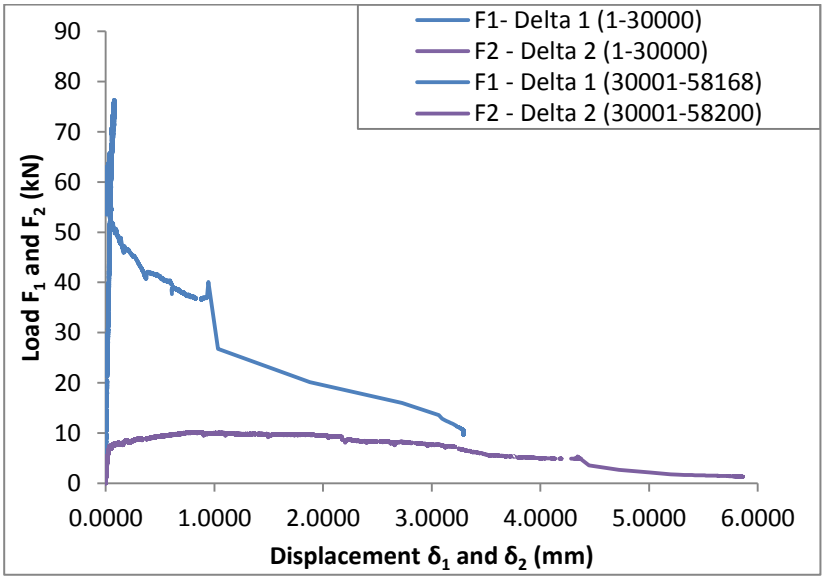

Figure 4.33 Load – Displacement Curve (F-δ) of SBRPMC Compo. Beam 2

4.4.2 PVAPMC Composite Beams with Full Notch

The PVAPMC material contains the same amount of steel fibre but with a different type of polymer, with more viscous behaviour. Only one interface crack was observed in PVAPMC compo beam 2, as shown in Figure 4.34. This complies with the results from interfacial bond tests, the testing procedures of which are as described in Chapter 4.3. The roughened SBRPMC-OPCC interface developed a splitting strength of 2.7MPa when tested in a block splitting test and a direct shear bond strength of 4.29MPa in a cylinder direct shear bond test. The roughened PVAPMC-OPCC interface achieved 4.53MPa and 4.83MPa respectively. It was found that the bonding strength of PVAPMC-OPCC interface is considerably higher than SBRPMC-OPCC interface.

However, with the same addition of steel fibre in PVAPMC, however, this group of specimens did not experience the same multi-cracking scenario. Generally, a single dominant crack propagated from the notch tip to the top roller. Despite a similar peak load achieved in PVAPMC, the latter seemed more brittle than the SBRPMC. In Hillerborg's fictitious crack model (1976), a characteristic length l_c is defined as per Eqn. 4.4. It is a material property proportional to the length of the fracture process zone. The larger the value, the more ductile the material becomes.

$$l_c = \frac{EG_f}{{\sigma_p}^2} \tag{4.9}$$

Where E is the young's modulus of concrete, G_f and σ_p are the fracture toughness and strength derived from uniaxial tensile tests. The corresponding values from the three point bending tests from a parallel study (Lin 2013) are employed for these two materials, as in Table 4.14. A much smaller l_c is derived in PVAPMC, which dictates a smaller fracture process zone and more brittleness. This correlates well with the experimental findings. An example of the corresponding F – δ curve of PVAPMC Compo Beam 3 is provided in Figure 4.36.

Table 4.14 Modified Characteristic Length

	l_c (mm)	Young's Modulus E (GPa)	Fracture Toughness in Mode I G_{fI} (N/mm)	Splitting Tensile Stren. σ_p (MPa)
PVAPMC	4215	37.357	15.71	11.8
SBRPMC	7994	32.355	18.53	8.66

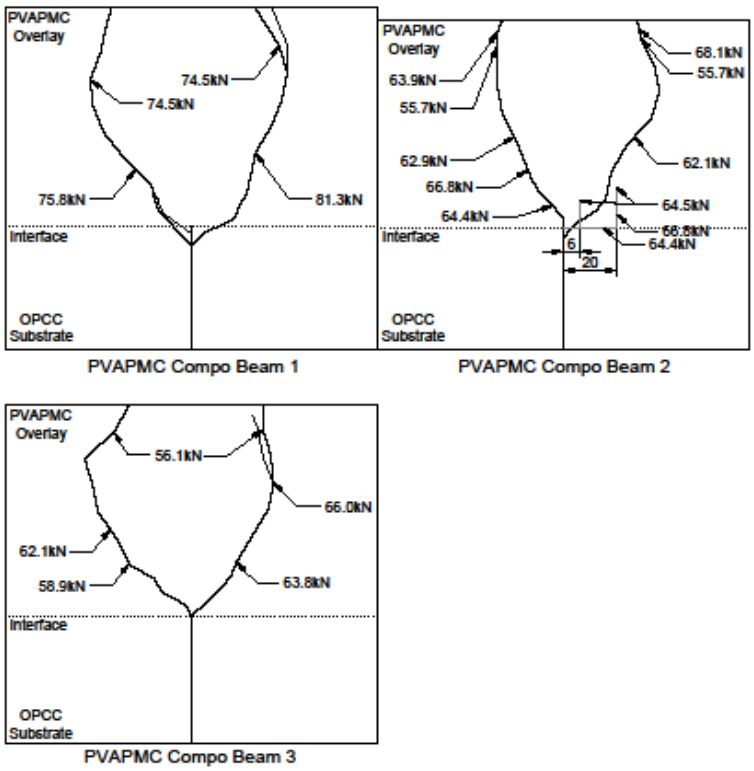

Figure 4.34 PVAPMC Compo Beam Crack Trajectory and Load

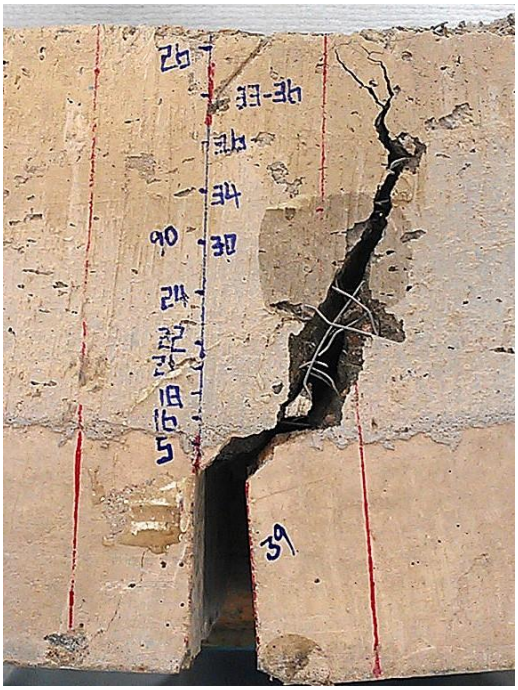

Figure 4.35 Failure Cracks in PVAPMC Compo. Beam 1

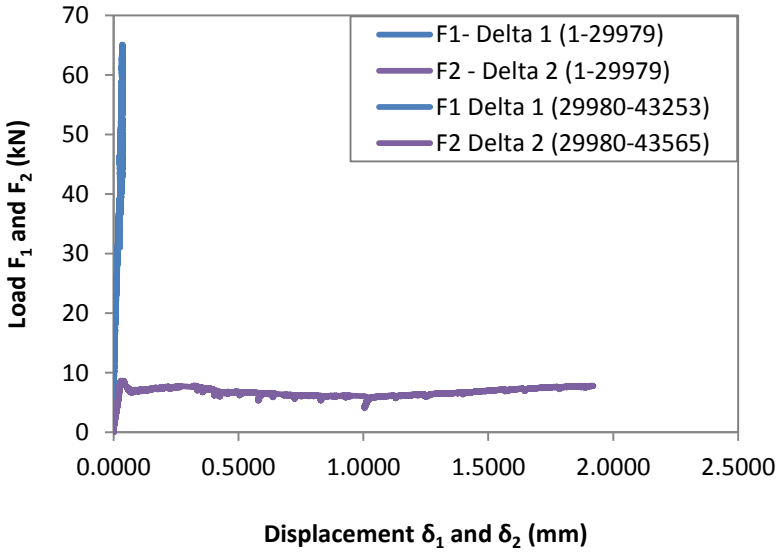

Figure 4.36 Load – Displacement Curve (F-δ) of PVAPMC Compo. Beam 3

4.4.3 SBRPMC Composite Beams with 30mm Notch

A pavement investigation is usually conducted prior to overlay construction. Actions are likely to be taken against any notable cracks appearing on the surface. Hence, this group of beams were prepared with 30mm notch in the substrate to investigate the propagation of

underlying crack under shear loading condition. The crack trajectories are plotted in Figure 4.37. A picture of the failed beam specimen is given in Figure 4.38.

The crack appeared at the notch tip in the OPCC substrate and rapidly developed into the overlay without any visible interface cracking. Usually the crack reached the overlay material at the controlled displacement (δ_2) of approx. 0.15mm, whilst the total displacement of $\delta 2$ is approx. 7-8mm, as shown in Figure 4.39. It can be seen that considerably more energy was required for the crack to propagate through the overlay section, which consisted with the findings in monolithic beams. In other words, it is proved that the overlay in the composite system acted as an effective crack arresting mechanism and potentially delayed appearance of the surface crack and crack propagation under shear loading condition.

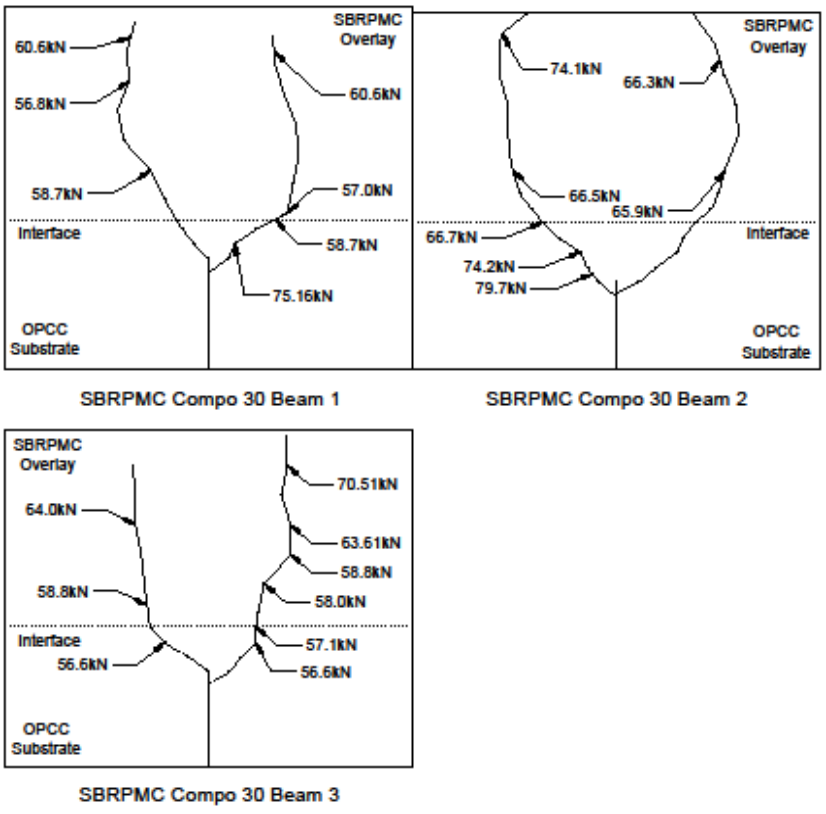

Figure 4.37 SBRPMC Compo 30 Beam Crack Trajectory and Load

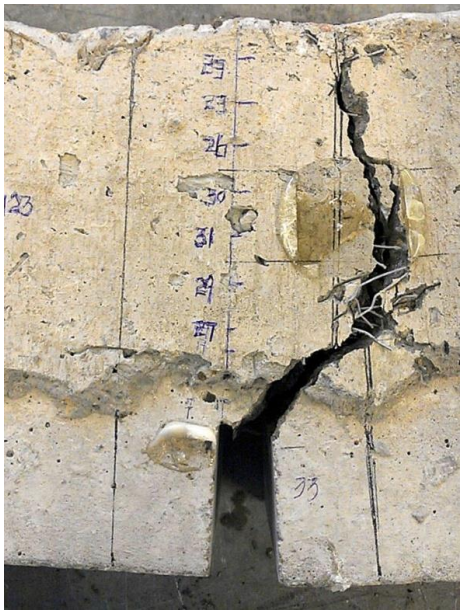

Figure 4.38 Failure Cracks in PVAPMC Compo. 30 Beam 1

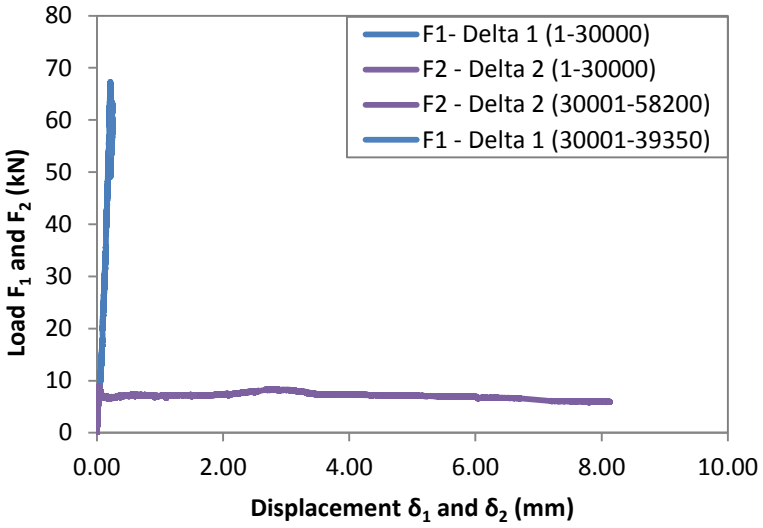

Figure 4.39 Load – Displacement Curve (F-δ) of SBRPMC Compo. 30 Beam 1

4.4.4 Crack Resistance

Table 4.15 Composite Beam Crack Resistance Parameters

Beam Specimens	Ave. Onset Load F_{CR} (kN)	Ave. Onset Shear Stren. (MPa)	Standard Deviation (MPa)	Ave. K_{II} ($kN \cdot m^{-3/2}$)	Ave. Shear Stren. (MPa)	Standard Deviation (MPa)

Beam Specimens	Ave. Onset Load F_{CR} (kN)	Ave. Onset Shear Stren. (MPa)	Standard Deviation (MPa)	Ave. K_{II} ($kN \cdot m^{-3/2}$)	Ave. Shear Stren. (MPa)	Standard Deviation (MPa)
SBRPMC Compo	47.5	6.25	0.91	4016	8.06	1.61
SBRPMC Compo 30	45.7	5.26	0.82	4318	7.21	0.53
PVAPMC Compo	50.6	6.00	0.41	4410	7.01	0.03

The onset cracking parameters and the average shear strengths are listed in Table 4.15. Comparing with the shear strength of OPCC, SBRPMC and PVAPMC as reported in 4.3.2-4.3.3, it is found that the onset shear strength and the ultimate shear strength in SBRPMC Compo 30 beams are all considerably higher than the corresponding values in OPCC. It is understood that the overlay reinforced the underlying substrate and significantly improved the overall shear resistance. The shear strength levels in the other two groups of composite beams resembled their performance in monolithic beam tests, despite the appearance of interfacial cracks. The $K_{IIonset}$ values in OPCC, SBRPMC and PVAPMC derived in previous monolithic beams were 2624, 4437 and 4792 $kN \cdot m^{-3/2}$, respectively. The equivalent K_{II} values at the onset loading in the composite beams were derived in the same way. Both the SBRPMC and PVAPMC composite beams reached slightly lower values than the corresponding $K_{IIonset}$. It abides the observation of interface cracks, for the fact that the interface is weaker than a monolithic material. However, the onset and ultimate shear strengths did not seem affected by the immediate crack development at the interface. Since the loading configuration was setup to introduce a high shear concentration to study the shear behaviour, it is possible the development of interfacial cracks was partially avoided. If the shear span to depth ratio increases, the phenomenon of interface delamination may dominate. If that is the case, the weighing factor of shear resistance in the failure mechanism may needs to be adjusted. As a result, more effort would need to be devoted to enhancing the interfacial bond. However, this would be outside the scope of the shear study and become a shear bond problem or flexural problem.

4.5 Foundation Test

The foundation test was set up to simulate the reflective cracking caused by rocking and pumping effects under shear loading near the weak supports, as illustrated in Figure 1.1. Some studies on asphalt overlays with underlying potholes and depressions are reported, but

limited literature on concrete overlays. The following test was conducted on composite beams to investigate crack initiation and opening under a static load up to 45kN.

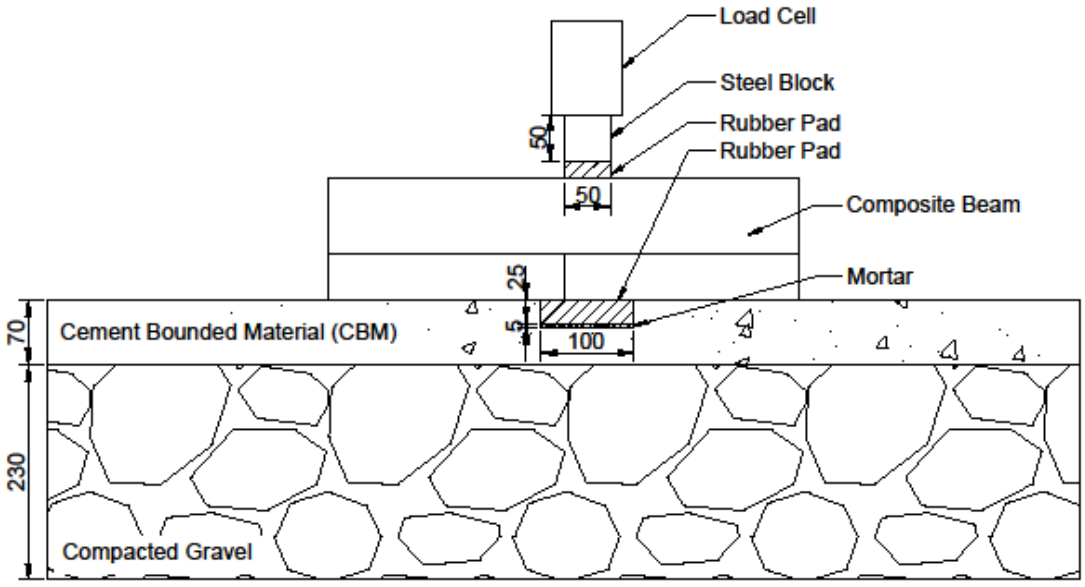

Figure 4.40 Foundation Test Setup

Figure 4.41 Foundation Preparation (a) Compacted Gravel (Left) (b) Cement Bound Material (CBM) Compacted with a Whacker Plate (Right)

A rectangular timber frame of 1100mm x 700mm x 300mm reinforced by angle steel bars on the outskirt was purposely made for the foundation test. It was placed on the strong-floor, inside-filled with the sub-base materials to act as the foundation. The sub-grade course of 230mm deep comprises compacted coarse aggregate of size 10 to 20mm and fine aggregate,

as shown in Figure 4.41. The 70mm sub-base course was cement bound mixture (CBM) of 10mm gritstone, sand, 4% cement mixed with a sprinkle of water, compacted by a wacker plate weighing 53kg, as shown in Figure 4.41. Water was splashed on the surface in the following 5 days for curing.

The plate loading test using a circular steel plate of 80mm diameter centrally positioned, prior to the foundation test showed that the resilient k-value was 10.182N/mm^3. The resilient modulus was calculated as 499.37MPa using the equation below, where γ is the poisson's ratio; b is the plate diameter; $\frac{\Delta p}{\Delta s}$ is the slope of applied pressure against plate settlement.

$$k_s = \frac{\Delta p}{\Delta s} \quad 4.10$$

$$E_{PLT} = \frac{\Delta p}{\Delta s} \times \frac{\pi b}{4}(1 - \gamma^2) \quad 4.11$$

As shown in Figure 4.42, a pothole of 100mm (length) x 110mm (width) x 30mm (depth) was excavated in the foundation. This was backfilled with 5mm of mortar and a piece of neoprene rubber (hardness: 70 Shore A) of the same size as the pothole, 25mm deep, to create a local deficiency, simulating the loss of support caused by pumping and rocking effect. The resilient modulus for the rubber foundation was calculated as 5.78MPa.

A uniform load of 50mm wide was applied on one side of the crack with a piece of rubber placed between the beam and the steel block (50mm x 50mm x 110mm) to ensure even load distribution, as illustrated in Figure 4.40. LVDTs 1 and 2 were placed on either side of the beam to measure the beam displacement Δ1 and Δ2 at the loading position. LVDT 3 was attached to the beam surface to measure the crack tip openning displacement (CTOD). The clip gauge was attached in the same way as in the single notch shear beam test to measure the crack mouth sliding displacement (CMSD). The arrangement of the test instrumentation is shown in Figure 4.43. Loading at the rate of 0.015 kN/s was conducted by the mobile "Si-Plan" data logging system connected to a 10 tonne jack.

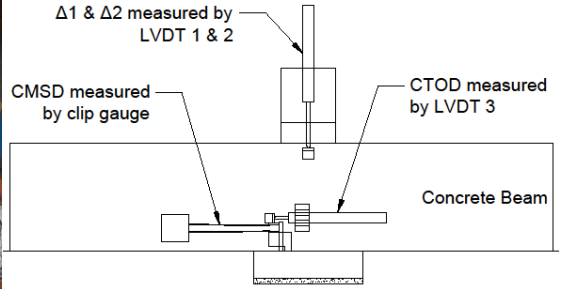

Figure 4.42 Local Deficiency in Foundation (Left)

Figure 4.43 Foundation Test Arrangement (Right)

4.5.1 Description of Failure Process

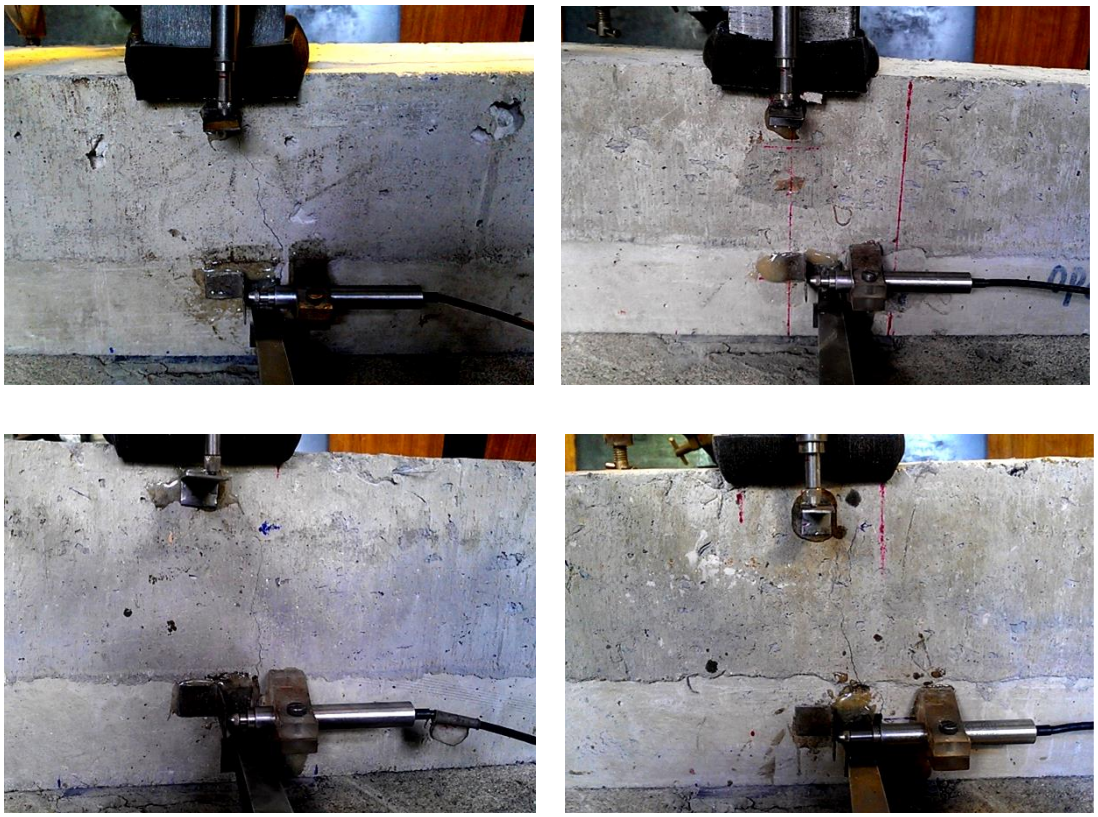

Figure 4.44 OPCC Composite Beam 1 (Top Left); SBRPMC Composite Beam 2 (Top Right); PVAPMC Composite Beam 1 (Bottom Left); SBRPMC Composite Beam 1 with 30mm Notch in Substrate

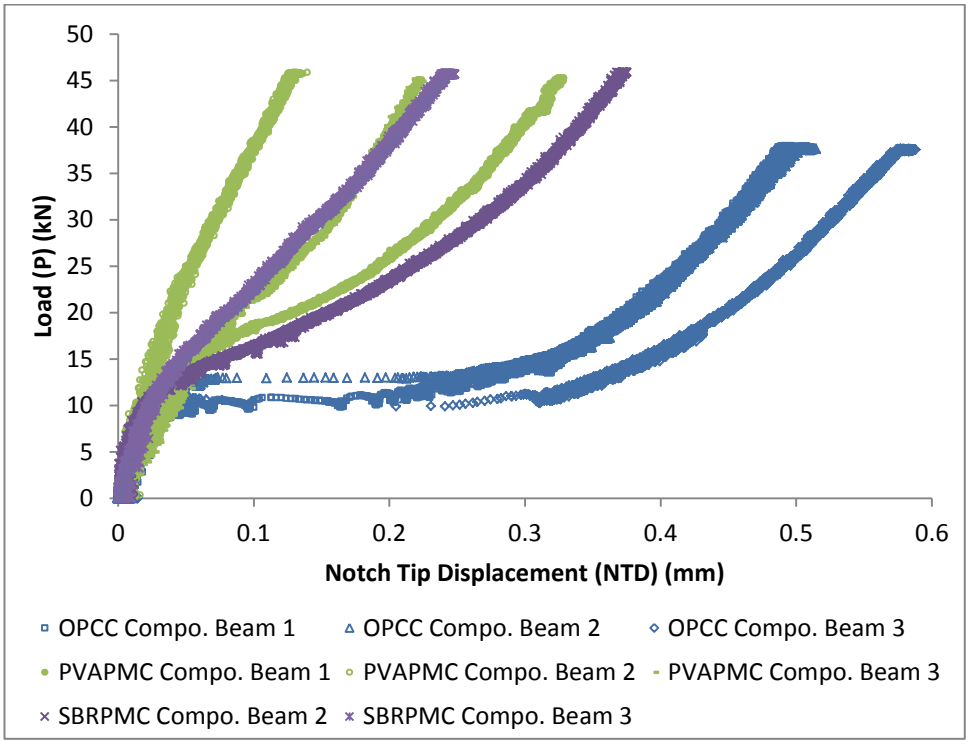

Figure 4.45 Load – Notch Tip Displacement (P-NTD) Diagram

Figure 4.45 shows the load-notch tip displacement relationship in fully notched OPCC/SBRPMC/PVAPMC composite beams. Crack initiation in OPCC composite beams took place at approx. 10kN, followed by a comparatively large notch tip displacement. The crack kept opening as load increased. On the contrary, the crack initiation in PVAPMC and SBRPMC composite beams was recorded at a much higher load, around 20kN. But an immediate enlargement of notch tip displacement was not noticed. It was concluded that the notch tip displacement was probably controlled by the fibre bridging in the overlay. Since it was loaded up to 45kN only, the peak load was not attained. However, hairline cracks propagated almost to the top. A load – crack position diagram plots the crack extension with the corresponding load, as in Figure 4.46. The crack tip position was measured from the notch tip. It can be seen that the red dots representing OPCC composite beams are concentrated on the top left corner. This implies the cracks appeared at the upper portion of the beam at a much lower load and accordingly the cracks reached the top surface at a lower load too. On the other hand, the cracks in SBRPMC and PVAPMC appeared at a higher load with an extension of as low as 10mm. Further extension of the crack required a higher load. Since the rig was setup to take a maximum load of 45kN, most of the cracks are only hairline crack, especially in the SBRPMC or PVAPMC overlaid beams, as presented in Figure 4.44.

The load was far from reaching the peak load. The test resembled the specimen behaviour in SNSBT and further affirmed that the overlay material managed to keep cracking under control. Nevertheless, the beam-on-foundation test is a closer simulation to the real scenario. Fatigue tests subjected to cyclic loading and large scale site trial are required for further verification in future studies.

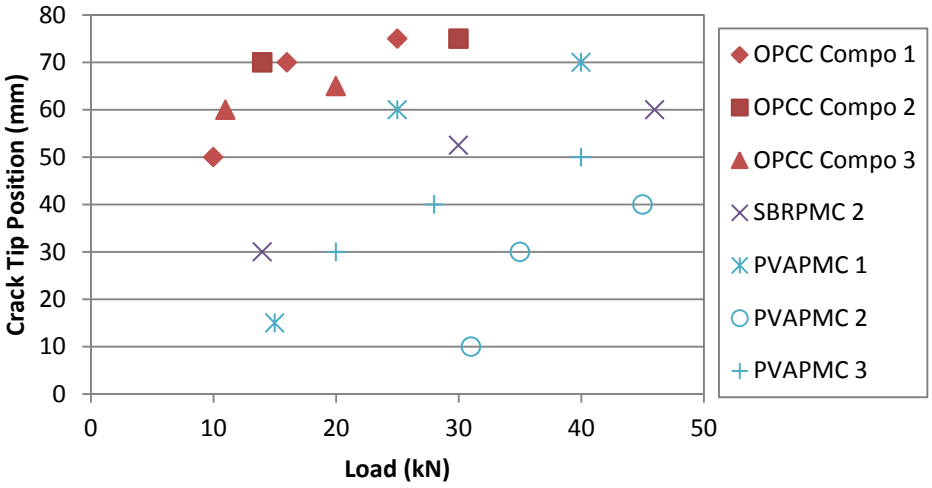

Figure 4.46 Load – Crack Tip Position

CHAPTER 5 EXPERIMENTAL RESULTS AND ANALYSIS

5. Experimental Results and Analysis

5.1 Introduction

This chapter analyses and discusses the strengths and fracture parameters obtained from laboratory tests.

Shear performance and resistance to cracking are generally evaluated by the level of shear strength and fracture parameters. It has been proved experimentally that SFRC has superior mechanical properties and resistance to reflective cracking over the common overlay material – OPCC. The following section investigates the relationship between shear strength of SFRC and steel fibre content. The mechanism is also discussed and semi-empirical models were established to predict the onset and ultimate shear strength.

The stress intensity factor (SIF) K is usually employed to describe the stress concentration level at a crack tip. Based on linear elastic fracture mechanics, the critical SIFs in mode I and mode II were determined in SNSBT. A mix-mode failure criterion was obtained and employed in the finite element modelling in the next chapter. The brittleness of the mixes was also assessed. The experimentally obtained relationship between crack displacement and the load level was analysed and adequate steel fibre content was determined.

5.2 Shear Strength Evaluation

5.2.1 First Crack Strength and Ultimate Shear Strength

The roller-compacted overlay material optimized by the M-L method described in Chapter 4 achieved a higher compressive strength than the conventional PMC or OPCC. This is presented in Table 4.6. Concluded from the three-point bending test (Lin 2013), the flexural strength follows the same trend. The high compressive and flexural strength of the optimized overlay material enables reduced thickness while strengthening the original pavement. However, it also raises some concerns regarding its shear performance due to the brittleness and relatively smooth fracture surface of high strength concrete. To mitigate the problem, steel fibre was introduced to the mix with the aim of enhancing shear resistance and ductility.

To assess the shear strength level of the mixes, the two basic parameters employed were the *Onset Shear Strength (OSS)* and the *Nominal Shear Strength (NSS)*. The OSS is deemed as the shear strength of the section when the first crack was observed. There was no visible crack before reaching the corresponding load. Hence, it is also quoted as "first crack strength". The nominal shear strength corresponds to the peak load in shear tests. Hence it is also referred to as "ultimate shear strength" or "shear strength" for short.

The averaged results from single notch shear beam tests (SNSBT) are summarized and interpreted below. As presented in

Table 5.1 and Figure 5.1, the nominal shear strengths of OPCC, plain conventional PMC and plain PMC, with no steel fibres, coincide with their onset shear strengths. In contrast, the difference between the onset shear strength and the nominal shear strength increases as the volume fraction of steel fibre increases, as plotted in

Table 5.1. The strain hardening effect was evident in the post crack stage. An even higher load can be achieved even after the appearance of crack.

Table 5.1 Designation

	Mix Designation ID
1	OPCC
2	Plain Conv. PMC
3	Plain PMC
4	Conv. PMC
5	PVAPMC
6	1%Vf PMC
7	SBRPMC
8	14Agg PMC
9	20Agg PMC
10	2%Vf PMC
11	LF PMC
12	3d PMC
13	7d PMC

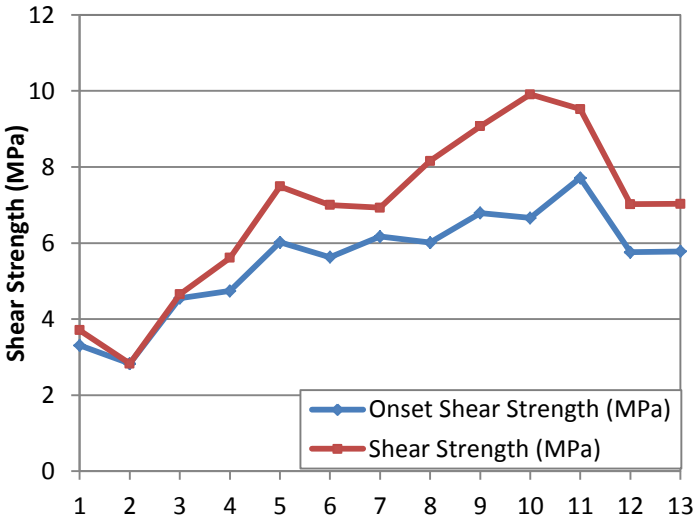

Figure 5.1 Shear Strength

5.2.2 Onset Shear Strength

Despite the employment of the maximum dry density principle in the mix design of SF-RC-PMC overlay, it does not eliminate the existence of microcracks and voids in the mix. As load increases, these defects coalesce and localize. Due to interfacial shear stresses, minor displacements occur at fibre-matrix interfaces, which also trigger the fibre bridging effect. Eventually a visible macro-crack can form from the coalescence of many microcracks. Subject to repetitive loading, the crack can propagate upwards until it reaches the surface. Then, the pavement deterioration speeds up due to water intrusion, constant repetitive traffic loading and temperature variance. It is then followed by the widening of the same crack and/or the appearance of more cracks.

The crack initiation is a very important status, which denotes the beginning of structural deterioration. Usually, it is considered that structural integrity is sustained before the first crack becomes visible. The SFRC may be regarded as normal concrete with enhanced mechanical properties. The addition of 2% steel fibre can enhance the onset shear resistance up to 1.7 times that of the plain concrete. Hence the effect of steel fibre on the onset shear resistance of SFRC cannot be neglected. It is worth noting that the ultimate shear strength of OPCC is 4.28MPa only. Considering the OPCC and SFRC of a similar size, a load which could cause complete failure in OPCC specimens, may not even crack a SFRC specimens with as little as 1% volume fraction of steel fibre.

In the past, there is hardly any investigation on the effect of steel fibre on onset crack development under shear action. It is always considered that steel fibre makes an indirect impact on nominal shear strength by enhancing flexural resistance. However, the above shows that the appearance of shear cracking can be effectively delayed by introducing steel fibre. It is evident that the onset shear strength increases linearly with the volume fraction of steel fibre up to 2%. Hence, based on the volume fraction of steel fibre (V_f) and the onset shear strength of unreinforced concrete (τ_{plain}), the following formula is proposed for onset shear strength (τ_{onset}).

$$\tau_{onset} = \tau_{plain} + C \cdot V_f \cdot DC \cdot \frac{l_f}{d_f} \cdot \frac{f_{tf}}{f_{tsf}} \cdot \frac{1}{S} \quad 5.1$$

$$S = 11.2\sqrt{\frac{b_f h_f}{(b_f + h_f)V_f l_f}} \quad 5.2$$

In Eqn. 5.1, C is the coefficient factor, which reflects the shape factor of steel fibre and the fibre-matrix interaction, such as the cohesion and the anchorage effect in the case of hook-end fibre. DC is the dispense coefficient based on the statistical analysis of number of fibres crossing a plane in the specimens in relation to its volume fraction, as listed in Table 5.2 and explained later in Section 5.2.3. l_f/d_f is steel fibre aspect ratio. l_f is fibre length. d_f is the equivalent fibre diameter. f_{tf}/f_{tsf} is the ratio of tensile strength of steel fibres compared to the short steel fibre, from which the coefficient factor C was derived. S is the spacing factor, the empirical formula of which was proposed by Swamy et al (1974) as in Eqn.5.2. It was stated that the parameter reflects not only the distance between centroids of steel fibres but also the fibre-matrix interaction and failure mode. b_f and h_f are fibre width and thickness respectively for rectangular steel fibres.

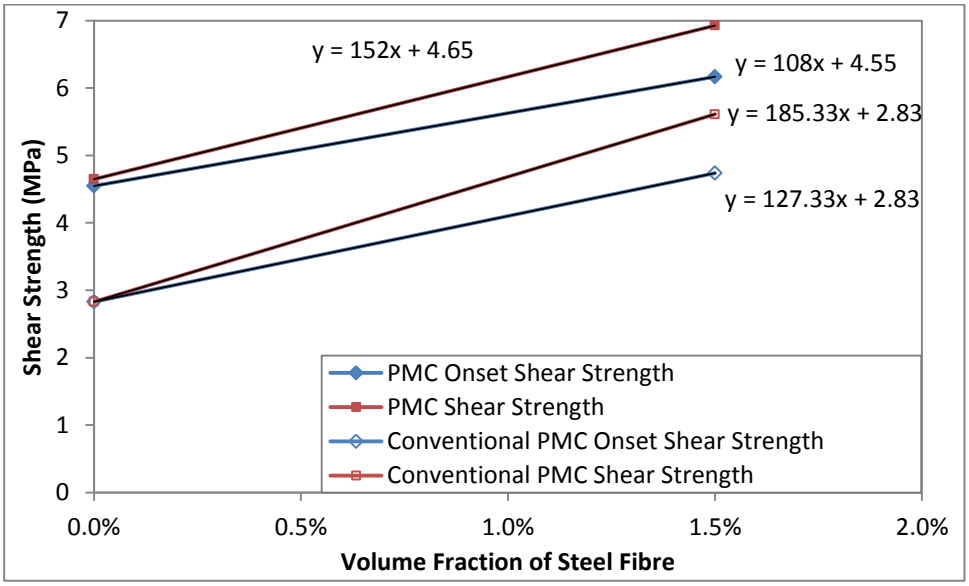

Figure 5.2 Shear Strength with Various Fibre Contents in Conv. PMC and SBRPMC

Based on SNSBT test results of plain PMC and SBRPMC with 1.5% steel fibre, the linear relation between the onset shear strength (y) and the volume fraction of steel fibre (x) is obtained, i.e. y=108x+4.55, as shown in Figure 5.2. The experimental onset shear strength for plain PMC (τ_{plain}) is 4.55MPa. The fibre used in this test was short fibre, as specified in Table 4.1. The aspect ratio is l_f/d_f = 35/0.59. Hence, the coefficient factor (C) is worked out as 17.19. Note the strengths are in MPa. Therefore the formula is re-written as Eqn. 5.3.

$$\tau_{onset} = \tau_{plain} + 17.19 \cdot V_f \cdot DC \cdot \frac{l_f}{d_f} \cdot \frac{f_t}{f_{tsf}} \cdot \frac{1}{S} \qquad 5.3$$

In terms of LF PMC, where long steel fibre is used, l/d = 50/0.62, V_f = 1.5%, $\frac{f_t}{f_{tsf}}$ = 1270/1050, S = 6.75 and τ_{plain}=4.55MPa. Substituting them in to the above, τ_{onset} is found to be 7.64MPa. The onset shear strength from experiments for LF PMC is 7.71MPa (error: 0.89%). The onset shear strengths for 1%V_f PMC and 2%V_f PMC were also calculated from the formula above and compared with experimental results as listed in the Table 5.2 and plotted in Figure 5.3.

Table 5.2 Predicted Onset Shear Strength of SFRC

	Spacing Factor (S)	Fibre Dispersion Coefficient (DC)	Analytical τ_{onset} (MPa)	Experimental τ_{onset} (MPa)	Percent Error
1%V_f PMC	9.60	0.81	5.41	5.63	-3.90%

	Spacing Factor (S)	Fibre Dispersion Coefficient (DC)	Analytical τ_{onset} (MPa)	Experimental τ_{onset} (MPa)	Percent Error
2% V_f PMC	6.79	0.72	6.71	6.66	0.80%
LF PMC	6.75	0.83	7.64	7.71	-0.89%
SBRPMC	7.84	0.83	6.17	6.17	0.00%
Conv. PMC	7.84	0.71	4.22	4.74	-11.06%

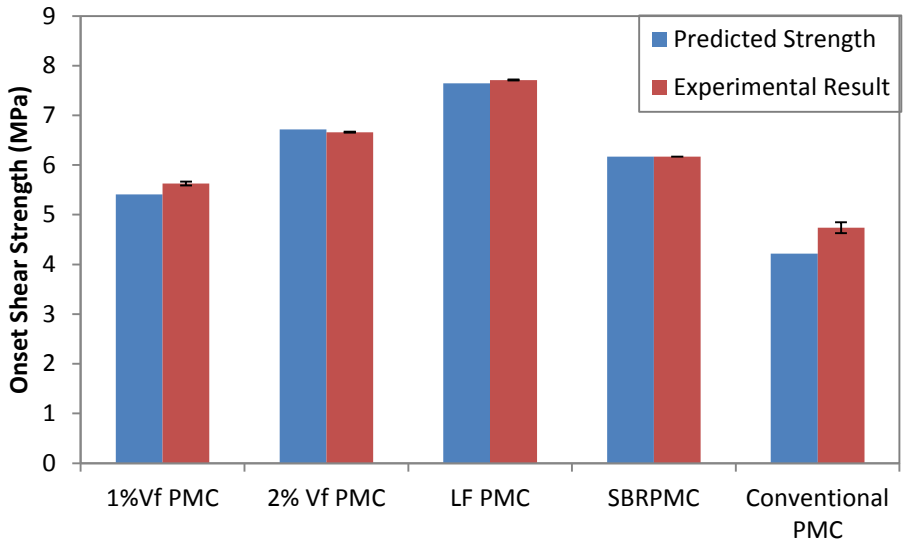

Figure 5.3 Comparison between Predicted and Experimental τ_{onset}

In comparing the predicted and experimental τ_{onset} values, it is found that they are reasonably close. Hence, Eqn.5.3 can predict the onset shear strength in SFR-RC-PMC to a reasonable accuracy, based on the onset shear strength of plain concrete and the mechanical properties of the steel fibre introduced. The above mixes are roller compacted concrete with relatively low water/cement ratio determined by the M-L method described in chapter 4.

In addition, the conventional PMC comprising the same amount of steel fibre as SBRPMC (i.e. 1.5%), but with higher water/cement ratio of 0.36 and slump of 180mm, was also cast to investigate the effect of high w/c ratio environment on fibre efficiency, and indirect impact on shear resistance. It is found that the first crack appeared at a lower load in plain conventional PMC than that in plain PMC. This was probably due to the relatively-low-strength cementitious matrix. The plain conventional PMC presented the onset shear strength of 2.83 MPa, whilst the reinforced conventional PMC reached 4.74 MPa, as plotted in Figure 5.3. If the coefficient factor C of 17.19 derived from SF-RC-PMC is applied on conventional

PMC, the predicted onset shear strength is calculated as 4.22 MPa. As previously mentioned, the coefficient factor reflects the properties of fibre-matrix interaction. In conventional PMC, the matrix is not as strong as in RC-PMC. Hence, the anchorage at the extreme of hooked-end fibre can be less efficient. However, a good bond/cohesion between fibre and matrix is expected, compared to SF-RC-PMC, due to sufficiently moisturized interface. As generally acknowledged, the appearance of crack in SFRC is triggered by slippage at fibre-matrix interface. In other words, the onset shear strength is largely affected by fibre-matrix cohesive performance. Despite the fact the matrix being weaker than RC-PMC, the bond at fibre-matrix interface in conventional PMC seems to be stronger. Hence, it is reasonable to assume the coefficient factor C in conventional PMC is actually higher than the value of 19.74 in RCC. This explains why the predicted onset shear strength in conventional PMC is relatively conservative. This further affirms that Eqn. 5.3 can predict the onset shear strength with reasonable accuracy in SF-RC-PMC. In conventional concrete, the value predicted using the Eqn.5.3 provides a safe lower boundary. Therefore, the effect of steel fibre on resistance to crack initiation can be correctly evaluated based on the plain concrete and the volume fraction of steel fibre. The same form may be adopted to develop a more rigorous formula with additional experimental tests conducted.

5.2.3 Quantitative Assessment of Steel Fibre Distribution

As abovementioned, the evaluation of the onset shear strength took into consideration the dispense coefficients (DC) of steel fibres, which was statistically derived as detailed below. To study and examine the fibre distribution at cross sections of cylindrical samples and beam specimens, the specimens were saw-cut at a cross-section parallel to the loading direction after tests and the number of steel fibres was counted. The surface was damped and divided into grids for ease of counting, as pictured in Figure 5.5. The steel fibres used were hooked-end, with a rectangular cross section of 0.45mm by 0.6mm, equivalent to 0.586mm in diameter, a tensile strength of 1050MPa and an aspect ratio of 60, as detailed in Section 4.2.1.

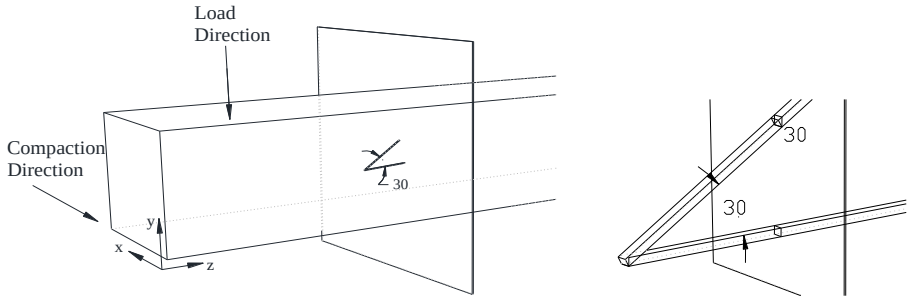

Figure 5.4 (a) Fibre Orientation (b) Fibre Cross Sectional Image on xy Cutting Plane

The cross sectional area varies, generally 80-100 by 100mm. The equivalent number of steel fibres was calculated based on a unit area of $100 \times 100\ mm$ cross section, namely N_{f100}. Assessment of the dispense coefficient (DC) was conducted using the relationship below.

$$DC = A_{fa} \div (V_f \times A) \qquad 5.4$$

Where A_{fa} is the actual area of steel fibres at a cross sectional plane parallel to the direction of the load; V_f is the volume fraction of steel fibre; A is the area of a cross section parallel to the load direction. As the actual number of steel fibres was converted to N_{f100}, A_{fa} is the individual steel fibre area at the cutting plane multiply by N_{f100} and $A = 100 \times 100 = 10000mm^2$. The cross-sectional area of an individual steel fibre is $0.45 \times 0.6 \approx 0.27$ mm^2. However, the fibres were dispensed randomly. In other words, the fibres were not necessarily perpendicular to the cutting plane. So A_{fa} depends on the orientation of each fibre. A study on steel fibre reinforced roller-compacted concrete (SFRCC) in Japan produced a statistical result on fibre orientation. (Kagaya et al. 2001) It reports that most fibres in FRCC mixes subject to surface vibrating compaction were oriented between 0 and 30 degrees to the horizontal. "Only 2% to 8% of fibres were in the range of 76 to 90 degrees." The average angle between the horizontal and a fibre is 29-30 degrees. Hence an orientation of 30° was assumed. Therefore, $A_{fa} = 0.45 \times 0.6 \div \cos 30° \approx 0.31$ mm^2 (see Figure 5.4 (b)).

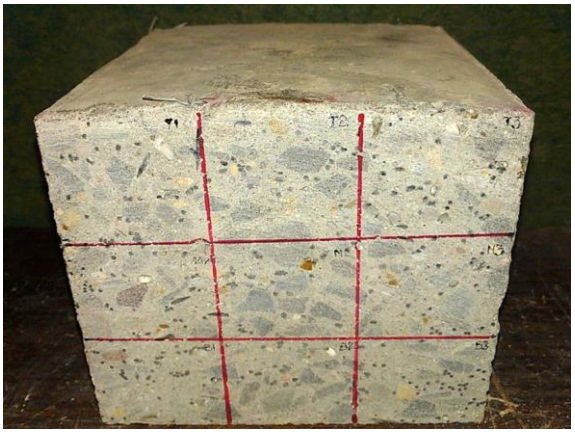

Figure 5.5 Steel Fibre in a PVAPMC Beam Cross Section

Table 5.3 Dispersion Coefficient

Beam Specimens	Vf (%)	No. of Samples	Ave. Equ. No. of SF per 100x100mm^2	Dispersion Coefficient
1%V_f PMC	1	14	260	0.81
SBRPMC	1.5	22	399	0.83
PVAPMC	1.5	4	403	0.84
2%V_f PMC	2	6	463	0.72
Conv. PMC	1.5	7	340	0.71
14Agg PMC	1.5	3	360	0.75
20Agg PMC	1.5	3	458	0.95
Cylinder Specimens	Vf (%)	No. of Samples	Ave. Equ. No. of SF per 100x100mm^2	Dispersion Coefficient
SBRPMC	1.5	3	186	0.67
20Agg PMC	1.5	3	230	0.83

Table 5.3 discloses that the dispersion coefficient ranges from 0.7 to 0.95. The cylinder specimens present slightly less DC than that in the corresponding beam specimens with the same mix. Due to surface compaction, the fibre orientation is likely to be horizontal. (Kagaya et al. 2001) For example, when the compaction takes place in x-direction, the fibres tend to be orientated in the plane of y-z, as illustrated in Figure 5.4 (a). In beam specimens, the critical plane subject to shear load was the x-y plane, whilst the critical plane subject to direct shear in cylinder specimens was the y-z plane. This explains the slightly lower values of N_{f100} and DC in cylinder specimens. Besides, all these fibre distribution appears to be uniform and not affected by the location of lift joints.

5.2.4 Nominal Shear Strength

The ultimate shear strength is derived from the peak load divided by the cross sectional area undergoing shear. This parameter reflects the material's nominal shear resistance in flexural shear condition. Hence, it is also referred to as nominal shear strength in some literature and here, in this study. (Leet and Bernal 1997)

Most of the current available shear design formulas are for conventional reinforced concrete, as detailed in Chapter 2. The following equation by Li et al (1992) was proposed for ultimate shear strength in fibre reinforced concrete beams with 2.5 or less shear span-to-depth ratio, derived through regression analysis. It was reported to have better accuracy than some other equations in the range, although longitudinal reinforcement was employed, reflected in the parameter of reinforcement ratio ρ. (Slater, Moni and Alam 2012)

$$f_c' = 9.16\left[\left(f_f\right)^{2/3}\rho^{1/3}(d/a)\right] \quad 5.5$$

To predict shear strength of steel fibre reinforced concrete beams, Slater et al (2012) derived the linear and non-linear regress equations experimentally based on a large database of 222 beams. For shear span-depth ratio of less than 3 and high concrete strength of above 50MPa, the following equation was specified.

$$v_u = 1 + \frac{9}{100}f_c' - 7.4 \times 10^{-4} f_c' \frac{l_f}{d_f} + 2V_f \frac{l_f}{d_f} \quad 5.6$$

It was found that it produced the closest results to the shear strength derived in the SNSBT among other established equations for SFRC in the state-of-art literature. Figure 5.6 presents the comparison results. Errors are relatively small, apart from the 2%V_f PMC and LF PMC, which implies it may need adjustment for high ductile SFRC with high fibre content or large fibre aspect ratio.

Most of the established formulas contain the parameter of reinforcement ratio ρ. Although Slater's model was an exception, it was based on experimental results from concrete without stirrups but with longitudinal reinforcement. Whereas in the application of roller-compacted concrete pavement overlay, longitudinal reinforcement is intentionally avoided for reasons discussed earlier. In other words, the overlay material herein was reinforced solely by steel fibre.

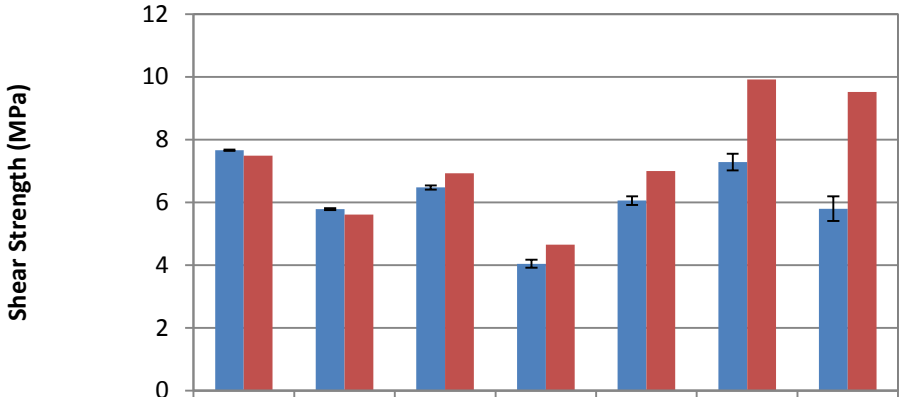

	PVAPMC	Conv. PMC	SBRPMC	Plain PMC	1%Vf PMC	2%Vf PMC	LF PMC
Slater (2012)	7.66	5.79	6.47	4.04	6.05	7.28	5.80
Experimental	7.49	5.61	6.93	4.65	7.00	9.91	9.52

Figure 5.6 Comparison between Slater's Model (2012) and Experimental Results

Furthermore, the existing shear design formulas for reinforced concrete are based on empirical studies and regression analysis. A number of researchers have developed semi-empirical formulae based on fracture mechanics for reinforced concrete beams. (Gastebled and May, 2001; Xu, Reinhardt and Zhang 2005, Nguyen-Minh and Rovnak 2011) However, an effective analytical model for fibre reinforced concrete is not available to date, due to the complexity in cracking trajectory and failure modes in FRC.

It may be noted that fibre reinforced concrete presents a very different strain hardening and softening behaviour from conventional concrete. Depending on the mechanical properties of fibre and the fibre-matrix interaction, the strain softening and hardening curve can vary considerably. This can be explained by the Voo and Foster's diagram as in Figure 5.7. (2003) Tension softening happens in unreinforced concrete following crack opening. In contrast, with the addition of a minor amount of fibre, the fibre bridging effect enables the loss of load-carrying capability at a reduced rate, as presented in the Figure 5.7(a). If the fibre bridging effect is enhanced due to increased fibre content, favourable fibre properties and/or effective fibre-matrix bond, the strain hardening may occur prior to the final softening section, as demonstrated in Figure 5.7(b). If a substantial fibre bridging effect is present, e.g. in SBRPMC specimens, the ultimate stress may be achieved even after the crack opens.

Thius image has been removed

Figure 5.7 Voo & Foster's Model (2003)

Only until recently, Gastebled and May's analytical model (2001) for flexural shear in conventionally reinforced concrete moved a step forward. Soon it was adopted and developed further by Xu and Reinhardt (2005) on reinforced concrete without stirrups. Nguyen-Minh and Rovnak (2011) also adapted the idea for reinforced concrete with steel fibre as shear reinforcement. The principle is that the flexural-shear failure is triggered by the splitting crack at reinforcement level. The fundamental basis of linear elastic fracture mechanism, as presented in Eqn. 5.7, was employed – "the unit extra work produced by the extra moment to the unit rotation at the tip of diagonal shear crack is equal to the fracture energy that is necessary to extend the unit unbonded length of longitudinal reinforcement." (Xu and Reinhardt 2005)

$$\delta G = \frac{1}{2}\delta W_{ext} \qquad 5.7$$

In single notch shear beam test, the crack initiated in shear loading condition followed by increasing involvement of bending moment. The crack development was the "end product" of the combined shear force and bending moment. The ultimate shear strength is governed by flexural-shear. Most of the equations established for conventional reinforced concrete are based on empirical research and lack of theoretical backup. It was attempted to find an analytical solution to nominal shear strength in SFRC based on its constitutive law on crack

bridging behaviour, which can be easily attained from three point bending test or uniaxial tensile test. To simplify the problem, the following assumptions were made:

- The crack development is caused by the combined work from shear force and bending moment. The work produced by shear force (F_s) to the sliding displacement (CSD), summed up with moment to the rotation at the crack tip, is equal to the crack bridging effort provided by steel fibre on the curved cracking plane.

- Compared to the fibre bridging effort, the cohesion between the two crack surfaces bonded by mortar can be omitted. Usually, a minor crack opening is required before fibre becomes fully engaged. However, this pre-engagement displacement was not detected in the currently developed crack bridging law (CBL). It implies that steel fibre reacted to provide resistance simultaneously with initial crack opening.

- It is considered that steel fibre does not work the same way as a traditional reinforcement. The energy required to bend a steel fibre is very small and can be neglected. (Voo and Foster 2003) Hence in this study it is assumed that steel fibres cannot provide dowel resistance. The contribution of steel fibre directly comes from its pull-out resistance, which keeps crack closed and provides flexural and tensile resistance. In other words, the shear resistance provided by steel fibre is indirect and can be quantifiable by its crack bridging law (CBL) based on flexural test results. The CBL derived in three point beam bending test on SBRPMC specimens in a parallel study (Lin 2013) is illustrated in Figure 5.8. The maximum stress of 5.5MPa was attained at the crack opening of 0.31mm followed by a descending curve as the crack further opened up.

- The distribution and orientation of steel fibre in the mix is uniform in the compaction plane y-z, as demonstrated in Figure 5.4(a). Hence the fibre bridging law is applicable either in the case of a vertical crack in three point bending test, or in the case of a curved crack in SNSBT.

- Fibre reinforced concrete generally failed with multiple cracks. To simplify the problem, a dominant crack was assumed, the crack trajectory of which was based on the experimental results, as presented in Figure 4.24 and Table 4.13.

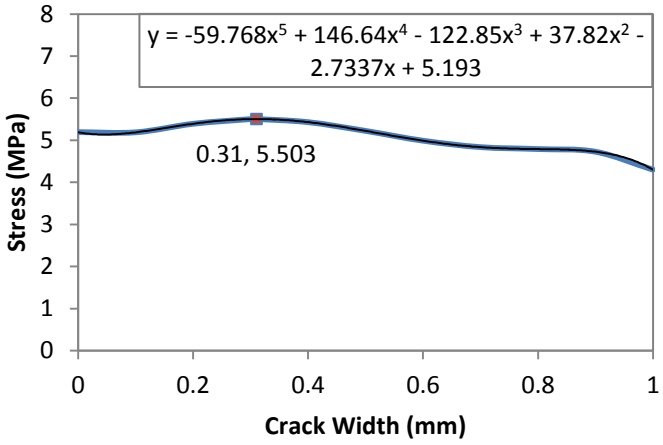

Figure 5.8 Crack Bridging Law in SBRPMC

- Size effect in fibre reinforced concrete has been studied in the manner of flexural tension. It was discovered that Bazant's size effect law, commonly applicable in ordinary concrete, is considerably relaxed in fibre reinforced concrete. Fibre length, fibre-matrix bond properties and fibre volume are considered more influential in the resulting flexural resistance. (Li, Lin and Matsumoto 1998) The proposed ideal overlay thickness is relatively thin, in the range of 100-150mm. Hence, size effect of shear strength in FRC may be inconspicuous.

- The overlay is more susceptible to shear failure when there is a weak support in the underlying sub-base, as intuitively sketched in Figure 1.1. The maximum bending stress occurs when traffic is right above the crack; whilst the shear stress occurs when the wheel load locates just before or after the underlying crack. It can be shown that the shear span-to-depth (a/d) ratio is relatively small. Thus, the experimental tests were setup with small a/d ratio accordingly.

Shear strength increases with fibre content. So does flexural strength from a standard three point bending test (Lin 2013) and prism splitting tensile strength, as presented in Figure 5.9. Nevertheless, compressive strength does not always follow the same tendency. Despite the increase of 20% in the compressive strength with 1% of steel fibre in the mix, further addition of steel fibre did not seem to affect the compressive strength very much. This has also been stated by previous researchers. (Li 1992, Li, Ward and Hamza 1992) This is partially attributed to the fibre orientation with regards to the surface compaction direction.

As illustrated in the previous section, if the compaction was applied in x-direction, the fibres are more likely to locate parallel to plane y-z. So when the compressive load was applied in y-direction, there could be insufficient fibre bridging parallel to x-y plane. Hence the compressive strength could be compromised. (Beaudoin 1990, Li 1992) Hence, the direct relationship between compressive strength and shear strength, as in some of the established literature (Ashour, Hasanain and Wafa 1992, Khaloo and Kim 1997, Kwak et al. 2002, Narayanan and Darwish 1988), is not adopted.

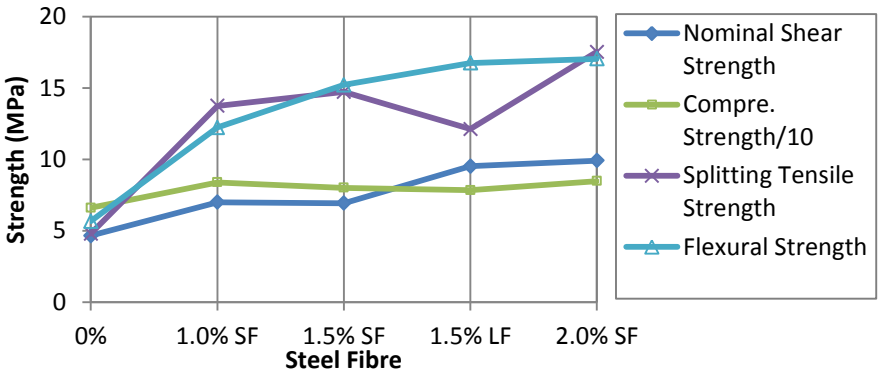

Figure 5.9 Steel Fibre vs. Concrete Strengths

As above-mentioned, the CBL derived from three point bending test was up to 1mm, it was further extended linearly as shown in Figure 5.10. It appears that the stress reduces to zero when the crack opening was approx. 2mm. This is very close to the notch tip displacement (NTD) of 2.1mm at the peak load in SNSBT. It can be interpreted from the figure below that a crack opening beyond 2mm corresponds to zero stress condition. This explains why the total fibre resistance could not increase further when the NTD reached 2.1mm. Hence, the CBL is divided into three segments:

when $w \leq 1\text{mm}$, $\sigma(w) = -59.768w^5 + 146.64w^4 - 122.85w^3 + 37.82w^2 - 2.7337w + 5.193$;

when $1\text{mm} < w < 2\text{mm}$, $\sigma(w) = -4.2602w + 8.5615$;

when $w \geq 2\text{mm}$, $\sigma(w) = 0$.

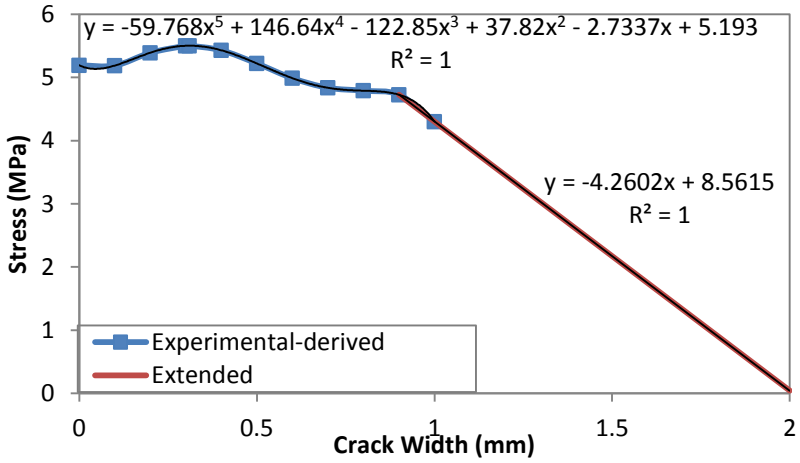

Figure 5.10 Fibre Bridging Law in SBRPMC

As presented in Figure 5.11, a representative dominant crack was plotted in a SNSBT setup. Based on the principle that the final result of crack extension is caused by the combined work from shear force and bending moment, Eqn. 5.8 is proposed, where F_s is the maximum shear force; F is the peak load applied, F= $\frac{196}{150}F_s$; CSD is the crack sliding displacement, measured by clip gauge; F_2 and a_2 are as shown in Figure 5.11, $F_2 = \frac{23}{196}F = \frac{23}{150}F_s$, a_2 ≈150mm; θ is the rotation angle; NTD_p is the notch tip displacement at the peak load; fibre bridging law is as described above; b is beam breath; CT is the length of dominant crack trajectory as listed in Table 4.13; d_c is the remaining ligament depth at the peak load.

$$F_s \cdot CSD + F_2 \cdot a_2 \cdot \theta = \int_0^{NTD_p} \sigma(w)dw \cdot b \cdot (CT - d_c) \qquad 5.8$$

The following parameters were derived from experiments of SBRPMC beams in SNSBT: CSD = 0.43mm; NTD_p = 2.1mm; (CT-d_c) = 72mm; $F_s = \tau_{ult} \cdot b \cdot 73$; $\theta \approx 2° = 0.035$. If the above are substituted in Eqn. 5.8, the following is reached.

$$(0.43 + 23 \times 0.035)\tau_{ult} \times 73 = (5.1 + 4.3) \times 72$$

$$\therefore \tau_{ult} = 7.5\text{MPa} \qquad 5.9$$

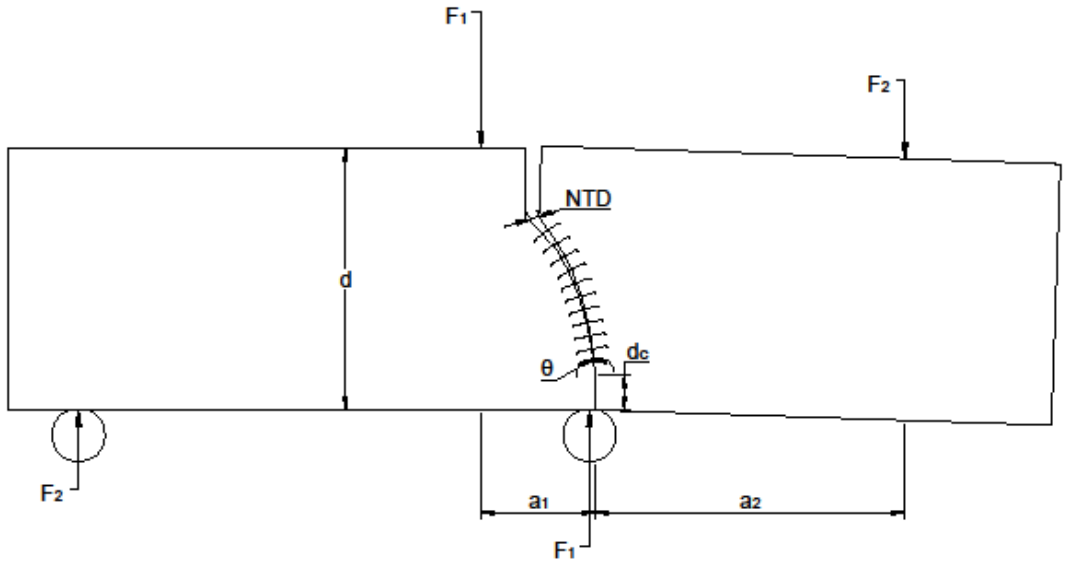

Figure 5.11 Crack Bridging in SNSBT

The averaged nominal shear strength in SBRPMC is 6.93MPa with the standard deviation of 0.54MPa. The predicted shear strength reached a fair proximity to the experimental result, located at the upper boundary. The above model, hence, produced a satisfactory result on this type of beams. So far the CBL was only obtained in SBRPMC beams from the parallel study (Lin 2013), additional verification can be conducted once further data become available.

The current CBL is an experimentally-derived relationship between tensile stress and crack width. Voo and Foster (2003) integrated the behaviour of a single fibre randomly orientated and distributed in a 3D space and proposed a variable engagement model, the general form of which is shown in Eqn.5.10. It was defined in terms of fibre aspect ratio α_f, volume fraction V_f, mean shear stress between fibre and matrix τ_b, fibre length l_f and material parameter α. Two scenarios were considered – with and without fibre fracture. However, this model failed to produce a matching result to the experimental results in three point bending test. Hence, it was not adopted. In the future, extra effort may be devoted to setup a

CBL of the similar form, thereafter the shear strength can be re-written in terms of the relevant parameters. A broad range of application may become possible.

$$\sigma(w) = f(\alpha_f, V_f, \tau_b, l_f, \alpha, w, etc) \qquad 5.10$$

The contribution of aggregate size is reflected through the length of crack trajectory (CT) in this model. As demonstrated in Figure 5.12, the larger the coarse aggregate size, the longer the crack length and the higher the shear strength. The red line in Figure 5.12 shows the curved crack length measured from the experiment. As predicted, the larger the aggregate size, the more the curvature involved.

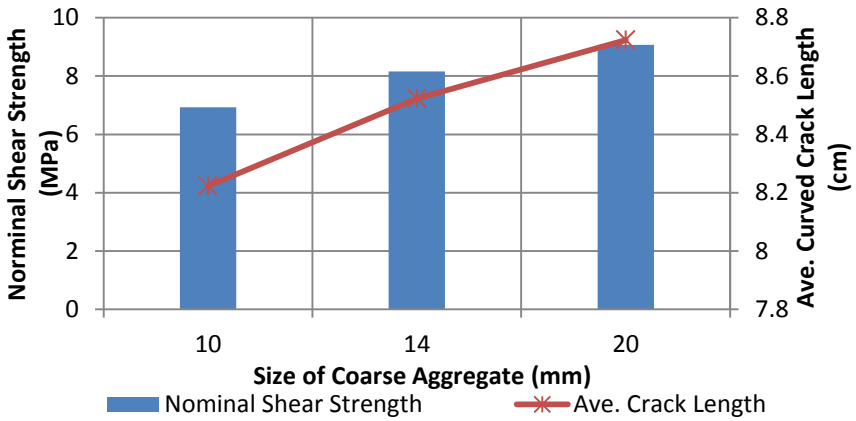

Figure 5.12 Effect of Coarse Aggregate on Shear Strength

5.2.5 Strength Development

Rigid pavements and their associated repairs suffer a serious drawback compared to their flexible counterparts. They take long time to develop suitable strengths. Hence, any early age concrete strength gain has an appreciable benefit on cost savings and less traffic disruption. Tests were carried out on PMC specimens with the same mix design incorporating 1.5% steel fibre on the 3rd, 7th and 28th day after casting, to assess its early age strength. The 3-day test beams were cured in water for one day followed by curing in ambient environment for one day before testing, while the other two groups were cured in the usual way detailed in Section 4.7. Conventional concrete overlay usually requires 7 days to cure. Depicted in Figure 5.13, the 3-day test PMC beams developed 77% of their 28-day compressive strength, 100% of their 28-day shear strength, 95% of their 28-day flexural strength and 81% of their 28-day splitting tensile strength. In addition, the 3-day onset shear strength recorded also

achieved 93.4% of the corresponding strength at 28-day. The 3-day onset shear strength (5.76 MPa) is much higher than the ultimate strength of the 28-day OPCC strength (3.71 MPa) and at a similar level as the 28-day conventional PMC strength of 5.61MPa, indicating the advantage of quick strength-gain of RCC.

Figure 5.13 Relationship between Curing Duration and Concrete Strengths

The overlay material presents the feature of rapid strength gain. Subject to further field test verification, results from the current stage suggest that it is possible to hand over the overlaid pavement to traffic the 3rd day after placing, although partial traffic control restrictions such as reduced speed limit may be required.

The bond between overlay and the substrate material was characterized by block splitting test, as described in Section 4.3. The bond also becomes stronger as material ageing. Figure 5.14 plots the block splitting tensile strength for roughened OPCC-OPCC, SBRPMC-OPCC and PVAPMC-OPCC interfaces at different ages. The strength continues to increase after 28 days but at a slower pace.

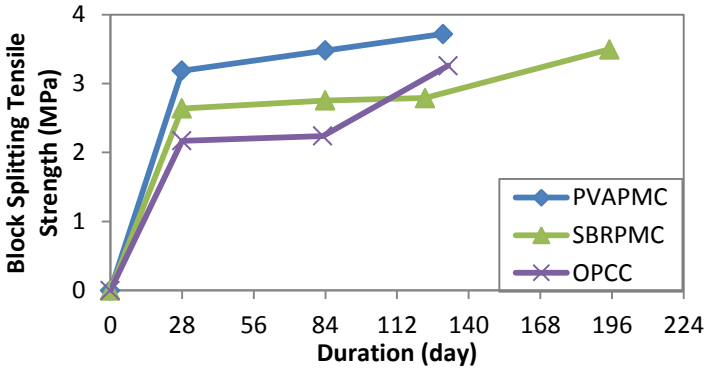

Figure 5.14 Block Splitting Test at Different Ages

5.3 Fracture Parameters

5.3.1 Fracture Energy

The shear performance of SFRC cannot be described explicitly by shear strength. The presence of fibre enables the ductile behaviour and comparably large capacity for energy absorption. Hence the parameter of fracture energy was obtained from the load-deflection curves and compared in Figure 5.30 and discussed below.

The load-deflection curves from SNSBT are plotted in Figure 5.15 for three groups of PMC – plain PMC, SBRPMC with 1.5% volume fraction of SF and 2%V_f PMC. The load F1 and the corresponding displacement δ1 are plotted in the same figure as the load F2 and the corresponding displacement δ2. As demonstrated in Chapter 5, load F1 is approx. 7.5 times larger than load F2. Hence, the F1 – δ1 relations are represented by the tall and steep curves. The shallow and smooth curves represent F2 – δ2 relations. It is seen from above that SFRC reached higher peak load than the plain PMC. The higher the content of steel fibre, the higher the peak load reached. Moreover, in plain PMC, the load dropped straight after the peak load; the cracking and the peak load occurred almost simultaneously. Whilst in SBRPMC the load continued to increase to the peak load after cracking, and fluctuated within a range of similar load level before decreasing. In the post-peak section, 2%V_f PMC beams allowed for large deformation while continuing to sustain certain load.

5.3.2 Stress Intensity Factor

Under repetitive traffic loading, a crack in the underlying substrate may reflect upwards and become a reflective crack in the overlay, when the crack tip stress exceeds a certain critical value. The stress intensity factor K defines the stress amplitude at the crack tip. Hence, the following criteria for crack development were documented in textbooks.

$$K_I > K_{IC} \quad , \quad K_{II} > K_{IIC} \quad , \quad K_{III} > K_{IIIC} \tag{5.11}$$

In terms of reflective cracking under shear loads, it generally involves mode I opening and mode II shearing. The mode III tearing is more complex with out-of-plane actions compared to the in-plane actions in mode I and II, but it is considered to be less influential than the other two modes. Hence, it is not taken into account in the current study. And the term "mix mode", herein, refers to a combination of mode I and II.

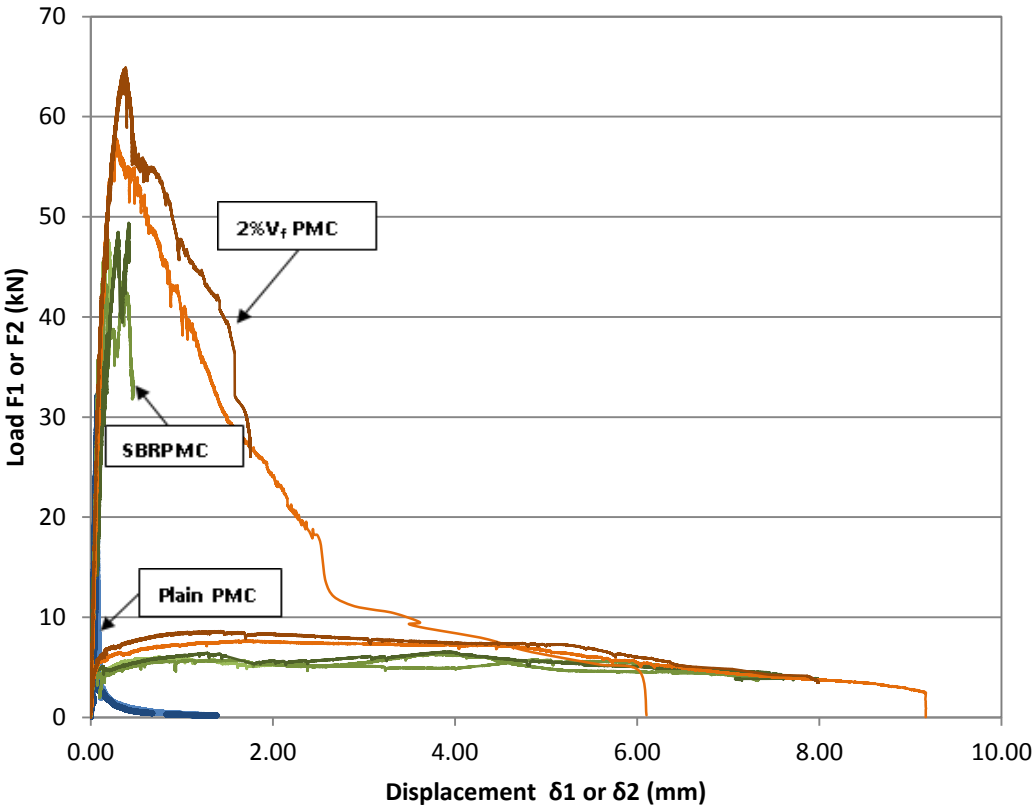

Figure 5.15 Load – Deflection Curve of FRCC and Plain PMC

Based on Linear Elastic Fracture Mechanics (LEFM), for plane stress, stress intensity factor can be obtained from Eqn.5.12. The experimentally derived elastic moduli E of SBRPMC, PVAPMC and OPCC were presented in section 3.8. The corresponding K can then be

calculated. It is regarded as a mix-mode stress intensity factor. Swartz et al (1988) once assumed Eqn. 5.13, that the mix-mode critical stress intensity factor K_C is the vector sum of K_{IC}, K_{IIC}. And the K_{IIC} was derived the same way as $K_{IIonset}$ in this experiment, as listed in Eqn.4.3. Should the above become valid, the predicted K_{IC} values can be calculated.

$$K = \sqrt{EG} \tag{5.12}$$

$$K_c^2 = K_{Ic}^2 + K_{IIc}^2 \tag{5.13}$$

Table 5.4 Stress Intensity Factors

	E_C (GPa)	G_C (kN/mm)	K_C (kN·m$^{-3/2}$)	$K_{IIonset}$ (kN·m$^{-3/2}$)	K_{IC}^a (kN·m$^{-3/2}$)	K_{IC}^a (N·mm$^{-3/2}$)
SBRPMC	32.365	0.00855	16635	5115	15829	500
PVAPMC	37.357	0.00377	11867	4792	10857	343
OPCC	25.195	0.00036	3012	2624	1478	47

As presented in chapter 5, K_C was derived from the energy release rate G_C and the Young's modulus E_C, using Eqn.5.12. Both parameters were available from the experiments. G_C is the total work applied on a beam divided by the area of fractured plane. E_C was obtained from the standard cylinder compression tests. K_{IIC} was the mode II SIF $K_{IIonset}$ at the onset of crack propagation, as obtained in SNSBT. The predicted K_{IC}^a values were calculated for OPCC, SBRPMC containing 1.5% volume fraction of steel fibre and PVAPMC containing 1.5% volume fraction of steel fibre. All are listed in Table 5.4.

A comparison is made between the following analytical values of K_{IC} and the experimentally derived K_{IC} in three point bending test. Three point bending tests were carried out in a parallel study on identical mixes: OPCC, SBRPMC and PVAPMC. (Lin 2013) The test configuration and geometries are provided in Figure 5.17 and Table 5.5. The experimental data were analyzed to work out the K_{IC}^e values in accordance with the procedure described in RILEM report using the equations below (Shah and Carpinteri 1991).

$$E = 6Sa_0V_1(\alpha)/(C_iW^2B) \tag{5.14}$$

$$E = 6S\underline{a}V_1(\alpha')/(C_uW^2B) \tag{5.15}$$

$$\alpha = a_0/W \tag{5.16}$$

$$\alpha' = \underline{a}/W \quad 5.17$$

$$V_1(\alpha) = 0.76 - 2.28\alpha + 3.87\alpha^2 - 2.04\alpha^3 + 0.66/(1-\alpha)^2 \quad 5.18$$

$$K_{IC}{}^{e} = \frac{3P_{max}S}{2BW^2}\sqrt{\pi \underline{a}}F(\alpha') \quad 5.19$$

$$F(\alpha') = \frac{1}{\sqrt{\pi}}\frac{1.99-\alpha'(1-\alpha')\left(2.15-3.93\alpha'+2.7{\alpha'}^2\right)}{(1+2\alpha')(1-\alpha')^{3/2}} \quad 5.20$$

Where S is span, 400mm in all beams; a_0 is notch depth; W is beam height; B is beam breath; as appeared in Figure 5.17. C_i is the initial linear compliance in the load-CMOD curve. A typical P-CMOD curve from beam SBRPMC 1 is provided in Figure 5.16 with the linear section in blue colour. The linear relationship of y=283.86x+0.239 was derived from a trendline estimation. Hence Ci = 1/284 = 0.0035. C_u is the compliance at the peak load. As the laboratory facility did not cater for a satisfactory controlled unloading, the C_u value was derived based on the peak load and the corresponding CMOD. An error is introduced due to omitting the inelastic CMOD at the peak load, which may result in a higher K_{IC} value than the ones calculated using the real unloading compliance. The thickness of knife edges at beam soffit was deducted in the derivation of CMOD. Eqn. 5.14 was applied to obtain the Young's modulus, which was later employed to back-calculate the effective critical crack length $\underline{a}$, according to Eqn. 5.15. The effective critical crack length $\underline{a}$ is equal to the sum of the original notch depth and the stable crack growth at peak load. This is used to obtain the critical stress intensity factor, as shown in Eqn. 5.19.

The mean value of $K_{IC}{}^{e}$ obtained from three identical OPCC beams was 1480 kN·m$^{-3/2}$, with only 0.1% error compared to $K_{IC}{}^{a}$. K_{IC} in similar mixes was reported to be in the range of 1475-1530 kN·m$^{-3/2}$ (Karihaloo 1995). Both $K_{IC}{}^{e}$ and $K_{IC}{}^{a}$ of OPCC are both very close to the reported values.

The parameters are listed in Table 5.5 for two SBRPMC beams with 20mm notch, three SBRPMC beams with 40mm notch and three PVAPMC beams with 20mm notch. The average E values derived from Eqn. 6.16 are 35.8GPa in SBRPMC and 29.5GPa in PVAPMC, compared to 32.4GPa in SBRPMC and 37.4GPa in PVAPMC from cylinder compression test, as presented in Chapter 4. The results in SBRPMC are reasonably consistent, although those of beams SBRPMC 3-6 with 40mm notch are more scattered. The

typical crack depth ratio α (notch depth/beam height) is no more than one-third. The notch depth of 40mm is more than one-third of the beam depth which may explain the more scattered results in beams SBRPMC 3-6 than in beams 1 and 2. The E value in PVAPMC appears less accurate though. It is mainly attributed to the fast rate of loading when testing PVAPMC beams and the brittleness of the material. The K_{IC}^{e} values from five SBRPMC beams and three PVAPMC beams are 15161 $kN{\cdot}m^{-3/2}$ and 8912 $kN{\cdot}m^{-3/2}$. The units in Table 5.5 are in mm, kN or GPa, except that K_{IC}^{e} is in $kN{\cdot}m^{-3/2}$. The analytical SIF K_{IC}^{a} of SBRPMC is 15829 $kN{\cdot}m^{-3/2}$ and that of PVAPMC is 10857 $kN{\cdot}m^{-3/2}$. The errors are 4.4% and 21.8%, respectively. The large error in PVAPMC is not satisfactory. As above-mentioned, the E values in PVAPMC are not convincing, due to fast loading rate in testing. The discrepancy was thought to have been caused by an error in E values. Hence, a more convincing E value from the standard cylinder compressive tests was employed instead in PVAPMC to obtain the effective critical crack length, and the consequent mode I SIF. The newly-obtained K_{IC}^{e} of the three specimens become 9770, 10069 and 11177, the mean value of which is 10339 $kN{\cdot}m^{-3/2}$. The error has now been reduced to 5.0%. The corrected parameters for PVAPMC are included in Table 5.6.

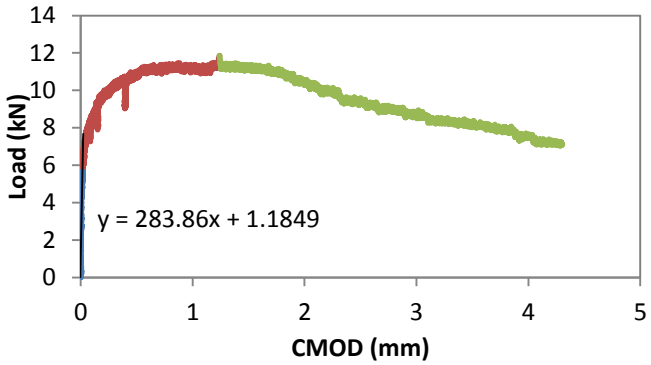

Figure 5.16 Load – CMOD Curve in Three Point Bending Test (SBRPMC Beam 1)

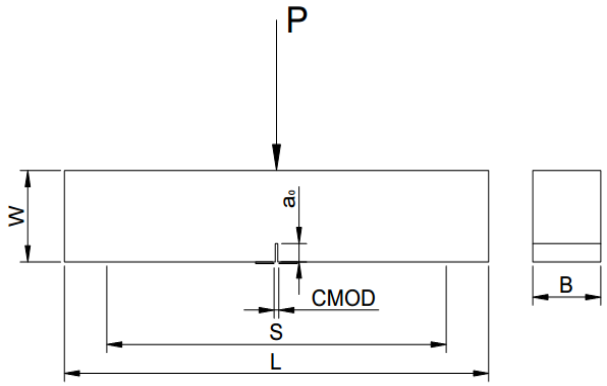

Figure 5.17 Three Point Bending Test Configuration and Geometry

Table 5.5 Experimental Mode I SIF K_{IC}^{e}

	a_0	W	α	B	C_i	E	P_{max}	CMOD	C_u	$\underline{a}$	α'	K_{IC}^{e}
SBRPMC1	23	99	0.2	73	0.004	34.0	11.9	1.240	0.105	76.6	0.778	19326
SBRPMC2	21	100	0.2	73	0.003	35.3	12.0	0.535	0.045	68.5	0.685	11264
SBRPMC3	40	100	0.4	71	0.006	44.6	7.0	0.779	0.110	80.7	0.807	14312
SBRPMC4	42	98	0.4	72	0.009	38.0	6.9	1.053	0.153	80.4	0.821	15865
SBRPMC5	44	101	0.4	69.5	0.013	26.9	6.1	1.480	0.242	83.7	0.829	15037
PVAPMC1	20	100	0.2	78	0.003	29.2	12.0	0.418	0.035	63.2	0.632	8364
PVAPMC2	20	100	0.2	76	0.003	30.2	14.8	0.382	0.026	58.7	0.587	8845
PVAPMC3	20	100	0.2	76	0.003	29.0	13.9	0.470	0.034	62.3	0.623	9525

Table 5.6 Corrected Mode I SIF K_{IC}^{e} for PVAPMC

	P_{max} (kN)	$CMOD_{max}$ (mm)	C_u (mm/kN)	$\underline{a}$(mm)	α' (mm)	K_{IC}^{e} ($kN{\cdot}m^{-3/2}$)	Ave. K_{IC}^{e} ($kN{\cdot}m^{-3/2}$)
PVAPMC1	12.0	0.4178	0.0347	66.75	0.6675	9770	10339
PVAPMC2	14.8	0.3823	0.0258	62.05	0.6205	10069	
PVAPMC3	13.9	0.4697	0.0339	66.05	0.6605	11177	

The errors in SBRPMC and PVAPMC are larger than that in OPCC. These may be due to the approximation made by omitting the inelastic CMOD prior to the peak load. FRC is known for its strain hardening behaviour. In other words, the FRC beams would have cracked before reaching their peak load. Obviously, the cracking is not reversible. It is beyond the elastic deformation. The mode I critical SIF K_{IC}, comparable with the experimentally derived K_{IC}^{e} following RILEM procedure, was obtained based on the mix mode equivalent SIF K and the onset K_{II} using Tada's estimation.

This affirms that the SNSBT is a mixed-mode configuration with the initial crack development dominated by mode II. As the crack propagated further from the notch tip, mode I took over and played a dominant role.

K_{IIC} in the PMC overlay material is increased by a factor of 1.8-1.95 compared to OPCC, implying a higher shearing resistance in PMC overlays. Moreover, K_{IC} in PMC overlay materials is 7.3-10.7 times larger than that in OPCC. It was proved during the foundation tests that the OPCC overlay system cracked at approx. 10kN whilst cracking in PMC overlay system was observed at a higher load, around 20kN. Furthermore, the cracking in PMC overlay system developed under a constantly increasing load and presented a much controlled manner than the OPCC. It was also dictated by the load – NTD diagram in Figure 4.46.

In Jenq and Shah's two parameter model (1988), another critical fracture parameter is the crack tip opening displacement ($CTOD_C$). Based on the RILEM procedure, it is calculated as follows: The parameters are defined the same way as in Eqn. 5.14-5.20. The $CTOD_C$ worked out for SBRPMC and PVAPMC are 0.60 and 0.31, respectively.

$$CTOD_C = \frac{6P_{max}Sa}{W^2BE} V_1(\alpha')[(1-\beta)^2 + (-1.149\alpha + 1.081)(\beta - \beta^2)]^{0.5} \quad 5.21$$

$$\beta = a_0/\underline{a} \quad 5.22$$

$$Q = \left(\frac{E \cdot CTOD_C}{K_{IC}^s}\right)^2 \quad 5.23$$

According to Jenq and Shah, once K_{IC} and $CTOD_C$ is available, some of the material properties can be obtained consequently, such as the material length Q, which is proportional to fracture process zone, indicating the material brittleness. The higher the value, the more ductile it is. It is calculated using Eqn. 5.23. SBRPMC achieved 1.87m whilst PVAPMC reached 1.29m. Usually the Q-value for concrete is between 150-350mm. It can be seen that the ductility in SFRC is enhanced four to five times than in normal concrete. PVAPMC is more brittle than SBRPMC, which corresponds well with the experimental results and indicated by the characteristic length l_c in Hillerborg's model in Section 4.4.2. (1976)

5.4 Cracking

The crack displacement was calculated based on the vector sum of crack sliding displacement (CSD) and crack mouth opening displacement (CMOD). The exaggerated diagram is shown in Figure 4.19. Due to the presence of coarse aggregate/steel fibre at the crack front, CMOD or CSD may be larger or smaller than the other. Hence the concept of notch tip displacement (NTD) is introduced to characterize the generalized crack displacement. The load – NTD diagrams are plotted in Figure 5.18 for plain PMC, SBRPMC with 1.5% and 2% steel fibre by volume fraction. It can be seen that the maximum load increases as the volume of steel fibre increases. The same applies to the maximum crack displacement. The maximum NTD in plain PMC is approx. 1mm, while 1.5% fibre content increased it to approx. 8mm and 2% fibre further enhanced it to 14mm. When reaching the peak load in plain PMC, SBRPMC presented an initial load decrease. But the load picked up again and allowed for further NTD. This corresponds to Voo's (2003) summary in Figure 5.7. Nevertheless, the 2%V_f PMC did not present the similar load descending section. It is dictated that the large volume of steel fibre did not allow for the development of tension softening in the PMC matrix and presented the strain hardening section of the load.

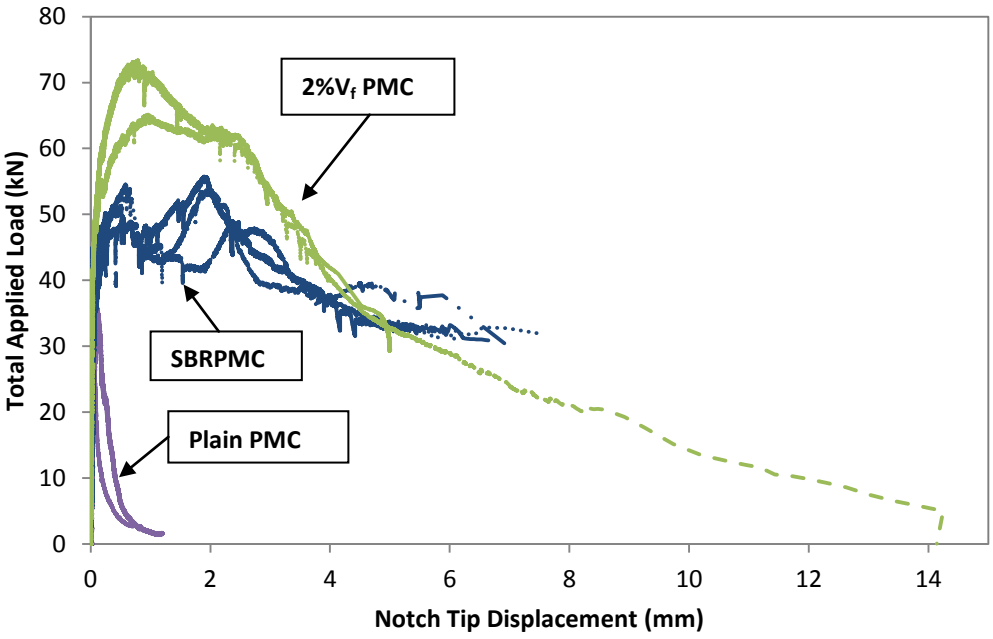

Figure 5.18 Load – Crack Displacement Diagram

The dominant crack propagation with the applied load was monitored manually during the tests. The results are plotted in Figure 5.19. The crack extension was measured from the notch tip in the vertical shear direction with the notch tip deemed as the zero-position. Beams dimensions are as indicated in Figure 4.13. The exact beam depths and notch depths were measured and used in the calculation. It is found that, in unreinforced specimens, e.g. OPCC and plain PMC, the load at onset cracking was very close to the peak load. As the crack is propagating in the shear direction, the load drops down rapidly. On the other hand, the load with 1% V_f PMC remained constant until the crack extended to approx. 45mm. At this point a smooth descending slope became evident. The load drop in SBRPMC with 1.5% V_f is barely noticeable in the figure. A comparable or even higher load was sustained after the crack propagated to as much as 64mm, which is 10mm to the surface. This suggests that the use of 1.5% steel fibre produced a satisfactory performance of resisting the same level of shear action even after cracking. As predicted, 2%V_f PMC with 2% of steel fibre required extra energy in the form of increased load to prolong the crack.

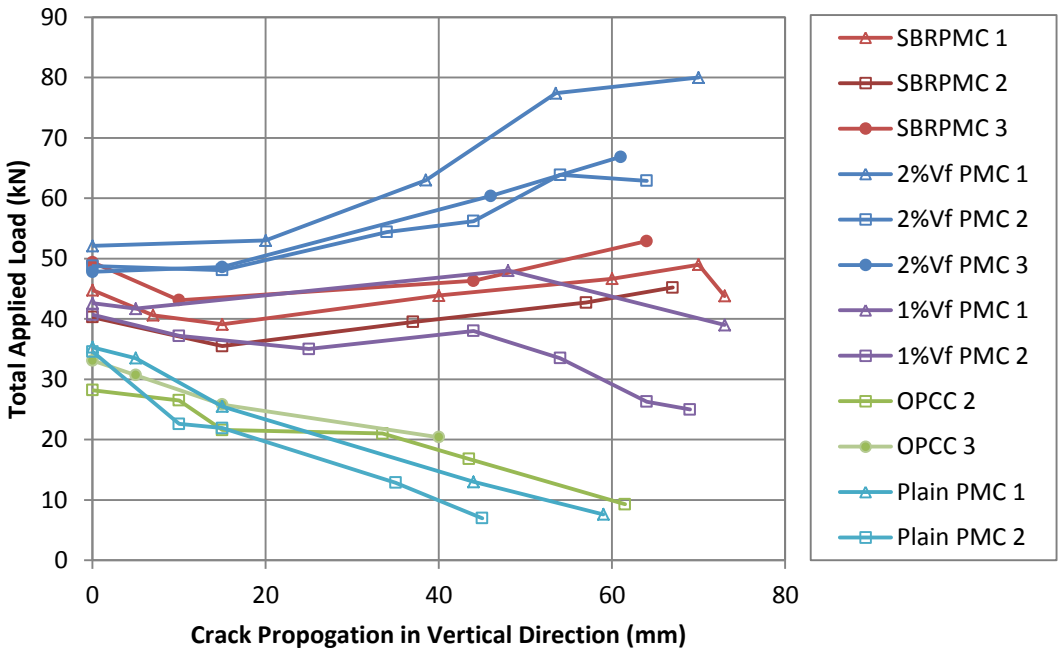

Figure 5.19 Crack Propagation in Vertical Direction

In plain PMCs, the crack initialization was recorded at 35kN, almost reaching the peak loads. At the time of observation, a hairline crack developed 5mm from the notch tip. In the load-NTD diagram, the initial linear path of the initial increase ends around 35kN as well.

Furthermore, in SBRPMC, 7-10 mm crack was noticed at approx. 40kN at the first strain softening section, while the linear path in the diagram finishes around 41kN. It can be seen that the end of the linear path always coincides with the onset crack loading. It was further proved by the path of 2%V_f PMC. The first cracks of approx. 5mm was noticed around 48.5kN in the initial load ascending section, while the linear path appeared to finish around 48kN in Figure 5.18.

Despite the fact that there is plenty of evidence proving that shear failure is brittle, here shear dilation is taking place by having steel fibre in the mix. In other words, all beams subjected to shear loading developed cracks in a mix mode (shearing and opening). These crack open as well as slide.

CHAPTER 6 FINITE ELEMENT ANALYSIS

AND COMPARISON

6. Finite Element Analysis and Comparison

6.1 Introduction

It is generally appreciated that dealing with concrete in the laboratory is hard work and time-consuming. With the aid of finite element modelling technique, it is possible to acquire the results instantly, or sometimes, within reasonable computing time. In the following chapter, the visualization of stress distribution of previously mentioned tests was facilitated using the finite element modelling software ANSYS v.14.0 (2013). Moreover, the impact of different parameters was investigated, which also point a direction for future improvement. The steel fibre reinforced concrete (SFRC) was modelled using the cohesive zone model (CZM), which tends to depict the enhancement to crack-resistance due to fibre bridging. Effort was also made to characterize the bond at the interfaces between overlays and substrate with the existing laboratory results. Employing the above CZM and coulomb law (ANSYS 2013) for the bond, the SNSBT and foundation test were simulated in ANSYS, the results of which presented a close resemblance. Furthermore, the calibrated models were applied to a typical pavement scenario. The overlay thickness and safe ligament thickness were discussed with various crack extensions in the OPCC overlay and SBRPMC overlay systems, which improved the understanding of the behaviour of the "green" overlay system under a typical shear loading condition and provided a valuable baseline for future studies.

6.2 Basis of Fracture Modelling in ANSYS

6.2.1 Three available fracture characterization methods

There are three methods available in ANSYS that could be utilized to evaluated fracture mechanics properties of materials.

Stress intensity factors K_I, K_{II}, K_{III} that correspond to three cracking modes: the opening, the shearing and the tearing modes. The stress-intensity factors can be calculated during (POST1) by the command KCALC.

Direct energy-release rates G_I, G_{II}, G_{III} calculation. The virtual crack-closure technique (VCCT) is based on the energy release rate theory by Hussain et al (1974). The basic

principle is that the energy needed to separate a surface is the same as the energy needed to close the same surface. It becomes available in ANSYS version 13. (ANSYS 2013)

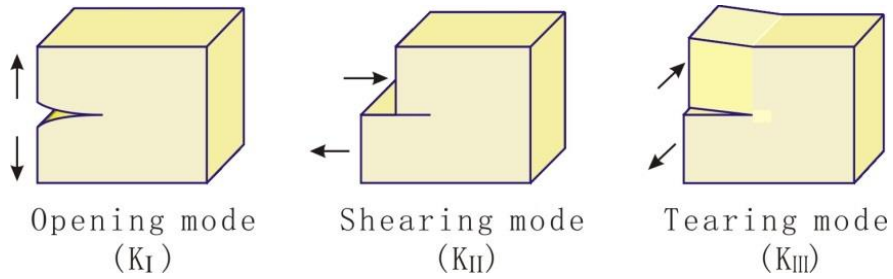

Figure 6.1 Basic Cracking Modes & Stress Intensity Factors

The J-Integral evaluation is based on the domain integral method by Shih (1986). Area and volume integrations are adopted and applied for 2D and 3D problems respectively. The method has good accuracy and is easy to use.

6.2.2 Simulation Process of Fractures by ANSYS

In general, a numerical analysis of a fracture problem includes the following steps: Firstly, a FE mesh with properly defined cracking zone is created in the pre-processor. It is followed by a standard linear elastic or nonlinear elastoplastic analysis. This is accomplished via the Solution module. Thirdly, fracture mechanics properties are calculated by some certain steps in postprocessing module.

Special attention is required for the crack tip region due to the local concentration of high stress gradients. In a 2D model, the tip of the crack is referred to as crack tip, while for a 3D model, the front edge of the crack is named crack front instead, as illustrated in Figure 6.2.

In order to capture the rapidly varying stress and deformation fields in the crack tip region, a refined mesh is necessary. For linear elastic analysis, the displacements near the crack tip (or crack front for 3D problem) vary as per $\sqrt{r}$ (r is the distance from the crack tip). The stresses and strains are singular at the crack tip, varying as $1/\sqrt{r}$. The elements around the crack tip should be quadratic, with the midside nodes placed at the quarter points. Such elements are named singular elements.

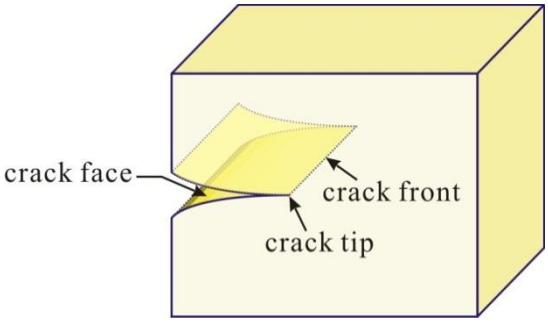

Figure 6.2 Schematic of a crack model

For a 2D fracture model, the 6-node triangular element type PLANE183 with two degrees of freedom (DOF) per node, supporting plasticity, large deflection and strain behaviour, is recommended in ANSYS after the version 13.0. This is defined by a quadratic shape function, considered to be well suited to model irregular meshes occurring at crack regions. All usual output is supported by the analysis, plus the displacement extrapolation method in calculating stress intensity factors. A "singularity" point was created at the crack tip with skewed nodes at quarter positions, using the KSCON command in the PREP7 pre-processor. It is particularly useful in a 2D fracture model, which automatically generates singular elements around the specified keypoint (crack tip). The KSCON command is not available for 3D modelling which makes the development of a 3D fracture model very complicated. In this thesis, all fracture modelling of our tests was performed in 2D analysis. For reasonable results, the first row of elements around the crack tip should have a radius of approximately a/8 or smaller, where a is the crack length. In the circumferential direction, roughly one element every 30 ° or 40 ° is recommended. (ANSYS 2013) A local coordinate system was setup at the crack tip with the X-axis aligned parallel to the crack face, as advised in the manual. However, the output for stress intensity factor was based on the global coordinate system, defaulting to K_I as the opening mode in relation to global X-axis. This is a "catch point" in the software. In the beam specimen orientation as plotted in Figure 6.4 where the crack face is parallel to the global Y-axis. The K_I values in the output file is in fact K_{II} and the output K_{II} should be K_I.

6.2.3 Cohesive Zone Models in ANSYS

Interface delamination can be modelled by traditional fracture mechanics methods such as the nodal release technique. (ANSYS 2013) Alternatively, techniques that directly introduce fracture mechanism by adopting softening relationships between tractions and the

separations, which in turn introduce a critical fracture energy that is also the energy required to break apart the interface surfaces. This technique is called the cohesive zone model (CZM). The interface surfaces of the materials can be represented by a special set of interface elements or contact elements. The CZM can be used to characterize the constitutive behaviour of the interface.

The CZM used with either interface elements or contact elements in ANSYS, is capable of simulating interfacial behaviours such as sticking, shearing and/or slipping, delamination, also known as debonding. The approach introduces a failure mechanism by gradually degrading the material elasticity between the surfaces. The material behaviour at the interface is characterized by the stresses (normal and tangential) and separation distances (normal gap and tangential sliding). Those three modes of cracking (separation) shown in Figure 6.3 can also be incorporated using the cohesive zone modelling technique.

As mentioned above, it can be implemented by the employment of either interface elements or bonded contact elements. The simulation of an entire assembly, consisting of the cohesive zone and the structural elements on either side of the cohesive zone, requires that the interface elements and structural elements have the same characteristics. In our study, the interface element, INTER205, was selected to model interfacial behaviour of composite beams which were modelled by SOLID65 elements. There are two built-in CZM in ANSYS for interface elements: the exponential form originally proposed by Xu and Needleman (1994), and the bilinear CZM proposed by Alfano and Crisfield (2001), as illustrated in Figure 6.3.

Debonding refers to separation of bonded contact. It is activated by associating CZM properties with contact elements using either the pure penalty method or augmented Lagrange method. (ANSYS, 2013)

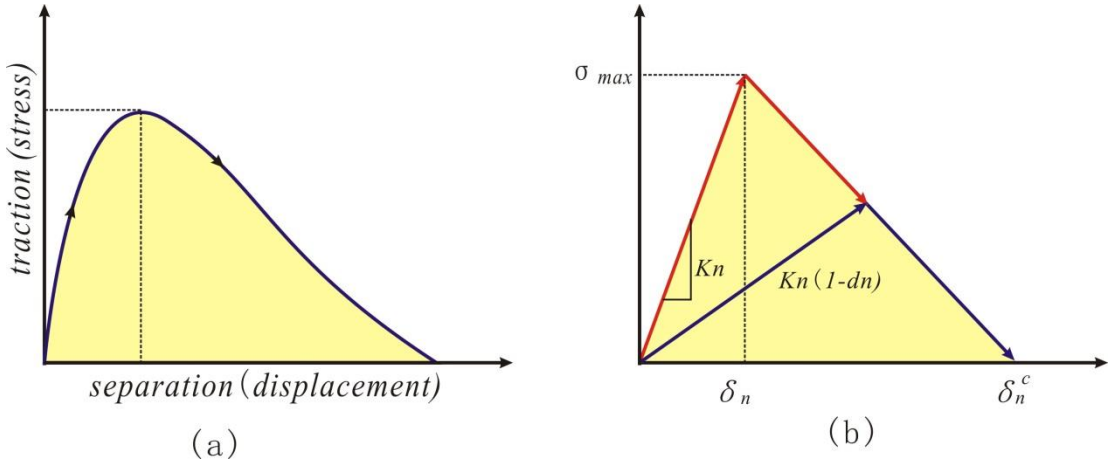

Figure 6.3 CZM Material Laws, (a) Exponential Form (b) Bilinear Criterion

The cohesive zone material model provided with bilinear behaviour (Alfano and Crisfield 2001) is defined as Eqn. 6.1.

$$\begin{cases} \sigma_n = K_n u_n (1-d) \\ \tau_1 = K_t u_1 (1-d) \\ \tau_2 = K_t u_2 (1-d) \end{cases} \tag{6.1}$$

where:

σ_n = normal contact stress (tension)

τ_1, τ_2 = tangential contact stresses in direction 1 and 2

Kn = normal contact stiffness

Kt = tangential contact stiffness

u_n = contact gap in normal direction

u_1, u_2= contact slip distances in direction 1 and 2

d = debonding parameter

direction 1 and direction 2 = principal directions in tangent plane

The debonding parameter is defined as Eqn. 6.2, with d=0 for $\Delta \le 1$ and $0 < d \le 1$ for $\Delta > 1$, Δ and χ are defined below.

$$d = \left(\frac{\Delta - 1}{\Delta} \right) \chi \tag{6.2}$$

Debonding allows three modes of separation: mode I, mode II and mixed mode.

Mode I debonding is defined by setting

$$\Delta = \Delta_n = \frac{u_n}{\bar{u}_n} \tag{6.3}$$

and

$$\chi = \chi_n = \left(\frac{u_n^c}{u_n^c - \bar{u}_n} \right) \tag{6.4}$$

where:

$\bar{u}_n$ =contact gap at the maximum normal contact traction (tension)

u_n^c =contact gap at the completion of debonding

Model II debonding is defined by setting

$$\Delta = \Delta_t = \frac{u_t}{\bar{u}_t} \tag{6.5}$$

$$u_t = \sqrt{u_1^2 + u_2^2} \tag{6.6}$$

$$\chi = \chi_n = \left(\frac{u_t^c}{u_t^c - \bar{u}_t} \right) \tag{6.7}$$

where

$\bar{u}_t$ =equivalent tangential slip distance at the maximum equivalent tangential stress, $\sqrt{\tau_1^2 + \tau_2^2}$

u_t^c =equivalent tangential slip distance at the completion of debonding

Mixed mode debonding is defined by setting

$$\Delta_m = \sqrt{\Delta_n^2 + \Delta_t^2} \tag{6.8}$$

$$\chi = \left(\frac{u_n^c}{u_n^c - \bar{u}_n} \right) = \left(\frac{u_t^c}{u_t^c - \bar{u}_t} \right) \tag{6.9}$$

The constraint on χ that the ratio of the contact gap distances be same as the ratio of tangential slip distances is enforced automatically by appropriately scaling the contact stiffness values. For mixed mode, debonding is complete when the following energy criterion is satisfied:

$$\left(\frac{G_n}{G_{cn}} \right) + \left(\frac{G_t}{G_{ct}} \right) = 1 \tag{6.10}$$

$$G_n = \int P du_n \quad 6.11$$

$$G_t = \int \sqrt{\tau_1^2 + \tau_2^2}\, du_t \quad 6.12$$

$$G_{cn} = \frac{1}{2}\sigma_{max} u_n^c \quad 6.13$$

$$G_{ct} = \frac{1}{2}\tau_{max} u_t^c \quad 6.14$$

where:

σ_{max} =maximum normal contact stress

T_{max} =maximum equivalent tangential contact stress

The debonding modes are based on input data by the TBDATA command:

Table 6.1 CZM Parameters

Constant	Symbol	Meaning
C1	σ_{max}	maximum normal contact stress
C2	u_n^c	contact gap at the completion of debonding
C3	T_{max}	maximum equivalent tangential contact stress
C4	u_t^c	tangential slip at the completion of debonding
C5	η	artificial damping coefficient
C6	β	flag for tangential slip under compressive normal contact stress

To activate debonding for a contact pair, the following contact options must be defined for the contact element: (ANSYS, 2013)

- Augmented Lagrange method or pure penalty method (KEYOPT(2) = 0 or 1)
- Bonded contact (KEYOPT(12) = 2, 3, 4, 5, or 6)

In addition, a CZM with bilinear behaviour for the contact elements must be specified. Two ways to specify the material data are available:

- Bilinear material behaviour with tractions and separation distances (TB,CZM command with TBOPT = CBDD)
- Bilinear material behaviour with tractions and critical fracture energies (TB,CZM command with TBOPT = CBDE)

The first method was chosen. It is a linear elastic material behaviour with linear softening characterized by maximum traction and maximum separation.

Sample command input for this material is shown below.

TB, CZM, 2, 1, , CBDD !materail 2#

TBDATA, 1, σmax, u_n^c , Tmax, u_t^c , η, β !TBDATA, 1, 2, 5, 2, 5, 100, 1

Normal contact stiffness (Kn): 10 MPa

Tangent contact stiffness (Kt): 10 MPa

Contact algorithm: Augmented Lagrange Method

Behaviour of contact surface: Bonded (always)

Other properties use default values.

6.3 2D Fracture Simulations of SNSBT

6.3.1 General

A series of 2D fracture FE models with pre-described crack tips of SNSBT were created in ANSYS. Based on the crack trajectory envelop depicted in Figure 4.26, a dominant cracking path was drawn in Figure 6.4 for the purpose of analyzing the crack propagation. Seven cracking status (cases) with cracking depths of 0mm (no cracking), 10mm, 20mm, 30mm, 40 mm , 50 mm and 60 mm were simulated to evaluate the fracture mechanics properties, especially the stress intensity factors (SIF) K_I and K_{II}.

The coordinates of each crack tip position are provided in the Figure 6.4. The dimensions of the model and the loading and boundary conditions and the coordinates of each crack tip position are illustrated in Figure 6.5.

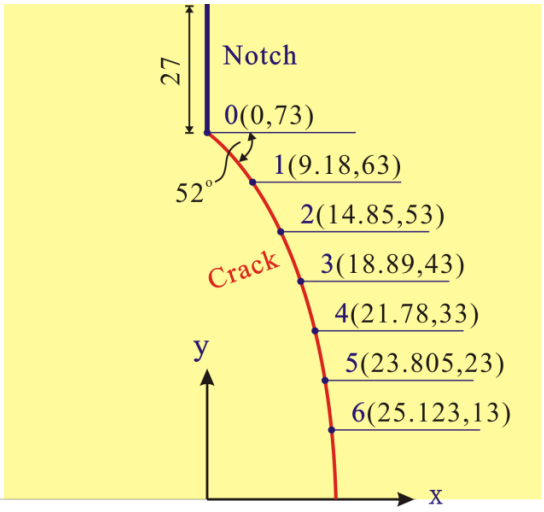

Figure 6.4 Six Simulated Cracking Depths on Dominant Cracking Path

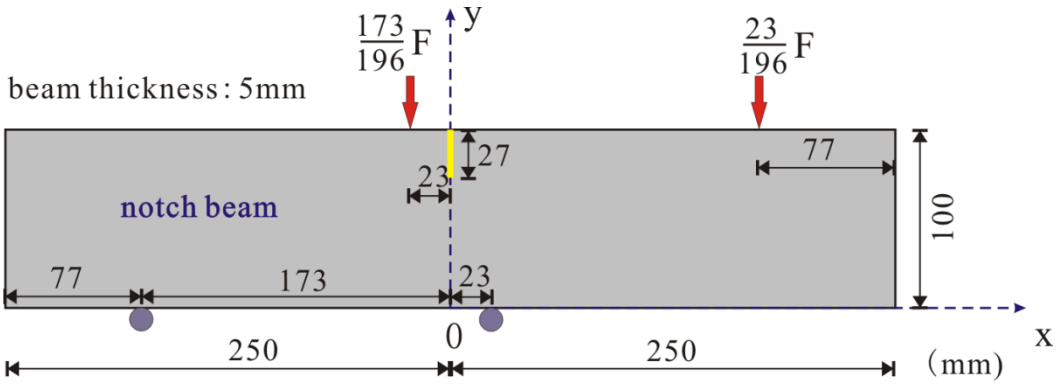

Figure 6.5 Loading and boundary conditions of SNSBT 2D model

The total loads applied onto SBRPMC specimens and the corresponding crack propagation depths were recorded during the test, which is provided in Figure 6.19. It was converted to the local coordinate system and specified in Table 6.2. The applied loads on left and right loading rollers were calculated accordingly, as shown in Figure 6.5.

Table 6.2 Simulation Applied Loads According to Experimental Data

Crack Depth (mm)		0	10	20	30	40	50	60
Total Applied Load (kN)		43	40	40	41	42	45	46.7
Loads on Loading Rollers (kN)	Left	37.95	35.31	35.31	36.19	37.07	41.22	42.37
	Right	5.05	4.69	4.69	4.81	4.93	5.48	5.63

6.3.2 Simulation Set #1: Cracking Depths from 0 to 60 mm

In this paragraph the results of the SIF of SNSBT beams with fixed material properties are presented. The compressive strength and tensile strength of SBRPMC, listed in Figures 4.8 and Table 4.8, were employed herein, i.e. 80.08MPa and 14.73MPa. The dimension of the SBRPMC specimen used was 500mm (length) × 100mm (depth) × 75mm (width), with a notch depth of 27mm in the mid-span. The average initiation angle for SBRPMC is 52 °.

A global impression of the computed stresses and deformations is given in Figure 6.6. High stress concentration is observed a cracking tip area.

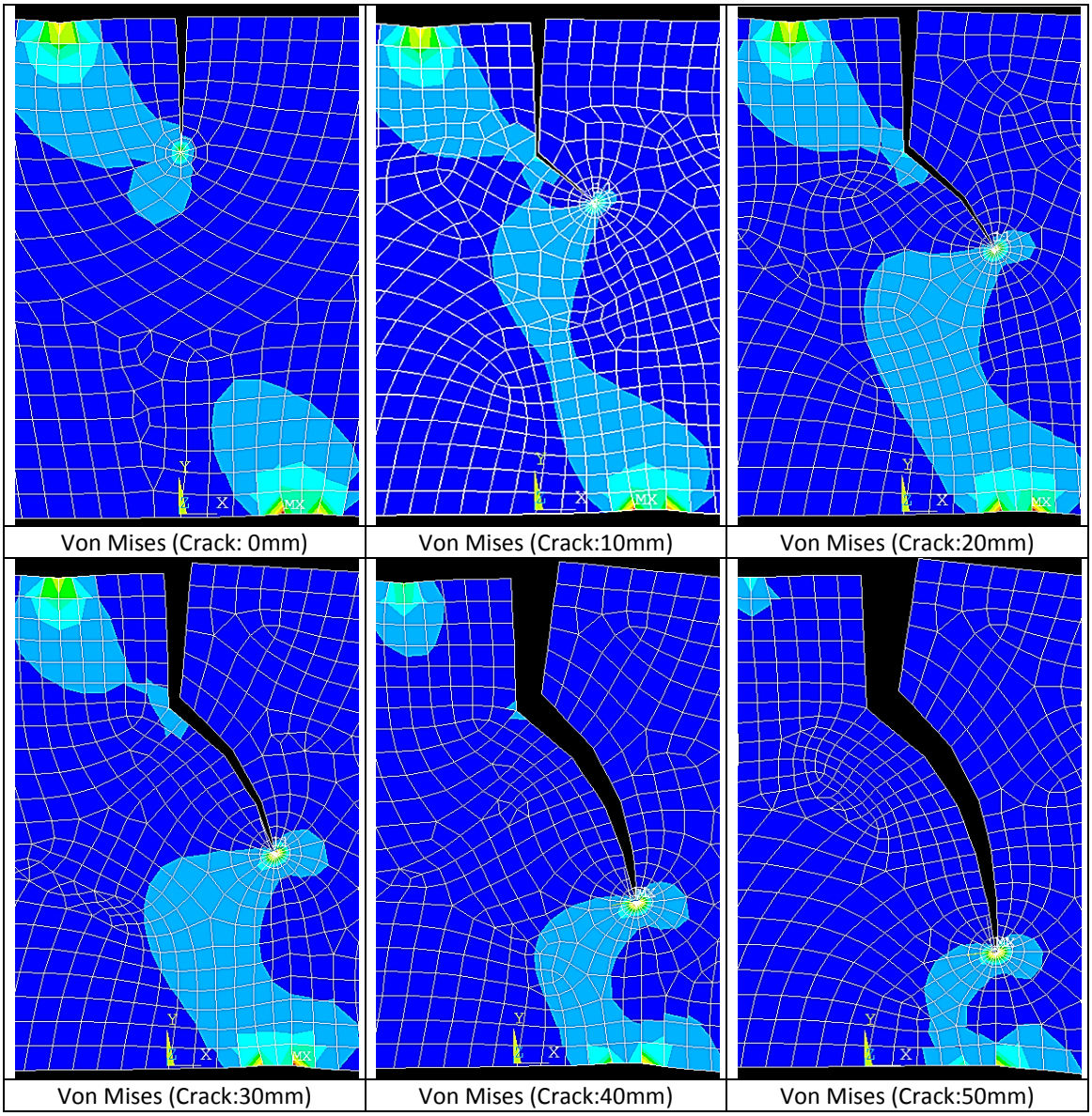

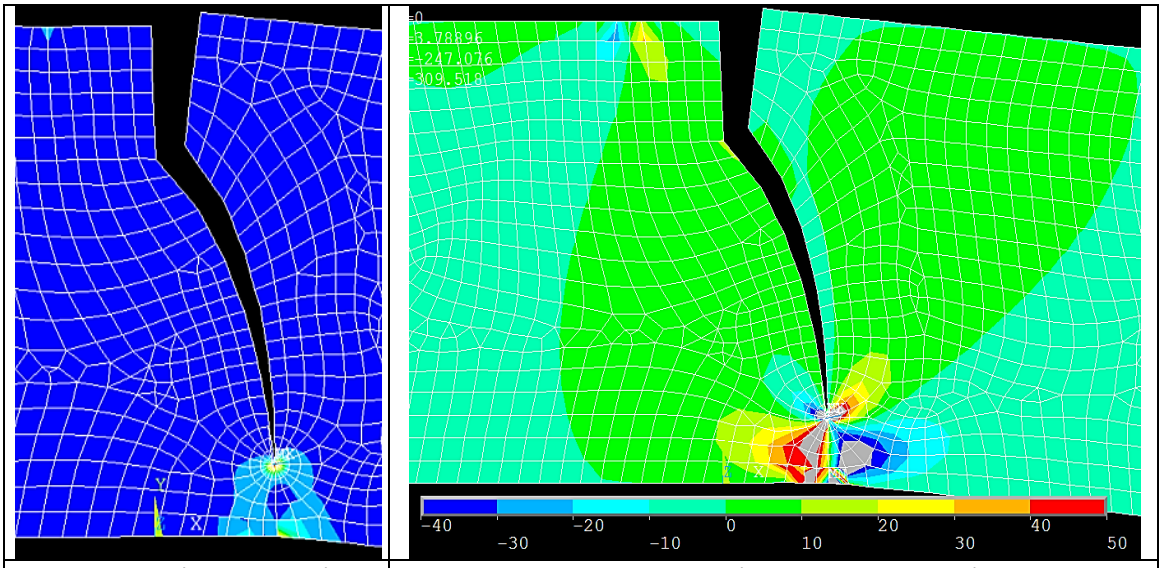

Von Mises (Crack:60mm) | Shear Stress XY (Crack Depth = 60mm)

Figure 6.6 Deformation & Stress Distribution at Various Crack Propagation Depths

Table 6.3 Stress Intensity Factors K_I and K_{II} at Various Crack Propagation Depths

Crack Depth	K_I	K_{II}
0	8.668	208.43
10	173.93	208.92
20	288.14	239.22
30	469.41	282.74
40	788.61	342.46
50	1526.5	469.64
60	3636.4	814.16

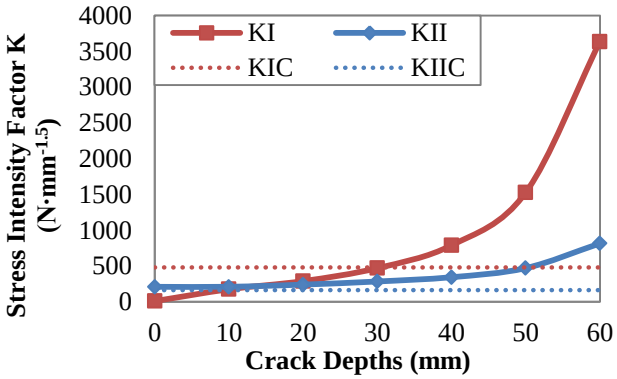

Table 6.3 shows the tendencies of the SIF K_I and K_{II} at different cracking depths. It shows that the K_I is only 8N·mm$^{-1.5}$ compared to 208N·mm$^{-1.5}$ of K_{II}. The shearing mode is clearly dominant at crack initiation. As the crack develops further, both K values increase substantially. However, K_I rises at a much steeper ratio and becomes the prevalent failure mode. Thus, in order to prevent reflective cracking, materials with high tensile strengths should be appreciated. To resist an "already-openned" crack, the shear strength of the pavement material may contribute further. However, extra verification by simulations or experimental works is required.

It is noticed that when the crack is approaching the beam's soffit, the K-values become extremely high. It is believed that the beam must have failed at such SIF level. As stated in Eqn. 5.10, the critical stress intensity values K_{IC} and K_{IIC} set the maximum stress

concentration level just before failure takes place. The experimentally derived K_{IC} and K_{IIC} are shown in dash lines in Table 6.3. Overall, the computed results of SIF are greater than the laboratory test results. This is because in this set of simulations, the crack was modelled as a complete discontinuity allowing no more load-transfer once it is formed. While in reality, a developing crack may continue to transfer shear load due to cohesive actions by aggregates and reinforcing materials. The introduction of a complete discontinuity in the FE mesh is a simplification of a real test, which neglects the material's post-cracking capacity. In other words, the FE simulations discussed in this section weaken the mechanical properties of SBRPMC beams and resulted in inappropriately high SIF results. It also implied that without fibre reinforcement, the plain concrete specimens could fail at a much lower load. In the next section, an improved set of simulations by adding CZM along cracks is presented.

6.3.3 Simulation Set #2: SBRPMC with Cohesive Cracks

From the previous set of simulations, we have come to know the necessity of involving residual material mechanical properties of cracks. The cohesive zone model (CZM) based on contact elements in ANSYS offers a solution to this problem.

The bilinear cohesive zone material model (input using "TB,CZM") based on the model proposed by Alfano and Crisfield (2001) presented in Section 6.2.3 is employed in modelling the cohesive mechanical behaviour of cracks in beam specimens. Details of the technique are already discussed, in this part the determination of model parameters and analysis of simulation results are addressed.

Based on experimental tests results, load – crack displacement diagrams are plotted for plain PMC, SBRPMC with 1.5% volume fraction of steel fibres and 2% steel fibre, as in Figure 6.7. The bilinear CZM model is presented as well for convenience. The crack displacement was calculated based on the vector sum of crack sliding displacement and crack mouth opening displacement. For SBRPMC specimens simulated in this section, the maximum load occurs around a crack displacement of 2mm, following which the load gradually decreases. Since only part of the decreasing phase was obtained, the maximum crack displacement of 15 mm was estimated based on the decline tendency.

The crack displacement is the vector sum of normal and tangential contributions. The ratio between local crack sliding displacement and opening displacement vary due to the heterogeneity of concrete. It is assumed that the normal and tangential displacements are equal. In other words, the characteristic displacement at the peak load δ_n (Mode I) equals to δ_t (Mode II); the maximum displacement δ_n^C (Mode I) equals to δ_t^C (Mode II). These four input parameters for CZM models are calculated as below.

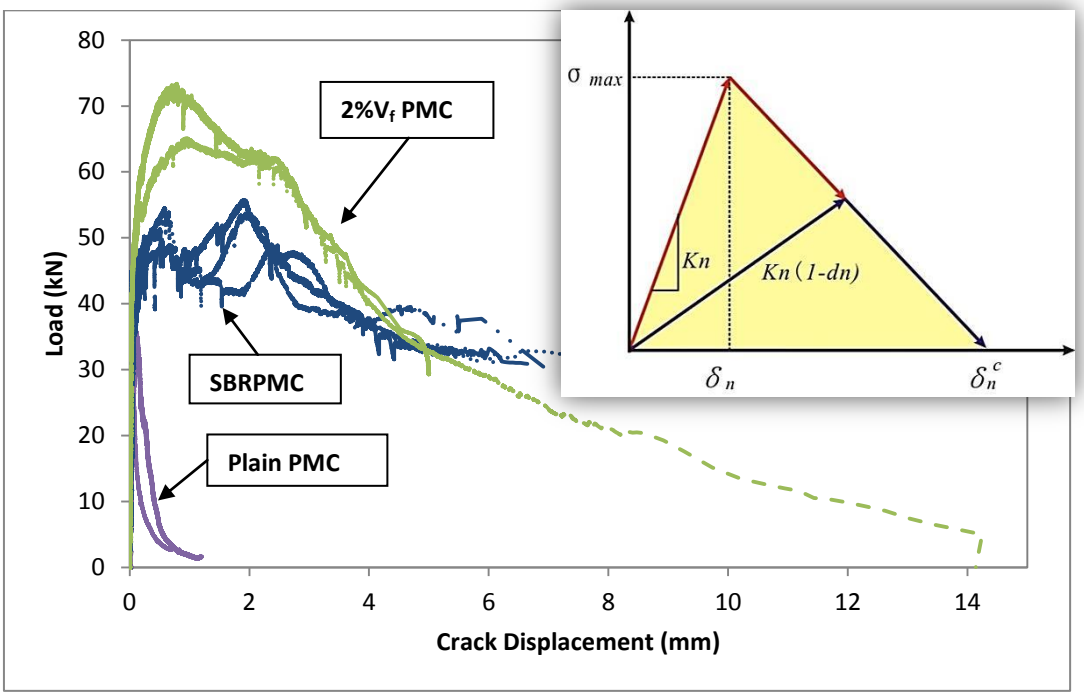

Figure 6.7 Nominal Shear Stress – Crack Displacement Diagram

$$\delta_n = \delta_t = 2mm \times \frac{\sqrt{2}}{2} = 1.414\ mm \qquad \delta_n^C = \delta_t^C = 15mm \times \frac{\sqrt{2}}{2} = 10.6\ mm$$

The maximum normal contact stress $\sigma_{\max}$ is based on the prism splitting tensile strength f_{st}. The maximum tangential contact stress $\tau_{\max}$ value is based on the cylinder direct shear strength f_s. Details of testing these material quantities are presented in Sections 4.2.3-4.2.4. For SBRPMC specimens, f_{st} =14.73 MPa, f_s = 8.93 MPa. The determined CZM models and parameters for SBRPMC are illustrated in Figure 6.8.

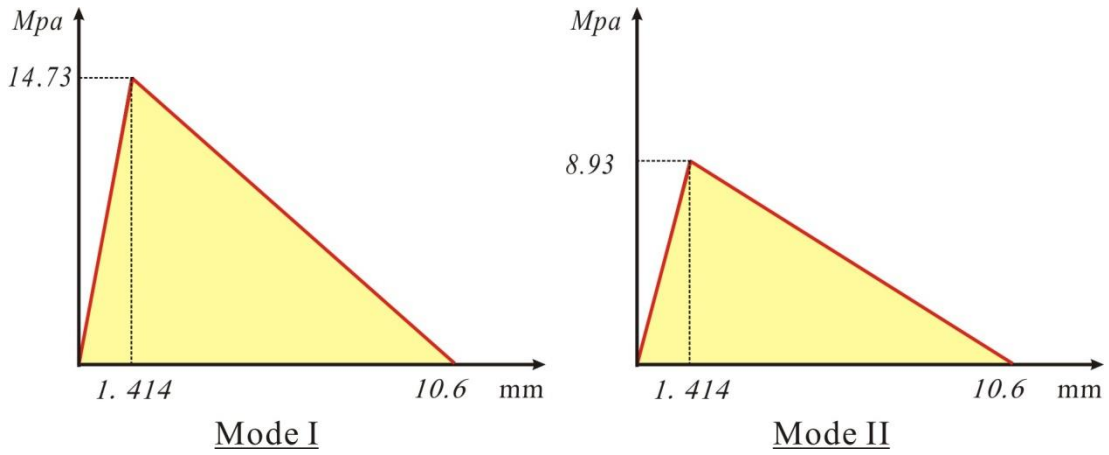

Figure 6.8 Bilinear CZM models for cracks of SBRPMC beams

The contact stress as the crack develops to various depths are demonstrated in Table 6.4. The positive/negative meanings of contact element are illustrated in Table 6.5. It shows that the contact stress is in tension mode and increasing as the crack develops. When the crack tip developed to 60mm deep, the opened crack at the notch tip still managed to provide approx. 2.7MPa tensile strength to prevent crack opening.

Table 6.4 Contact Stress at Cracks (Deformation: × 10; Label Unit: MPa))

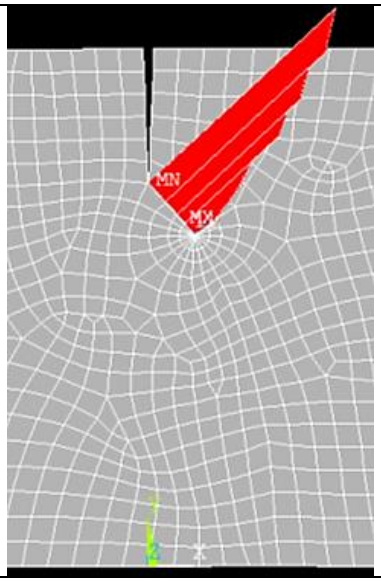	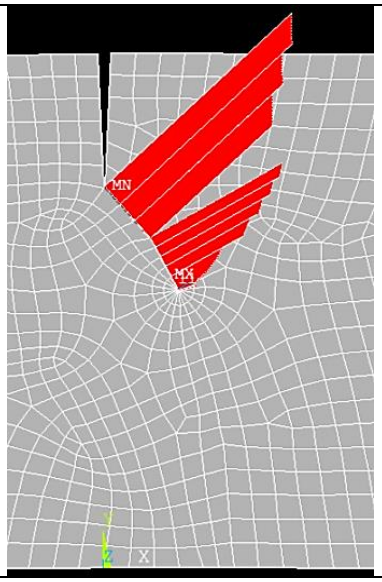	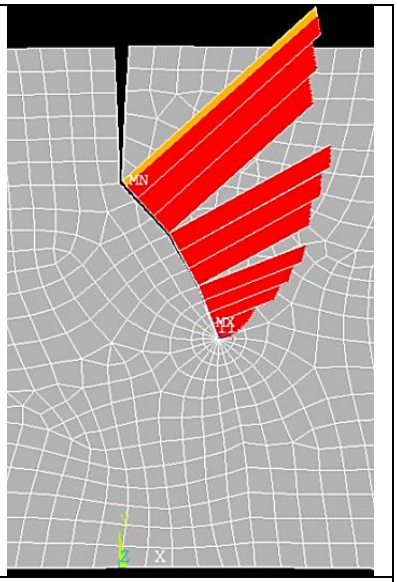
10mm	20mm	30mm

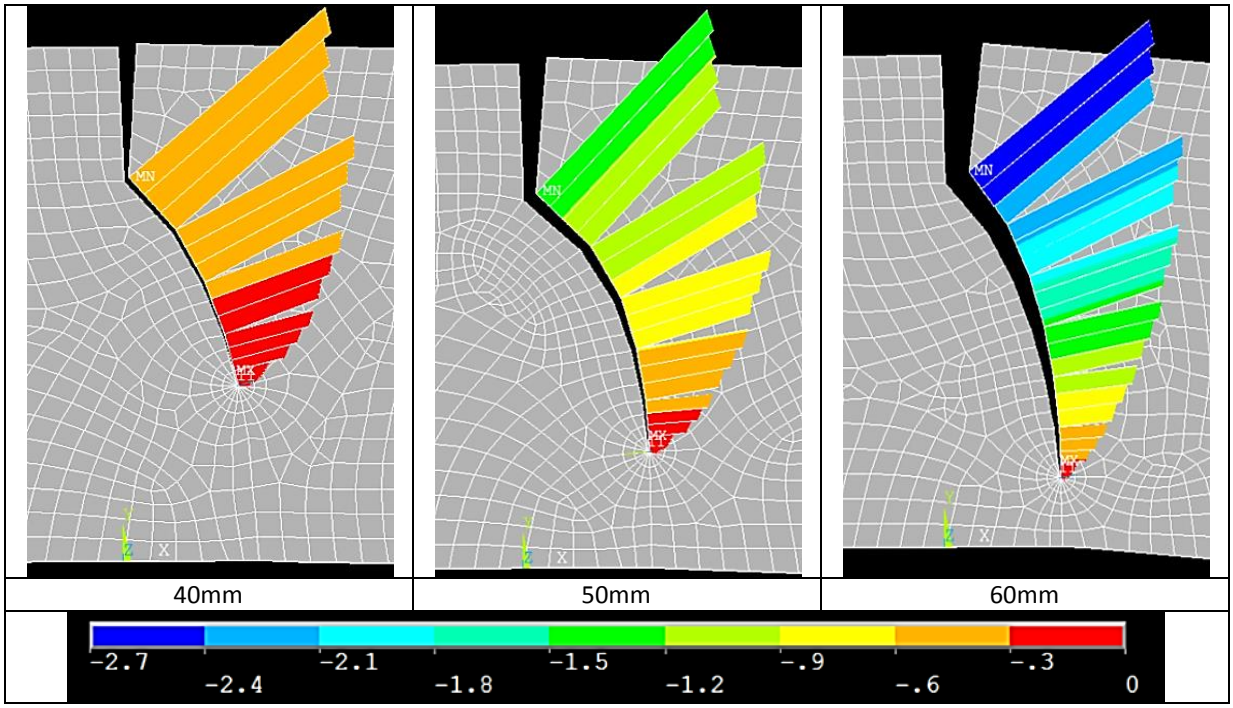

Table 6.5 Contact Element - Positive/Negative Meanings

Items of Contact Post-Processing	Meaning	
	Positive (+)	Negative (-)
Contact State	Opening	Closing
Contact Penetration	Intrusion	Egress
Contact Stress	Compression	Tension
Contact Total Stress	Tension &/ Shearing	Compression &/ Shearing
Contact Gap Distance	Closing	Opening
Contact Friction Stress	Directional signs only	
Contact Sliding Distance	Directional signs only	

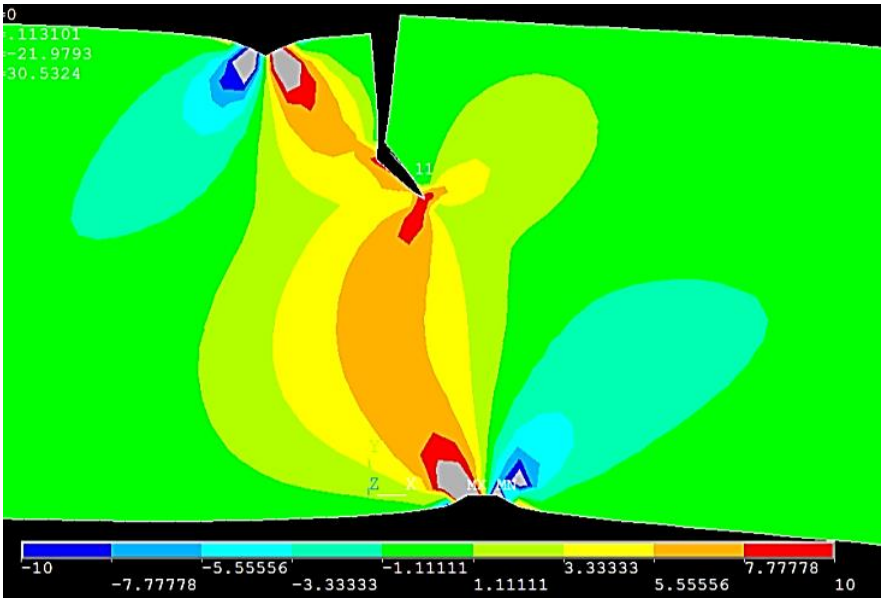

Figure 6.9 Shear Stress XY when Crack Tip is at 10mm deep

Table 6.6 Stress Intensity Factors K_I and K_{II} (Cohesive Cracks)

Crack Depth	K_I	K_{II}
0	8.668	208.43
10	150.88	181.79
20	203.09	177.13
30	243.61	169.21
40	278.79	160.35
50	366.45	131.31
60	375.51	135.37

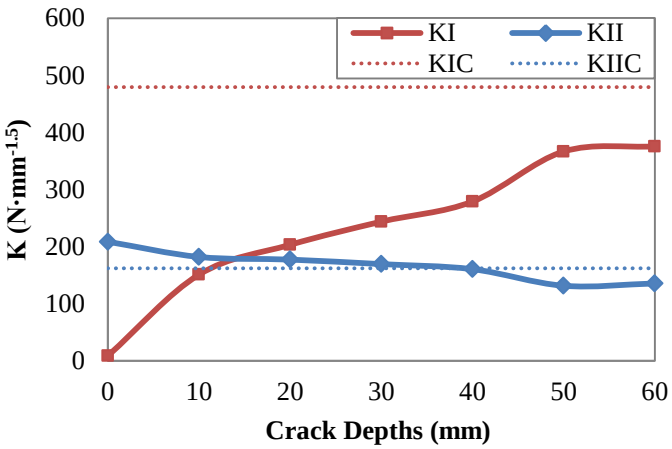

Since the CZM was not activated before crack opens, the same K_I and K_{II} was obtained at crack depth zero. A predominant mode II was revealed at crack initiation. Comparing with the previous simulation, the SIFs are considerably reduced as a result of effective bridging and aggregate interlocking on crack control. As crack further extends, mode II transforms into mode I due to the bridging effect. It has been pointed out by many other researchers that the addition of steel fibre causes the transition from shear failure mode to flexural failure mode. (ACI Committee 544 2002, Ashour, Hasanain and Wafa 1992, Narayanan and Darwish 1987, Nguyen-Minh and Rovnak 2011)

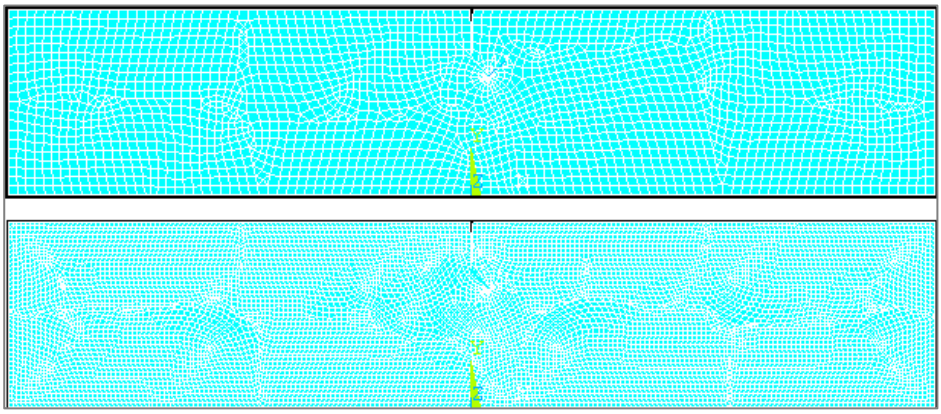

Figure 6.10 Mesh Element Size 5mm and 2.5mm

The element employed above had a global edge length of 5mm. To examine the sensitivity of K-values on element sizes, the model of crack depth at 10mm was re-calculated with a reduced element size of 2.5mm, as picture in Figure 6.10. The K_I and K_{II} were 151.18 and 183.60 $N{\cdot}mm^{-1.5}$ respectively, that is very close to the previous results of 150.88 and 181.79 $N{\cdot}mm^{-1.5}$. Hence, it is considered the K-values are not sensitive to mesh density.

6.3.4 Simulation Set #3: Different Overlay Material with Fixed Crack

In this section, we analyse the structural effectiveness of the overlay material of composite SNSBT beams. The composite beam consists of two structural layers: a 50mm thick notch beam layer with a notch of 30mm in depth at midspan, with a branched crack initiated from the notch tip which develops down to a depth of 10mm at a direction of 45°, and an 80mm overlay bonded with the notch beam layer. Figure 6.11 is a diagram of the modelled composite beam. A unit load (F) of 1kN is applied.

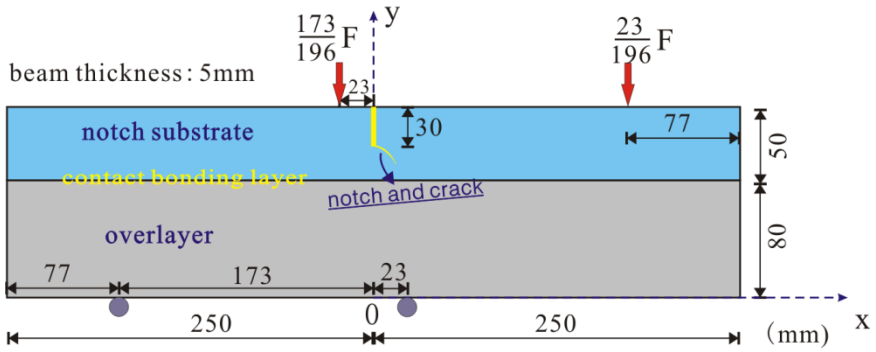

Figure 6.11 Composite SNSBT beam with a crack

Figure 6.12 presents the shear and Von Mises stress distributions around the notch and crack area of a SNSBT beam. Due to the cohesive interface between the two material layers, the shear stresses around the cohesive interface between the two beam materials are weakened. High stress concentrations are observed at the crack tip, and around the loading support locations which explains the co-existence of splitting cracks in some beams. When splitting cracking occurred, the crack tip shear resistance was at least equivalent to the splitting resistance.

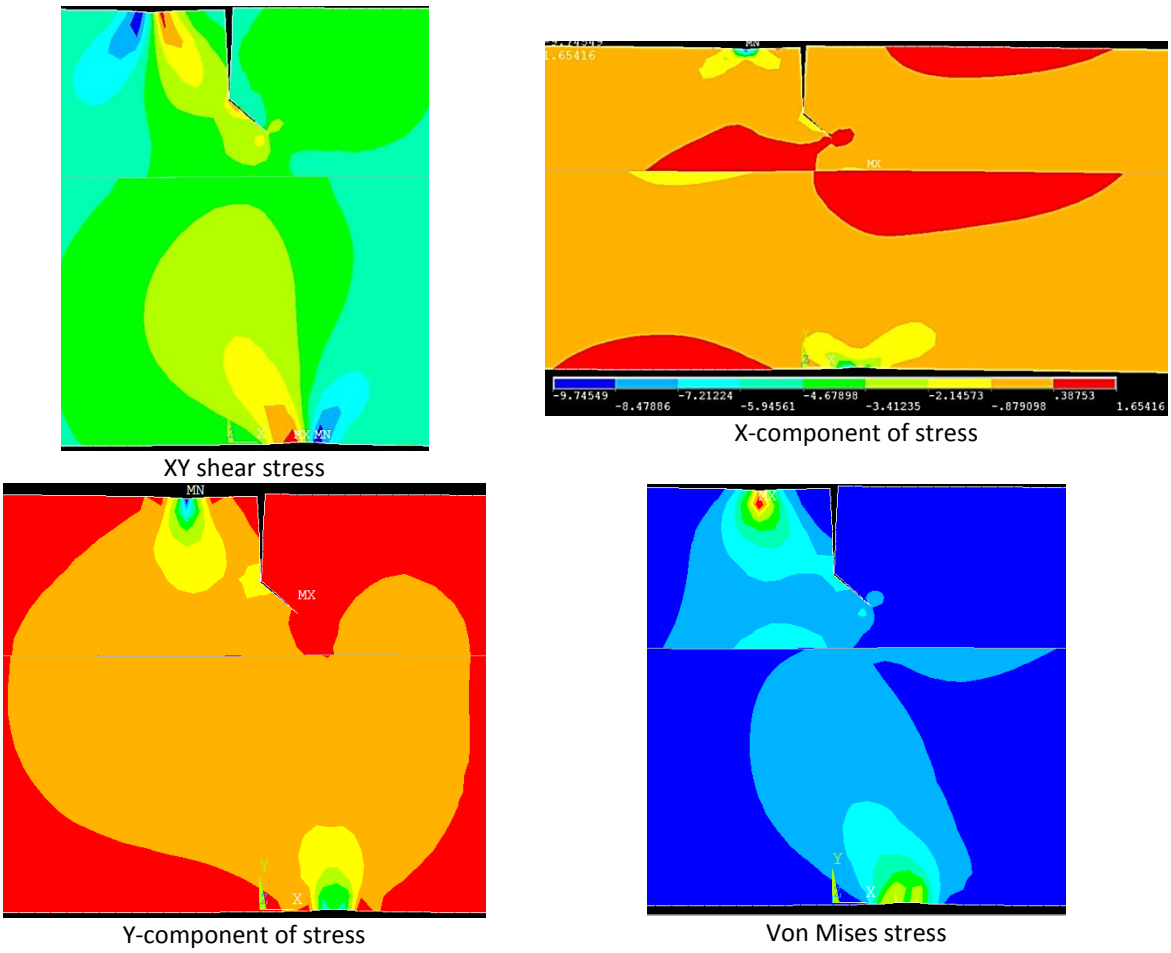

Figure 6.12 Stress Distribution in Composite Beams. (Deformation Factor: ×200).

Here, the conditions of material properties, loads, interface bonding properties and the crack depth were kept constant, only the stiffness of the overlay was varied in the typical range for concrete material from 20GPa to 40GPa. By comparing the SIF at the crack tip, the effects of overlay stiffness are evaluated.

Table 6.7 shows both K_I and K_{II} values decreasing with increasing overlay stiffness. Based on the above, the overlay material with a higher stiffness seems to have provided better

resistance in mode I and mode II. This was also evident in the experimental tests. The load – notch tip displacement (P-NTD) plot of the foundation test in Figure 4.45 revealed that the OPCC overlaid system cracked at a much lower load than the SBRPMC overlaid system, acknowledging that the E-values are 25GP in OPCC and 32GPa in SBRPMC.

Table 6.7 Stress Intensity Factors as a Function of Overlay Stiffness

Stiffness (GPa)	K_I	K_{II}
20	1.760	2.412
25	1.524	2.088
30	1.351	1.851
35	1.216	1.666
40	1.109	1.519

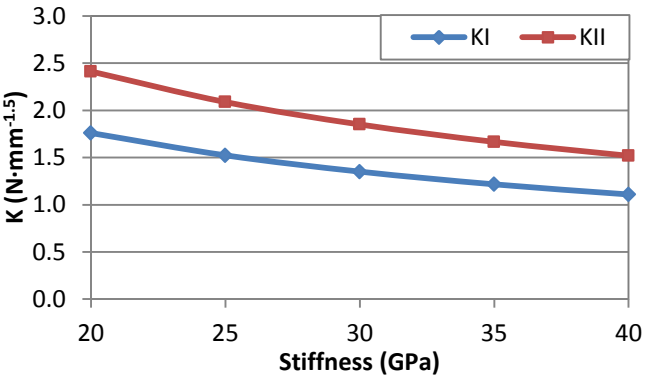

6.3.5 Simulation Set #4: Bonding Conditions of Composite Beams

The same FE model as presented in the previous section is used here. The results of composite beams in SNSBT with different bonding conditions of the cohesive interface are discussed. By differing the friction coefficient value of the contact element layer between the two beam layers from 0.01 to 1, the bonding conditions from weak to strong are simulated.

At the bonding layer between the two material layers of the composite beam, contact sliding can be obtained as a result of the load acting on the beam, and so can the friction stress. The computed contact friction stresses and sliding deformations are portrayed in Figure 6.13 and Figure 6.14. The maximum contact friction stress is observed in the middle of the beam, below the notch. By comparing computed results from two different cases with friction coefficients set to 0.1 and 0.3 respectively, it is evident that higher friction stress and smaller friction displacement are achieved by increasing the friction coefficient.

(a)

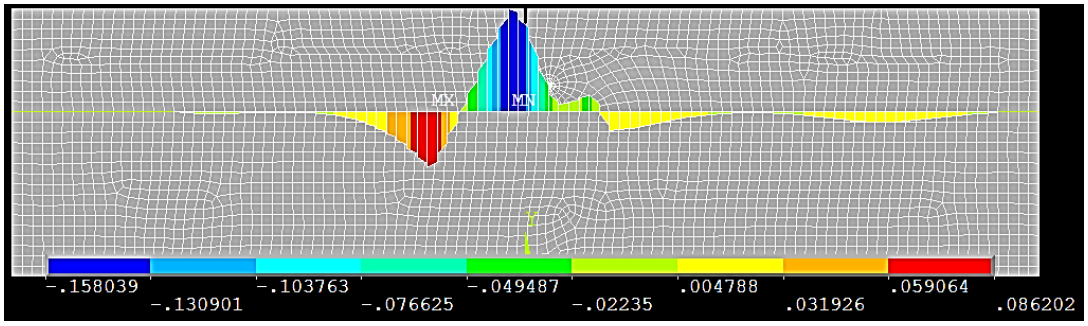

(b)

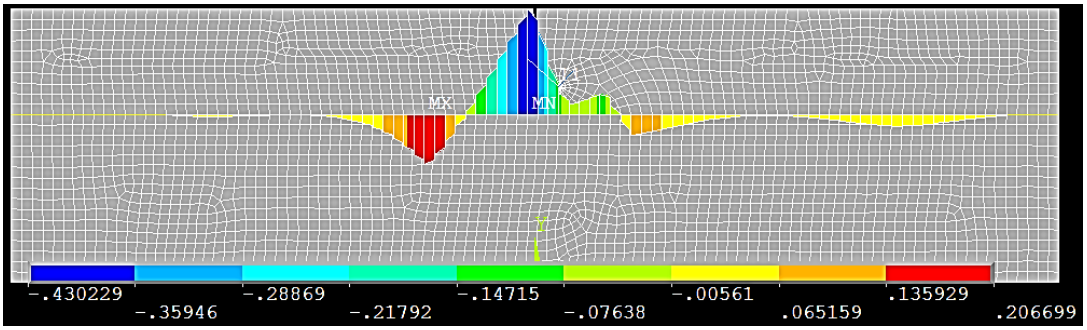

Figure 6.13 Contact Friction Stress (a) Friction Coefficient = 0.1; (b) Friction Coefficient = 0.3

(a)

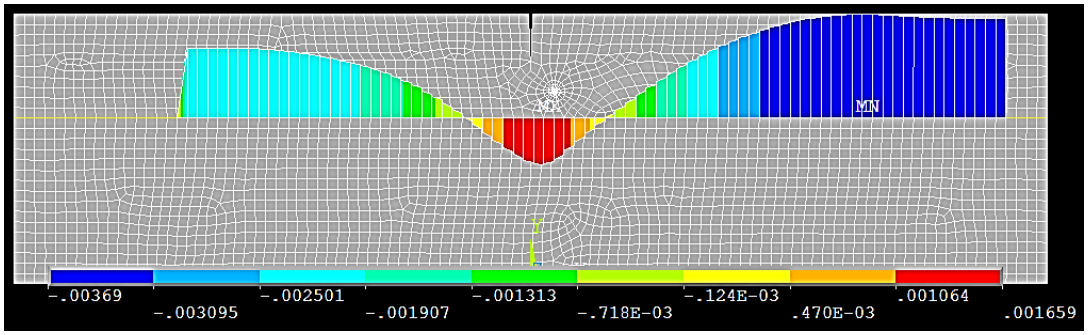

(b)

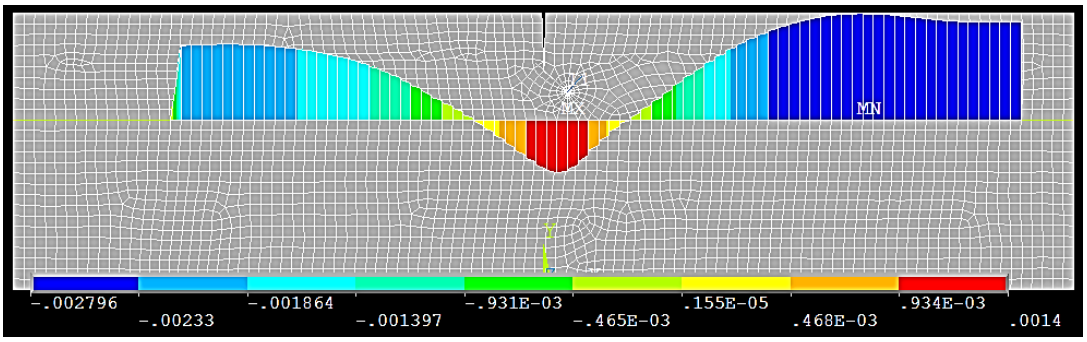

Figure 6.14 Contact Sliding Distance, (a) Friction Coefficient = 0.1; (b) Friction Coefficient = 0.3

Table 6.8 shows the effects of the friction coefficient of interface between the two beam layers on stress intensity factors at the crack tip. An effectively bonded system will enable the composite system to behave simultaneously and achieve excellent integrity. Hence, the stress intensity factor appeared to increase with the friction coefficient. On the contrary, an unbonded overlay system may be able to reduce the level of stress concentration at the crack tip and relax the stresses. However, it will not be able to utilize the remaining strength in the substrate and consequently, will lead to greater overlay thickness and a less efficient rehabilitating program.

Table 6.8 Stress Intensity Factors as a Function of Interface Friction Coefficient

Friction Coefficient	K_I	K_{II}
0.01	1.176	1.722
0.1	1.211	1.740
0.2	1.246	1.757
0.3	1.275	1.772
0.5	1.323	1.795
0.7	1.361	1.814
1	1.369	1.809

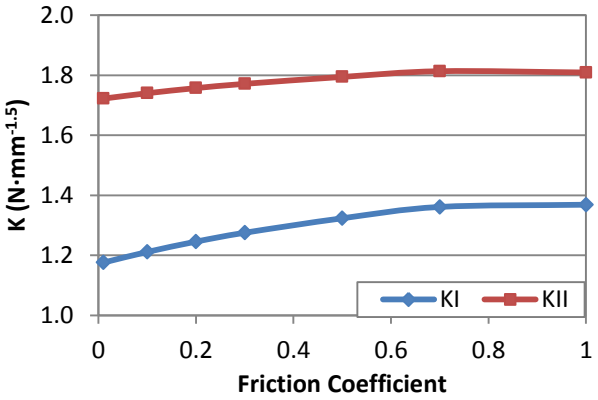

6.3.6 Simulation Set #5: Four Scenarios of Composite Systems

In the composite system, to characterize the bond properties between overlay and substrate, the cylinder direct shear bond test and block splitting test were carried out as detailed in Section 3.3. The test results are summarized in Table 6.9. The basic Coulomb's friction law describing the contact friction between two solid materials was employed to define the bond properties between the overlay material and the substrate, i.e. OPCC. There are two components in the coulomb shear friction, as illustrated in Eqn. 6.15, where COHE is the cohesive stress; $MU \cdot \sigma$ is the friction caused by normal stress; MU is the friction coefficient.

$$\tau = MU \cdot \sigma + COHE \qquad 6.15$$

The cylinder direct shear setup produces a direct shear failure mechanism with failure planes being vertical and parallel to the loading direction. However, if the self weight of testing rig and the overhanging section of the specimen were taken into account, it would involve bending moment and normal stresses on the shearing plane. As sketched in Figure 6.15, the

self weight of the loading piece and the overhanging section in the specimen yields the shear force F and the bending moment M on the bonded interface. Hence the shear stress τ and the normal stress σ can be calculated as follows.

The self weight of the loading piece was measured as 3203.5g, equivalent to 31.43N. The weight of the PMC section was equivalent to 15.04N, if the length of the section was assumed to be 80mm and the material density of SBRPMC, 2440kg/m^3, was employed. At the interface, the total shearing force is 46.47N. Thus, the shear stress caused by the self weight is 0.006 MPa. It is considered neglectable. The normal stress caused by the self weight is 0.109 MPa.

It is clear that the direct shear bond strength determined in the above setup involves some normal stress on the shearing plane. Although the load was applied very close to the plane, the slight offset still contributed to the normal stress on the interface. In contrast, the bond tensile strength derived from the block splitting test delineates the cohesion between the two materials in the normal direction. Hence the block splitting tensile strength f_{stb} was regarded as the cohesive stress (COHE) in Coulomb's law, also referred to as "contact cohesion". The direct shear bond strength f_{sb} was taken as the maximum friction stress between the two materials (τ_{max}). The normal stress caused by the self-weight is regarded as the normal stress (σ). The testing results for four combinations are provided in Table 6.9. Table 6.10 shows the coefficients of friction and plots the coulomb relationships for all four scenarios. It can be seen that PVAPMC-OPCC exhibited the greatest cohesion at interface. The roughened SBRPMC-OPCC interface manifested higher coefficient of friction than the smooth interface. These properties were assigned to the contact elements in the modelling of composite beams, by the following command lines.

```
MP,MU,1,2.74          !friction coefficient 2.74
R,3,9,4.83            !real constant, τmax=4.83
R,3,13,4.53           !real constant, COHE = 4.53
```

Table 6.9 Bond Strength Determined in Experiments

		Direct Shear Bond Strength f_{sb} (MPa)	Block Splitting Tensile Strength f_{stb} (MPa)
A	Roughened OPCC-OPCC Interface	4.09	2.17
B	Smooth SBRPMC-OPCC	2.1	1.80

		Direct Shear Bond Strength f_{sb} (MPa)	Block Splitting Tensile Strength f_{stb} (MPa)
	Interface		
C	Roughened SBRPMC-OPCC Interface	4.29	2.70
D	Roughened PVAPMC-OPCC Interface	4.83	4.53

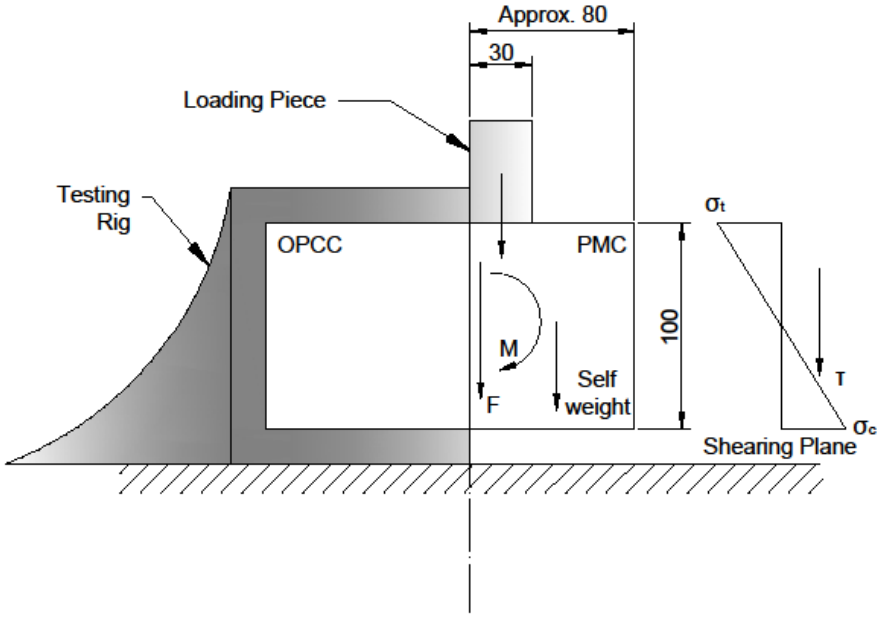

Figure 6.15 Cylinder Direct Bond-Shear Test

Table 6.10 Coulomb Law and Coefficient of Friction

		MU
A	Roughened OPCC-OPCC	17.57
B	Smooth SBRPMC-OPCC	2.74
C	Roughened SBRPMC-OPCC	14.55
D	Roughened PVAPMC-OPCC	2.74

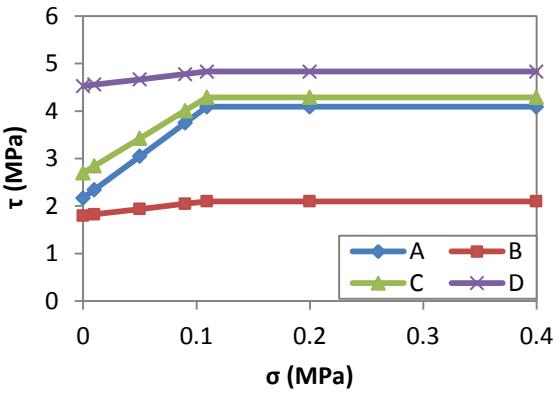

Based on the results from SBRPMC composite beams with 30mm notch in the substrate, when the crack developed for approx. 10mm, the total applied force was around 60kN. This force as well as the corresponding elastic modulus, poisson's ratios and the coulomb relations were adopted in the simulation. The mode I and mode II stress intensity factors K_I

and K_{II} were obtained and plotted in Figure 6.16. The vertical deformations were plotted in Figure 6.17. When the bond is robust (e.g. scenario D-PVAPMC overlay system), the deformation is largely reduced. Also, the smallest SIF values were obtained in the PVAPMC overlay system (scenario D) due to its high elastic modulus and small friction coefficient as above-mentioned. On the other hand, OPCC bonded overlay system (scenario A) presented the highest stress level at crack tip and the maximum deformation due to the relatively low elastic modulus and large friction coefficient. The SBRPMC composite system managed to reduce the stress intensity factor compared to OPCC overlay, mainly attributed to its higher elastic modulus. The roughened interface in SBRPMC composite system does not seem to generate too much difference in SIF at this crack position. However, the deformation in smooth interface system is larger. Zhang and Li (2002) conducted bending tests of a similar PVAPMC overlay system (referred to as ECC overlay) to study the influence of interfacial properties on overall bending performance. It was revealed that the fatigue life of the overlay was not influenced by the interfacial roughness. However, the deformation was larger where the interface was a smooth casting surface under both monotonic and fatigue loading. This agrees well with the FE results herein.

The SNSBT was setup to analyze the overlay material behaviour under shear. It is understood that it is significantly different from the real application. For example, the horizontal movement is restrained by the adjacent material and roadside kerbs in real scenario. However, in the above test configuration, no horizontal restraint was applied. Although a stringent testing system with horizontal constraint was not available in the lab, it can be achieved easily using the FE modelling. The K_I' and K_{II}' plotted in Figure 6.16 were derived when the condition of UX=0 was applied at both ends of beams. The SIFs were considerably reduced but followed the same tendency as K_I and K_{II}. The previous analysis served as a true indicator in this case.

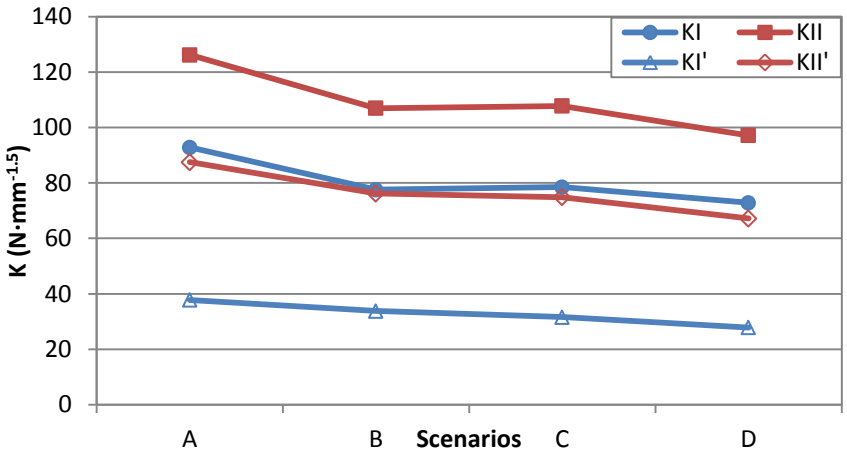

Figure 6.16 Stress Intensity Factor of Four Scenarios

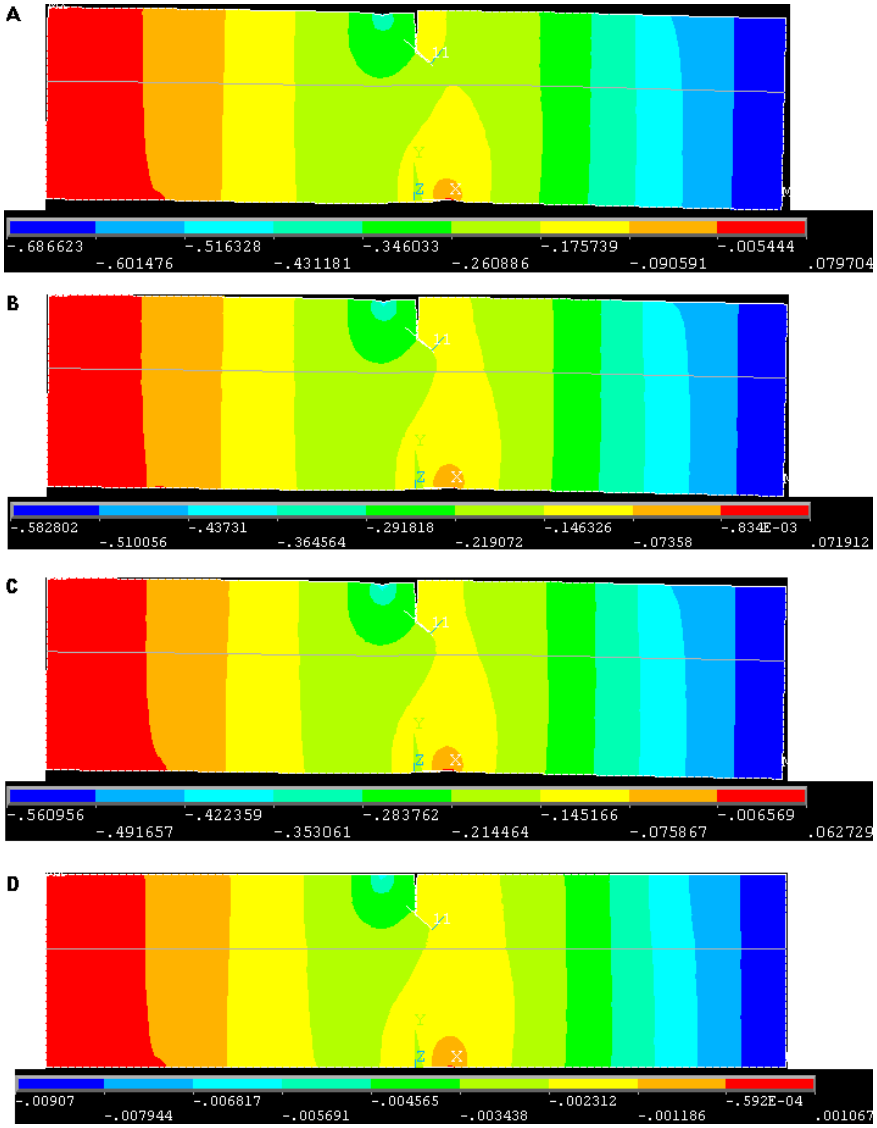

Figure 6.17 Y-Direction Deformation

6.4 Modelling Reinforced Concrete in ANSYS

The SOLID65 element available in ANSYS is particularly suitable for 3D modelling of the concrete material with or without reinforced bars. Four different materials are allowed within the SOLID65 element: one matrix material (e.g. concrete) and a maximum of three independent reinforcing materials. The element is capable of modelling cracking in tension and crushing in compression. Especially, this element is applicable for reinforced composites. In this case, steel fibres are assumed to smear evenly in all directions throughout the element. The reinforced concrete is regarded as a continuous and homogeneous material.

The concrete is treated as an isotropic material. Cracking is allowed in three orthogonal directions at integration points. After the crack initiation at an integration point, it is simulated by modifying the corresponding material properties. In such a way, the crack is effectively treated as a "smeared band" of small cracks, rather than one continuous discrete crack. In other words, the development and directions of crack propagation can be properly modelled, despite that the modelling of crack width is not readily available in ANSYS.

As mentioned previously, the concrete material is capable of nonlinear behaviour such as plasticity, creep, cracking and crashing. If elastic behaviour is assumed, the concrete can be regarded as a linear elastic material. If cracking or crushing occurs, the elastic, stress-strain matrix will need to be adjusted for each failure mode. The appearance of a crack at an integration point is represented through adjustment of the stress-strain relations by introducing a weak plane in the direction normal to the crack face. And, a shear transfer coefficient β_t (the constant C_1 with command TB, CONCR) is introduced to represent shear strength degradation for those subsequent loads that induce sliding (shear) deformations across the crack face.

If the material at an integration point fails in uniaxial, biaxial, or triaxial compression, the material is assumed to crush at that point. In SOLID65 crushing is defined as the complete deterioration of the structural integrity of the material, e.g. material spalling. Under the conditions where crushing has occurred, material strength is assumed to have degraded to an extent such that the contribution to the stiffness of an element at the integration point in question can be neglected.

In this simulation, attentions are paid to the shear cracking failure of reinforced concrete. From the initial simulations of our test setup, it was revealed that crushing tends to happen underneath the supports. It causes a convergence problem and it is outside of our interest. To prevent this, a large element size can be applied at the supports. Alternatively, elastic cushion blocks can be introduced. The latter was adopted in the study.

6.4.1 3D FE Analysis of Single Notch Shear Beam Test

In this section, two 3D FE models of SNSBT were introduced to portray the stress distribution in the specimens, and therefore, provide a better understanding of the failure phenomena. The simulation of SNSBT with a single beam is presented first, followed by the modelling of SNSBT with a composite beam. The beam was modelled with SOLID65 elements available in ANSYS. For composite beams, the contact element using cohesive zone material model was adopted in simulating the interface between two beam layers. Modelling of concrete material using the element SOLID65 is a complex nonlinear FE problem which requires copious resources (Karadelis 2009). The contact simulation with CZM makes the problem even more complicated.

To save computational time, the FE mesh engaged symmetry in the thickness direction by modelling 40mm of the beam, half of the full thickness. The rest of the dimensions can be found in Figure 6.5. Four elastic strips were elaborately added to the beam at the two loading positions and the two supporting positions. Each strip was 6mm in width and of the same thickness as the beam. As above-mentioned, they were added to abate stress concentrations, and hence, to mitigate convergence issues. To simulate the crack development process, two linearly increasing surface pressures up to 110.0MPa and 14.6MPa, equivalent to the total applied load of 60kN (≈ peak load in SBRPMC beams), were applied on the loading strips in ten sub-loading steps. The distribution of steel fibres was assumed to be uniform in all directions, where the same volume ratio 1.5% was applied. The tensile and compressive strength of concrete were set to 15MPa and 80MPa, according to the material testing results in Chapter 5. It is recognized that the shear capacity is contributed by aggregate interlock (45%), dowel action (25%) and compression (35%). (Taylor 1974) In the case of SFRC, fibres provide effective resistance to crack opening. But once the crack opens, the randomly distributed fibres in the concrete do not act as dowel bars. Hence, a minimal shear transfer coefficient β_t was assumed to be 0.1 for open crack, and 1 for closed crack. The tensile

strength and compressive strength were set as failure criteria. A non-linear, large displacement analysis was performed, converging after a few iterations.

The computed shear stress contours at the load of 30kN and the maximum stress failure criterion were plotted in Figure 6.18 and Figure 6.19. Despite the local stress concentration at loading positions, the maximum failure position was found to be at the notch tip, which correlates well with the laboratory observations. Relatively high compressive stresses are observed along the line between the two central loading positions. The shear stress distribution depicted in Figure 6.18 shows high shear stress between middle loading positions with the maximum shear stress at the notch front.

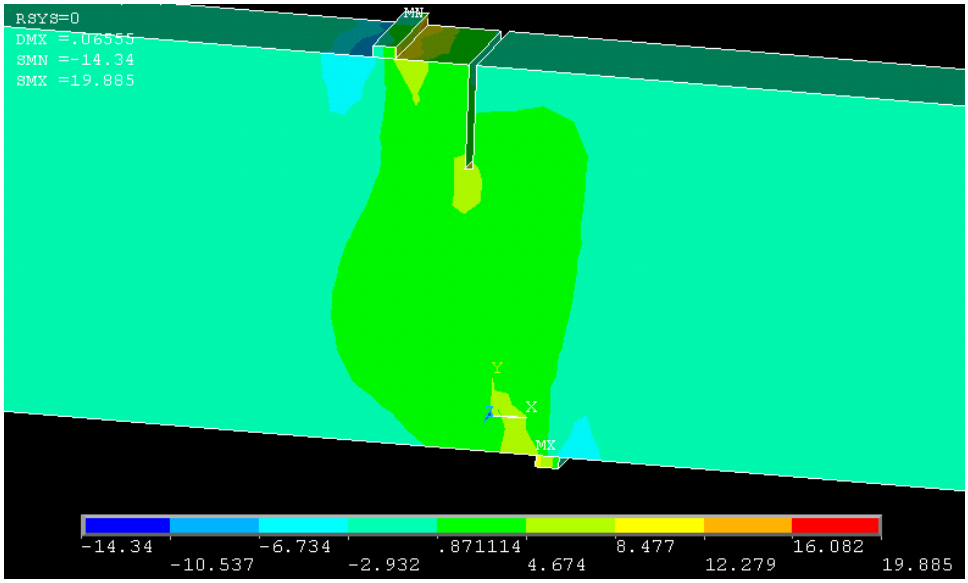

Figure 6.18 Shear Stress (Single Beam) at 30kN

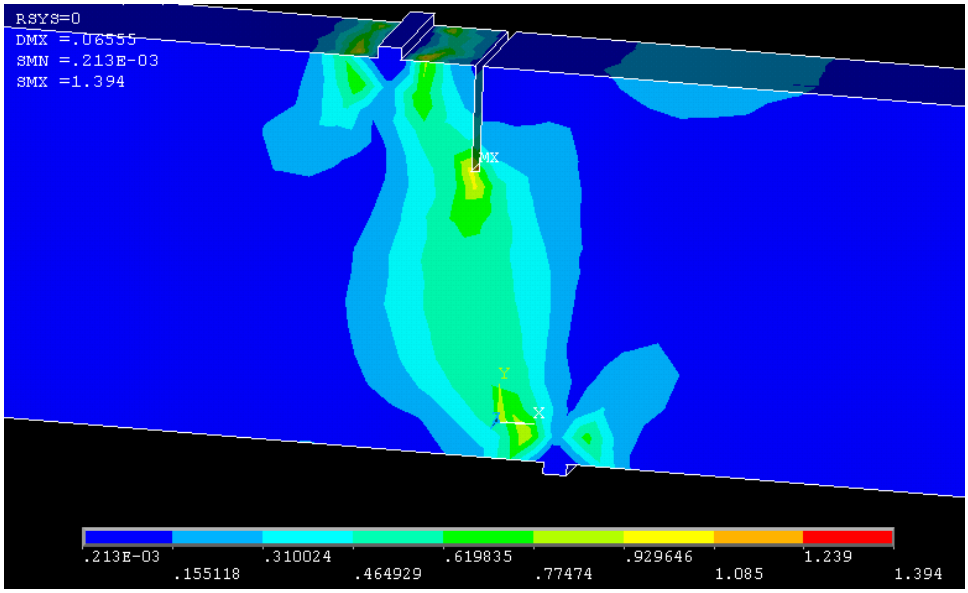

Figure 6.19 Maximum Stress Failure Criterion

Table 6.11 describes the process of the numerically predicted cracks/crushes development as the load increases at equal incremental steps. The calculated failure is shown as red dots around the specific nodal points. Sub-step 2 shows some signs of cracking initiated from notch tip. As load increases, the cracks extend further down towards the supporting strip at the beam's soffit. The smeared cracks together form a dominant cracking band, which obviously shows a good agreement with the observed experimental results shown in Figure 4.24. The cracks were observed at the load of 34-43kN in the laboratory and the peak load was approx. 57kN. The expansion of cracking in the simulation process agrees well with the laboratory results.

Table 6.11 Crack Development at Representative Sub-steps

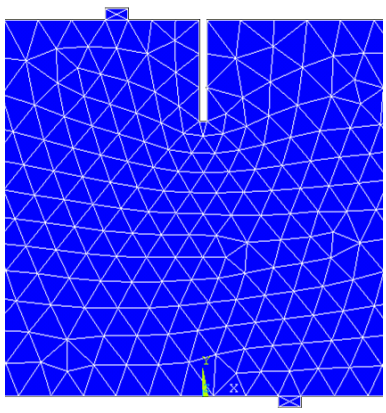	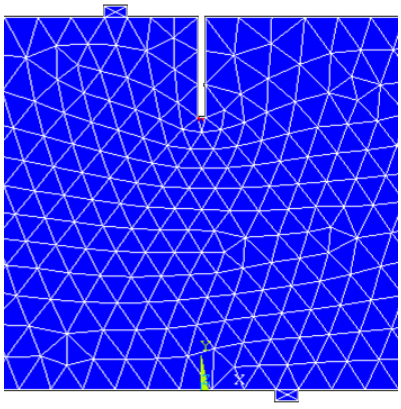
Crack Initiation at Sub-step 1 (6kN)	Crack Initiation at Sub-step 5 (30kN)

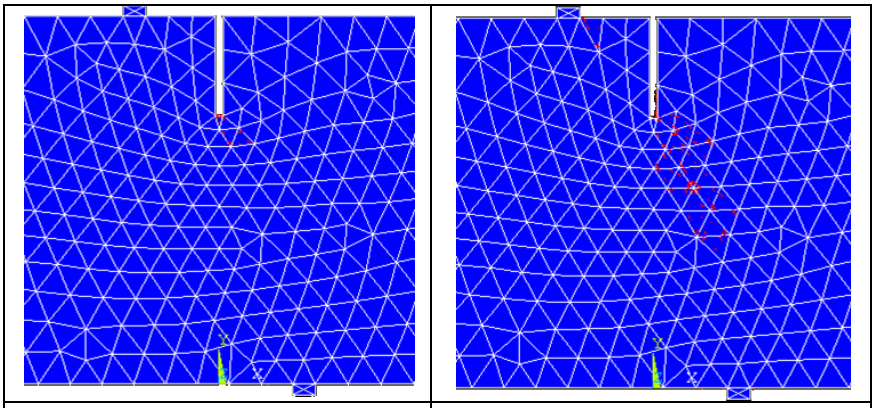

Crack Propagation at Sub-step 8 (48kN) | Crack Propagation at Sub-step 10 (60kN)

The same parameters in the single beam simulation described above were input for the overlay material in composite beams below. The OPCC substrate was defined by the following parameters: Elastic modulus E, Poisson's ratio ν, density ρ, shear transfer coefficient for open crack $\beta_{t,Open}$ and close crack $\beta_{t,Close}$, tensile strength f_t and compressive strength f_c, as listed in Table 6.12. The interface was characterized by the coulomb's law parameters as in the scenario of SBRPMConOPCC roughened interface in Section 6.3.6. The peak load of 80kN adopted from the experimental work was applied at two loading blocks as 117.7MPa and 15.6MPa. The load was applied in 10 equal incremental steps with the line search to help convergence. Line search is "an option to improve Newton-Raphson solution by scaling the solution vector". (ANSYS 2013) The cracking and crushing conditions at selected sub-steps were output in Table 6.13.

Table 6.12 Parameter Input

	OPCC	SBRPMC		OPCC	SBRPMC		OPCC	SBRPMC
E (GPa)	25.195	32.365	$\beta_{t,Open}$	0	0.1	f_t (MPa)	4.6	15
ν	0.21	0.187	$\beta_{t,Close}$	0.75	1	f_c (MPa)	68	80
ρ (kg/m^3)	2386	2440						

The computed X-component and shear stress of SBRPMC composite beam at the load of 56kN (sub-step 7) are plotted in Figure 6.20 and Figure 6.21. The shear stress distribution depicted in Figure 6.21 shows high shear stress between middle loading positions with the maximum shear stress at the notch front. The shear stress magnitude drops at the interface. As discussed earlier, a weak bond can trigger an interfacial delamination before the occurrence of shear failure. The high X-component stress at the interface indicates the tendency to delaminate locally. The cracking and crushing graphs at the onset loading approx. 56kN and the peak load of approx. 80kN are shown in Table 6.13. The cracking

trajectory from the notch tip extending further into the overlay has a close resemblance to the one obtained from the lab results, although crushing under the top loading position is significantly exaggerated.

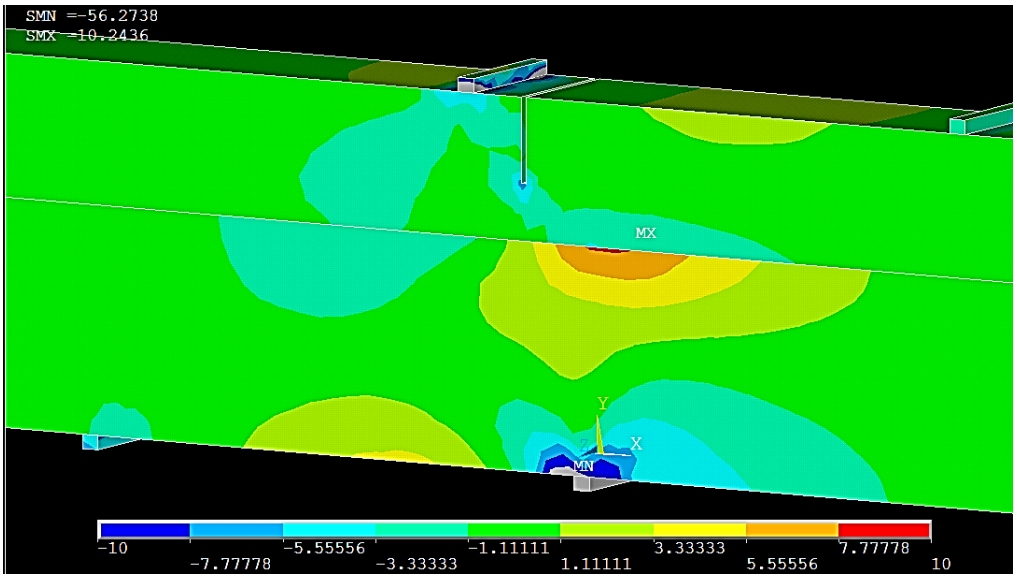

Figure 6.20 X-Component of Stress

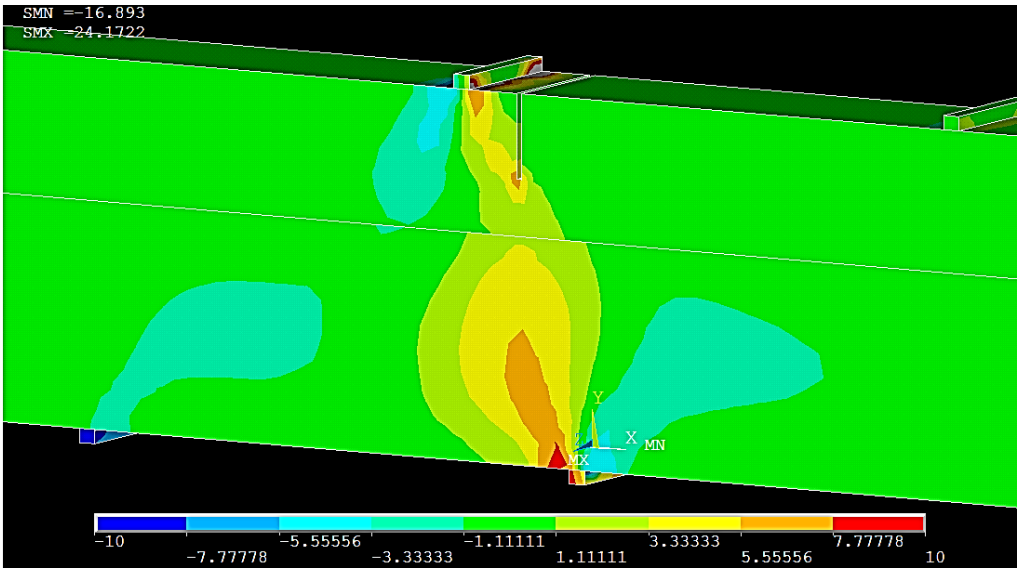

Figure 6.21 Shear Stress

Table 6.13 Crack Development at Onset Cracking Load and Peak Load

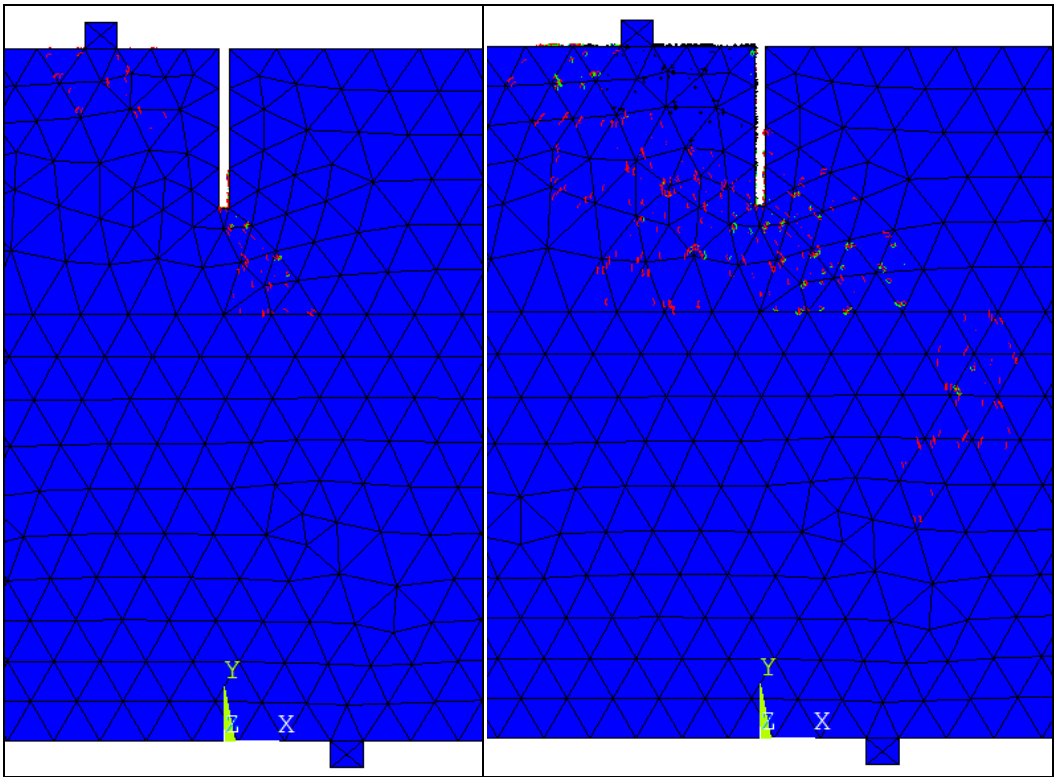

Crack Initiation at Sub-step 7 (56kN)	Crack Propagation at Sub-step 10 (80kN)

6.4.2 Virtual Foundation Test

In the concrete foundation test, the FE mesh engaged symmetry in the thickness direction by modelling 50mm of the beam, half of the full thickness, as illustrated in Figure 6.22. The concrete material properties in Table 6.12 were employed. The cement bonded material (CBM), the compacted gravel and the rubber pad were simulated using the following parameters in Table 6.14. The neoprene rubber with the hardness of 70A shore and the thickness of 20mm was tested in CBR machine, from which the elastic modulus was evaluated. The remaining parameters in the table were estimated based on engineering judgement.

Table 6.14 Foundation Simulation Input Parameters

	Rubber	CBM	Gravel Base
E (MPa)	13	5000	50
v	0.49	0.3	0.3

The contact pair of TARGE170 and CONTA174 with the roughened SBRPMConOPCC interface parameters in Section 6.3.6 was created. The load was increased to 100kN in 10 equal sub-steps, each step being equal to 10kN.

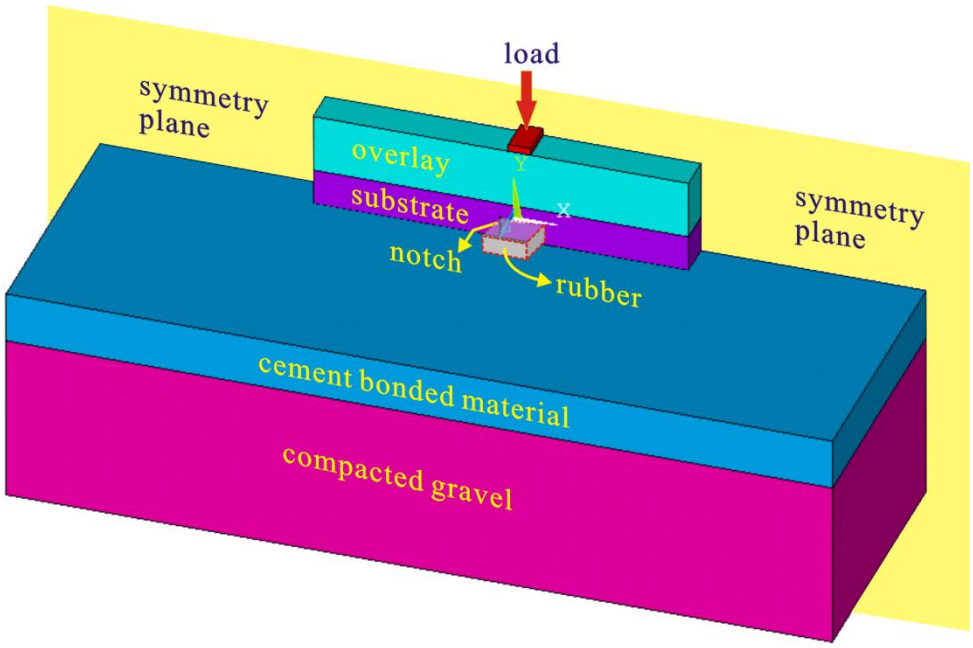

Figure 6.22 General Layout of Foundation Test Simulation

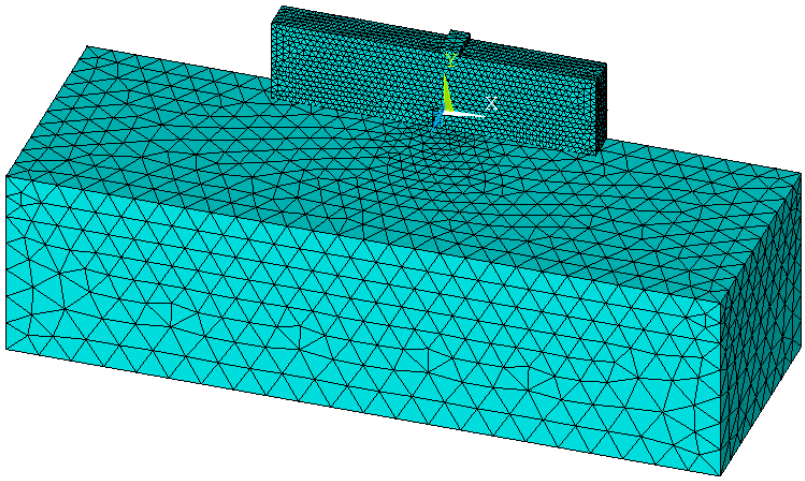

Figure 6.23 Meshing Plot

The test was conducted upto the load of 45kN as per lab. As pictured in Figure 4.45, the SBRPMC composite beam with 30mm notch in substrate showed a hairline crack propagating from the notch tip upwards into the overlay towards the loading position. The direction and extend of cracking in sub-step 5 (50kN) appears to be in harmony with the lab

results. The FE model predicted the crack to continue developing towards the loading point, accompanied by more smeared cracks (Table 6.15).

Table 6.15 Crack Propagation in Foundation Test

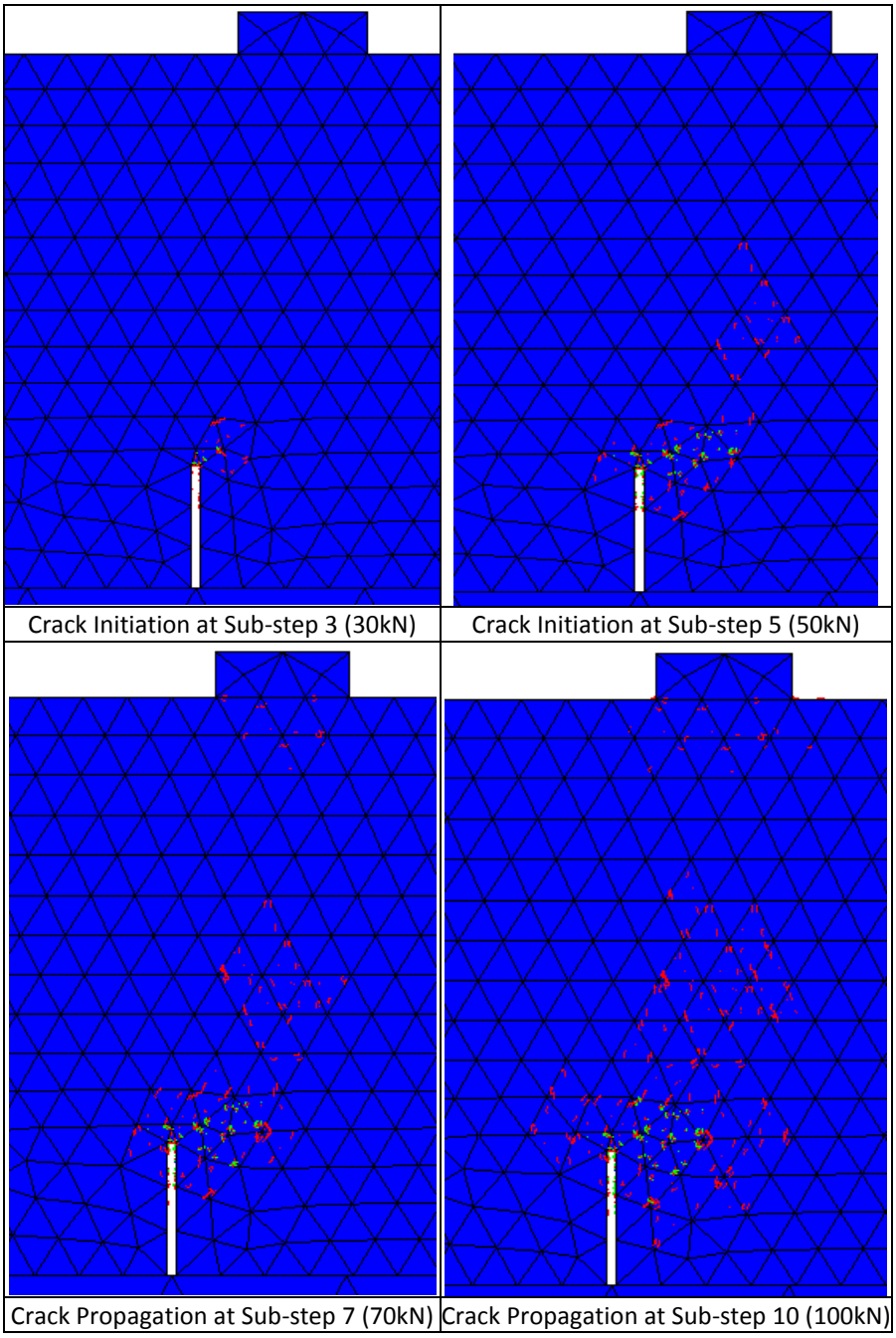

6.5 Modelling of BCO in Pavement

So far it has been proved that the new overlay material has superior mechanical properties over the conventional OPCC overlay in both the SNSBT and the foundation test. The

corresponding simulations achieved close resemblance to the experimental results. Based on the developed models, a typical pavement structure with reflective cracking was simulated to compare the stress state and displacement level of the two overlay systems in reaction to monotonic vehicle wheel loading.

A typical pavement multi-layer structure was set up as in Figure 6.24 – in the order from top down as overlay, continuously reinforced concrete pavement (CRCP), hydraulically bound material (HBM) and sub-grade. Only traffic loading is considered in this case. A typical Drucker-Prager material property (cohesion c = 0.001MPa, angle of internal friction ϕ = 32°) (Darestani et al. 2007) was employed for the soil behaviour in the sub-grade. It extended 1m wider from the edge of the sub-base. Vertical and horizontal displacement controls were applied on the base and side of the sub-grade respectively. The rest of the layers were assumed to contain isotropic elastic materials, the elastic modulus and poisson's ratios of which are listed in As predicted, the maximum stress occured at the crack tip. The maximum vertical displacement takes place to the right of the crack above the void as shown in Figure 6.25. As the overlay thickness increases from 100 to 200, the shear mode stress intensity factor K_{II} and the maximum vertical displacement decreased. It is manifested that increasing overlay thickness can effectively reduce the susceptibility to shear failure and reflective cracking and minimise the differential displacement at underlying joints/ cracks. On the other hand, K_I suffered a slight increase, as shown in Figure 6.26. Considering the ratio $\gamma = o/d$; where o is the distance between vehicle loading and crack, and d is the remaining thickness above crack tip, as γ decreases, the dominant failure mode transforms from shear to flexure. When a vehicle load is located right above the crack (o = 0), the flexural failure mode dominants. In this simulation, although o was fixed, the increasing overlay thickness led to a larger γ ratio, indicating the same tendency of transforming from mode II to mode I. Hence, a slight increase in K_I was evident.

Comparing the performance between SBRPMC and OPCC overlay systems, shearing is the dominant failure mode in both cases. Since the crack tip located in the OPCC substrate, the K_{IC} and K_{IIC} values in OPCC were employed as the crack propagation criteria, as shown by the dash lines in Figure 6.27. In this design case it dictates a safe thickness design of approx. 170mm in OPCC overlay system and 150mm in SBRPMC overlay system to resist the reflective cracking in the CRCP. SBRPMC showed little advantage of reducing the overlay

thickness compared to the OPCC overlay. The slight reduction in overlay thickness is probably attributed to the enhanced stiffness in SBRPMC. However, it is believed that the advanced cracking resistance of SBRPMC is activated only when the crack is present in the overlay itself. Hence the following simulation was conducted.

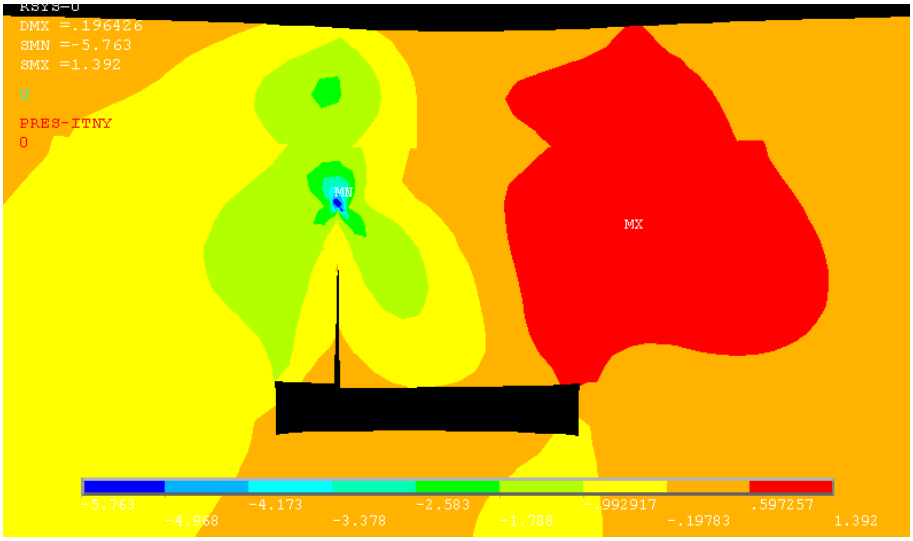

Figure 6.25 Pavement Model Crack in CRCP Shear Stress S_{XY} (Deformation × 100)

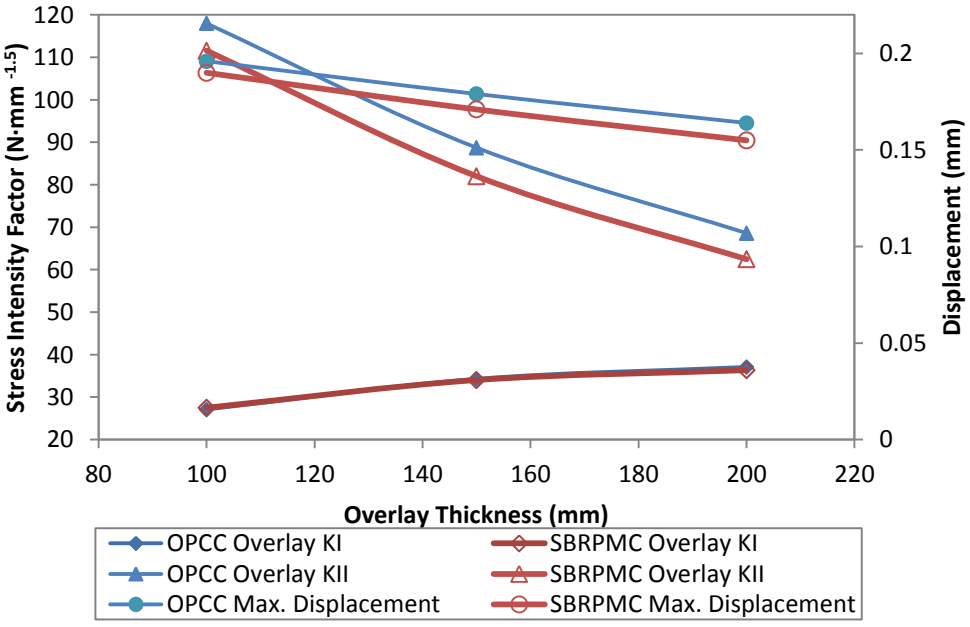

Figure 6.26 Comparison Between OPCC and SBRPMC Overlay

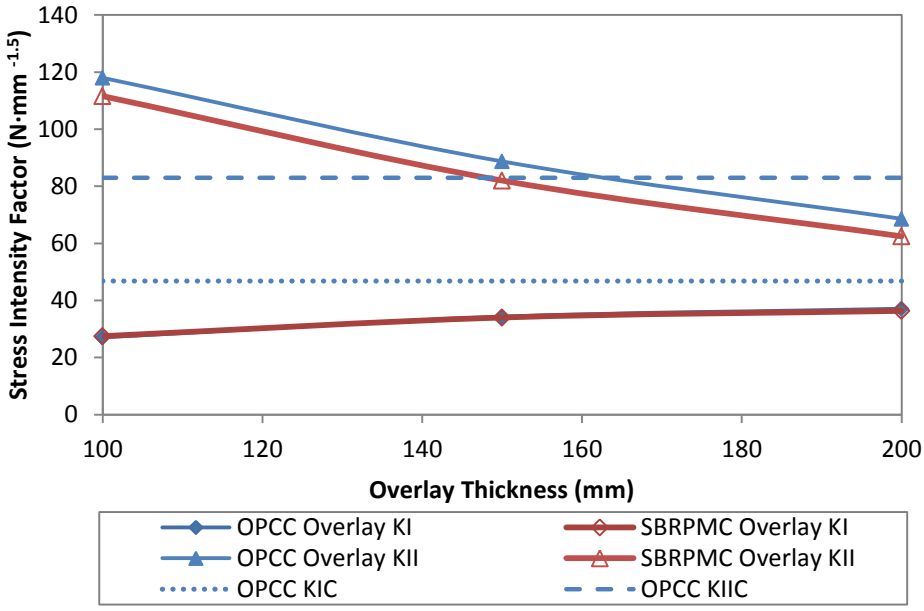

Figure 6.27 SIF in OPCC /SBRPMC Overlay System Compared with Critical SIF

To examine the overlay performance after the crack has extended to the overlay, a developing crack of various lengths was introduced in the 150mm thick overlay. The cohesive zone model was applied on the crack faces in the SBRPMC overlay to simulate the crack bridging effect as per Section 6.3.3. Again, the relevant interface properties were applied for OPCC overlay and SBRPMC overlay respectively, as defined in Section 6.3.6. The crack deformation and the shear stress contours are shown in Figure 6.28.

The SIFs and their critical values in OPCC and SBRPMC were plotted against crack depths and ligament depth, as shown in Figure 6.29. As the crack was approaching the surface, the rise in K_{II} and crack tip shear stress was evident. The dotted lines represent the critical SIFs. The SBRPMC managed to enhance both K_{IC} and K_{IIC} values, compared to OPCC, although the fibre bridging effect appears more effective in reducing the K_{IC}. As a matter of fact, the direct result from fibre bridging is to prevent cracks from opening. The reduction in crack sliding (mode II SIF) is a secondary and indirect result from steel fibre reinforcement.

If $K_{II} = K_{IIC}$ is adopted as the failure criterion, the overlay fractures when the K_{II} curve meets the corresponding K_{IIC} lines. In other words, the SBRPMC overlay system appeared to reach the critical value when the crack was 90mm deep into the overlay (ligament depth of 60mm). In contrast, the OPCC overlay fractured when the crack was only 30mm into the overlay. It is manifested that the fibre bridging effect in conjunction with the enhanced mechanical

properties in the SBRPMC have a significant advantage in controlling the deformation and the stress concentration at the crack tip.

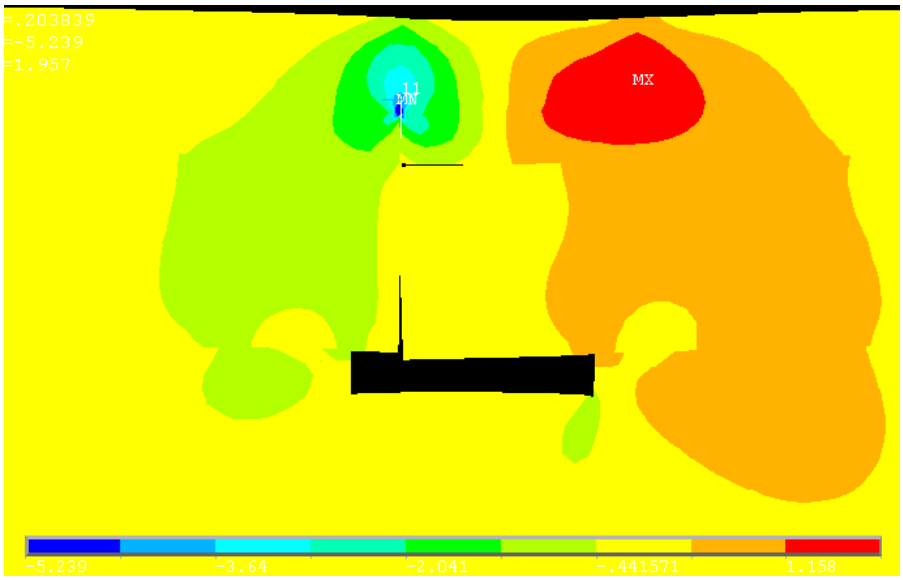

Figure 6.28 Pavement Model Crack in Overlay Shear Stress S_{XY} (Deformation × 100)

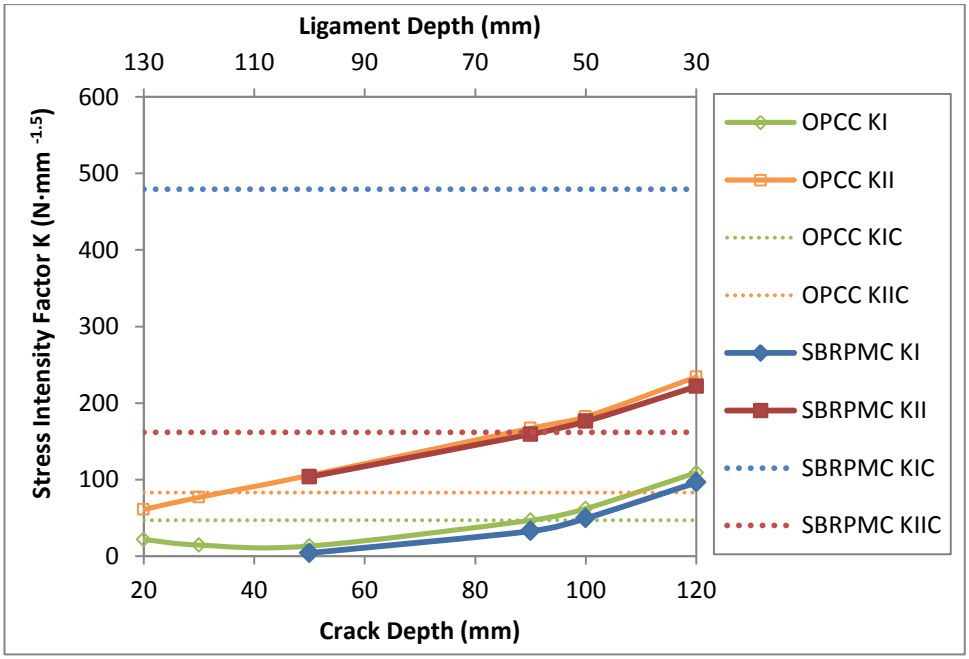

Figure 6.29 Reflective Cracking in Pavement Overlay

. The overlay thickness varies from 100, 150 to 200. A hairline crack was created in the mid-span developing from the base of CRCP, where a void (30 × 250mm) was introduced in the adjacent HBM simulating a local defect due to rocking and pumping effect. A typical

inflated tyre pressure of 0.7MPa was applied immediately to the right of the crack on the pavement top distributed over a length of 0.25m.

Table 6.16 Basic Input Data of Pavement Layers

Material		E Modulus (MPa)	Poisson's Ratio	Thickness (mm)
Overlay	OPCC	25195	0.21	100,150,200
	SBRPMC	32365	0.187	
CRCP		25195	0.21	200
HBM		5000	0.2	150
Sub-grade		33	0.4	1000

The 6-node triangular element PLANE183 was deployed in this 2D fracture model. It is assumed that any well-developed cracks appearing on top of an existing worn pavement will be sealed or treated at the stage of site preparation. However, the underlying cracks could be overlooked in the initial site investigation, which potentially could reflect upwards at a later stage. Hence, the initial crack tip was assumed to be 50mm below the top of CRCP layer. Contact elements with the interface properties defined in Section 6.3.6 were employed at the overlay – CRCP interface.

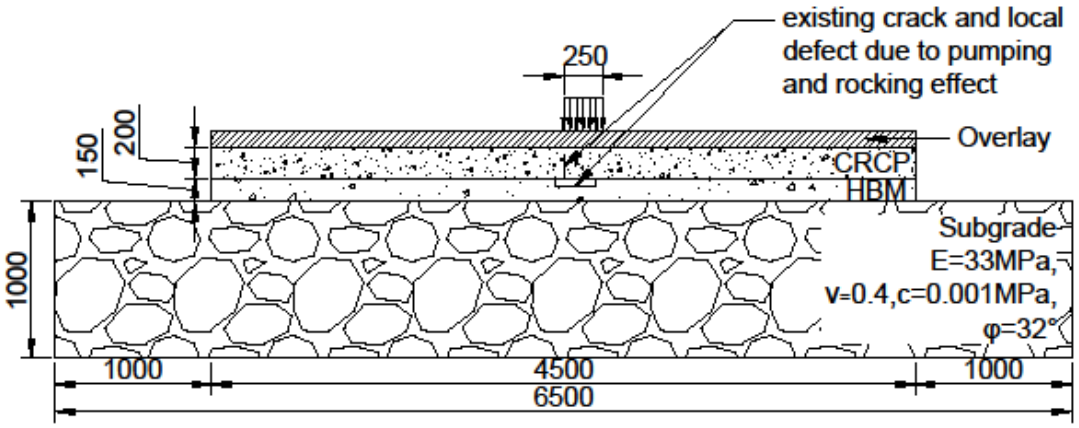

Figure 6.24 Diagram of a Concrete Pavement Structure. in FEA

As predicted, the maximum stress occured at the crack tip. The maximum vertical displacement takes place to the right of the crack above the void as shown in Figure 6.25. As the overlay thickness increases from 100 to 200, the shear mode stress intensity factor K_{II} and the maximum vertical displacement decreased. It is manifested that increasing overlay thickness can effectively reduce the susceptibility to shear failure and reflective cracking and minimise the differential displacement at underlying joints/ cracks. On the other hand, K_I suffered a slight increase, as shown in Figure 6.26. Considering the ratio $\gamma = o/d$; where o is the distance between vehicle loading and crack, and d is the remaining thickness above crack tip, as γ decreases, the dominant failure mode transforms from shear to flexure. When a vehicle load is located right above the crack (o = 0), the flexural failure mode dominants. In this simulation, although o was fixed, the increasing overlay thickness led to a larger γ ratio, indicating the same tendency of transforming from mode II to mode I. Hence, a slight increase in K_I was evident.

Comparing the performance between SBRPMC and OPCC overlay systems, shearing is the dominant failure mode in both cases. Since the crack tip located in the OPCC substrate, the K_{IC} and K_{IIC} values in OPCC were employed as the crack propagation criteria, as shown by the dash lines in Figure 6.27. In this design case it dictates a safe thickness design of approx. 170mm in OPCC overlay system and 150mm in SBRPMC overlay system to resist the reflective cracking in the CRCP. SBRPMC showed little advantage of reducing the overlay thickness compared to the OPCC overlay. The slight reduction in overlay thickness is probably attributed to the enhanced stiffness in SBRPMC. However, it is believed that the advanced cracking resistance of SBRPMC is activated only when the crack is present in the overlay itself. Hence the following simulation was conducted.

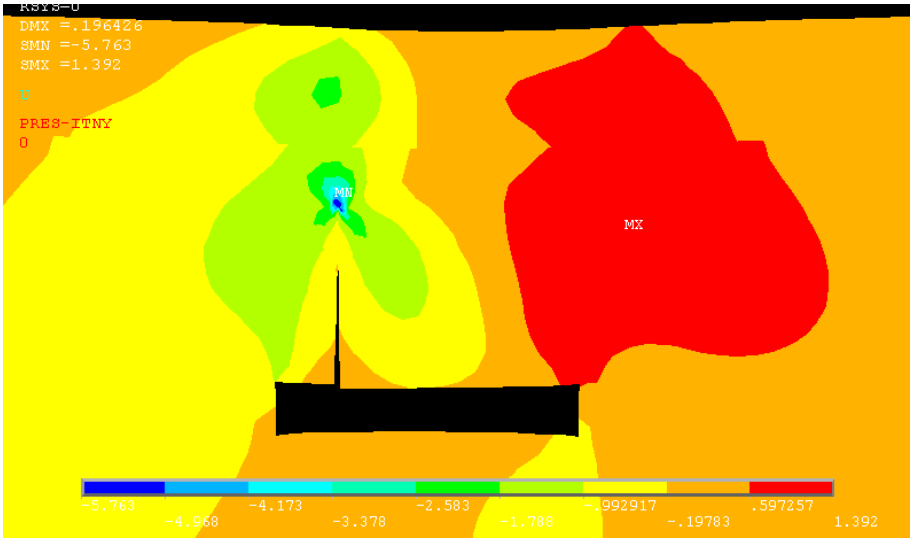

Figure 6.25 Pavement Model Crack in CRCP Shear Stress S_{XY} (Deformation × 100)

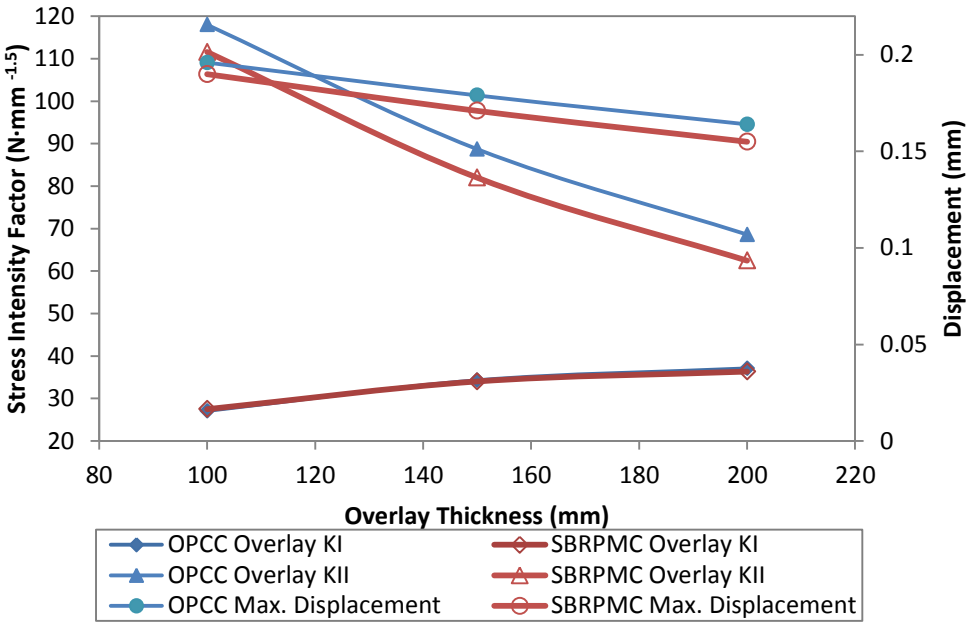

Figure 6.26 Comparison Between OPCC and SBRPMC Overlay

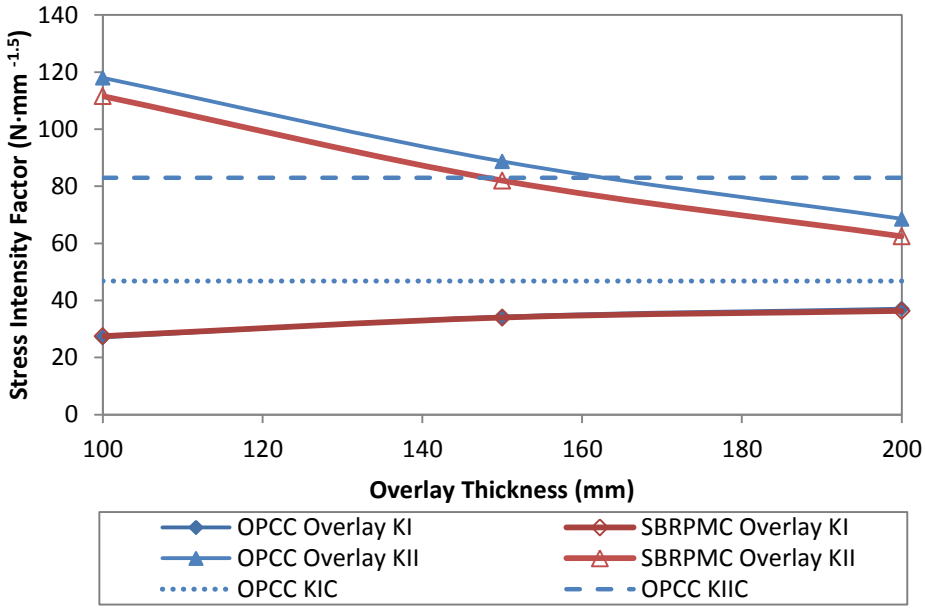

Figure 6.27 SIF in OPCC /SBRPMC Overlay System Compared with Critical SIF

To examine the overlay performance after the crack has extended to the overlay, a developing crack of various lengths was introduced in the 150mm thick overlay. The cohesive zone model was applied on the crack faces in the SBRPMC overlay to simulate the crack bridging effect as per Section 6.3.3. Again, the relevant interface properties were applied for OPCC overlay and SBRPMC overlay respectively, as defined in Section 6.3.6. The crack deformation and the shear stress contours are shown in Figure 6.28.

The SIFs and their critical values in OPCC and SBRPMC were plotted against crack depths and ligament depth, as shown in Figure 6.29. As the crack was approaching the surface, the rise in K_{II} and crack tip shear stress was evident. The dotted lines represent the critical SIFs. The SBRPMC managed to enhance both K_{IC} and K_{IIC} values, compared to OPCC, although the fibre bridging effect appears more effective in reducing the K_{IC}. As a matter of fact, the direct result from fibre bridging is to prevent cracks from opening. The reduction in crack sliding (mode II SIF) is a secondary and indirect result from steel fibre reinforcement.

If $K_{II} = K_{IIC}$ is adopted as the failure criterion, the overlay fractures when the K_{II} curve meets the corresponding K_{IIC} lines. In other words, the SBRPMC overlay system appeared to reach the critical value when the crack was 90mm deep into the overlay (ligament depth of 60mm). In contrast, the OPCC overlay fractured when the crack was only 30mm into the overlay. It is manifested that the fibre bridging effect in conjunction with the enhanced mechanical

properties in the SBRPMC have a significant advantage in controlling the deformation and the stress concentration at the crack tip.

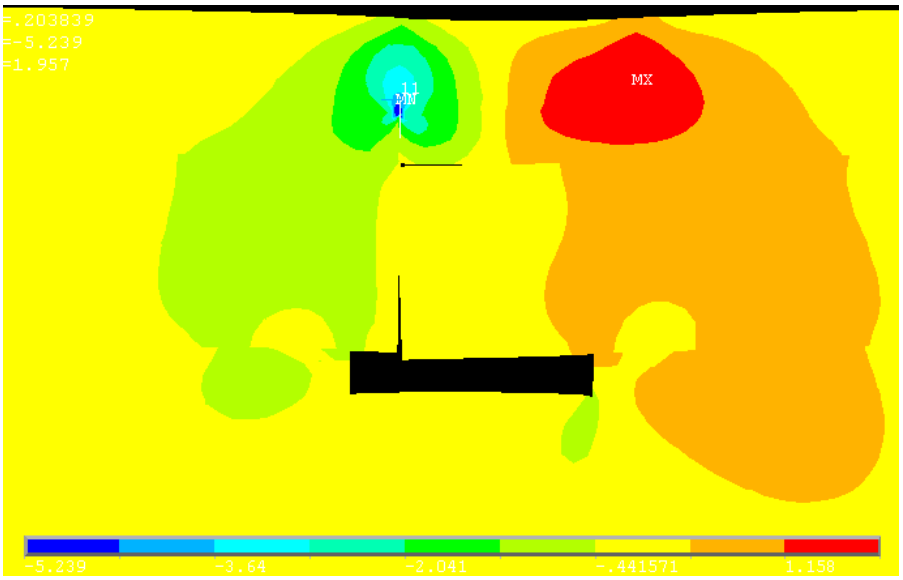

Figure 6.28 Pavement Model Crack in Overlay Shear Stress S_{XY} (Deformation × 100)

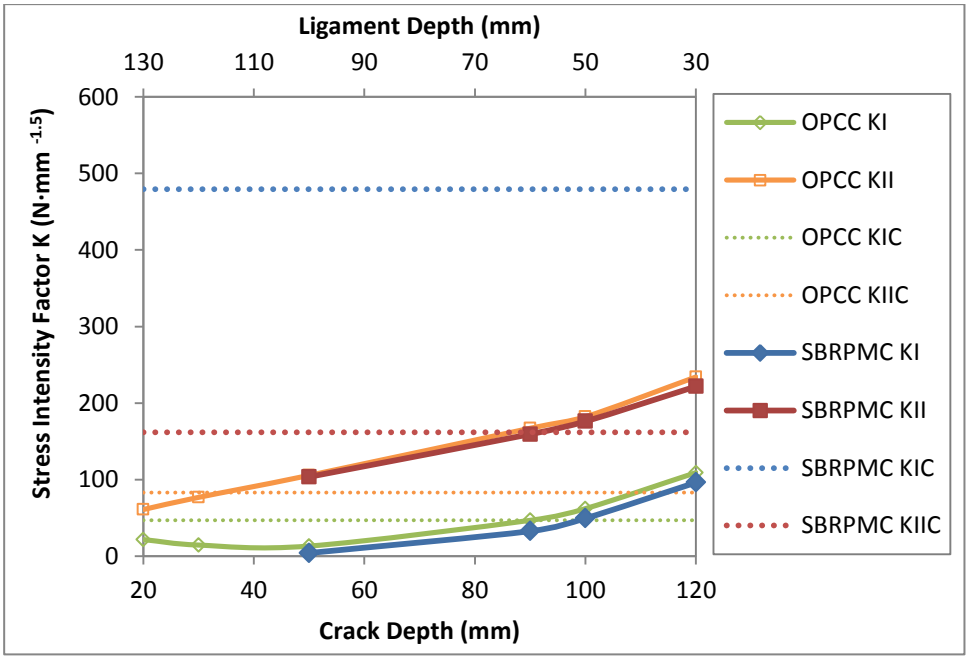

Figure 6.29 Reflective Cracking in Pavement Overlay

Moreover, one single sharp crack was assumed in the SBRPMC overlay in order to calculate the crack tip SIF. However, if the phenomenon of multiple cracking is taken into consideration, the stress concentration at any crack tip could be deviated and considerably

reduced. Therefore, a safety margin is allowed in the above simulation. The results are valuable in understanding the behaviour of the “green” overlay system under a typical shear loading condition and provide an important baseline for future verifications in large-scale field trials.

CHAPTER 7 CONCLUDING REMARKS AND FUTURE WORK

7. Conclusions and Future Work

Based on the experimental and numerical work illustrated in the previous chapters, the research has reached a number of useful conclusions regarding the continuous development of the pavement repair and strengthening system (PRSS). The aim of the PRSS is to provide a cost effective and technologically efficient method for concrete pavement repairs. Existing investigations and reports on the application of traditional BCO identify the potential potholes, such as poor bonding with substrate, inadequate crack control to prevent reflective cracking, inadequate resistance to flexure and shear. Research at Coventry University (CU) has been directed towards perfecting the PRSS with careful attention to the above-mentioned design parameters as well as the practical issues during the construction phase.

It is appreciated that the structural performance and application of the PRSS is not fully underwritten by the current research. There are still some points to be looked at and improvements to be done in the future.

7.1 Scientific Contributions of the Thesis

7.1.1 Experimental Investigation

1. The key to success lies on the development of a material mix with superior mechanical properties and the versatility to enable fast construction. Based on existing literature and previous research at CU, the overlay mix has been designed to incorporate some stimulating elements such as steel fibres, polymers and at the same time achieve roller compactability. The integrated new mix is referred to as “steel fibre reinforced, roller-compacted, polymer modified, bonded concrete overlays (SF-RC-PM-BCO)”. To achieve the versatility and a good bond with substrate, a mix design method (M-L method) has been developed to determine the optimal water content in SF-RC-PM-BCO. It was experimentally verified to produce a satisfactory mix, meeting the criteria of “roller compactability”, “paver placability” and adequate bond to underlying concrete. The mix developed with the above method is suitable for use with fast construction technologies and can demonstrate superior structural integrity in combination with the old pavement.

2. The shear capacity of the developed mix was scrutinized experimentally and proven to be higher than the conventional concrete overlay materials. Explicit evaluation of shear capacity is a highly complex task. Existing literature points out that shear strength of concrete always present large scatter and could be influenced by concrete heterogeneity, reinforcement details, boundary conditions and test configurations. The single notch shear beam test was developed specifically to evaluate the material performance under mixed mode conditions with shear being the predominant mode. Not only it enabled the acquisition of a number of key strengths and fracture parameters but also allowed for analysis on a progressive failure process.
3. The addition of steel fibre managed to enhance concrete strength and ductility, despite the fact that the compressive strength was not found to be as sensitive to the amount of steel fibres as the shear, flexural and splitting tensile strengths. The inclusion of steel fibre provides an enhanced post-peak performance. The load bearing capacity of the steel fibre reinforced specimens did not drop rapidly after reaching the peak load, as it would occur in conventional concrete. Instead, the specimens continued to carry a large proportion of the peak load for a considerably long time before gradually losing their load bearing capacity. The fracture energy of SFRC was ten times larger than that of OPCC or plain PMC. It was evident that the concrete specimens could continue to resist shear even after a crack opens.
4. The appearance of first crack was found to be at a higher load than that of OPCC or plain PMC. Therefore, the onset cracking resistance was also increased. In SFR-RC-PMC, a relationship was proposed to predict the onset shear strength based on the plain concrete strength, fibre properties, fibre content and fibre "dispersion coefficient". This has been verified against a series of mixes and a very good accuracy was attained. The "magical" properties of steel fibres only work when the latter bridge over and keep the two parts of the material together, resisting their tendency to break up. In other words, the fibre orientation in concrete is extremely important and it is largely dependent on the direction of compaction. A compaction in z-direction would result in the fibres lying within a small angle to the x-y plane. Hence, the SFRC performance could be compromised if failure tends to take place in that plane. This special observation in compacted SFRC has been quantified using the term "dispersion coefficient" and addressed in the above-mentioned relationship.

5. Most of the current design formulae on nominal shear strength are for conventional reinforced concrete and are based on empirical results and regression analysis. On the contrary, SFRC presents a very different strain hardening and softening behaviour from conventional concrete. An effective analytical model for SFRC is not available to date, due to the complexity in cracking trajectory and failure mechanism in SFRC. A semi-empirical model incorporating the crack bridging law and the energy balancing principle to evaluate the nominal shear strength in SFRC was developed. It was anticipated that the work done by the shear force onto the sliding displacement plus the moment to the rotation at the crack tip, is equal to the crack bridging effort provided by the steel fibres on the curved cracking plane. A close resemblance was achieved. It is hoped that this model can shed some light on a new way of looking at the shear performance of SFRC.
6. It was shown that the superior quality of the new overlay material provided an efficient resistance to reflective cracking. The initial cracking resistance was considerably higher than that of the conventional concrete. Moreover, following the appearance of reflective cracks, the overlay can serve as an effective crack control measure and maintain a suitable load carrying capacity.
7. High early age strength was achieved in the PMC specimens, with generally 80% - 95% of the 28-day strength developed within the first 3 days. This signals that the PRSS system has the prospect potential of early opening to traffic, which adds to the advantages of being a sustainable and economical solution compared to traditional pavement rehabilitation methods.
8. The SF-RC-PMC was proved to be at least twice more efficient than the OPCC, judging by (a) onset shear strengths; (b) ultimate shear strengths and (c) critical, Mode II, stress intensity factor, K_{IIC}. The introduction of steel fibres managed to prevent cracks from opening and hence, improved the crack resistance in Mode I. In contrast, steel fibres did not behave as dowel bars. They effectively keep the crack closed contributing to the shear resistance in an indirect manner. As a result, the K_{IC} and K_{IIC} were increased by approx. 10 times and 1.4 times respectively, by adding 1.5% steel fibre (by volume) in the mix.
9. The mix design method (M-L method) developed in this study, laboratory testing data and recorded performance are instructive for the industry, and for future development of pavement overlay design guidance.

7.1.2 Finite Element Study

10. An unbonded overlay system may be able to reduce the level of stress concentration at the crack tip and relax the stresses a bit. However, it will not be able to utilize the remaining strength in the substrate and consequently, will lead to greater overlay thickness and a less efficient rehabilitating program. On the other hand, an effectively bonded interface will enable the composite system to behave simultaneously and combine its integrity. Hence, the stress intensity factors at the crack tip located in the underlying layer appeared to increase with the friction coefficient.
11. The progressive failure process was successfully simulated using finite element modelling techniques. The stresses, deformations and stress intensity factors were obtained at various crack tip positions. The fibre bridging effect was replicated by the cohesive crack model, the highlight of which was a set of very informative video clips demonstrating the crack propagation and bridging process. It is manifested that increasing overlay thickness can effectively reduce the susceptibility to shear failure and reflective cracking and minimise the differential displacement at underlying joints/ cracks.
12. It is essential to apply the cohesive zone model (CZM) in fracture simulations of SNSBT to reflect the fibre bridging effect and aggregate interlock at the crack interface. Modelling the crack as a complete discontinuity led to inappropriately high SIF results. On the contrary, by incorporating the residual material mechanical properties of the cracks using the CZM, the simulation not only showed good results but also demonstrated the transformation from mode II into mode I as the crack proceeded.
13. Nomographs deduced from finite element analysis showed the influence of the overlay thickness on the maximum vertical crack movement and shear resistance under traffic loads. It was predicted that when the crack tip is located in the underlying substrate, the overlay thickness design can benefit little from employing the new overlay material. A reduction of thickness from 170mm to 150m was achieved using finite element modelling techniques. The superior crack resistance of the new overlay is significantly more pronounced when the crack extends into the overlay itself. As reflective cracking is inevitable, the crack will eventually propagate

into the overlay. The multi-cracking feature of SFRC overlay can provide a safe buffering zone and an effective crack control.

14. Good agreement was achieved between the 3D numerical simulations of the SNSBT and the observed experimental response. Close resemblances were also obtained between the FE simulation results of foundation tests and lab observations. Those FE models are valuable in understanding the behaviour of the "green" overlay system under a typical shear loading condition and provide important baselines for future verifications in large-scale field trials. Finally, they can be the foundation for optimum overlay design.

7.2 Limitations and Future Works

The experimental work carried so far was restricted to laboratory level. With the results and information collected it is apparent that the overlay performance was successfully analyzed and a good understanding was achieved. The significant follow-up work would be to evaluate the PRSS system in full scale field tests. The results assisted by the laboratory findings, could be used to identify practical issues and rectify the design process as needed. Furthermore, long term effectiveness and overall economy performance will need to be monitored and evaluated for justification.

The intrinsic nature of pavement design is based on limiting traffic and residual stress conditions in the concrete slab before fatigue cracking becomes unacceptable, which also defines the end of the pavement life. Due to limited laboratory facilities associated with cyclic loading, this research focuses on the static structural loads. A valid fatigue model will be needed as an extended study for this work.

A reflective crack caused by shear fracture usually occurs when there is already a defect in the sub-base layer. It is considered vital to perform a site investigation prior to constructing the overlay. The falling weight deflectometer method may be employed to find any potential underlying defects. The latter must be classified and treated before overlaying.

Despite the effort made and care taken in the laboratory to obtain of the most accurate results, there are some limitations and room for improvement. Although the sand patch method was used to obtain the surface roughness from the top of substrate material, the

method was found unsuitable for the cracking plane resulting after shear tests. So far only gridline measurements were taken for the crack trajectories, from which the potential surface roughness was estimated. In future experimental work, a delicate scanning system could be advantageous in quantifying the surface roughness and investigating the influence of various components in shear resistance.

References

AASHTO (1993) AASHTO GDPS-4-M Guide for Design of Pavement Structures and 1998 Supplement. America: American Association of State and Highway Transportation Officials

ACI Committee 207 (1999) Roller-Compacted Mass Concrete. United States of America: American Concrete Institute

ACI Committee 318 (2002) Building Code Requirements for Structural Concrete (ACI 318-02) and Commentary (318R-02). Farmingtong Hills, Michigan, the United States: American Concrete Institute

ACI Committee 325 (2006) Concrete Overlays for Pavement Rehabilitation. [2006] available from <http://www.concrete.org/pubs/newpubs/3251306_2pager.pdf> [09 November 2009]

ACI Committee 548 (2003) Polymer-Modified Concrete: American Concrete Institute

American Concrete Pavement Association (2014). Guide to Concrete Overlay Solutions. TB021.03P. National Concrete Pavement Technology Center

American Concrete Pavement Association (ACPA) (2000) Traffic Management - Handbook for Concrete Pavement Reconstruction and Rehabilitation, Engineering Bulletin EB213P. Skokie, IL: American Concrete Pavement Association

Anon(1994) 'HD 32/94 Maintenance of Concrete Roads'. in Design Manual for Roads and Bridges. ed. by AnonUK: The Highways Agency

Anon(2002) JSCE Guidelines for Concrete no. 3, Structural Performance Verification, Standard Specification for Concrete Structures. Japan: Japan Society of Civil Engineers (JSCE)

ANSYS (2013) ANSYS Mechanical APDL 14.0 User's Manual

Arrea, M. and Ingrafea, A.R. (1982) 'Mixed-mode Crack Propagation in Mortar and Concrete'. Report No. 81-13. Dept. of Sturct. Engrg., Cornel Univ., Ithaca, N.Y., 143

ASTM (1999) ASTM Designation: C1439-99 Standard Test Methods for Polymer-Modified Mortar and Concrete. 1st edn. United States: ASTM International

ASTM (2001) ASTM Designation: C138/C138M-01a Standard Test Method for Density (Unit Weight), Yield, and Air Content (Gravimetric). United States: ASTM International

ASTM (2005) ASTM Designation: D5379/D5379M-05 Standard Test Method for Shear Properties of Composite Materials by the V-Notched Beam Method. 2005th edn. United States: ASTM International

ASTM (2006) ASTM Designation: C1170-06 Standard Test Method for Determining Consistency and Density of Roller-Compacted Concrete using a Vibrating Table. United States: ASTM International

ASTM (2010) ASTM Designation: C469/C469M-10 Standard Test Method for Static Modulus of Elasticity and Poisson's Ratio of Concrete in Compression. United States: ASTM International

ASTM D1557 (2012): Standard Test Methods for Laboratory Compaction Characteristics of Soil Using Modified Effort, West Conshohocken, PA: ASTM International

Bache, H. H. (1987) Report 41 Compact Reinforced Composite - Basic Principles. Aalborg Portland, Denmark: Composite Materials, 87

Barr, B. and Derradj, M. (1990) 'Numerical Study of a Shear (Mode II) Type Test Specimen Geometry'. Engineering Fracture Mechanics 35 (1/2/3), 171-180

Bazant, Z. P. and Pfeifer, P. A. (1986) 'Shear Fracture Tests of Concrete'. Materials and Structures 19, 111-121

Beaudoin, J. J. (1990) Handbook of Fiber-Reinforced Concrete. the United States of America: Noyes Publications, 57-63

Beeby, A. W. and Narayanan, R. S. (1995) Designers' Handbook to Eurocode 2 Part 1.1, Design of Concrete Structures. London: Telford

Bekaert (2012) Dramix 5D4D3D [online] available from <http://www.bekaert.com/en/Product%20Catalog/Application/Construction/Concrete%20reinforcement.aspx> [April 2012]

British Standards Institution (1990a) BS 812-110:1990 Testing Aggregates. Methods for Determination of Aggregate Crushing Value (ACV). United Kingdom: British Standards Institution

British Standards Institution (1990b) BS 812-112:1990 Testing Aggregates. Methods for Determination of Aggregate Impact Value (AIV). United Kingdom: British Standards Institution

British Standards Institution (1997) BS 8110-1:1997 Structural use of Concrete. Code of Practice for Design and Construction.: British Standards Institution

British Standards Institution (1998) BS 598-105:1990 Sampling and Examination of Bituminous Mixtures for Roads and Other Pavement Areas. Methods of Tests for Determination of Texture Depth. United Kingdom: British Standards Institution

British Standards Institution (2000) BS EN 1097-6:2000 Tests for Mechanical and Physical Properties of Aggregates. Determination of Particle Density and Water Absorption. United Kingdom: British Standards Institution

British Standards Institution (2002) BS1377-4:1990 Methods of Test for Soil for Civil Engineering Purposes. Compaction-Related Tests. United Kingdom: British Standards Institution

British Standards Institution (2009a) BS EN 12390-6:2009 Testing Hardened Concrete. Tensile Splitting Strength of Testing Specimens.: British Standards Institution

British Standards Institution (2009b) PD 6681-1:2009 Published Document Aggregates. Aggregates for Concrete - Guidance on the use of BS EN 12620. Second edn. United Kingdom: British Standards Institution

British Standards Institution (2009c) BS EN 12390-7:2009 Testing Hardened Concrete. Density of Hardened Concrete. United Kingdom: British Standards Institution

British Standards Institution (2010) BS EN 12350-10:2010 Testing Fresh Concrete. Self-compacting Concrete.: British Standards Institution

Canadian Standards Association Technical Committee on Reinforced Concrete Design (1994) Design of Concrete Structures A23.3-94. Rexdale, Ontario, Canada: The Canadian Standards Association

Carpinteri, A. (1989) 'Size Effects on Strength, Toughness and Ductility'. Journal of Engineering Mechanics 115, 1375-1392

Clear, K. C. and Chollar, B. H. (1978) FHWA-RD-78-35 Styrene-Butadiene Latex Modifiers for Bridge Deck Overlay Concrete: National Technical Information Service

Delatte Jr., N. J. (2008) Concrete Pavement Design, Construction, and Performance. UK: Taylor & Francis, 110

Delatte Jr., N. J. and Fowler, D. W. (1998) 'Investigating Performance of Bonded Concrete Overlays'. Journal of Performance of Constructed Facilities 12 (2), 62

Design Code, Comité Euro-International du Béton (1993) CEB-FIP Model Code 1990. London: Thomas Telford Services Limited

Djazmati, B. and Pincheira, J. A. (2004) 'Shear Stiffness and Strength of Horizontal Construction Joints'. ACI Structural Journal 101 (4), 484-493

Donegan, J. (2012) 'Quiet Revolution Underway'. Insitu Engineering Special Report, 6-7

Gastebled, O. J. and May, I. M. (2001) 'Fracture Mechanics Model Applied to Shear Failure of Reinforced Concrete Beams without Stirrups'. ACI Structural Journal 98 (2), 184-190

Geers, M. G. D., de Borst, R., and Peerlings, R. H. J. (2000) 'Damage and Crack Modeling in Single-Edge and Double-Edge Notched Concrete Beams'. Engineering Fracture Mechanics 65 (2-3), 247-261

Hamadi, Y. D. and Regan, P. E. (1980) 'Behaviour in Shear of Beams with Flexural Cracks'. Magazine of Concrete Research 32 (111), 67-78

Hughes, B. (2003) 'A New Look at Rigid Concrete Pavement Design'. Transport 156 (1), 29-36

Hughes, B. P. (2006) 'Optimum Design of Sustainable Concrete Pavements'. Proceedings of the Institute of Civil Engineers: Engineering Sustainability 159 (3), 127-132

Hughes, B. P. and Lubis, B. (1996) 'Roller Compacted Sheets of Polymer Modified Mortar'. Cement and Concrete Composites 18 (1), 41-46

Hutchinson, R. L. (1982) 'Resurfacing with Portland Cement Concrete'. National Cooperative Highway Research Program, Synthesis of Highway Practice

Ingraffea, A. R. and Panthaki, M. J. (eds.) (1985) Proceedings of Finite Element Analysis of Reinforced Concrete Structures. 'Analysis of 'Shear Fracture' Tests of Concrete Beams' at Tokyo, Japan: American Society of Civil Engineers

Iosipescu, N. (1967) 'New Accurate Procedure for Single Shear Testing of Metals'. Journal of Materials 2 (3), 537-566

Iowa Department of Transportation (2000) Method of Test for Determining the Shearing Strength of Bonded Concrete. Iowa, the USA: Iowa Department of Transportation

Jayawickrama, P. W. and Lytton, R. L. (eds.) (1987) Proceeding of the 6th International Conference on Structural Design of Asphalt Pavements. 'Methodology for Predicting Asphalt Concrete Overlay Life Against Reflection Cracking' at Ann Arbor, Michigan, the United States. the United States

Jenq, Y. S. and Shah, S. P. (1988) 'Mixed Mode Fracture of Concrete'. International Journal of Fracture 38, 123-142

JSCE (1990) 'Method of Test for Shear Strength of Steel Fiber Reinforced Concrete (SFRC)'. Japan Society of Civil Engineer (SF6), 67-69

Kagaya, M., Suzuki, T., Kokubun, S., and Tokuda, H. (2001) 'A Study on Mix Proportions and Properties of Steel Fiber Reinforced Roller-Compacted Concrete for Pavements'. Proceeding of Japan Society of Civil Engineers 50 (669)

Karihaloo, B. L. (1995) Fracture Mechanics and Structural Concrete. London: Longman Group Ltd, 484-499

Kazimierowicz-Frankowska, K. (2008) 'Comparison of Stress and Strain States in Pavements with and without Reflective Cracks'. Journal of Transportation Engineering 134 (11), 483-492

Koutselas, K. (2010) Sustainable 'Green' Overlays for Strengthening and Rehabilitation of Concrete Pavements. Unpublished Degree of Doctor of Philosophy thesis or dissertation. Coventry, UK: Coventry University

Koutselas, K. (2010) Sustainable 'Green' Overlays for Strengthening and Rehabilitation of Concrete Pavements. PhD thesis. Coventry, UK: Coventry University

Leet, K. M. and Bernal, D. (1997) Reinforced Concrete Design: Conforms to 1995 ACI Codes. 3rd edn. New York; London: McGraw-Hill

Li, V. C., Ward, R., and Hamza, A. M. (1992) 'Steel and Synthetic Fibers as Shear Reinforcement'. ACI Materials Journal 89 (5), 499-508

Lin, Y. (2013) Optimum Design for "Green" Concrete Overlays - Flexural Failure. Unpublished PhD thesis or dissertation. Coventry, UK: Coventry University

Londhe, R. S. (2010) 'Experimental Investigation on Shear Strength of SFRC Beams Reinforced with Longitudinal Tension Steel Rebars'. Asian Journal of Civil Engineering (Building and Housing) 11 (3), 385-395

Mattock, A. H. and Hawkins, N. M. (1972) 'Shear Transfer in Reinforced Concrete – Recent Research'. Journal of the Prestressed Concrete Institute 17 (2), 55-75

McGhee, K. H. (1994) Portland Cement Concrete Resurfacing. Illustrated edn: Transportation Research Board

Mokarem, D. W., Galal, K. A., and Sprinkel, M. M. (2007) 'Performance Evaluation of Bonded Concrete Pavement Overlays After 11 Years'. Transportation Research Record: Journal of the Transportation Research Board 2007 (2005), 3-10

Nanni, A. and Johari, A. (1989) 'RCC Pavement Reinforced with Steel Fibers'. Concrete International 11 (3), 64-69

Narayanan, R. and Darwish, I. Y. S. (1987) 'Use of Steel Fibers as Shear Reinforcement'. ACI Structural Journal 84 (3), 216-227

National Concrete Pavement Technology Center (2010). Guide to Roller-compacted concrete pavements. America: Portland Cement Association, Page 2

National Concrete Pavement Technology Centre (2008) Guide to Concrete Overlays Solutions. Second edn. United States: American Concrete Pavement Association (ACPA)

Neocleous, K., Angelakopoulos, H., Pilakoutas, K., and Guadagnini, M. (2011) 'Fibre-Reinforced Roller-Compacted Concrete Transport Pavements'. Proceedings of the Institute of Civil Engineers: Transport 164 (TR2), 97-109

Nguyen-Minh, L. and Rovnak, M. (2011) 'New Formula for the Estimation of Shear Resistance of Fibre Reinforced Beams'. Canadian Journal of Civil Engineering 38 (1), 23-35

Nicolae, I. (1967) 'New Accurate Procedure for Single Shear Testing of Metals'. Journal of Materials, 2(3), 537-566

Ohama, Y. (1995) Handbook of Polymer-Modified Concrete and Mortars: Properties and Process Technology (Building Materials Science). the United States of America: Noyes Publications

Olubanwo, A. (2014) Optimum design for sustainable green bonded concrete overlays: failure due to shear and delamination. PhD thesis. Coventry University

Per Jonson and Bengt-Ake Hultqvist (2008) 'Measurement of Fuel Consumption on Asphalt and Concrete Pavements'. Swedish National Road and Transport Research Institute report, page 7

Reinhardt, H. W. and Xu, S. (1998) 'Experimental Determination of KIIC of Normal Strength Concrete'. Materials and Structures 31 (June), 296-302

RILEM (1989) Proceeding: 1st International RILEM Conference on Reflective Cracking in Pavements. Assessment and Control. CEP-LMC University de Liege, Belgium

RILEM (1993) Proceeding of 2nd International RILEM Conference on Reflective Cracking in PAvement - State of the Art and Design Recommendations. Belgium: E & FN Spon London

RILEM (1996) Proceeding of 3rd International RILEM Conference on Reflective Cracking in Pavements - Design and Performance of Overlay Systems. Maastricht, The Netherlands: E & FN Spon London

RILEM (2000) Proceeding PRO 11: 4th International RILEM Conference on Reflective Cracking in Pavement Research in Practice. Ottawa, Ontario, Canada

RILEM (2004) Proceedings pro037 : 5th International RILEM Conference on Cracking in Pavements: Mitigation, Risk Assessment and Prevention. Limoges, France

RILEM (2008) Pavement Cracking - Mechanisms, Modeling, Detection, Testing and Case Histories: Proceeding of 6th International RILEM Conference on Cracking in Pavements. Chicago, Illinois: Taylor & Francis Group, London

RILEM (2012) Proceeding of 7th International RILEM Conference on Cracking in Pavements: Mechanisms, Modeling, Testing, Detection and Prevention Case Histories. The Netherlands: Springer, London

Schlangen, E. (1993) 'Computational Aspects of Fracture Simulations with Lattice Models'. Fracture Mechanics of Concrete Sturctures. Proceedings FRAMCOS-2, 913-928

Shi, Z. (2004) 'Numerical Analysis of Mixed-Mode Fracture in Concrete using Extended Fictitious Crack Model'. Journal of Structural Engineering 130 (11), 1738-1747

Slater, E., Moni, M., and Alam, M. S. (2012) 'Predicting the Shear Strength of Steel Fiber Reinforced Concrete Beams'. Construction and Building Materials 26 (1), 423-436

Song, J., Kang, W., Kim, K. S., and Jung, S. (2010) 'Probablistic Shear Strength Models for Reinforced Concrete Beams without Shear Reinforcement'. Structural Engineering and Mechanics 34 (1), 15-38

Soroushian, P., Elyamany, H., Tlili, A., and Ostowari, K. (1998) 'Mixed-Mode Fracture Properties of Concrete Reinforced with Low Volume Fractions of Steel and Polypropylene Fibers'. Cement and Concrete Composites 20 (1), 67-78

Sudheer Reddy, L., Ramana Rao, N. V., and Gunneswara Rao, T. D. (2010) 'Shear Resistance of High Strength Concrete Beam without Shear Reinforcement'. International Journal of Civil and Structural Engineering 1 (1), 101-113

Swartz, S. E. and Tada, N. M. (1990) 'Mixed Mode Crack Propagation and Fracture in Concrete'. Engineering Fracture Mechanics 35 (1/2/3), 137-144

Swartz, S. E., Lu, L. W., Tang, L. D., and Refai, T. M. E. (1988) 'Mode II Fracture-Parameter Estimates for Concrete from Beam Specimens'. Experimental Mechanics 28 (2), 146-153

Tada, H., Paris, P. C., and Irwin, G. R. (2000) The Stress Analysis of Cracks Handbook. third edn. New York, the USA: The American Society of Mechanical Engineers

Taerwe, L. and Gysel, A. (1996) 'Influence of Steel Fibers on Design Stress-Strain Curve for High-Strength Concrete'. Journal of Engineering Mechanics 122 (8), 695-704

Taylor, H. P. J. (1974) 'The Fundamental Behavior of Reinforced Concrete Beams in Bending and Shear'. American Concrete Institute Journal Special Publication 42, 43-78

The Highways Agency (1992) 'Highway Construction Details'. in Manual of Contract Documents for Highway Works. ed. by AnonUK: The Highways Agency, B9

Theiner, Y. and Hofstetter, G. (2009) 'Numerical Prediction of Crack Propagation and Crack Widths in Concrete Structures'. Engineering Structures 31 (8), 1832-1840

Vanelstraete, A. and Francken, L. (1997) RELEM REPORT 18 Prevention of Reflective Cracking in Pavements. First edn. UK: E & FN Spon, 35

Voo, J. Y. L. and Foster, S. J. (2003) 'Variable Engagement Model for Fibre Reinforced Concrete in Tension'. in Uniciv Report no. R-420,. ed. by AnonSydney, Australia: The University of New South Wales, 88

Walraven, J. C. (1981) 'Fundamental Analysis of Aggregate Interlock'. Journal of the Structural Division, ASCE 107 (ST11), 2245-2270

Watkins, J. and Liu, K. L. W. (1985) 'A Finite Element Study of the Short Beam Test Specimen Under Mode II Loading'. International Journal of Cement Composites and Lightweight Concrete 7 (1), 39-47

Westergaard, H. M. (1926) 'Stresses in Concrete Pavements Computed by Theoretical Analysis '. Public Roads 7 (2), 25-35

Xu, S., Reinhardt, H. W., and Zhang, X. (eds.) (2005) 11th International Conference on Fracture. 'Shear Capability of Reinforced Concrete Beams without Stirrups Predicted using a Fracture Mechanical Approach'. held 20-25 March at Turin, Italy

Zhang, J. and Li, V. C. (2002) 'Monotonic and Fatigue Performance in Bending of Fiber-Reinforced Engineered Cementitious Composite in Overlay System'. Cement and Concrete Research 32 (3), 415-423

Zhou, F., Hu, S., Hu, X., Scullion, T., Mikhail, M., and Walubita, L. F. (2010) 'Development, Calibration, and Verification of a New Mechanistic-Empirical Reflective Cracking Model for HMA Overlay Thickness Design and Analysis'. Journal of Transportation Engineering 136 (4), 353-369

Zsutty, T. C. (1968) 'Beam Shear Strength Prediction by Analysis of Existing Data'. American Concrete Institute Journal, Proceedings V 65 V 65 (11), 943-951

Zsutty, T. C. (1971) 'Shear Strength Prediction for Separate Categories of Simple Beam Tests'. American Concrete Institute Journal 68, 138-143

Appendix Input Files for Simulations in ANSYS

A.1 2D Fracture Simulations of SNSBT

```
FINI
/CLEAR
/FILNAME, SNSBT2D_CRACKED 6_COH
/TITLE,ANALYSIS OF THE STRESS INTENSITY FACTOR

/PREP7
ET, 1, PLANE183
KEYOPT, 1, 3, 3
R, 1, 5
MP, EX, 1, 4E4
MP, PRXY, 1, 0.25
TBDELE, CZM, 2,,
TB, CZM, 2, 1, , CBDD
TBDATA, 1, 4, 5 , 4, 5, 0.1,  1

/PNUM, KP, 1
/PNUM, LINE, 1
/PNUM, AREA, 1
K, 1, 0
K, 2, 20
K, 3, 26
K, 4,250
K, 5, 250, 100
K, 6, 176, 100
K, 7, 170, 100
K, 8, 1, 100
K, 9, 0, 74
K, 10,9.18,64
K, 11, 14.85, 54
K, 12, 18.89, 44
K, 13, 21.78, 34
K, 14, 23.805, 24
K, 15, 25.123, 14
K, 16, 0,74
K, 17, 9.18,64
K, 18, 14.85, 54
K, 19, 18.89, 44
K, 20, 21.78, 34
K, 21, 23.805, 24

K, 22, -1, 100
K, 23, -20, 100
K, 24, -26, 100
K, 25, -250, 100
K, 26, -250
K, 27, -176
K, 28, -170
K, 29, 25.123, 14, 1
L, 1, 2
L, 2, 3
L, 3, 4
L, 4, 5
L, 5, 6
L, 6, 7
L, 7, 8
L, 8, 9
L, 9, 10
L, 10, 11
L, 11, 12
L, 12, 13
L, 13, 14
L, 14, 15
L, 15, 3
L, 15, 21
L, 21, 20
L, 20, 19
L, 19, 18
L, 18, 17
L, 17, 16
L, 16, 22
L, 22, 23
L, 23, 24
L, 24, 25
L, 25, 26
L, 26, 27
L, 27, 28
L, 28, 1
LSEL, S,,, 3, 15,
AL, ALL
LSEL, S,,,15,29
LSEL, A,,,1,2
AL, ALL
KSCON, 15, 3, 1, 10, 0.75
TYPE, 1
MAT, 1
ESIZE, 5, 0
MSHKEY,0
AMESH, ALL
/COM, CONTACT PAIR CREATION - START
CM,_NODECM,NODE
CM,_ELEMCM,ELEM
CM,_KPCM,KP
CM,_LINECM,LINE
CM,_AREACM,AREA
CM,_VOLUCM,VOLU
/GSAV,CWZ,GSAV,,TEMP
MP,MU,2,
MAT,2
MP,EMIS,2,7.88860905221E-031
R,3
REAL,3
ET,2,169
ET,3,172
```

```
R,3,,,-5,,0,
RMORE,,,1.0E20,0.0,1.0,-5
RMORE,0.0,0,1.0,,1.0,0.5
RMORE,0,1.0,1.0,0.0,,1.0
KEYOPT,3,3,0
KEYOPT,3,4,0
KEYOPT,3,5,0
KEYOPT,3,7,0
KEYOPT,3,8,0
KEYOPT,3,9,0
KEYOPT,3,10,0
KEYOPT,3,11,0
KEYOPT,3,12,5
KEYOPT,3,2,0
! GENERATE THE TARGET SURFACE
LSEL,S,,,16
LSEL,A,,,17
LSEL,A,,,18
LSEL,A,,,19
LSEL,A,,,20
LSEL,A,,,21
CM,_TARGET,LINE
TYPE,2
NSLL,S,1
ESLN,S,0
ESURF
CMSEL,S,_ELEMCM
! GENERATE THE CONTACT SURFACE
LSEL,S,,,9
LSEL,A,,,10
LSEL,A,,,11
LSEL,A,,,12
LSEL,A,,,13
LSEL,A,,,14
CM,_CONTACT,LINE
TYPE,3
NSLL,S,1
ESLN,S,0
ESURF
ALLSEL
ESEL,ALL
ESEL,S,TYPE,,2
ESEL,A,TYPE,,3
ESEL,R,REAL,,3
/PSYMB,ESYS,1
/PNUM,TYPE,1
/NUM,1
EPLOT
ESEL,ALL
ESEL,S,TYPE,,2
ESEL,A,TYPE,,3
ESEL,R,REAL,,3
CMSEL,A,_NODECM
CMDEL,_NODECM
CMSEL,A,_ELEMCM
CMDEL,_ELEMCM
CMSEL,S,_KPCM
CMDEL,_KPCM
CMSEL,S,_LINECM
CMDEL,_LINECM
CMSEL,S,_AREACM
CMDEL,_AREACM
CMSEL,S,_VOLUCM
CMDEL,_VOLUCM
/GRES,CWZ,GSAV
CMDEL,_TARGET
CMDEL,_CONTACT
/COM, CONTACT PAIR CREATION - END
EPLOT
FINISH

/SOLU
ANTYPE, STATIC
KPLOT
CSKP,11,0,15,14,29,1,1,
LSEL, ALL
FLST,2,1,4,ORDE,1
FITEM,2,24
SFL,P51X,PRES, 91.6,
FLST,2,1,4,ORDE,1
FITEM,2,6
SFL,P51X,PRES, 12.18,
FLST,2,2,4,ORDE,2
FITEM,2,2
FITEM,2,28
DL,P51X, ,ALL,0
EPLOT
SOLVE
FINISH

/POST1
FLST,2,5,1
FITEM,2,276
FITEM,2,282
FITEM,2,280
FITEM,2,3670
FITEM,2,3672
PATH,60MMCOH,5,30,20,
PPATH,P51X,1
PATH,STAT
KCALC,0,1,3,0
PLNSOL, U, SUM
PLNSOL, S, EQV
```

A.2 3D Cracking and Crushing Models of SNSBT

```
FINI
/CLEAR
/FILNAME, SNSBT3D_COMPOSITE
/TITLE, CRACKING AND CRUSHING ANALYSIS OF SNSBT

/PREP7
ET, 1, SOLID65
MP, EX, 1, 2.1E5
MP, NUXY, 1, 0.15
MP, DENS, 1, 2480E-9
R, 1, 1,0.015,0,0, 1,0.015,90,0, 1,0.015,90,90
TB,CONCR,1
TBDATA, 1, 0.1, 1, 9, 80
KEYOPT,1,7,1
ET, 2, SOLID65
MP, EX, 2, 2.1E5
MP, NUXY, 2, 0.15
!MP, DENS, 2, 2480E-9
R, 2, 1,0.015,0,0, 1,0.015,90,0, 1,0.015,90,90
TB,CONCR,2
TBDATA, 1, 0.1, 1, 9, 80
KEYOPT,1,7,1
ET, 3, SOLID45
MP, EX, 3, 1E5
MP, PRXY, 3, 0.3
ET, 4, INTER205
TB,CGCR,4,,3,LINEAR
TBDATA,1,0.28,0.8,0.8

/PNUM, VOLUME, 1
BLOCK, -250, 250, 0, 80, 0, 50
BLOCK, -250, 250, 80, 130, 0, 50
BLOCK, -1, 1, 100, 130, 0, 50
VSBV, 2, 3
BLOCK, -26, -20, 130, 135, 0, 50
BLOCK, 170, 176, 130, 135, 0, 50
BLOCK, -176, -170, -5, 0, 0, 50
BLOCK, 20, 26, -5, 0, 0, 50
VGLUE,4,2,3
VGLUE,1,5,6
ALLSEL
TYPE, 1
MAT, 1
MSHAPE, 1, 3D
MSHKEY,3
ESIZE, 9, 0
VMESH, 7
TYPE, 2
MAT, 2
MSHAPE, 1, 3D
MSHKEY,3
ESIZE, 9, 0
VMESH, 4
TYPE, 3
MAT, 3
MSHAPE, 1, 3D
MSHKEY, 3
VMESH, 2, 3
VMESH, 5, 6
EPLOT
/COM, CONTACT PAIR CREATION - START
CM,_NODECM,NODE
CM,_ELEMCM,ELEM
CM,_KPCM,KP
CM,_LINECM,LINE
CM,_AREACM,AREA
CM,_VOLUCM,VOLU
/GSAV,CWZ,GSAV,,TEMP
MP,MU,1,0.2
MAT,1
MP,EMIS,1,7.88860905221E-031
R,3
REAL,3
ET,5,170
ET,6,174
R,3,,,1.0,0.1,0,
RMORE,,,1.0E20,0.0,1.0,
RMORE,10,0,1.0,,1.0,0.5
RMORE,0,1.0,1.0,0.0,,1.0
KEYOPT,6,4,0
KEYOPT,6,5,0
KEYOPT,6,7,0
KEYOPT,6,8,0
KEYOPT,6,9,0
KEYOPT,6,10,2
KEYOPT,6,11,0
KEYOPT,6,12,0
KEYOPT,6,2,0
KEYOPT,5,5,0
! GENERATE THE TARGET SURFACE
ASEL,S,,,9
CM,_TARGET,AREA
TYPE,5
NSLA,S,1
ESLN,S,0
ESLL,U
ESEL,U,ENAME,,188,189
NSLE,A,CT2
ESURF
CMSEL,S,_ELEMCM
! GENERATE THE CONTACT SURFACE
ASEL,S,,,4
CM,_CONTACT,AREA
TYPE,6
NSLA,S,1
ESLN,S,0
NSLE,A,CT2
ESURF
!* CREATE COMPANION PAIR - START
R,4
REAL,4
```

```
ET,7,170
ET,8,174
R,4,,,1.0,0.1,0,
RMORE,,,1.0E20,0.0,1.0,
RMORE,10,0,1.0,,1.0,0.5
RMORE,0,1.0,1.0,0.0,,1.0
KEYOPT,8,4,0
KEYOPT,8,5,0
KEYOPT,8,7,0
KEYOPT,8,8,0
KEYOPT,8,9,0
KEYOPT,8,10,2
KEYOPT,8,11,0
KEYOPT,8,12,0
KEYOPT,8,2,0
KEYOPT,7,1,0
KEYOPT,7,3,0
KEYOPT,7,5,0
TYPE,7
ESEL,S,TYPE,,6
NSLE,S
ESLN,S,0
ESURF
TYPE,8
ESEL,S,TYPE,,5
NSLE,S
ESLN,S,0
ESURF
!* CREATE COMPANION PAIR - END
ALLSEL
ESEL,ALL
ESEL,S,TYPE,,5
ESEL,A,TYPE,,6
ESEL,R,REAL,,3
/PSYMB,ESYS,1
/PNUM,TYPE,1
/NUM,1
EPLOT
ESEL,ALL
ESEL,S,TYPE,,5
ESEL,A,TYPE,,6
ESEL,R,REAL,,3
ESEL,A,TYPE,,7
ESEL,A,TYPE,,8
CMSEL,A,_NODECM
CMDEL,_NODECM
CMSEL,A,_ELEMCM
CMDEL,_ELEMCM
CMSEL,S,_KPCM
CMDEL,_KPCM
CMSEL,S,_LINECM
CMDEL,_LINECM
CMSEL,S,_AREACM
CMDEL,_AREACM
CMSEL,S,_VOLUCM
CMDEL,_VOLUCM
/GRES,CWZ,GSAV
CMDEL,_TARGET
CMDEL,_CONTACT
/COM, CONTACT PAIR CREATION - END
/MREP,EPLOT
TYPE,4
MAT,4
CSYS,0
NSEL,S,LOC,Y,80-0.1E-5,80+0.1E-5
!NSEL,ALL
NUMMRG,NODES
ESLN
CZMESH,,,0,Y,80,

/SOLU   !ENTER SOLVER
APLOT
ASEL, S, , , 13
SFA, ALL, , PRES, 34.6
ASEL, S, , , 26
SFA, ALL, , PRES, 4.3
ASEL, S, , , 31
ASEL, A, , , 37
DA, ALL, ALL, 0, 1
ASEL, S, , , 23
ASEL, A, , , 7
ASEL, A, , , 45
ASEL, A, , ,22
ASEL, A, , , 35
ASEL, A, , , 29
DA,ALL,SYMM
SOLCONTROL,OFF
LNSRCH,ON
NCNV,0
EQSLV,-1
DELTIM,1,0,0
OUTRES,ERASE
OUTRES,ALL,1
AUTOTS,0
TIME,50
ALLSEL
SOLVE

/POST1
PLNSOL, U, SUM
PLNSOL, S, EQV
PLCRACK, 0, 0
```

A.3 3D Simulations of Foundation Tests

```
FINI
/CLEAR
/FILNAME, FOUNDATION_TEST
/TITLE, FOUNDATION TEST

/PREP7
ET, 1, SOLID65
MP, EX, 1, 2.1E5
MP, NUXY, 1, 0.15
!MP, DENS, 1, 2480E-9
R, 1, 1,0.015,0,0, 1,0.015,90,0, 1,0.015,90,90
TB,CONCR,1
TBDATA, 1, 0.1, 1, 9, 80
KEYOPT,1,7,1
ET, 2, SOLID65
MP, EX, 2, 2.1E5
MP, NUXY, 2, 0.15
!MP, DENS, 2, 2480E-9
R, 2, 1,0.015,0,0, 1,0.015,90,0, 1,0.015,90,90
TB,CONCR,2
TBDATA, 1, 0.1, 1, 9, 80
KEYOPT,1,7,1
ET, 3, SOLID45
MP, EX, 3, 100
MP, PRXY, 3, 0.3
ET, 4, SOLID45
MP, EX, 4, 30000
MP, PRXY, 4, 0.3
ET, 5, SOLID45
MP, EX, 5, 500
MP, PRXY, 5, 0.3
ET, 6, INTER205
!KEYOPT,0
!TB,CZM,,,,
!TBDATA,1,10,0.5,0.5
TB,CGCR,6,,3,LINEAR
TBDATA,1,0.28,0.8,0.8

/PNUM, VOLUME, 1
BLOCK, -250, 250, 0, 50, 0, 50
BLOCK, -250, 250, 50, 130, 0, 50
BLOCK, -1, 1, 0, 30, 0, 50
VSBV, 1, 3
BLOCK, 10, 40, 130, 140, 0, 50
BLOCK, -25, 75, -25, 0, 0, 50
BLOCK, -550, 550, -70, 0, 0, 375
VSBV, 5, 3
BLOCK, -25, 75, -25, 0, 0, 50
BLOCK, -550, 550, -300, -70, 0, 375
VGLUE,1,2
VGLUE,3,5,6
ALLSEL
TYPE, 1
MAT, 1
MSHAPE, 1, 3D
MSHKEY,3
ESIZE, 10, 0
VMESH, 7

TYPE, 2
MAT, 2
MSHAPE, 1, 3D
MSHKEY,3
ESIZE, 10, 0
VMESH, 4
TYPE, 3
MAT, 3
MSHAPE, 1, 3D
MSHKEY, 3
ESIZE, 15, 0
VMESH, 1
VMESH,3
EPLOT
TYPE, 4
MAT, 4
MSHAPE, 1, 3D
MSHKEY,3
ESIZE, 40, 0
VMESH, 2
TYPE, 5
MAT, 5
MSHAPE, 1, 3D
MSHKEY,3
ESIZE, 50, 0
VMESH, 5

/COM, CONTACT PAIR CREATION - START
CM,_NODECM,NODE
CM,_ELEMCM,ELEM
CM,_KPCM,KP
CM,_LINECM,LINE
CM,_AREACM,AREA
CM,_VOLUCM,VOLU
/GSAV,CWZ,GSAV,,TEMP
MP,MU,2,0.2
MAT,2
MP,EMIS,2,7.88860905221E-031
R,3
REAL,3
ET,7,170
ET,8,174
R,3,,,1.0,0.1,0,
RMORE,,,1.0E20,0.0,1.0,
RMORE,0.0,0,1.0,,1.0,0.5
RMORE,0,1.0,1.0,0.0,,1.0
KEYOPT,8,4,0
KEYOPT,8,5,0
KEYOPT,8,7,0
KEYOPT,8,8,0
KEYOPT,8,9,0
KEYOPT,8,10,2
KEYOPT,8,11,0
```

```
KEYOPT,8,12,0
KEYOPT,8,2,0
KEYOPT,7,5,0
! GENERATE THE TARGET SURFACE
ASEL,S,,,19
ASEL,A,,,20
CM,_TARGET,AREA
TYPE,7
NSLA,S,1
ESLN,S,0
ESLL,U
ESEL,U,ENAME,,188,189
NSLE,A,CT2
ESURF
CMSEL,S,_ELEMCM
! GENERATE THE CONTACT SURFACE
ASEL,S,,,32
ASEL,A,,,50
CM,_CONTACT,AREA
TYPE,8
NSLA,S,1
ESLN,S,0
NSLE,A,CT2
ESURF
ALLSEL
ESEL,ALL
ESEL,S,TYPE,,7
ESEL,A,TYPE,,8
ESEL,R,REAL,,3
/PSYMB,ESYS,1
/PNUM,TYPE,1
/NUM,1
EPLOT
ESEL,ALL
ESEL,S,TYPE,,7
ESEL,A,TYPE,,8
ESEL,R,REAL,,3
CMSEL,A,_NODECM
CMDEL,_NODECM
CMSEL,A,_ELEMCM
CMDEL,_ELEMCM
CMSEL,S,_KPCM
CMDEL,_KPCM
CMSEL,S,_LINECM
CMDEL,_LINECM
CMSEL,S,_AREACM
CMDEL,_AREACM
CMSEL,S,_VOLUCM
CMDEL,_VOLUCM
/GRES,CWZ,GSAV
CMDEL,_TARGET
CMDEL,_CONTACT
/COM, CONTACT PAIR CREATION - END
/MREP,EPLOT
/DIST,1,1.08222638492,1
/REP,FAST
/DIST,1,1.08222638492,1
/REP,FAST
/DIST,1,1.08222638492,1
/REP,FAST
/DIST,1,1.08222638492,1
/REP,FAST

/COM, CONTACT PAIR CREATION - START
CM,_NODECM,NODE
CM,_ELEMCM,ELEM
CM,_KPCM,KP
CM,_LINECM,LINE
CM,_AREACM,AREA
CM,_VOLUCM,VOLU
/GSAV,CWZ,GSAV,,TEMP
MP,MU,1,
MAT,1
MP,EMIS,1,7.88860905221E-031
R,4
REAL,4
ET,9,170
ET,10,174
R,4,,,1.0,0.5,0,
RMORE,,,1.0E20,0.0,1.0,
RMORE,0.0,0,1.0,,1.0,0.5
RMORE,0,1.0,1.0,0.0,,1.0
KEYOPT,10,4,0
KEYOPT,10,5,0
KEYOPT,10,7,0
KEYOPT,10,8,0
KEYOPT,10,9,0
KEYOPT,10,10,2
KEYOPT,10,11,0
KEYOPT,10,12,0
KEYOPT,10,2,0
KEYOPT,9,5,0
! GENERATE THE TARGET SURFACE
ASEL,S,,,9
CM,_TARGET,AREA
TYPE,9
NSLA,S,1
ESLN,S,0
ESLL,U
ESEL,U,ENAME,,188,189
NSLE,A,CT2
ESURF
CMSEL,S,_ELEMCM
! GENERATE THE CONTACT SURFACE
ASEL,S,,,4
CM,_CONTACT,AREA
TYPE,10
NSLA,S,1
ESLN,S,0
NSLE,A,CT2 ! CZMESH PATCH (FSK QT-40109 8/2008)
ESURF
ALLSEL
ESEL,ALL
ESEL,S,TYPE,,9
ESEL,A,TYPE,,10
ESEL,R,REAL,,4
/PSYMB,ESYS,1
```

```
/PNUM,TYPE,1
/NUM,1
EPLOT
ESEL,ALL
ESEL,S,TYPE,,9
ESEL,A,TYPE,,10
ESEL,R,REAL,,4
CMSEL,A,_NODECM
CMDEL,_NODECM
CMSEL,A,_ELEMCM
CMDEL,_ELEMCM
CMSEL,S,_KPCM
CMDEL,_KPCM
CMSEL,S,_LINECM
CMDEL,_LINECM
CMSEL,S,_AREACM
CMDEL,_AREACM
CMSEL,S,_VOLUCM
CMDEL,_VOLUCM
/GRES,CWZ,GSAV
CMDEL,_TARGET
CMDEL,_CONTACT
/COM, CONTACT PAIR CREATION - END

/SOLU
APLOT
ASEL, S, , , 13
SFA, ALL, , PRES, 10

ASEL, S, , , 41
DA, ALL, ALL, 0, 1
ASEL, S, , , 1
ASEL, A, , , 47
ASEL, A, , , 21
ASEL, A, , ,23
ASEL, A, , , 49
ASEL, A, , , 39
DA,ALL,SYMM
SOLCONTROL,OFF
LNSRCH,ON
NLGEOM,0
NCNV,0
EQSLV,-1
DELTIM,1,0,0
OUTRES,ERASE
OUTRES,ALL,1
AUTOTS,0
TIME,10
ALLSEL
SOLVE

/POST1
PLNSOL, U, SUM
PLNSOL, S, EQV
PLCRACK, 0, 0
```

A.4 3D Simulations of Pavement

```
INI
/CLEAR
/FILNAME, PAVEMENT
/TITLE,ANALYSIS OF THE STRESS INTENSITY FACTOR

/PREP7
ET, 1, PLANE182
KEYOPT, 1, 1, 2
KEYOPT,1,3,2
R, 1, 5
MP, EX, 1, 3.2E4
MP, PRXY, 1, 0.19

ET, 1, PLANE182
KEYOPT, 1, 1, 2
KEYOPT,1,3,2
R, 1, 5
MP, EX, 2, 2.5E4
MP, PRXY, 2, 0.21

ET, 1, PLANE182
KEYOPT, 1, 1, 2
KEYOPT,1,3,2
R, 1, 5
MP, EX, 3, 5000
MP, PRXY, 3, 0.2

ET, 1, PLANE182
KEYOPT, 1, 1, 2
KEYOPT,1,3,2
R, 1, 5
MP, EX, 4, 33
MP, PRXY, 4, 0.4
TB,DP,4,,,
TBMODIF,4,1,0.001
TBMODIF,4,2,32
TBMODIF,4,3,0


/PNUM, KP, 1
/PNUM, LINE, 1
/PNUM, AREA, 1

K, 1, -2250, 350
K, 2, 0, 350
K, 31, 0, 350
K, 3, 2250, 350
K, 4, 2250, 500
K, 5, 250, 500
K, 6, 0, 500
K, 7, -2250, 500

K, 8,-2250,150
K, 9, 0,150
K, 10, 0, 150
K, 11, 2250, 150
K, 12, 2250, 350
K, 13, 0, 350
K, 28, 0, 350
K, 30, 0, 400
K, 14, -2250, 350

K, 15, -2250, 0
K, 16, 2250, 0
K, 17, 2250, 150
K, 18, 200, 150
K, 19, 200, 100
K, 20, -50, 100
K, 21, -50, 150
K, 22, -2250, 150

K, 23, -3250, -500
K, 24, 3250, -500
K, 25, 3250, 0
K, 26, -3250, 0

K, 27, 0, 400, 1
K, 29, 0, 0


L, 2, 3
L, 3, 4
L, 4, 5
L, 5, 6
L, 6, 30
L, 30, 2

L, 1, 31
L, 31, 30
L, 30, 6
L, 6, 7
L, 7, 1

L, 8, 9
L, 9, 13
L, 13, 14
L, 14, 8

L, 10, 11
L, 11,12
L, 12,28
L, 28, 10

L, 15, 16
L, 16, 17
L, 17, 18
L, 18, 19
L, 19, 20
L, 20, 21
L, 21, 22
L, 22, 15

L, 23, 24
L, 24, 25
```

```
L, 25, 26
L, 26, 23


LSEL, S,,, 1, 6
AL, ALL
LSEL, S,,,7,10
LSEL, A,,,5
AL, ALL

LSEL, S,,,11, 14
AL, ALL

LSEL, S,,, 15, 18
AL, ALL

LSEL, S,,, 19, 26
AL, ALL

LSEL, S,,, 27, 30
AL, ALL
AGLUE, 3, 5
AGLUE, 4, 8
AGLUE, 5, 6


KSCON, 30, 5, 1, 10, 0.75
TYPE, 1
MAT, 1
ESIZE, 15, 0
MSHKEY,0
AMESH, 1,2

TYPE, 1
MAT, 2
ESIZE, 15, 0
MSHKEY,0
AMESH,3
AMESH,7

TYPE, 1
MAT, 3
ESIZE, 15, 0
MSHKEY,0
AMESH, 5

TYPE, 1
MAT, 3
ESIZE, 50, 0
MSHKEY,0
AMESH, 4


CONTACT CRACKING
/COM, CONTACT PAIR CREATION - START
CM,_NODECM,NODE
CM,_ELEMCM,ELEM
CM,_KPCM,KP
CM,_LINECM,LINE
CM,_AREACM,AREA
CM,_VOLUCM,VOLU
/GSAV,CWZ,GSAV,,TEMP
MP,MU,5,0
MAT,5
MP,EMIS,5,7.88860905221E-031
R,4
REAL,4
ET,4,169
ET,5,172
R,4,,,-8.93,0.1,0,
RMORE,,,1.0E20,0.0,1.0,-5.3
RMORE,0.0,0,1.0,,1.0,0.5
RMORE,0,1.0,1.0,0.0,,1.0
KEYOPT,5,3,0
KEYOPT,5,4,0
KEYOPT,5,5,0
KEYOPT,5,7,0
KEYOPT,5,8,0
KEYOPT,5,9,0
KEYOPT,5,10,0
KEYOPT,5,11,0
KEYOPT,5,12,5
KEYOPT,5,2,0

LSEL,S,,,6
CM,_TARGET,LINE
TYPE,4
NSLL,S,1
ESLN,S,0
ESURF
CMSEL,S,_ELEMCM

LSEL,S,,,8
CM,_CONTACT,LINE
TYPE,5
NSLL,S,1
ESLN,S,0
ESURF
ALLSEL
ESEL,ALL
ESEL,S,TYPE,,4
ESEL,A,TYPE,,5
ESEL,R,REAL,,4
/PSYMB,ESYS,1
/PNUM,TYPE,1
/NUM,1
EPLOT
ESEL,ALL
ESEL,S,TYPE,,4
ESEL,A,TYPE,,5
ESEL,R,REAL,,4
CMSEL,A,_NODECM
CMDEL,_NODECM
CMSEL,A,_ELEMCM
CMDEL,_ELEMCM
CMSEL,S,_KPCM
CMDEL,_KPCM
CMSEL,S,_LINECM
```

```
CMDEL,_LINECM
CMSEL,S,_AREACM
CMDEL,_AREACM
CMSEL,S,_VOLUCM
CMDEL,_VOLUCM
/GRES,CWZ,GSAV
CMDEL,_TARGET
CMDEL,_CONTACT
/COM, CONTACT PAIR CREATION - END

TBDELE, CZM, 5,,
TB, CZM, 5, 1, , CBDD
TBDATA, 1, 14.73, 5.3 , 8.93, 5.3, 0.1,  1

/COM, CONTACT PAIR CREATION - START
CM,_NODECM,NODE
CM,_ELEMCM,ELEM
CM,_KPCM,KP
CM,_LINECM,LINE
CM,_AREACM,AREA
CM,_VOLUCM,VOLU
/GSAV,CWZ,GSAV,,TEMP
MP,MU,1,14.55
MAT,1
MP,EMIS,1,7.88860905221E-031
R,3
REAL,3
ET,2,169
ET,3,172
R,3,,,1.0,0.1,0,
RMORE,,,4.29,0.0,1.0,
RMORE,2.7,0,1.0,,1.0,0.5
RMORE,0,1.0,1.0,0.0,,1.0
KEYOPT,3,3,0
KEYOPT,3,4,0
KEYOPT,3,5,0
KEYOPT,3,7,0
KEYOPT,3,8,0
KEYOPT,3,9,0
KEYOPT,3,10,2
KEYOPT,3,11,0
KEYOPT,3,12,0
KEYOPT,3,2,0

LSEL,S,,,1
LSEL,A,,,7
CM,_TARGET,LINE
TYPE,2
NSLL,S,1
ESLN,S,0
ESURF
CMSEL,S,_ELEMCM

LSEL,S,,,13
LSEL,A,,,17
CM,_CONTACT,LINE
TYPE,3
NSLL,S,1
ESLN,S,0
ESURF
ALLSEL
ESEL,ALL
ESEL,S,TYPE,,2
ESEL,A,TYPE,,3
ESEL,R,REAL,,3
/PSYMB,ESYS,1
/PNUM,TYPE,1
/NUM,1
EPLOT
ESEL,ALL
ESEL,S,TYPE,,2
ESEL,A,TYPE,,3
ESEL,R,REAL,,3
CMSEL,A,_NODECM
CMDEL,_NODECM
CMSEL,A,_ELEMCM
CMDEL,_ELEMCM
CMSEL,S,_KPCM
CMDEL,_KPCM
CMSEL,S,_LINECM
CMDEL,_LINECM
CMSEL,S,_AREACM
CMDEL,_AREACM
CMSEL,S,_VOLUCM
CMDEL,_VOLUCM
/GRES,CWZ,GSAV
CMDEL,_TARGET
CMDEL,_CONTACT
/COM, CONTACT PAIR CREATION - END

PLOT    !SHOW ELEMENTS
FINISH

/SOLU   !ENTER SOLVER
ANTYPE, STATIC          !STATIC ANALYSIS
KPLOT !SHOW KEYPOINTS

CSKP,11,0,30,10,27,1,1,

LSEL,ALL

FLST,2,1,4,ORDE,1
FITEM,2,4
SFL,P51X,PRES,3.5,

FLST,2,1,4,ORDE,1
FITEM,2,27
DL,P51X, ,ALL,0

FLST,2,2,4,ORDE,2
FITEM,2,30
FITEM,2,28
DL,P51X, ,UX,0

SOLCONTROL,OFF
LNSRCH,ON
NCNV,0
EQSLV,-1
```

```
NEQIT,200
DELTIM,1,0,0
OUTRES,ERASE
OUTRES,ALL,1
 AUTOTS,0

TIME,1
ALLSEL

EPLOT
SOLVE  !START SOLVING
FINISH

/POST1  !ENTER POST1 POSTPROCESSER
FLST,2,5,1
FITEM,2,313
FITEM,2,325
FITEM,2,1760
FITEM,2,326
FITEM,2,1761
PATH,50MM,5,30,20,
PPATH,P51X,1
PATH,STAT
KCALC,0,1,3,0
```